12-2014

INVESTIGATION OF SUBGRID-SCALE MIXING IN TURBULENT PLANE JETS AND TURBULENT JET FLAMES

Shuaishuai Liu
Clemson University, shuaisl@clemson.edu

INVESTIGATION OF SUBGRID-SCALE MIXING IN TURBULENT PLANE JETS AND TURBULENT JET FLAMES

A Dissertation
Presented to
the Graduate School of
Clemson University

In Partial Fulfillment
of the Requirements for the Degree
Doctor of Philosophy
Mechanical Engineering

---

by
Shuaishuai Liu
Dec 2014

Accepted by:
Dr. Chenning Tong, Committee Chair
Dr. Richard Miller
Dr. Xiangchun Xuan
Dr. Jay Ochterbeck

Abstract

The subgrid-scale (SGS) mixing of mixture fraction, temperature, and species mass fraction in turbulent partially premixed (Sandia) flames is studied. We focus on the effects of the SGS mixing regimes and the spatial relationships among the scalars on the SGS mixing of the species mass fractions. High resolution lines images are used to obtain the scalar filtered mass density function and the conditionally filtered diffusion. The results show that for small SGS variance the scalar fields have a relatively simple structure. For large SGS variance the structure is more complex. The spatial relationships among the scalars result in different SGS scalar structures and SGS mixing characteristics, with the mass fraction of CO_2 being the simplest and that of CO being the most complex. The results in this study present a challenging test for SGS mixing models.

Recent studies of subgrid-scale (SGS) mixing and turbulence-chemistry interaction have shown that turbulent flames contain different structures. In flamelets diffusion of reactive scalars and chemical reaction are tightly coupled. Most mixing models used in probability density and filtered density methods, however, are based on non-reactive scalars. To investigate the effects of the coupling on the diffusion we decompose a reactive scalar into a steady flamelet part and perturbations from it. The diffusion of the former can be obtained from a flamelet solution while the latter is unclosed. The conditionally filtered diffusion and dissipation of the reactive scalar perturbations are analyzed using high-resolution line images obtained in turbulent partially premixed (Sandia) flames. For SGS scalar containing flamelets, the perturbation diffusion has characteristics similar to that of a non-reactive scalar, in contrast with the flamelet part. The functional form of the conditionally filtered diffusion is well described by the Interaction by Exchange with the Mean (IEM) model. Our perturbation analysis of the flamelet equation shows that for perturbations having length scales smaller than the reaction zone width, the reactive scalar diffusion are largely controlled by the mixture fraction field, thus have the characteristics of non-reactive scalar mixing. For perturbations with length scales larger than the reaction width, the conditionally filtered diffusion has the same form as non-reactive scalar

mixing, with the mixing time scale given by the flamelet. The IEM model predictions based on this mixing time scale are in good agreement with the experimental results for a range of SGS conditions, suggesting that the perturbations for the conditions studied are consistent with unsteady flamelets. Thus, mixing models based on non-reactive scalars can potentially model the SGS mixing accurately. The results in the present study can be useful for developing a unified mixing model that can predict all combustion regimes accurately.

There already have extensive studies about turbulent mixing based on two-scalars. However, in many applications such as reactive flows, at least three scalar (two reactants and one product) are involved. The mixing process is multiscalar and more complex. In the present study, we investigate three-scalar mixing in temporally developing plane jets using direct numerical simulation (DNS). The flow configuration consists of five streams: a central jet, two off-central jets surround the central jet, and two coflows surround the off-central jets. The mixing process is analyzed in detail using joint probability density functions (JPDF), conditional diffusion, and conditional dissipation rate. The results show that the mixing process is greatly influenced by the upstream conditions, with high quality of mixing favored by high initial velocity gradients and high ratios between the central and off-central jet widths. The scalar JPDF and the conditional dissipation rates obtained in current simulations show some similarities to these of mixture fraction and temperature in turbulent flames. The present study, therefore, provide a basis for understanding the multiscalar mixing in reactive flows.

Dedication

To my parents

Acknowledgments

First and foremost, I would like to express my gratitude to my advisor, Dr. Chenning Tong, for the opportunity to work with him, for giving me the freedom to do things my way, for constantly guiding and supporting me, for finally, introducing me to the world of turbulent combustion. I would like to thank Dr. Richard S. Miller, Dr. Xiangchun Xuan, Dr. Jay Ochterbeck, for giving up their valuable time for serving on my advisory committees.

I would also like to thank all the Palmetto staffs for quickly responding my questions. Without their patience and generosity, the completion of the simulations would not be possible. I am thankful for all of my colleagues, Jian Cai, Khuong Ngyuan, Wei Li, who have provided all kinds of help when it was needed.

I would not be finishing my doctoral studies without the support and encouragement from my parents. Anything I say here will not justify their contribution to my progress. I am forever indebted to them. Five years is a long time, and during my stay in Clemson I made many friends who enriches my life in numerous ways, and I am very grateful for their support and friendship.

Table of Contents

List of Tables

List of Figures

Chapter 1

Introduction

Combustion of fossil fuels supplies more than 80% of the total energy needs in the world despite the large variety of energy sources such as nuclear, solar, wind, etc [1]. Combustion technology will remain important for the foreseeable future because of this dominance of fossil fuels. In addition for generating heat, combustion also produces pollutants such as nitrogen oxides, soot, and hydrocarbons. Moreover, the unavoidable byproduct of hydrocarbon combustion, CO_2, are generally considered to be the primary cause of global warming. Improving the combustion process, therefore, is key for reducing the emissions as well as increasing fuel economy.

For combustion process in engineering devices, such as furnaces, boilers, gas-turbines, and internal combustion engines, the flows involved are generally turbulent because of their large Reynolds numbers. Turbulence greatly increases the mixing rate and thereby the fuel consumption rate [2]. Combustion processes in these devices are often characterized by complex turbulence-chemistry interactions that span multiple combustion regimes, such as premixed flame propagation, mixing-controlled burning, and chemical-kinetics-controlled processes may occur simultaneously within a single device [3]. While there may be many other complexities involving spray, radiative heat transfer, acoustics, heterogeneous combustion (wall,catalysts), etc, occurring in tortuous three-dimensional geometric configurations [3], turbulence chemistry interaction is the most fundamental process in turbulent combustion. It is, therefore, of great importance to understand turbulence-chemistry interaction occurring in the combustion devices.

Turbulent combustion can be described by the conservation equations of mass, momentum, chemical species, and energy. In order to solve these equations, it is necessary to resolve all the time and length scales involved [4]. However, in turbulent flames, the velocity and scalar fields contain a wide range of length and

time scales. The length scales vary from the size of device down to the smallest scales, i.e., the Kolmogorov length scale of turbulence, or, the smallest scales in the reaction zone. The relevant time scales range from the residence time down to the Kolmogorov timescale or the smallest chemical time scale [5]. Moreover, the chemical reactions for many fuels typically involve hundreds of species. Even for simple hydrocarbon fuels, an accurate description of the chemical reactions over a wide range of conditions requires 20-40 species. Because of the large range of scales and complex chemical mechanisms, direct numerical simulation (DNS) of turbulent combustion in engineering devices will not be possible for the coming decades. Hence, it is inevitable that a tractable and accurate approach is needed to model some parts of the combustion process rather than resolving all of them.

Several approaches have already been developed for predicting turbulent flows in the context of either RANS (Reynolds-averaged Navier Stokes) or LES (large eddy simulation). In the RANS approaches turbulent fluctuations at all scales are treated statistically. In LES, on the other hand, the large scales are resolved, and only the small, subgrid scale (SGS) are treated statistically. LES has gained popularity as a predictive method for turbulence reactive flows in recent years and has been applied to a variety of combustion problems in laboratory-scale as well as device-scale combustion systems [6, 7, 8, 9, 10, 11, 12, 13, 14, 15, 16, 17, 18, 19, 20, 21, 22]. These system and devices are often characterized by very complicated flow patterns, such as swirling flows, breakdown of large-scale vortical structure, and recirculation regions [6]. The accuracy required for prediction in such flows typically cannot be achieved using RANS simulations. Because LES resolve the large scales of velocity and scalar fields, and only the effects of small scales (SGS stress and scalar fluxes) are modeled, LES is expected to be more accurate than RANS model [23].

In LES approaches for turbulent combustion, the equation for the resolved species mass fraction and temperature contains the filtered reaction rates. The chemical reaction rates in combustion are generally highly non-linear functions of temperature. In turbulent flames temperature fluctuations are very large, typically more than several hundred Kelvin [5]. As a consequence, it is not possible to model the filtered chemical reaction rate accurately using the resolved field. Instead, the instantaneous distribution of the scalar values in each SGS grid volume, i.e. the species filtered density function (FDF), is needed. Thus, accurate modeling the FDF is critical for LES approaches to predict turbulent combustion process.

There are generally two approaches to determine the joint FDF. The first approach, the presumed FDF method assumes that the joint FDF has particular form and can be parameterized by its first and second moments, for which moments conservation equations are solved. The presumed PDF method has been used for simulating diffusion flames with simple chemistry [24, 25]. But for more generally cases, i.e., combus-

tion process involving many species, it's difficult to determine the functional form for the joint FDF in a confined irregular high-dimensional sample space. Moreover, the number of equations for first and second moments increase quadratically [4]. To overcome these difficulties, flamelet-like models [13, 18, 26, 2] were developed with the assumption that the species mass fractions are confined to a low-dimensional manifold. In that case, the species mass fraction can be parameterized by one or two variables, i.e., mixture fraction and its dissipation rate, such that solely (or primarily) the FDF of inert scalar need to be determined. However, restricting the species to a low-dimensional manifold is a very strong assumption. In turbulent flames with strong turbulence-chemistry interaction (extinction and reignition), a low-dimensional manifold may not exist.

The second approach is to directly solve the (modeled) FDF transport equations. The FDF formulation was first proposed by Pope [4] and its transport equations of a composition FDF was derived and modeled by Gao and O'Brien [27]. Perhaps the greatest advantage of these FDF approaches is that the chemical source terms are treated exactly without any model assumptions. On the other hand, the SGS mixing of reactive scalars still needs to be modeled. Previously Colucci et al [28] have developed and implemented a Lagrangian Monte Carlo method to solve the composition FDF in a constant density turbulent flow. Jaberi et al [29] extended the FDF method to variable density flows. The velocity FDF and velocity-scalar FDF were developed and exercised in turbulent reacting flow [30, 31, 32]. More recently, Sheikhi, Givi and Pope [33] developed Frequency-velocity-scalar FDF method to account for the local flow scales.

The species FDF is greatly affected by different SGS mixing regimes, i.e., the SGS mixing scenarios for non-reactive scalar (i.e. mixture fraction) and reactive scalar (i.e. temperature) are quite different. Much of the understanding of mixing of non-reactive scalars is based on the Kolmorogov-Obukhov-Corrsin theory, in which the SGS scalar is considered to have certain self-similar properties through the turbulent cascade process. In the case of mixing of reactive scalars, both turbulence and reaction can steepen the scalar gradients. The coupling effects between the molecular diffusion and chemistry depend on the ratio between reaction zone width (δ_l) and the Kolmogorov lengths scale (η)[34]. When $\delta_l/\eta \gg 1$ (distributed reaction), reaction rate is too small for it to affect the SGS mixing significantly. The coupling effect is weak such that a mixing model which successfully describe the mixing of non-reactive scalars is sufficient for distributed combustion. When $\delta_l/\eta \ll 1$ (flamelet combustion), the SGS structure of reactive scalar fields is dominated by reaction (strongly coupled with diffusion) rather than being determined by the large scales via a cascade process. The flamelet locally behaves like a plane laminar flame. Because of the locally high dissipation and heat release rate, the flamelet might play an important role for the dynamics of the flame structure.

The most challenge arises when δ_l/η is moderate. In that case, both turbulence and reaction affect molecular diffusion. Then neither distributed reaction nor flamelet combustion paradigm is sufficient to determine SGS scalar structure and the SGS scalar mixing rate. Finite reaction rate effects become important. In some particular case of turbulent combustion, there may be great spatial variations of Kolmogorov length scale and different species can have very different reaction zone width such that different combustion regimes may exist at the same instance. Consequently, it's of great value to have a general model applicable over the full range of the length scale ratio between the reaction zone width and the Kolmogorov length scale.

Previous experimental studies of the SGS mixing of conserved scalars in nonreacting jet have shown that the SGS scalar has two different structures and distributions depending on the instantaneous SGS scalar variance [35, 36, 37, 38, 39]. When the SGS variance is small compared to its mean value, the distribution of the SGS scalar is close to Gaussian, indicating well mixed SGS scalar fields. When the SGS variance is large compared to its mean value, the distribution is bimodal, indicating highly nonpremixed SGS scalar fields.

Recently, the same mixing regimes were found by analyzing the SGS mixing of mixture fraction (a non-reactive scalar) in a turbulent partially premixed flame [40, 41, 42]. The former regime essentially follows the turbulent cascade process which generally supports distributed reaction zones. The latter regime are caused by so-called ramp-cliff structures, which is a direct results of the large-scale turbulent motions. The sharp interface (cliff) separates the fuel lean and rich regions of the SGS fields in a flame. This regime generally supports flamelets.

Recent studies have also shown that different SGS mixture fraction mixing regimes have strong influence on SGS mixing of reactive scalars. Cai et al.[43] studied the effects of the SGS mixing regimes on the SGS mixing of the temperature in the Sandia flames. It was found that for small SGS scalar variance, the SGS mixing of temperature has some characteristics similar to those of a non-reactive scalar. For large SGS scalar variance, the mixing process is more complex. These studies have shown that it is important for mixing models to be able to account for these mixing process. To further understand the effect of different SGS mixing regimes on SGS mixing of reactive scalars, we investigate the SGS mixing of mixture fraction, temperature, species mass fractions in turbulent partially premixed flames using experimental data.

In the context of LES/FDF method, the quantity to be modeled is the conditionally filtered diffusion. The models for that are called mixing models which represents the effects of SGS mixing on the evolution of the scalar FDF. The desirable properties for mixing models include: (1) scalar means must remain unchanged; (2) scalar variances must decrease; (3) scalar must to remain within their convex hull, (4) mixing should be local in composition space; (5) mixing rate should depend on scalar length scalar; (6) Reynolds, Schmidt

dependencies should be takin to account, etc [44, 45, 46]. Currently there are no models completely satisfying all these desirable properties. Most mixing models do not accounting for the direct influence of chemical reaction on mixing [9], which may not work well for turbulent combustion under flamelet regime. In that case, molecular transport and chemical reaction are tightly coupled. To account for the coupling effect at sufficiently high Reynolds number, Pope [47] noted that the molecular mixing and chemical reaction source terms can be combined in the PDF equation, and the combined terms appears in close form by using a flamelet library. This formulation has been successfully applied to premixed turbulent flames in flamelet regime [48, 49]. Here, to understand the extend of coupling between mixing and reaction when flamelet exist and how mixing may be modeled more accurately, we investigate the diffusion and dissipation of temperature perturbations from flamelets in turbulent partially premixed flames in the context of LES/FDF.

There already have extensive studies about turbulent mixing based on two-scalars, such as a single scalar mixed with a background flow. However, in many applications such as reactive flows, at least three scalar (two reactants and one product) are involved. Thus the mixing process is inherently multiscalar, and is more complex. Recently Cai et al.[50] has studied the non-reactive three-scalar mixing in a turbulent coaxial jet. In this flow a central jet and an annulus flow, consisting of acetone-doped air and ethylene, are mixed with the co-flow air, thus two of the scalars (the central jet and the co-flow air) are separated by the third (annulus flow); therefore better approximates the mixing process in a non-premixed turbulent reactive flow. They found the conditional scalar diffusion velocity streamlines in scalar space generally converge quickly to a manifold along which they continue at lower velocities. This trend cannot be explained by the simplest and widely used mixing model-exchange with the mean (IEM) model. In IEM model, the rate of mixing is proportional to the inverse of the time scale of energy-containing turbulent motions and is independent of molecular diffusivity. Rowinski & Pope [51] performed PDF calculations of the same three-scalar mixing problem. They found that in RANS/PDF calculation with different mixing models, the joint PDFs show a wide variability with the experimental data. In LES/FDF calculation with IEM model, the prediction for joint PDFs is better than RANS-PDF calculations. However, both methods can not reproduce the fast mixing manifold. These results suggest the mixing models should take into account the spatial (physical-space) scalar structure. Previous numerical and experimental studies also found the upstream conditions, such as velocity ratio between the central jet and off-central jet, have a great impact on the turbulent structure and mixing properties in turbulent coaxial jets [52, 53, 54, 55, 56, 57]. To further understand the dependencies of SGS mixing on different velocity and length ratio between the central and off-central jet, we investigate the three scalar mixing in temporally developing turbulent plane jets using direct numerical simulation.

The rest of this dissertation is organized as follows. Chapter 2 includes the FMDFs and conditionally filtered diffusion of mixture fraction, temperature and species mass fractions in partially premixed piloted flames. The results on JMDFs, conditional dissipation rate, and conditional diffusion are given in chapter 3. Chapter 4 presents the results of SGS mixing of reactive scalar perturbations from flamelets in turbulent partially premixed flames. Chapter 5 and 6 include the direction numerical simulation results of three scalar mixing in turbulent plane jets. Conclusions are contained in chapter 7.

Chapter 2

Subgrid-scale mixing of mixture fraction, temperature, and species mass fractions in turbulent partially premixed flames

2.1 Introduction

Turbulent mixing and turbulence-chemistry interaction are key processes that must be accurately accounted for in turbulent combustion models. In large-eddy simulation (LES) of turbulent combustion mixing by the large, resolved scales is computed. The effects of the subgrid scales including the subgrid-scale (SGS) scalar mixing and the resulting instantaneous distribution of scalar values in each grid volume, i.e. the species filtered joint mass density function (FMDF), are modeled[4, 28]. Modeling the FMDF, therefore, is the main challenge in LES and requires knowledge of SGS mixing and its interaction with chemistry.

Our previous studies ([39, 37, 35, 38, 36, 40]) have shown that SGS mixing of the mixture fraction has two regimes depending on the *instantaneous* SGS scalar variance. When the SGS variance is small compared to its mean value, the distribution of the SGS scalar is close to Gaussian, indicating well mixed SGS scalar fields. This regime generally supports distributed reaction zones. When the SGS variance is large

compared to its mean value, the distribution is bimodal, indicating highly nonpremixed SGS scalar fields, i.e., the fuel lean and rich regions of the SGS fields in a flame are highly segregated. There is a sharp interface (cliff) separating the two regions. This regimes supports flamelets. The conditional SGS scalar structure resembles that of a counter-flow diffusion flame, which is a model for laminar flamelets.

The well-mixed and the highly-nonpremixed SGS mixture fraction mixing regimes have strong influences on SGS mixing of reactive scalars. Cai et al.[43] studied the effects of the SGS mixing regimes on the SGS mixing of temperature in Sandia flames. It was found that for small SGS scalar variance, the conditionally filtered diffusion of the mixture fraction and temperature for the burning samples, represented by streamlines, generally move towards the ridgeline of the FMDF and then move along it towards a stagnation point. Mixing between burning and extinguished samples generally causes the streamlines to converge to a stagnation point at a lower temperature. The SGS mixing of temperature has some characteristics of those of a non-reactive scalar. For large SGS scalar variance, the mixing process is more complex. The streamlines not far from the equilibrium are consistent with flamelets. The samples at lower temperatures are largely due to extinguished flamelets, which initially cause the streamlines to move predominately in the direction of the mixture fraction and then in the direction of temperature toward a stagnation point. The latter is likely due to diffusion along the iso-mixture fraction surfaces among burning and extinguished flamelets. These results show that it is important for mixing models to be able to account for these SGS mixing processes.

In this study we investigate the effects of the SGS mixture fraction structure on the conditionally filtered scalar diffusion, temperature diffusion, and species mass fraction diffusion in turbulent partially premixed flames, which evolve the FMDF of mixture fraction, temperature, and species mass fractions:

$$F_{\xi TY_i}(\hat{\xi},\hat{T},\hat{Y}_i;\mathbf{x},t) = \langle \rho(\mathbf{x},t)\delta(\xi-\hat{\xi})\delta(T-\hat{T})\delta(Y_i-\hat{Y}_i)\rangle_\ell = \int \rho(\mathbf{x}',t)\delta(\xi-\hat{\xi})\delta(T-\hat{T})\delta(Y_i-\hat{Y}_i)G(\mathbf{x}-\mathbf{x}')d\mathbf{x}' \tag{2.1}$$

where ξ, T, Y_i, $\hat{\xi}$, $\hat{T}$ and $\hat{Y}_i$ are the mixture fraction, temperature, species mass fraction and their sample-space variables, respectively, and ρ is the fluid density. The subscripts ℓ and L denote conventional and Favre filtered variables, respectively. The knowledge of these diffusion terms is important for understanding SGS mixing of multiple reactive scalars and the SGS turbulence-chemistry interaction.

2.2 Experimental data and processing procedures

We use experimental data obtained in piloted turbulent partially premixed methane flames with a 1:3 ratio of CH_4 to air by volume (Sandia flame D and E, see Ref.[58, 59]). The measurements employed combined line-imaging of Raman scattering, Rayleigh scattering, and laser-induced CO fluorescence. Simultaneous measurements of the major species (CO_2, O_2, CO, N_2, CH_4, H_2O, and H_2), the mixture fraction (obtained from all major species), the temperature, and the radial component of the scalar dissipation rate were made. The mixture fraction is calculated using a variation of Bilger's definition, which has been modified by excluding the oxygen terms. The length of the imaging line is 6.13 mm with a pixel resolution of 0.2044 mm. The overall resolution of the imaging system is capable of resolving 98% of the highest scalar dissipation ([41]).

Measurements of the filtered density functions require spatial filtering of scalar fields. In this work one-dimensional filtering is employed. In LES filtering is generally performed in three dimensions. Our previous results [35] have shown, however, that the FDF obtained using a one-dimensional filter is qualitatively the same as those using a two-dimensional filter, which has been shown to be a very good approximation of three-dimensional filters, with errors of approximately 5% for the rms resolvable- and subgrid-scale variables[60]. For a similar FDF and conditionally filtered diffusion the corresponding SGS variance is somewhat larger for a one-dimensional filter. To ensure that the results are relevant to LES, the filter sizes employed in this work (3.0 mm and 4.9 mm) are significantly larger than the dissipative (Corrsin) scales (0.065 - 0.106 mm[61]), such that the subgrid scales contain sufficient fluctuations to interact with the chemistry, allowing the physics of the SGS mixing and its interaction with the chemistry to be related to the inertial-range dynamics. Previous studies (e.g., Refs. [39, 35]) have shown that when the filter size is much larger than the dissipation scales the properly scaled conditional statistics are not sensitive to the filter size.

2.3 Results

In this section the FMDF and the conditionally filtered diffusion of the mixture fraction, temperature, and species mass fractions are analyzed using their conditional means. We use the Favre filtered mixture

fraction, $\langle\xi\rangle_L = \langle\rho\xi\rangle_\ell/\langle\rho\rangle_\ell$, and the Favre SGS scalar variance,

$$\langle\xi''^2\rangle_L \equiv \frac{1}{\langle\rho\rangle_\ell}\int F_{\xi L}(\hat{\xi};\mathbf{x},t)(\xi-\langle\xi\rangle_L)^2 d\xi = \langle\rho\xi^2\rangle_\ell/\langle\rho\rangle_\ell - \langle\xi\rangle_L^2, \tag{2.2}$$

as conditioning variables. The filtered mixture fraction, $\langle\xi\rangle_L$, is set to the stoichiometric mixture fraction, $\xi_s(=0.35)$, to maximize the probability of the SGS fields containing reaction zones. At each measurement location, two SGS variance values, one small and one large (much smaller and much larger than the mean SGS variance respectively), are chosen to sample SGS fields representing the limiting cases of the two mixing regimes. For the flame studied, the percentages of the the scalar dissipation rate in the reaction zones (the approximate heat release rate) from the distributed reaction zones and flamelet regimes are approximately 55% and 45% respectively ([40]).

To obtain reasonable statistical convergence for the FMDF and the conditionally filtered diffusion for all the major species, a data sample size much larger than that available is needed. In this study we include one major species at a time, i.e., we consider the FMDF of mixture fraction, temperature, and one species mass fraction and the related SGS mixing terms in the FMDF transport equation. Using the analysis described in ([62]), the maximum rms uncertainty of the FMDF obtained are determined to be approximately 10% of the peak FMDF values, comparable to the uncertainty in the species data ([63]). To fully represent the FMDF and the SGS mixing terms, a three-dimensional scalar space is needed. We present them as functions of the three sample-space variables.

The conditionally filtered diffusion of the mixture fraction, the temperature, and a species mass fraction, $\langle\langle\frac{1}{\rho}\frac{\partial}{\partial y}(\rho D\frac{\partial\xi}{\partial y})|\xi,T,Y_i\rangle_\ell|\langle\xi\rangle_L,\langle\xi''^2\rangle_L\rangle$, $\langle\langle\frac{1}{\rho}\frac{\partial}{\partial y}(\rho D_T\frac{\partial T}{\partial y})|\xi,T,Y_i\rangle_\ell|\langle\xi\rangle_L,\langle\xi''^2\rangle_L\rangle$, and $\langle\langle\frac{1}{\rho}\frac{\partial}{\partial y}(\rho D\frac{\partial Y_i}{\partial y})|\xi,T,Y_i\rangle_\ell|\langle\xi\rangle_L,\langle\xi''^2\rangle_L\rangle$ appear in the FMDF equation as terms transporting the FMDF in the ξ, T, and Y_i spaces, respectively. Thus, they are the three components of the diffusion velocity of the FMDF in the sample space. We use streamlines and isocontours to present the direction and the magnitude of the diffusion velocity. The diffusion terms are calculated using 10th-order central finite difference and non-dimensionalized by the filtered scalar dissipation rate and SGS variance, respectively. In the following we discuss the results for each major species mass fraction. We show the results for flame D and E with the 3.0 mm filter size. The results for $\Delta = 4.9$ mm are qualitatively similar and are not shown.

The FMDF of ξ, T and Y_{CO_2} appears to be largely limited to a two-dimensional manifold and has a similar shape to the FMDF of ξ and T due to the strong correlation between T and Y_{CO_2} (Figs.2.1 and

2.2), since the latter is directly related to the heat release. Consequently, although there are four scalars in the mixing problem, i.e., ξ, T, Y_{CO_2}, and the co-flow, the SGS mixing is similar to three-scalar SGS mixing. Thus, the mixing problem for these scalars is a degenerated case. At $x/D = 7.5$ the flame is close to fully burning, with T and Y_{CO_2} not far from the equilibrium values. For small SGS variance, the FMDF is unimodal and is concentrated near the peak T and Y_{CO_2} (Fig. 2.1a). There are only a small number of extinguished samples. For large SGS variance, the FMDF is bimodal (Fig. 2.1b), indicating that the rich and lean mixtures in the SGS field (i.e., a grid cell) are essentially segregated. The SGS scalar contains two relatively well-mixed mixtures corresponding to the two peaks of the FMDF. The difference between the ξ values of the two mixtures is greater than the reaction zone width in the ξ space, $\Delta\xi_R$ (≈ 0.23), for the Sandia flames. Such a mixture fraction structure limits the reaction zones to thin diffusion layers, thereby resulting in laminar flamelets. For flame E both T and Y_{CO_2} are lower than those for flame D (Fig. 2.15b), and there is a relatively large probability of local extinction due to the higher scalar dissipation rate, but the results are otherwise similar to those for flame D. At $x/D = 15$ there is a significant number of local extinguished samples, with flame E having approximately 5 times that in flame D (Fig. 2.16b). At $x/D = 30$, the probability of local extinction is approximately 2-3 times lower than at $x/D = 15$ due to reignition as a result of the decay of the scalar dissipation rate (Fig. 2.3b).

The diffusion velocity streamlines for ξ, T and Y_{CO_2} are shown in Figs. 2.1&2.2. For small SGS variance the streamlines at $x/D = 7.5$ generally converge first to a one-dimensional manifold, which is the ridgeline of the FMDF, and then continue towards a stagnation point. The diffusion velocity magnitude is larger during the approach to the manifold, indicating that the approach to the manifold is a faster process than the convergence to the stagnation point. This trend is similar to that for ξ and T, and can be understood largely in the context of quasi-equilibrium distributed reaction zones, in which reactive scalar diffusion is closely coupled to the diffusion of the mixture fraction dissipation [43]. At $x/D = 15$ (Fig. 2.2c) the streamline for the burning samples are similar to those at $x/D = 7.5$. For the samples at lower T and Y_{CO_2}, there is another stagnation point near $\xi = 0.4$, $T = 1600K$, and $Y_{CO_2} = 0.075$ (0.4, 1600K, 0.075). The mixing here is primarily between the burning and extinguished samples, and therefore is different from that for the samples near equilibrium. The results for $x/D = 30$ is similar to those at $x/D = 15$ (Fig. 2.3c).

For large SGS variance at $x/D = 7.5$ the streamlines for very rich ($\xi > 0.6$) and lean ($\xi < 0.2$) mixtures generally move in the direction of the ridgeline of the FMDF (Fig. 2.1d) towards the stoichiometric mixture fraction. For strained flamelets the mixture fraction profiles have an approximately error-function shape (ramp-cliff structure). Thus, the diffusion of ξ is towards the center of the profiles (appears to be near

$\xi = 0.45$). For very rich and lean mixtures T and Y_{CO_2} depend approximately linearly on ξ; therefore, their diffusion is proportional to the ξ diffusion, resulting in straight diffusion streamlines along the ridgeline.

Near the peak T and Y_{CO_2} the ξ diffusion is small because this region is close to the center of the error-function profiles where the curvatures of the profiles are small. The T diffusion and Y_{CO_2} diffusion are negative due to the negative curvatures of their profiles (as a function of ξ) and the approximately linear ξ profiles. Consequently, the streamlines starting from the equilibrium curve near $\xi = 0.45$ move towards lower T and Y_{CO_2} values. As the streamlines move towards lower temperatures, the scalar dissipation rate increases, corresponding to more strongly strained flamelets and higher diffusion. The largest magnitude of the diffusion velocity vector occurs near $T = 1600 - 1800K$. Below this temperature range T and Y_{CO_2} profiles become broader (smaller curvatures) in the ξ space, resulting in lower T diffusion and Y_{CO_2} diffusion. There appears to be a stagnation point at (0.4, 1300K, 0.058). Note that although this point appears to be the "center" of diffusion, it does not correspond to the conditional mean temperature and conditional mean Y_{CO_2} for this mixture fraction value. Since the FMDF is transported by both diffusion and reactions, their combined action keeps the FMDF in the FMDF manifold. Individually they generally transport the FMDF out of the manifold unless one of them is small. Near the peak temperature both the reaction rates and diffusion are large, thus the diffusion streamlines move out of the FMDF manifold.

The streamlines starting from the very rich and lean regions move up along the ridgeline and turn near (0.27, 1600K, 0.082) and near (0.55, 1600K, 0.0760), respectively, towards the stagnation point. The T and Y_{CO_2} diffusion changes sign near these points, where the inflection points of T and Y_{CO_2} profiles are located. Below these points the diffusion is dominated by mixing whereas above it the diffusion is strongly influenced by both mixing and reaction. This streamline pattern is also consistent with the structure of flamelets.

At $x/D = 15$, the overall diffusion pattern for the burning samples (Fig. 2.2d) is similar to that at $x/D = 7.5$. For the extinguished samples the diffusion streamlines move primarily in the direction of mixture fraction towards $\xi \approx 0.4$, with only modest increases in T and Y_{CO_2}. These trends indicate that for these samples the ξ diffusion is initially much faster than T diffusion. Previous results [43] have shown that this trend is due to extinguished flamelets. Near $\xi = 0.4$ streamlines move largely in the direction of T and Y_{CO_2} towards higher values. This ξ value is close to the center of the ramp-cliff structure where the ξ diffusion is small. For each flamelet, the T and Y_{CO_2} diffusion is negative at this mixture fraction. Thus, the observed positive T and Y_{CO_2} diffusion is likely due to the interaction between burning and extinguished flamelets resulting in diffusion along the iso-mixture fraction surface. At $x/D = 30$ the results (Fig. 2.3d) are similar

to those at $x/D = 15$. The results for flame E are qualitatively similar to those for flame D at $x/D = 15$ and 30 except the earlier onset of local extinction (Fig. 2.15-2.17). The results for H_2O are similar to CO_2 and are not shown.

The FMDF and the conditionally filtered diffusion involving Y_{O_2} are shown with the ξ axis plotted differently for clarity. Due to partial premixing mixing, the FMDF at $x/D = 7.5$ (Figs. 2.7a-b) is similar to the inverted FMDF of ξ, T and Y_{CO_2}, with higher Y_{O_2} values for both lean and rich mixtures but low values near ξ_s. The FMDF, although not in a plane, is largely limited to a two-dimensional manifold. At $x/D = 15$ (Fig. 2.8a), for small SGS variance the FMDF is again similar to the inverted FMDF containing Y_{CO_2}. For large SGS variance (Fig. 2.8b), the extent of the rich side is reduced due to consumption. There are some samples with higher Y_{O_2} at lower temperatures due to local extinction. At $x/D = 30$ the rich side has further diminished (Fig. 2.9b).

At $x/D = 7.5$ the diffusion streamline pattern (Fig. 2.7c-d) involving Y_{O_2} is similar to the inverted streamlines involving Y_{CO_2}. Moving downstream to $x/D = 15$, for small SGS variance, the streamlines converge to the stagnation points (Fig. 2.8c). For large SGS variance, the streamlines (Fig. 2.8d) are also similar to the inverted streamlines for Y_{CO_2}, but those on the rich side start from lower Y_{O_2} values than at $x/D = 7.5$. At $x/D = 30$, the streamlines start from even lower Y_{O_2} values (Fig. 2.9d).

The FMDF of ξ, T, and Y_{CH_4} at $x/D = 7.5$ is concentrated near equilibrium values (Fig. 2.10b). The CH_4 levels on the lean side are very low. At $x/D = 15$ the FMDF extends to higher Y_{CH_4} values and lower T values (Fig. 2.11b). The FMDF also appear to be limited to a plane. The diffusion streamlines have a similar structure to those for Y_{CO_2} (Fig. 2.11d). Near the peak temperature they move towards lower T and higher Y_{CH_4} values. The streamlines from the far rich and lean sides move along the FMDF ridgeline. For the extinguished samples the streamlines move towards $\xi = 0.4$ and then converge to a stagnation point.

The FMDF for T and Y_{CO} at $x/D = 7.5$ are not far from the equilibrium values for these burning flamelets. For small SGS variance, the FMDF is concentrated on the lean side of the peak Y_{CO} (Fig. 2.3a). There is a sharp drop of Y_{CO} due to the consumption reactions. For large SGS variance, the FMDF consists of three segments, one on the rich side of the peak Y_{CO} and two on the lean side (Fig. 3b). They connect four vertices that are not in the same plane; therefore, unlike that of ξ, T and Y_{CO_2}, the FMDF of ξ, T and Y_{CO} is not limited to a two-dimensional manifold and must be represented in a three-dimensional scalar space. Thus, the mixing problem is non-degenerated. On the far rich side the FMDF ridgeline is largely a straight line, due to the low reaction rates resulting in linear relationships among the scalars. The production rate of Y_{CO} is highest near the peak, and is balanced by the negative diffusion. Just to the lean side of the peak Y_{CO},

where the consumption rate is highest, Y_{CO} decreases rapidly to reach very low values at $\xi = 0.2$. Here the consumption rate is balanced by positive diffusion. Further to the lean side Y_{CO} remains low and T decreases linearly with ξ.

At $x/D = 15$ for small SGS variance, the FMDF is still largely concentrated on the lean side of the peak Y_{CO}, but extends to the rich side as well as regions of lower T and Y_{CO} due to local extinction (Fig. 2.4a). For large SGS variance the FMDF regions for the burning samples are similar to those at $x/D = 7.5$ (Fig. 2.4b). The burning samples and the samples with lower temperatures, which are extinguished flamelets, form a triangular pyramid-shaped FMDF manifold. A plane on the lean side (left plane) containing three vertices $(0.01, 378K, 0.001)$, $(0.26, 1745K, 0.001)$ and $(0.49, 1934K, 0.07)$ is formed due to the rising Y_{CO} values resulting from the imbalance between Y_{CO} diffusion and the (reduced) CO consumption rate. These are flamelets that are strained or close to extinction. A front plane connecting the left plane and the ridgeline on the rich side is also formed. The elevated CO levels due to the diffusion and the reduced CO consumption result in similar profiles of Y_{CO} and T (hence the profiles are on the front plane). At this downstream location the pyramid is only partially filled, i.e., the FMDF values are low inside the pyramid.

At $x/D = 30$ the overall shape of the FMDF (Fig. 2.6a-b) is similar to that at $x/D = 15$. For large SGS variance, the pyramid appears to be filled to a larger extent. The elevated CO levels inside the pyramid provides the possibility for mixing between the rich mixtures at high temperatures and the lean mixtures at low temperatures. The SGS mixing is likely between burning and extinguished flamelets.

For small SGS variance, the diffusion streamlines at $x/D = 7.5$ converge to a manifold and then to a stagnation point (Fig. 2.3c). At $x/D = 15$ (Fig. 2.4c) there is a second stagnation point at lower Y_{CO} values, towards which the streamlines converge. The results for $x/D = 30$ are similar. For large SGS variance at $x/D = 7.5$ (Fig. 2.3d) near the peak Y_{CO}, the diffusion streamlines move largely towards lower T and Y_{CO} values because of the negative curvature of the their profiles in flamelets. Here both the reaction rates and the negative diffusion are high and largely balance each other. Their combined action transports the FMDF within the FMDF manifold. Thus, the diffusion alone transports the FMDF out of the manifold, as shown in Fig. 2.3d. On the far lean side and the far rich side, the streamlines move along the ridgeline of the FMDF. Here the reaction rates are low, and the streamlines stay inside the FMDF manifold. On the lean side between 1000K to 1500K, the diffusion streamlines move towards higher Y_{CO} but remain at approximately the same T. Due to the high CO consumption rate in these mixtures, the streamlines tend to move out of the FMDF manifold. The streamlines then turn towards lower T and Y_{CO}, and converge to a stagnation point in the interior of the pyramid (not on the front or the back plane).

At $x/D = 15$ the streamline pattern for the burning samples are similar to that at $x/D = 7.5$ (Fig. 2.4d). For the extinguished samples, the streamlines from low T and Y_{CO} on the far lean side first move upward towards higher Y_{CO}. Here the reaction rates are low and the streamlines are located within the FMDF manifold (the left plane), which is generated by the diffusion. The streamlines then move towards ξ_s. On the rich side, the streamlines for the extinguished flamelets also move towards ξ_s, and together with those from the lean side forming the front plane. Since the reaction rates are low, the FMDF is transported in the direction of the streamlines. Near ξ_s the streamlines move towards the stagnation point at higher T and lower Y_{CO}. Again, for each flamelet the diffusion for both T and Y_{CO} is in the opposite direction of the streamlines. The diffusion here, therefore, is along the iso-mixture fraction surface (ξ_s), indicating diffusion among burning and extinguished flamelets. At $x/D = 30$, the overall streamline pattern is similar to that at $x/D = 15$ (Fig. 2.6c-d). The results for H_2 are generally similar to those of CO. One difference is that at $x/D = 15$ (Fig. 2.14), the FMDF is broader than that of CO potentially due to higher noise as well as differential diffusion effects resulting from the higher diffusion coefficient of H_2.

The results show that the SGS mixing of Y_{CO_2} and that of Y_{CO} have significantly different characteristics. Being strongly correlated with the temperature, the SGS mixing of Y_{CO_2} is similar to that of the temperature. The four-scalar (ξ, T, Y_{CO_2}, and co-flow ($1-\xi$)) SGS mixing problem is similar to that of the three scalar (T, Y_{CO_2}, and co-flow) SGS mixing, and therefore, is a degenerated case. On the other hand, the SGS mixing of ξ, T, Y_{CO}, and co-flow is more complex because Y_{CO} is depleted rapidly towards the lean side, resulting in a FMDF with four vertices that must be represented in a three-dimensional scalar space. Thus, the SGS mixing problem is non-degenerated. From a more general point of view, the different SGS mixing characteristics of Y_{CO_2} and Y_{CO} are a result of the different mixing configurations, i.e., the spatial relationships among the scalars in physical space, which are closely tied to the chemistry: The peak location of Y_{CO} approximately coincides with that of the temperature whereas the FMDF vertex near $\xi = 0.2$ is located between the co-flow and the peak temperature. In the Sandia flames the major species can be divided into several categories: CO_2 and H_2O, CO and H_2, CH_4, and O_2, each having a different spatial relationship with the mixture fraction, the temperature, and the co-flow. Except CO and H_2, the FMDFs for all the species have vertices near the peak temperature indicating relatively simple mixing configurations. In flames with more complex chemistry, additional mixing configurations may exist, resulting in different SGS mixing characteristics.

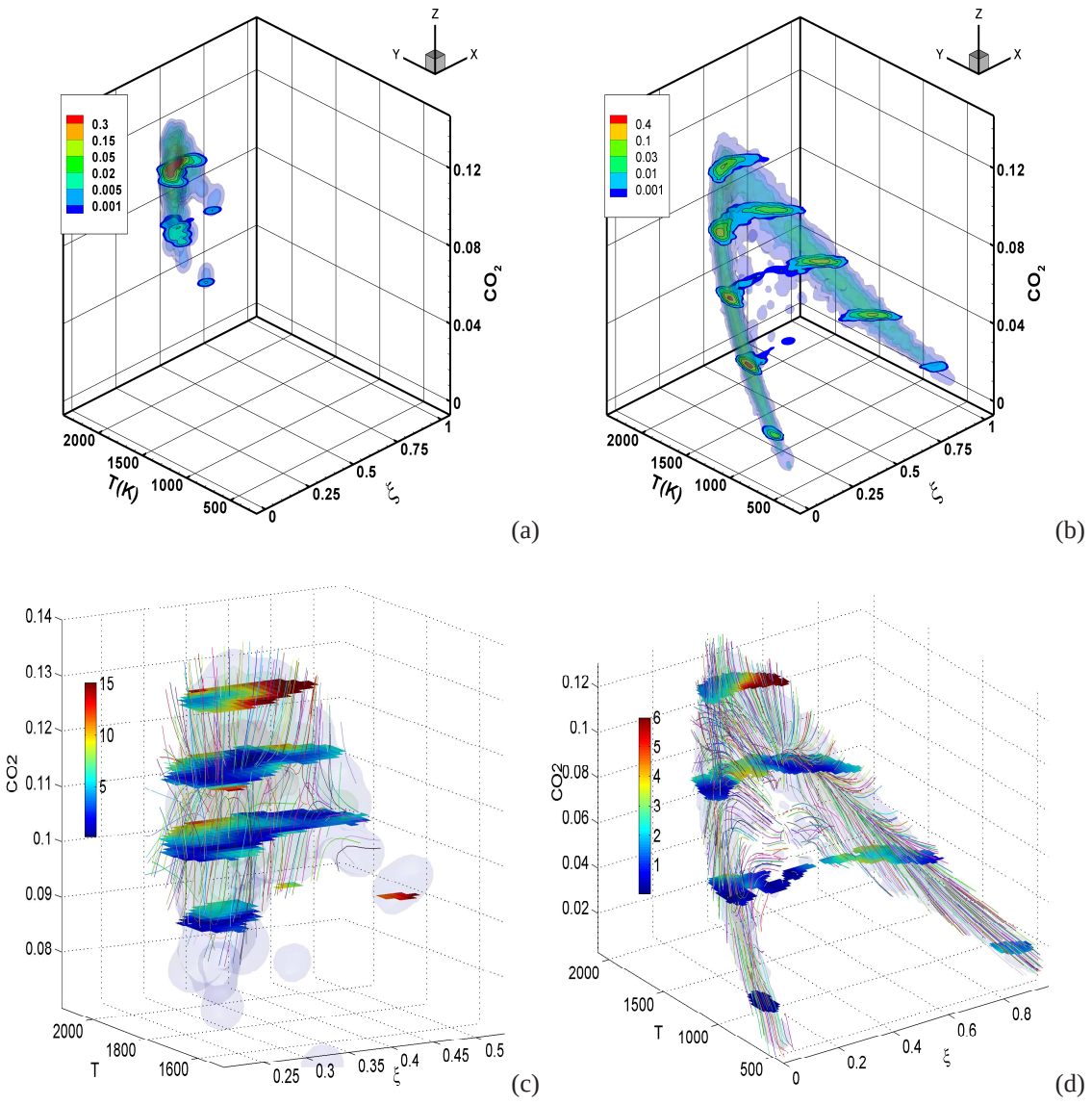

Figure 2.1: FMDF and diffusion velocity streamlines for ξ, T and Y_{CO_2} at $x/D = 7.5$ in flame D. (a & c) small SGS variance ($\langle \xi''^2 \rangle_L = 0.0013$, $\langle \langle \xi''^2 \rangle_L \rangle = 0.0272$). The color isosurfaces and contours denote the FMDF values; (b & d) large SGS variance ($\langle \xi''^2 \rangle_L = 0.066$). The color contours on the horizontal planes represent the magnitude of the diffusion velocity vectors.

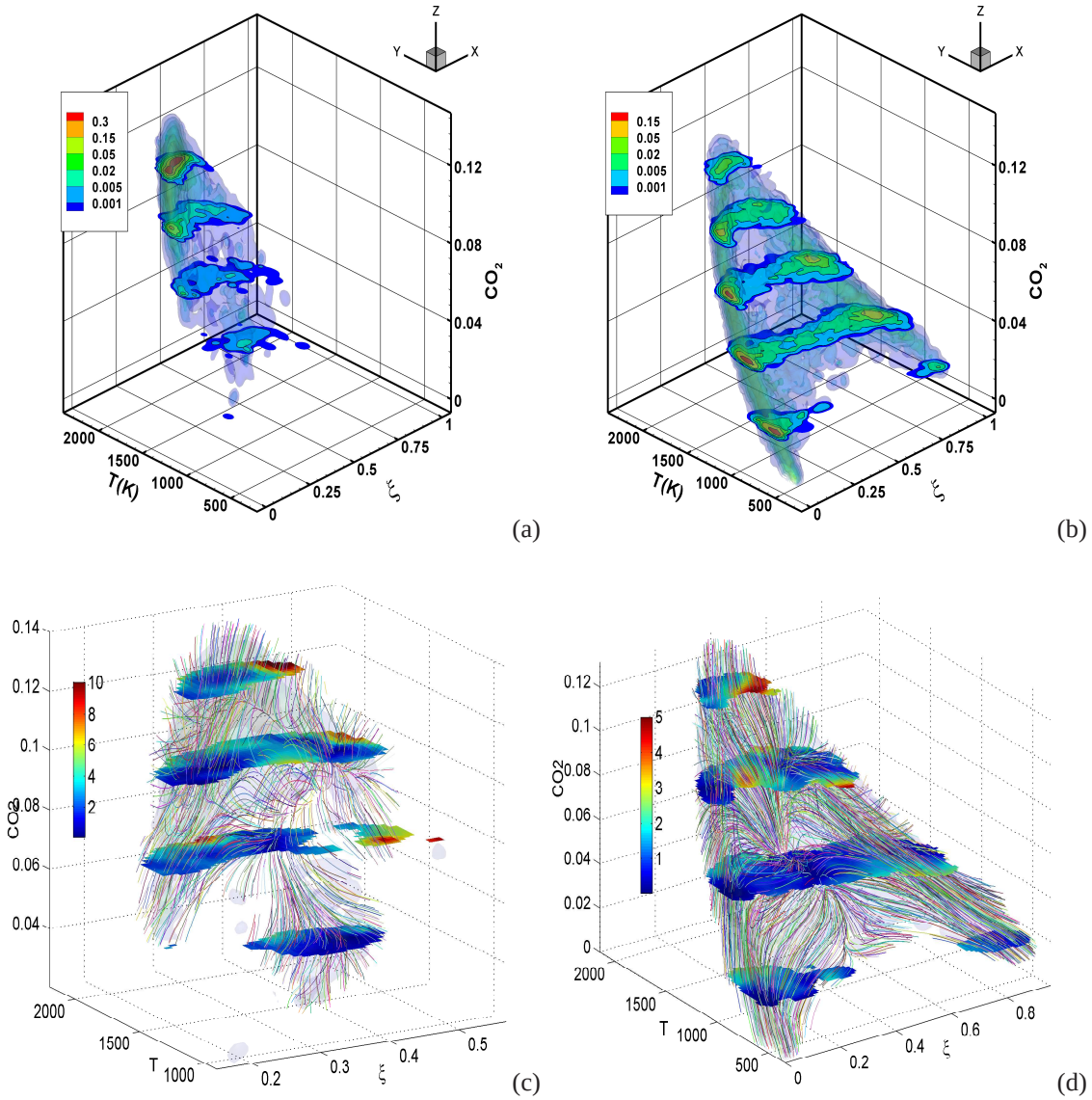

Figure 2.2: FMDF and diffusion velocity streamlines for ξ, T and Y_{CO_2} at $x/D = 15$ in flame D. (a & c) small SGS variance ($\langle \xi''^2 \rangle_L = 0.003$, $\langle \langle \xi''^2 \rangle_L \rangle = 0.0251$); (b & d) large SGS variance ($\langle \xi''^2 \rangle_L = 0.069$).

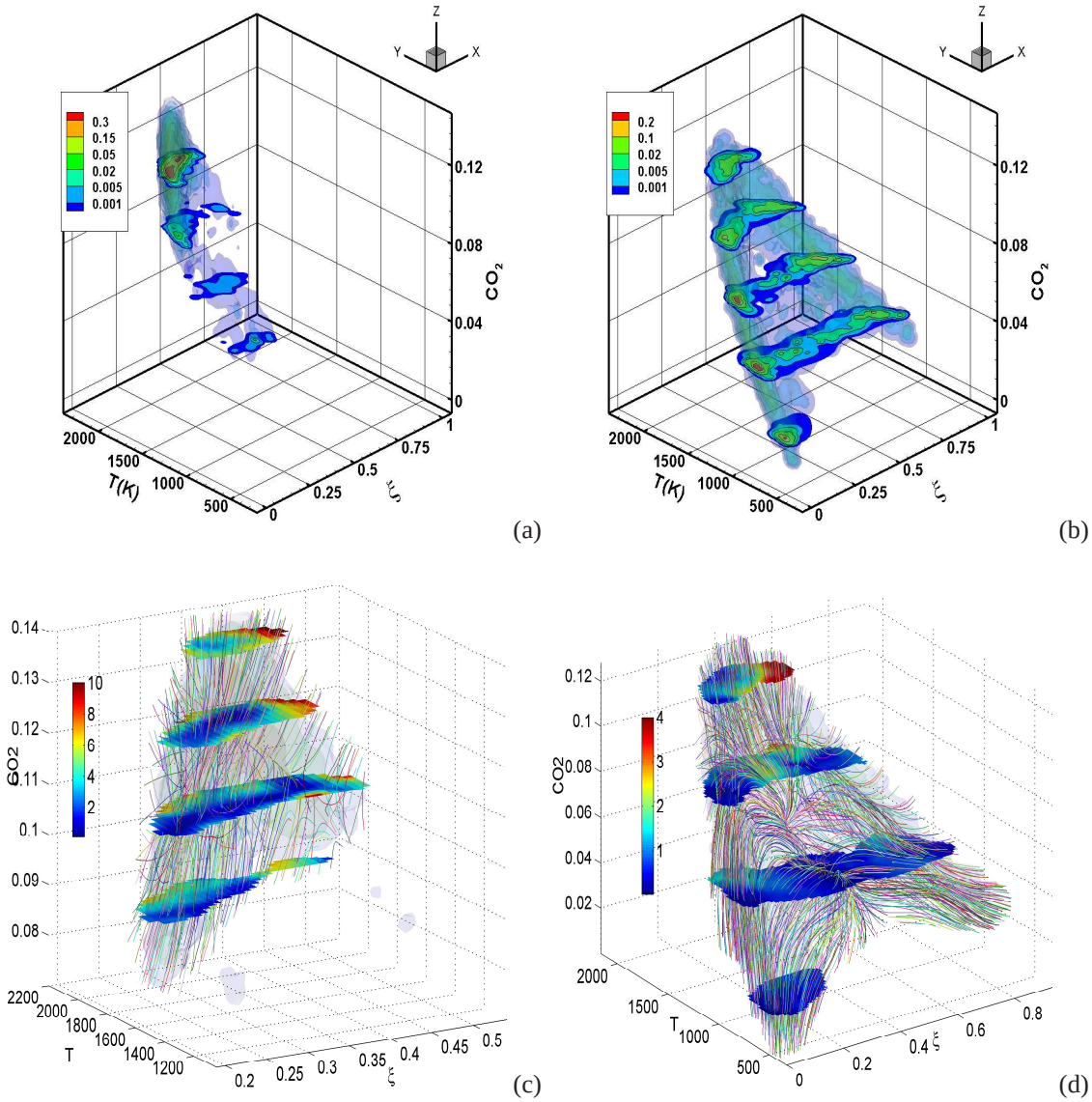

Figure 2.3: FMDF and diffusion velocity streamlines for ξ, T and Y_{CO_2} at $x/D = 30$ in flame D. (a & c) small SGS variance ($\langle \xi''^2 \rangle_L = 0.0019$, $\langle \langle \xi''^2 \rangle_L \rangle = 0.0105$); (b & d) large SGS variance ($\langle \xi''^2 \rangle_L = 0.059$).

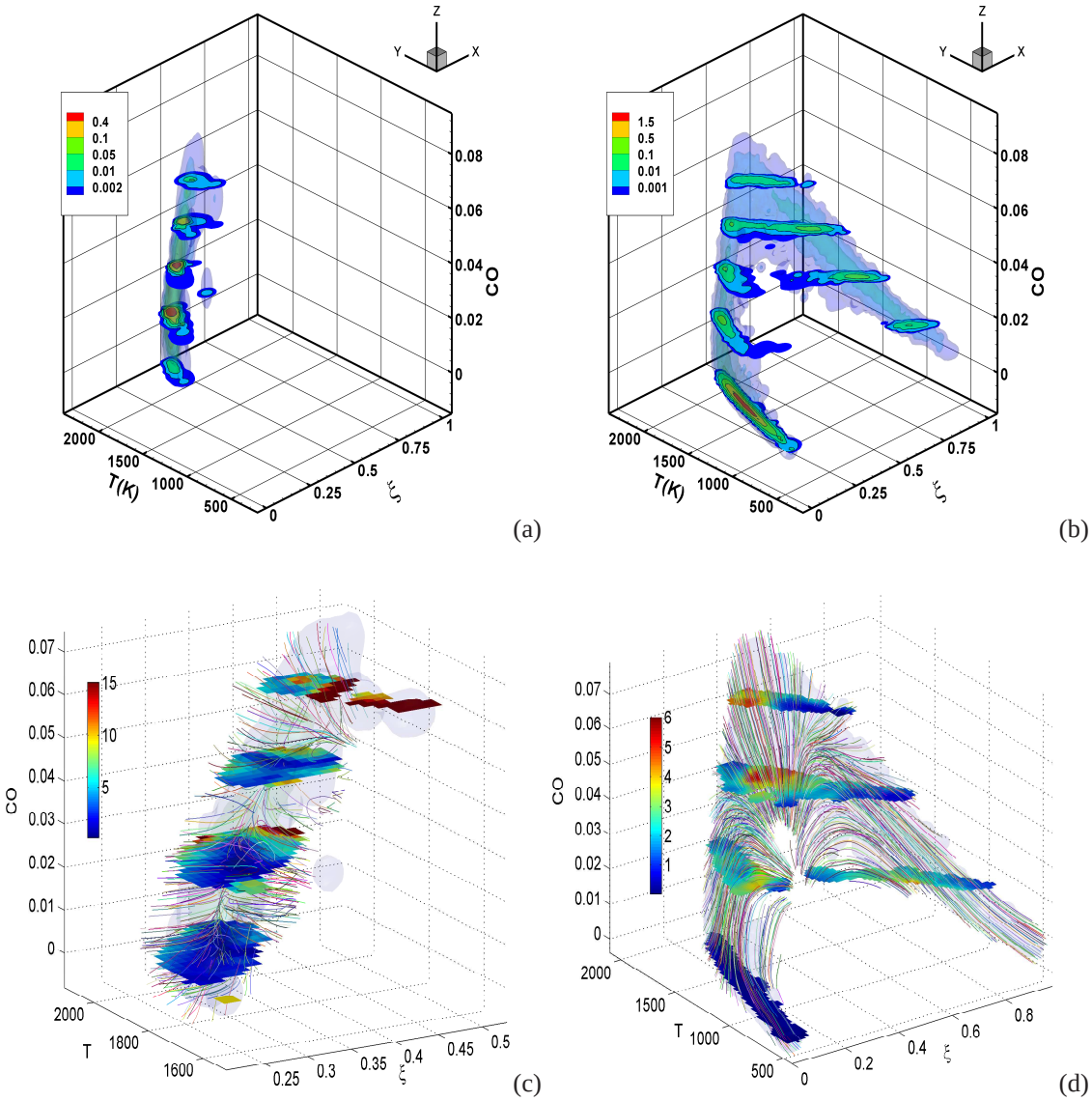

Figure 2.4: FMDF and diffusion velocity streamlines for ξ, T and Y_{CO}. Conditions same as in Fig. 2.1.

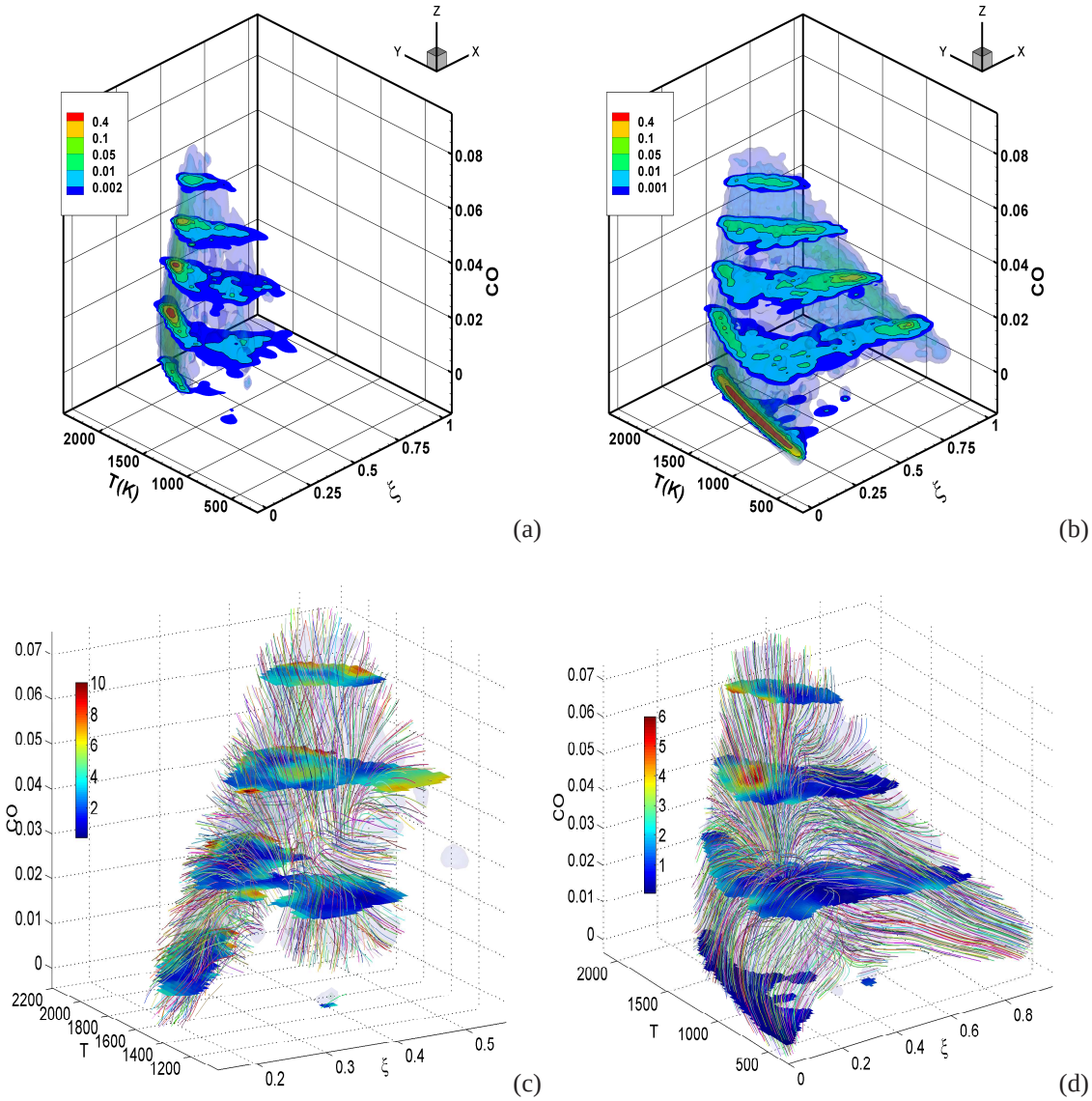

Figure 2.5: FMDF and diffusion velocity streamlines for ξ, T and Y_{CO}. Conditions same as in Fig. 2.2.

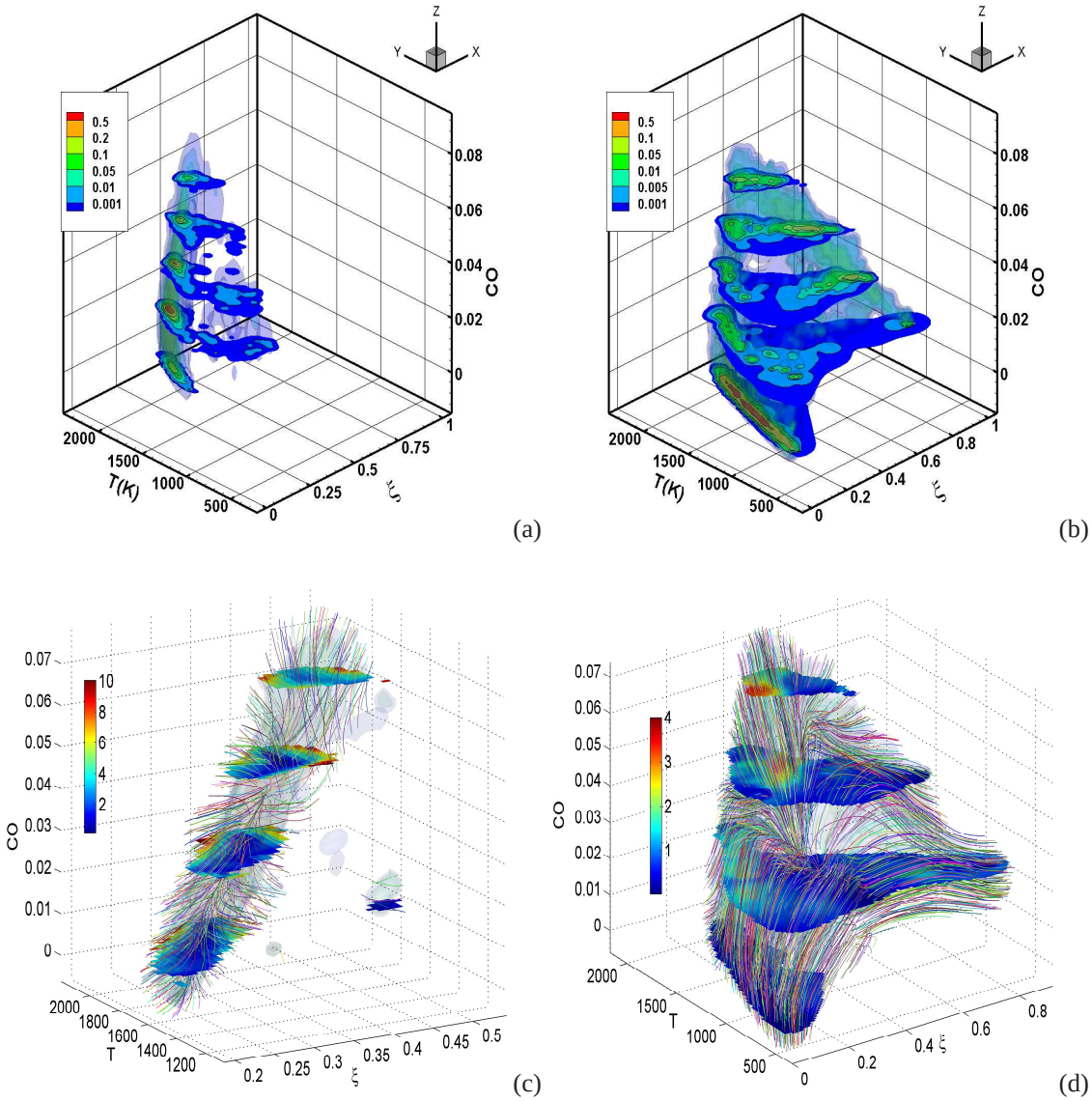

Figure 2.6: FMDF and diffusion velocity streamlines for ξ, T and Y_{CO}. Conditions same as in Fig. 2.3.

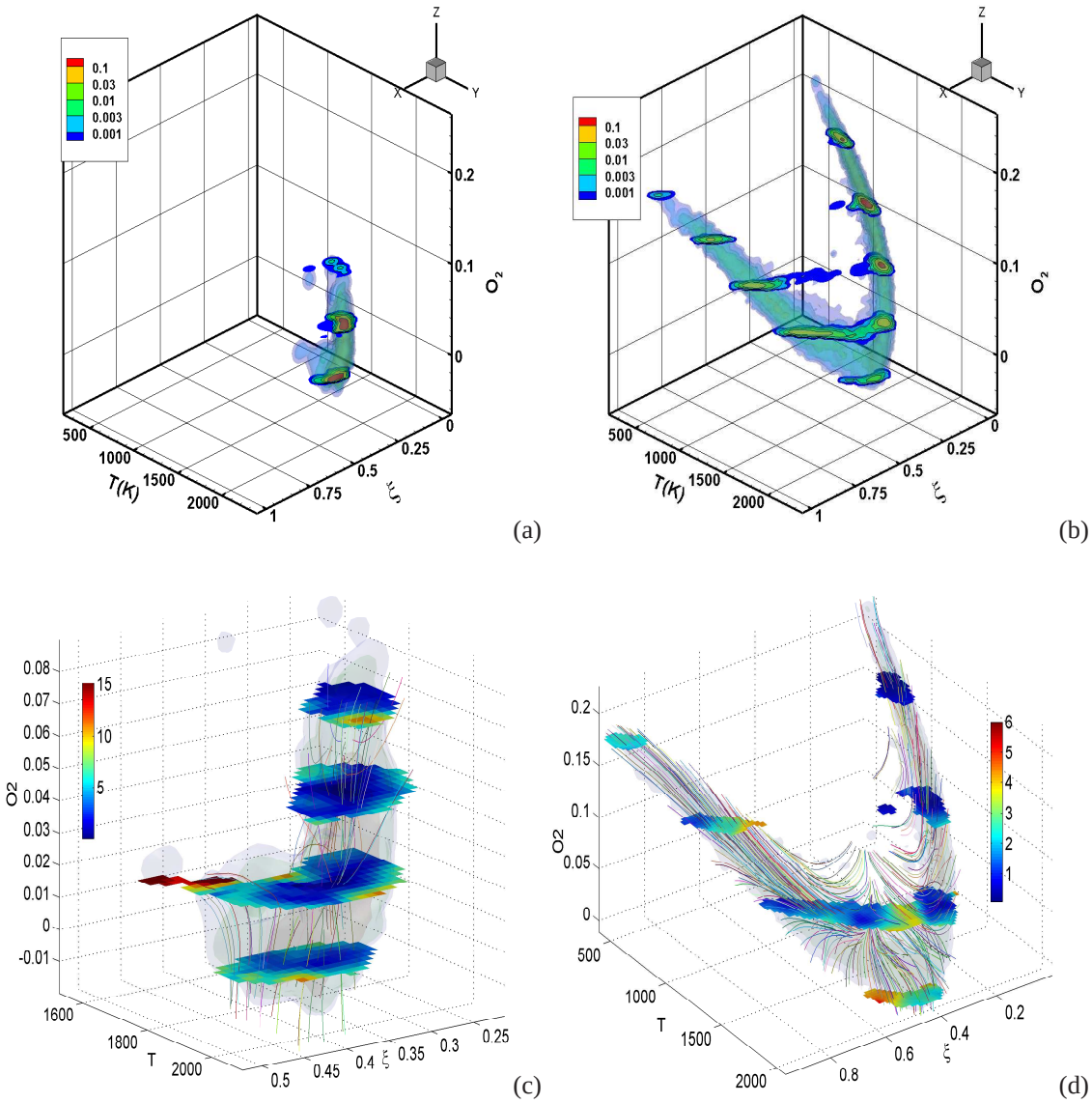

Figure 2.7: FMDF and diffusion velocity streamlines for ξ, T and Y_{O_2}. Conditions same as in Fig. 2.1.

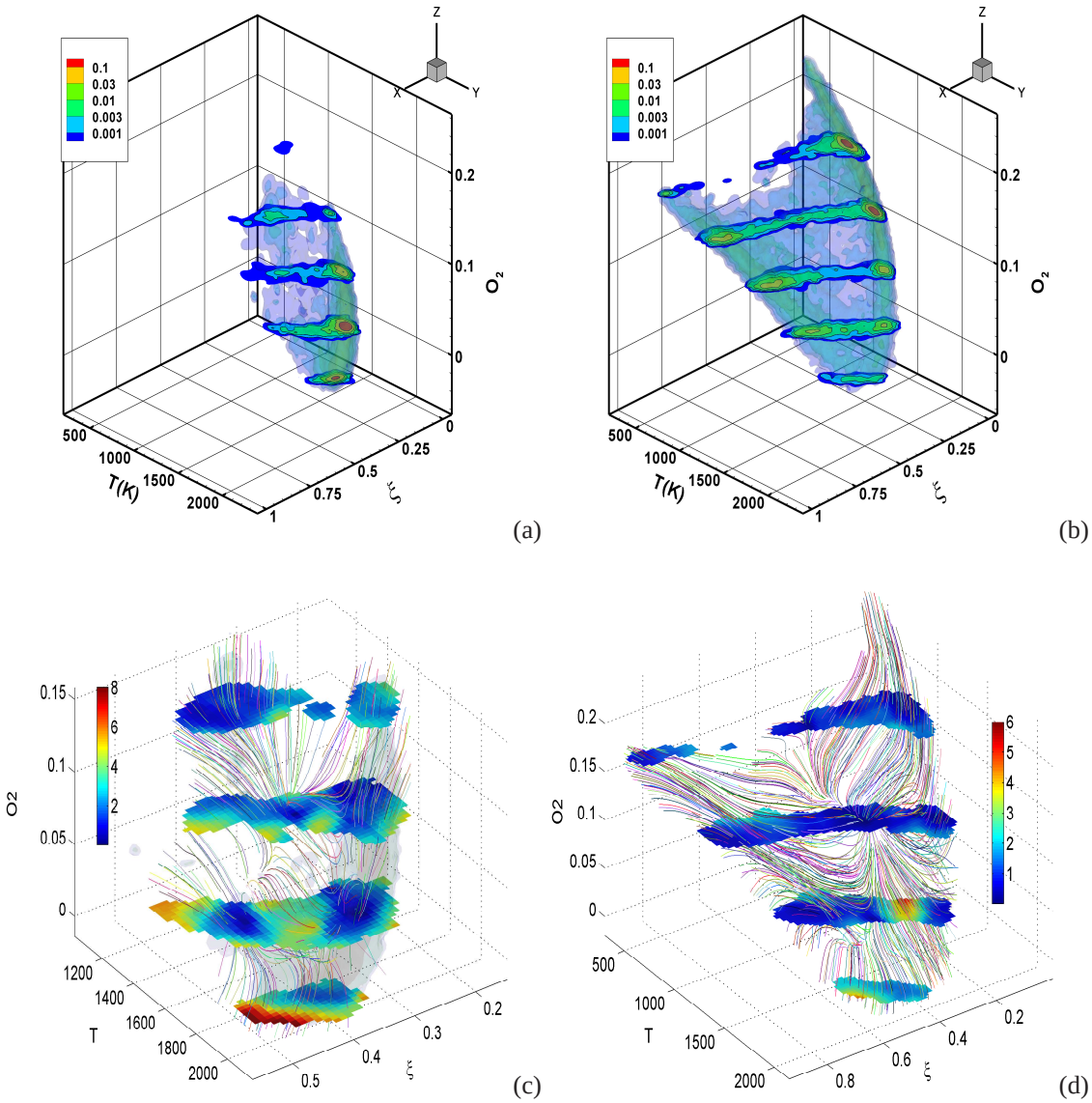

Figure 2.8: FMDF and diffusion velocity streamlines for ξ, T and Y_{O_2}. Conditions same as in Fig. 2.2.

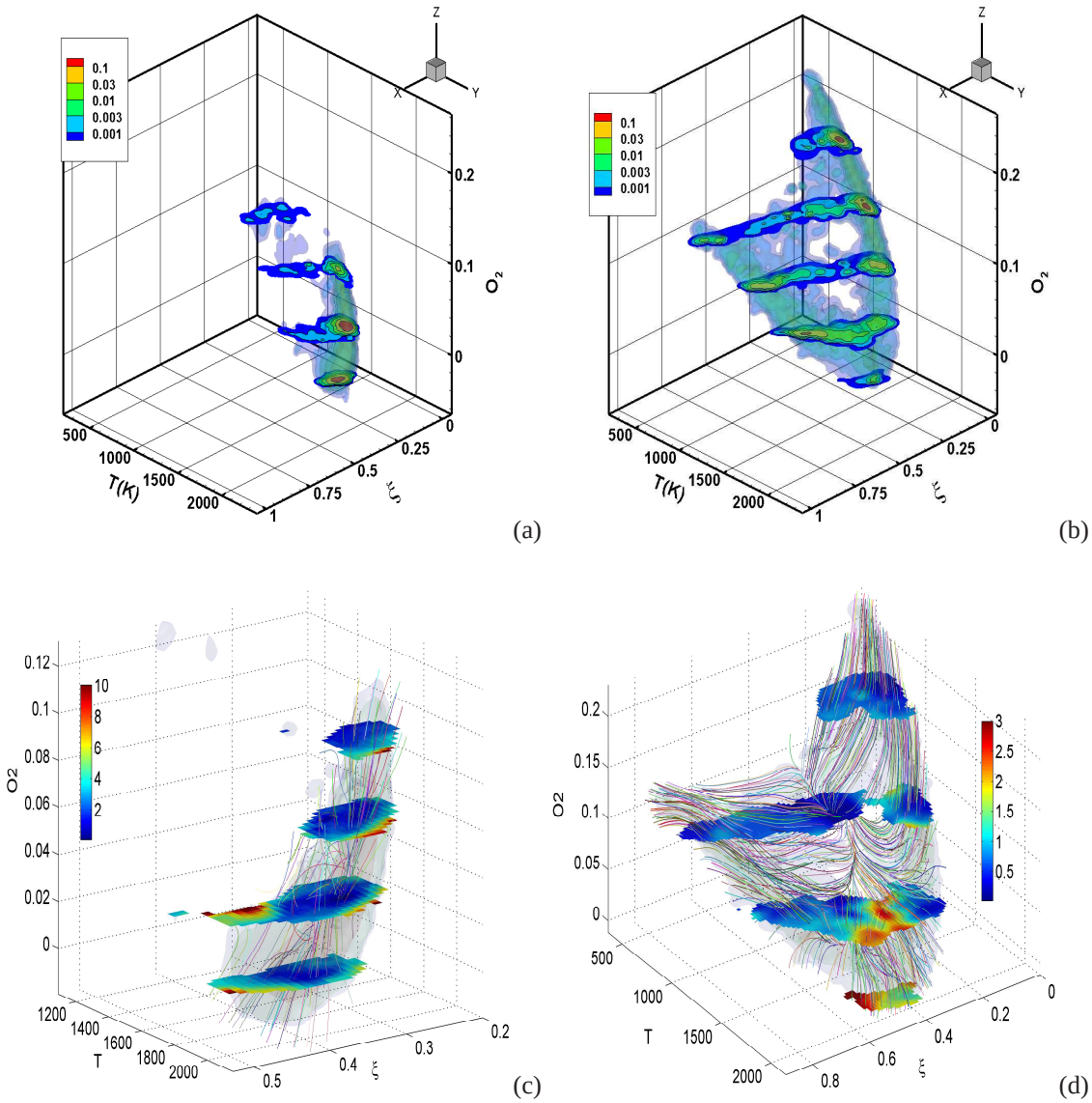

Figure 2.9: FMDF and diffusion velocity streamlines for ξ, T and Y_{O_2}. Conditions same as in Fig. 2.3.

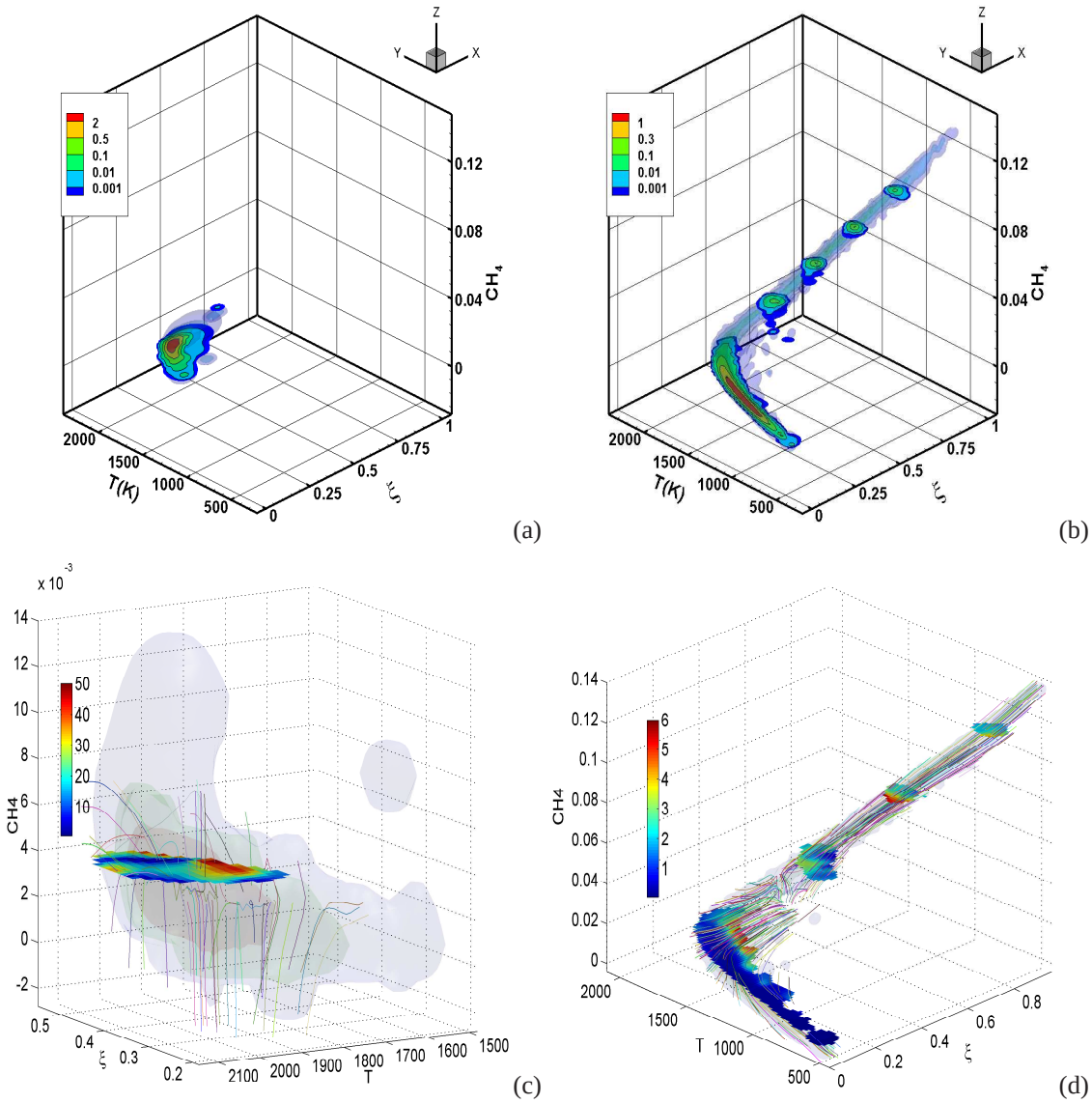

Figure 2.10: FMDF and diffusion velocity streamlines for ξ, T and Y_{CH_4}. Conditions same as in Fig. 2.1.

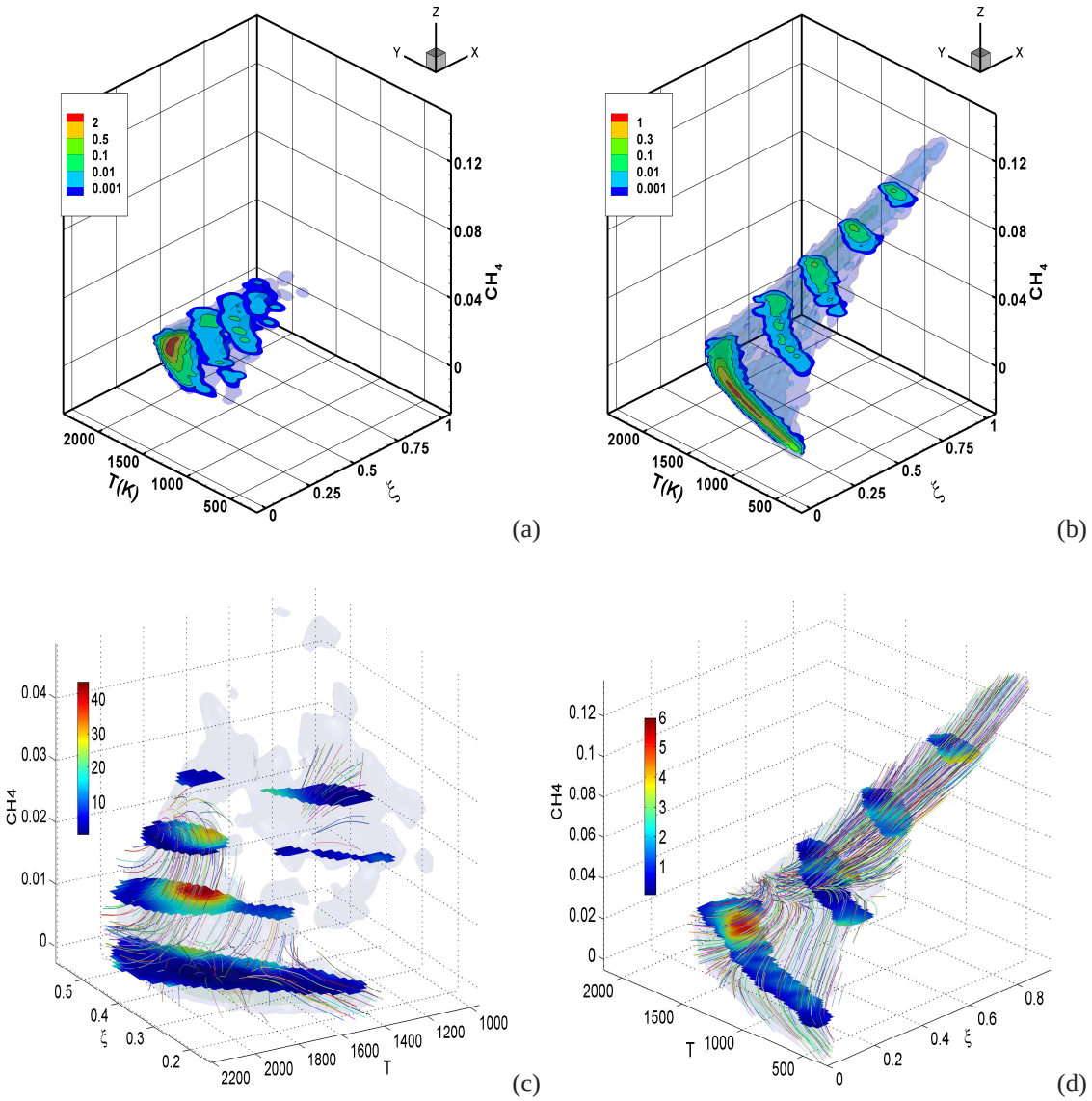

Figure 2.11: FMDF and diffusion velocity streamlines for ξ, T and Y_{CH_4}. Conditions same as in Fig. 2.2.

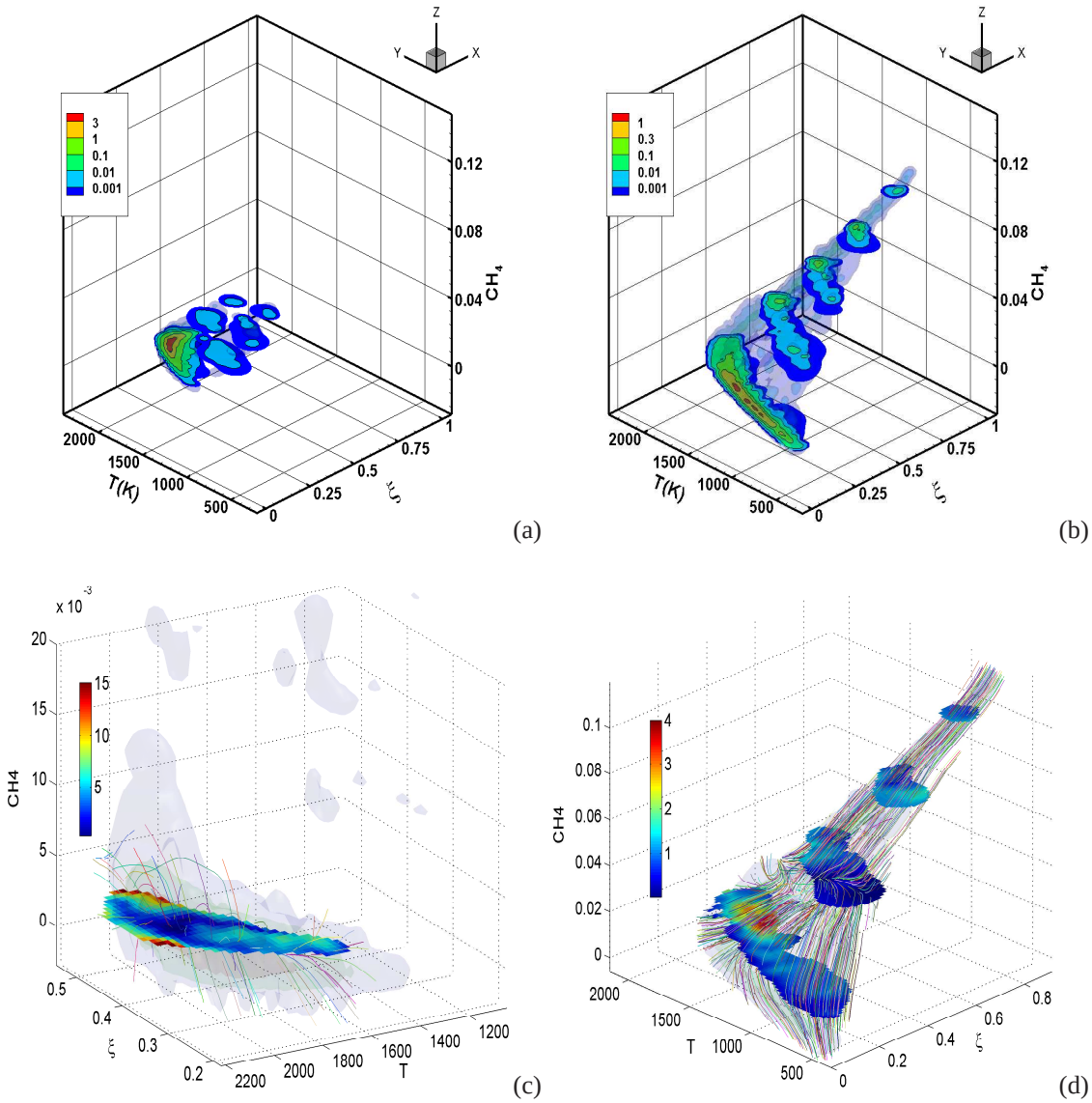

Figure 2.12: FMDF and diffusion velocity streamlines for ξ, T and Y_{CH_4}. Conditions same as in Fig. 2.3.

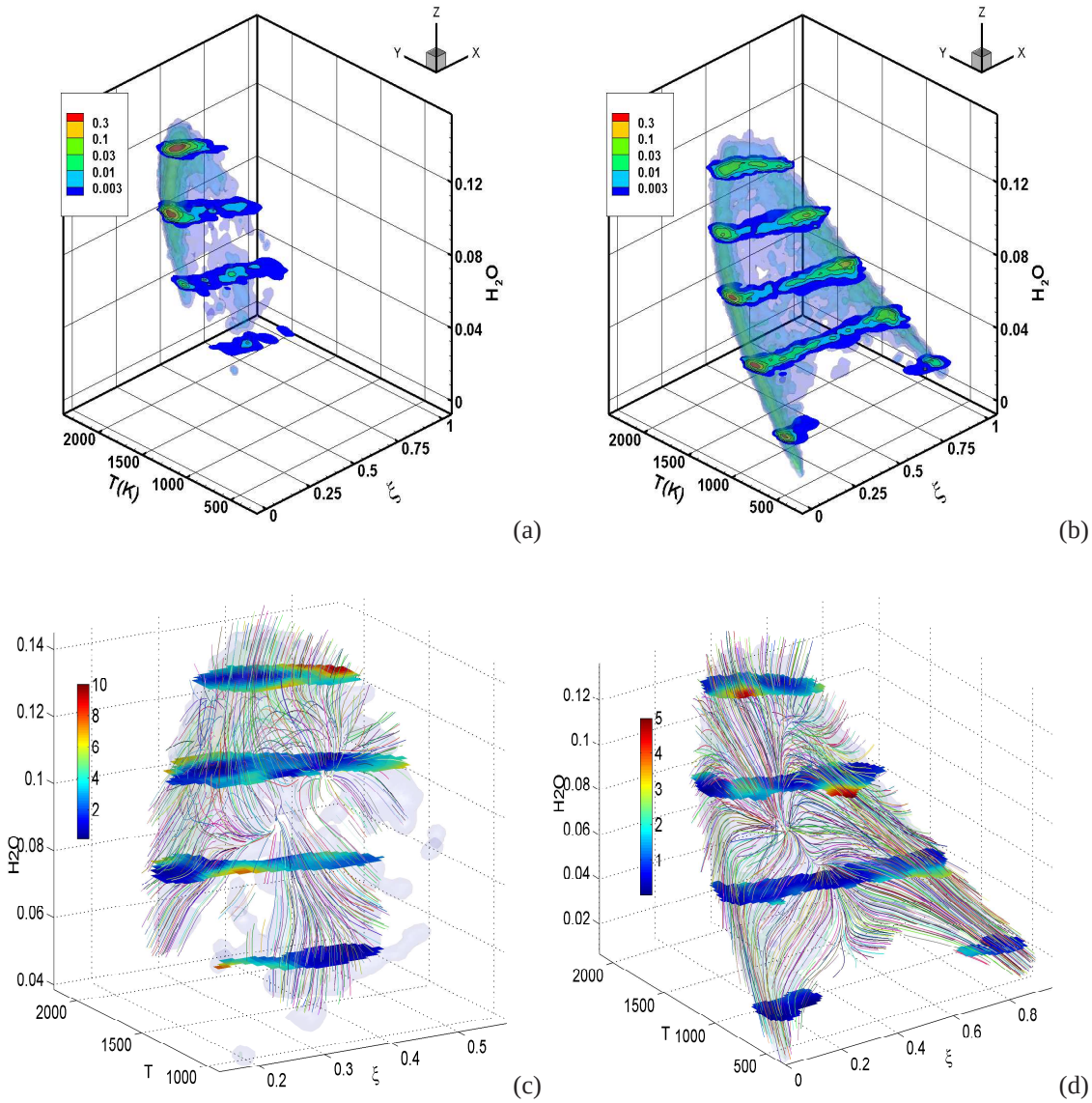

Figure 2.13: FMDF and diffusion velocity streamlines for ξ, T and Y_{H_2O}. Conditions same as in Fig. 2.1.

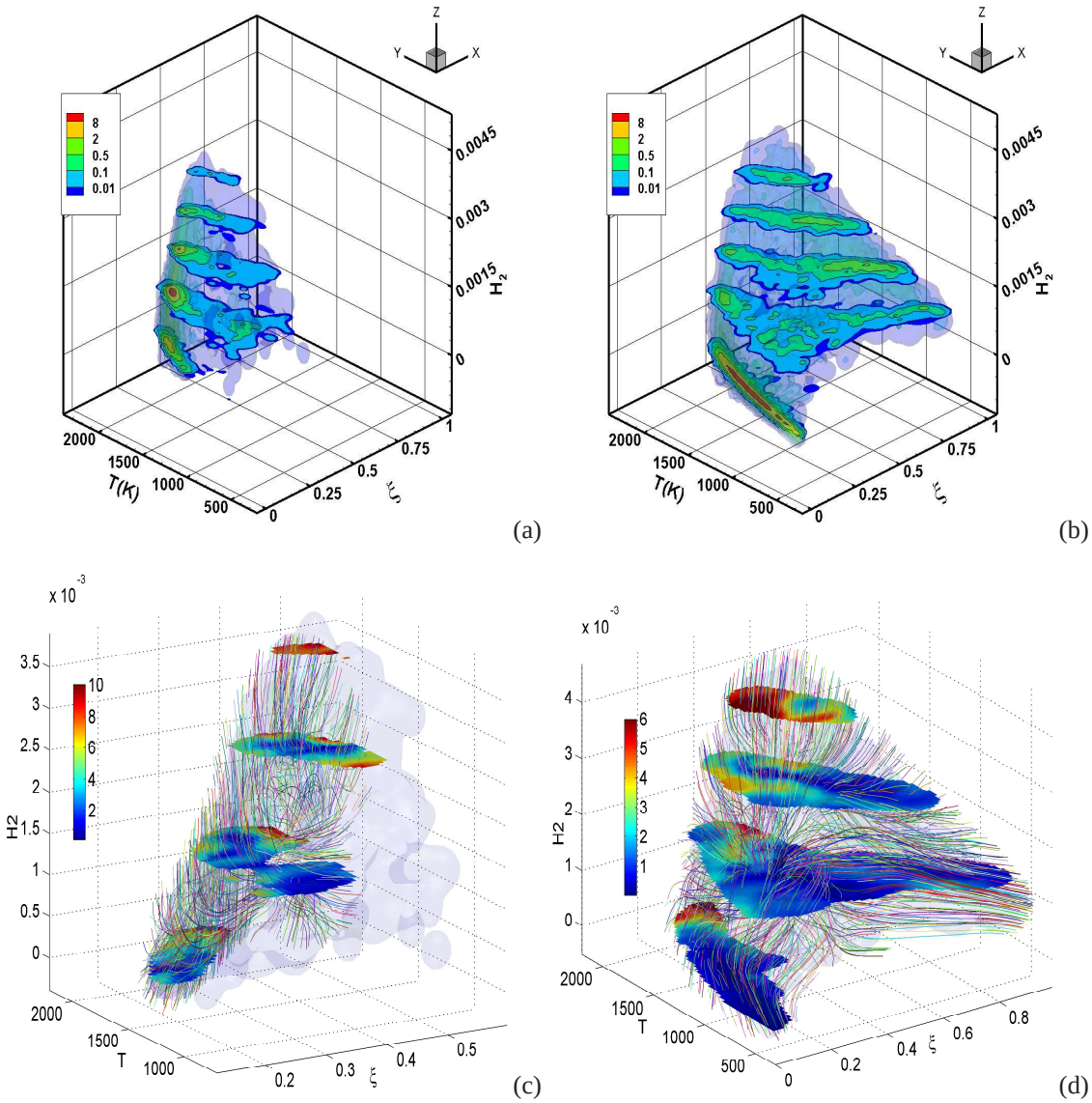

Figure 2.14: FMDF and diffusion velocity streamlines for ξ, T and Y_{H_2}. Conditions same as in Fig. 2.2.

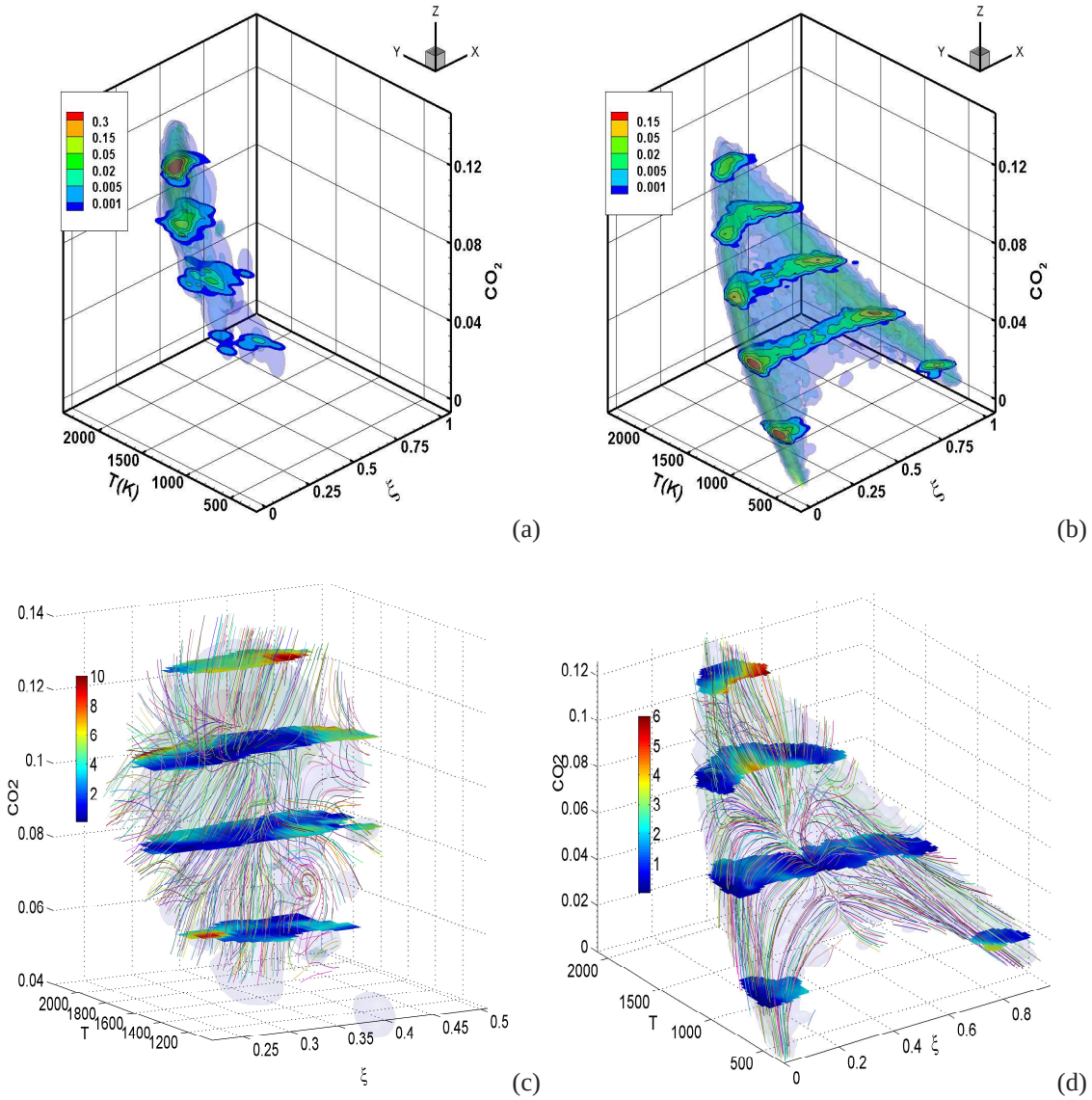

Figure 2.15: FMDF and diffusion velocity streamlines for ξ, T and Y_{CO_2} at $x/D = 7.5$ in flame E. (a & c) small SGS variance ($\langle\xi''^2\rangle_L = 0.0011$, $\langle\langle\xi''^2\rangle_L\rangle = 0.0394$), (b & d) large SGS variance ($\langle\xi''^2\rangle_L = 0.081$).

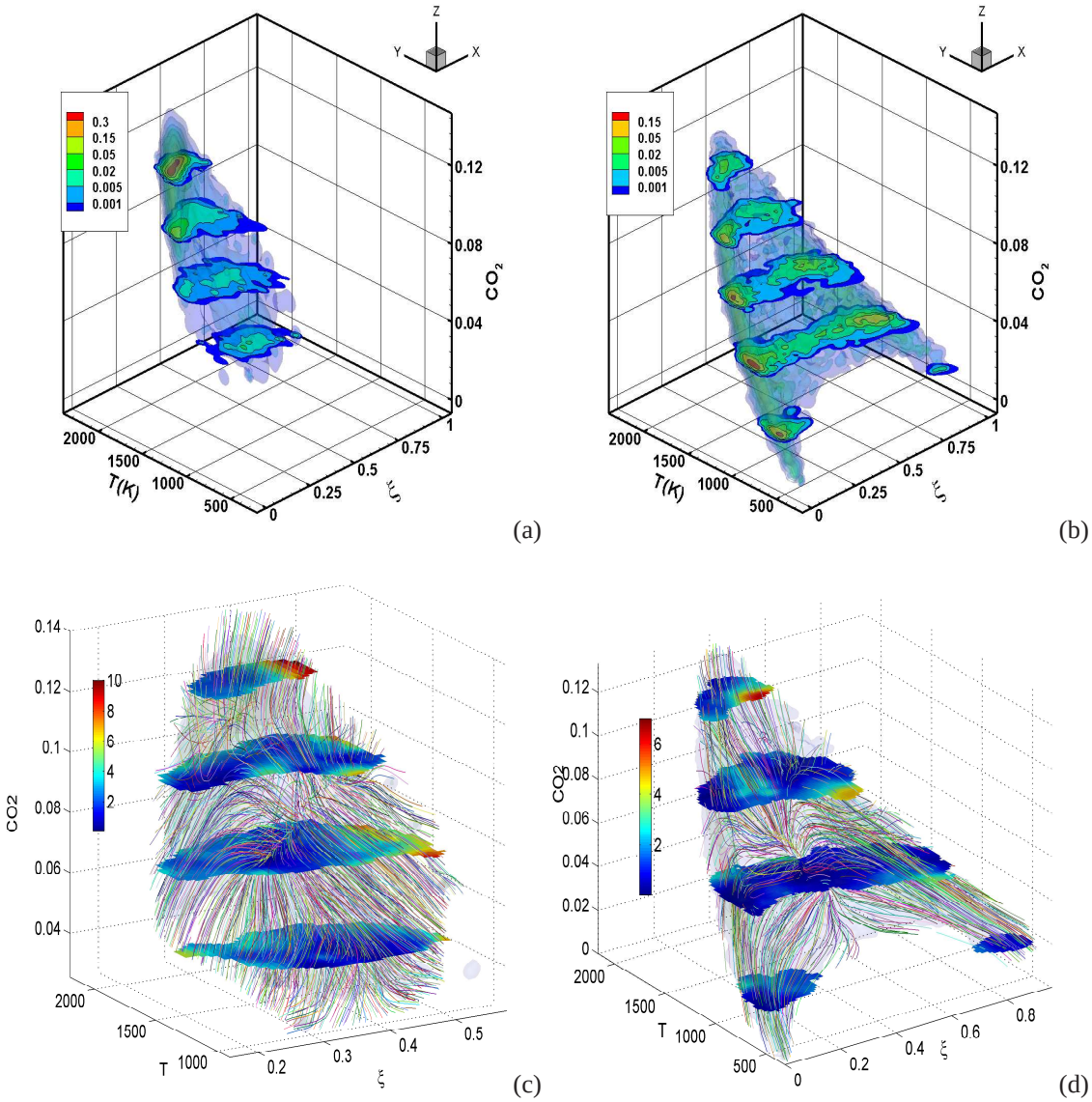

Figure 2.16: FMDF and diffusion velocity streamlines for ξ, T and Y_{CO_2} at $x/D = 15$ in flame E. (a & c) small SGS variance ($\langle\xi''^2\rangle_L = 0.0028$, $\langle\langle\xi''^2\rangle_L\rangle = 0.0206$), (b & d) large SGS variance ($\langle\xi''^2\rangle_L = 0.064$).

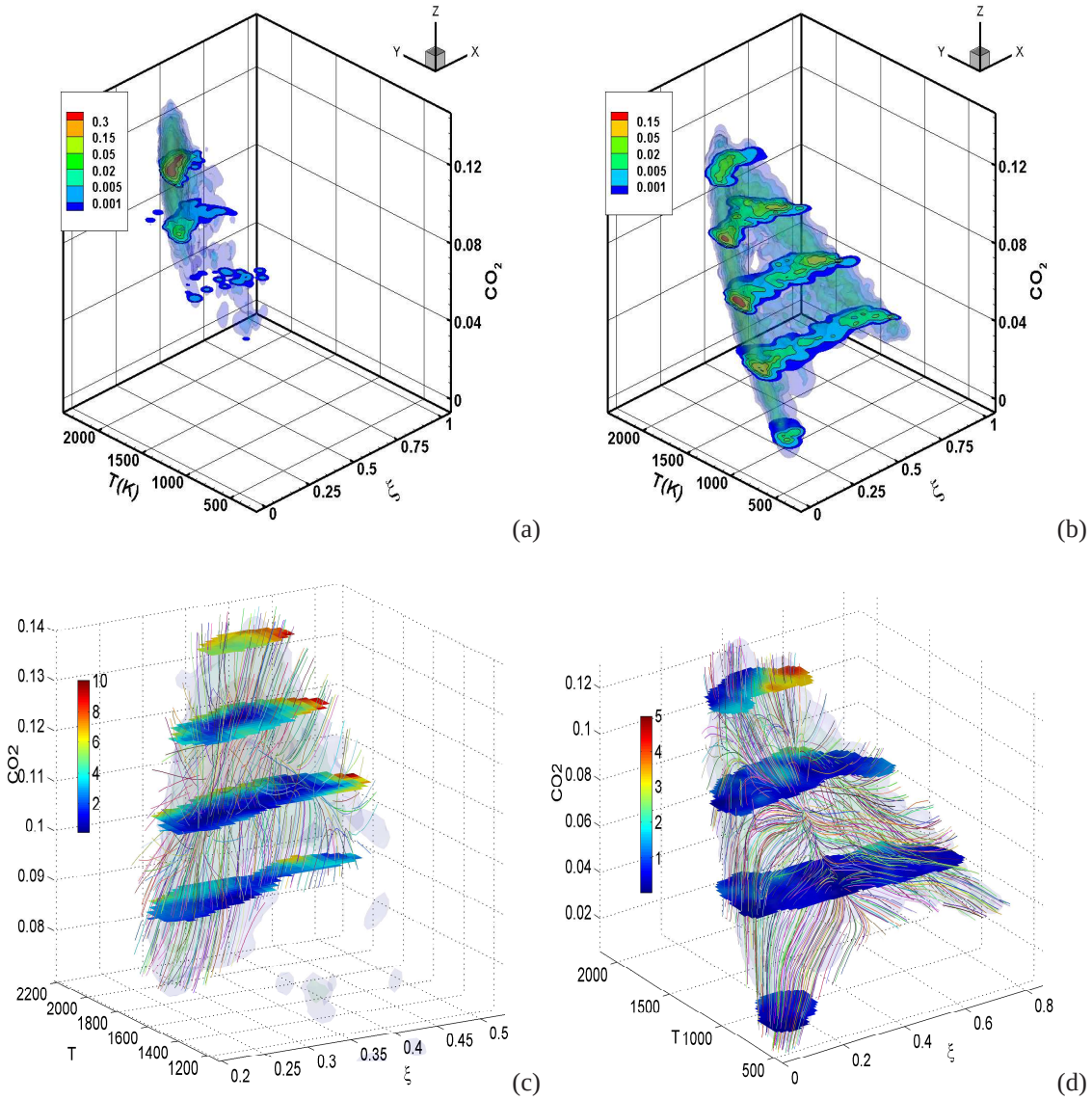

Figure 2.17: FMDF and diffusion velocity streamlines for ξ, T and Y_{CO_2} at $x/D = 30$ in flame E. (a & c) small SGS variance ($\langle\xi''^2\rangle_L = 0.0018$, $\langle\langle\xi''^2\rangle_L\rangle = 0.0098$), (b & d) large SGS variance ($\langle\xi''^2\rangle_L = 0.044$).

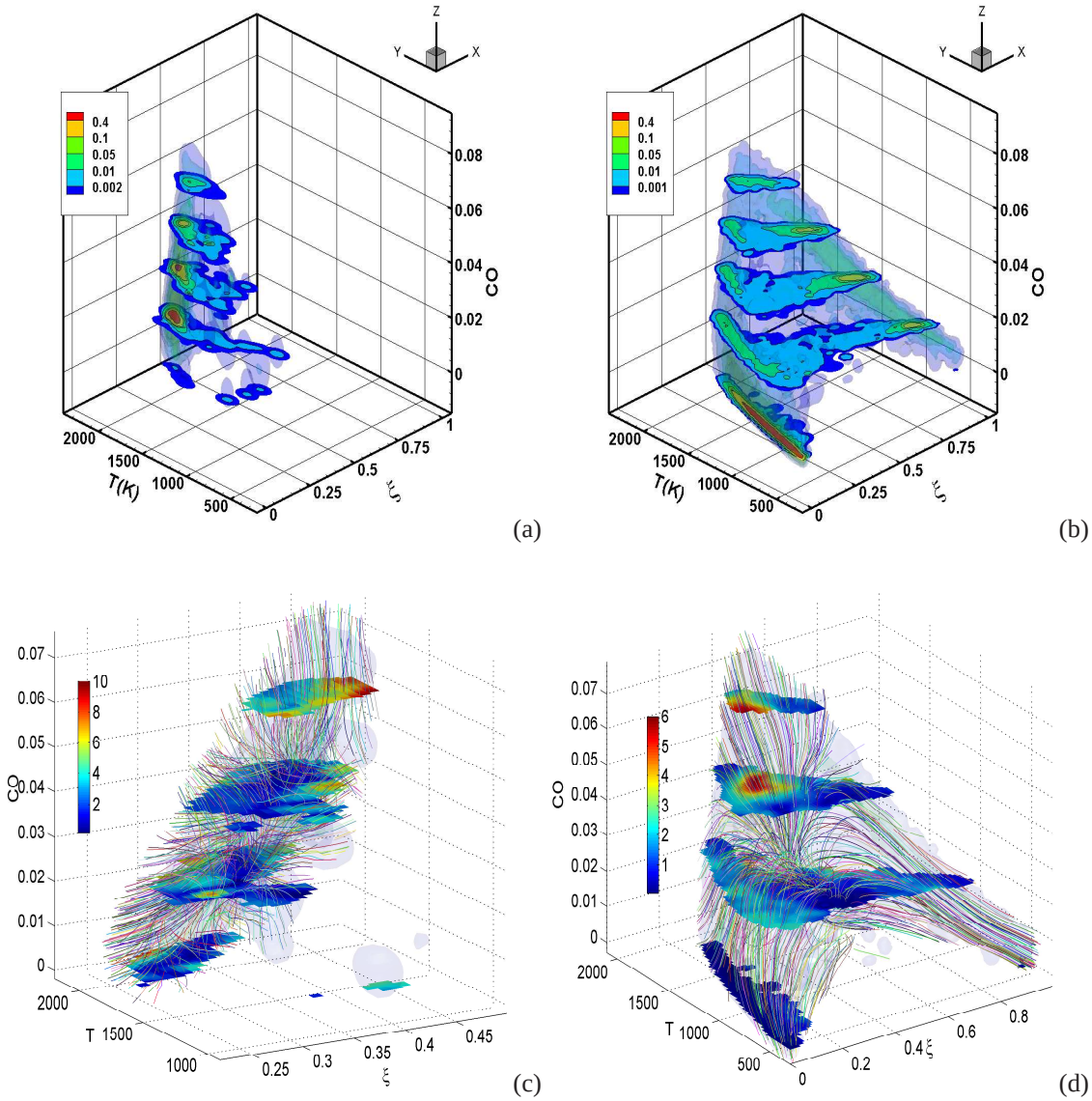

Figure 2.18: FMDF and diffusion velocity streamlines for ξ, T and Y_{CO}. Conditions same as in Fig. 2.15.

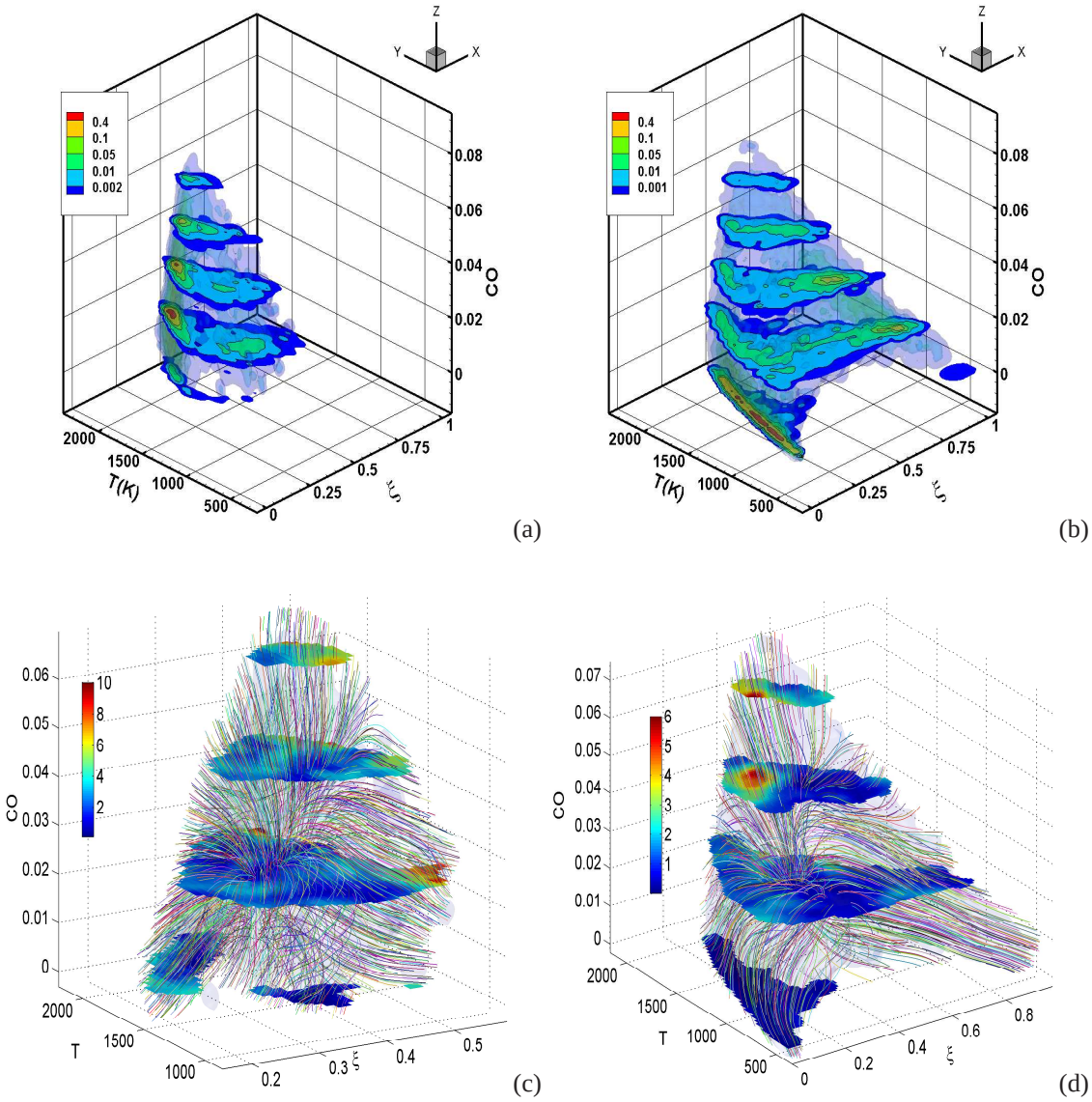

Figure 2.19: FMDF and diffusion velocity streamlines for ξ, T and Y_{CO}. Conditions same as in Fig. 2.16.

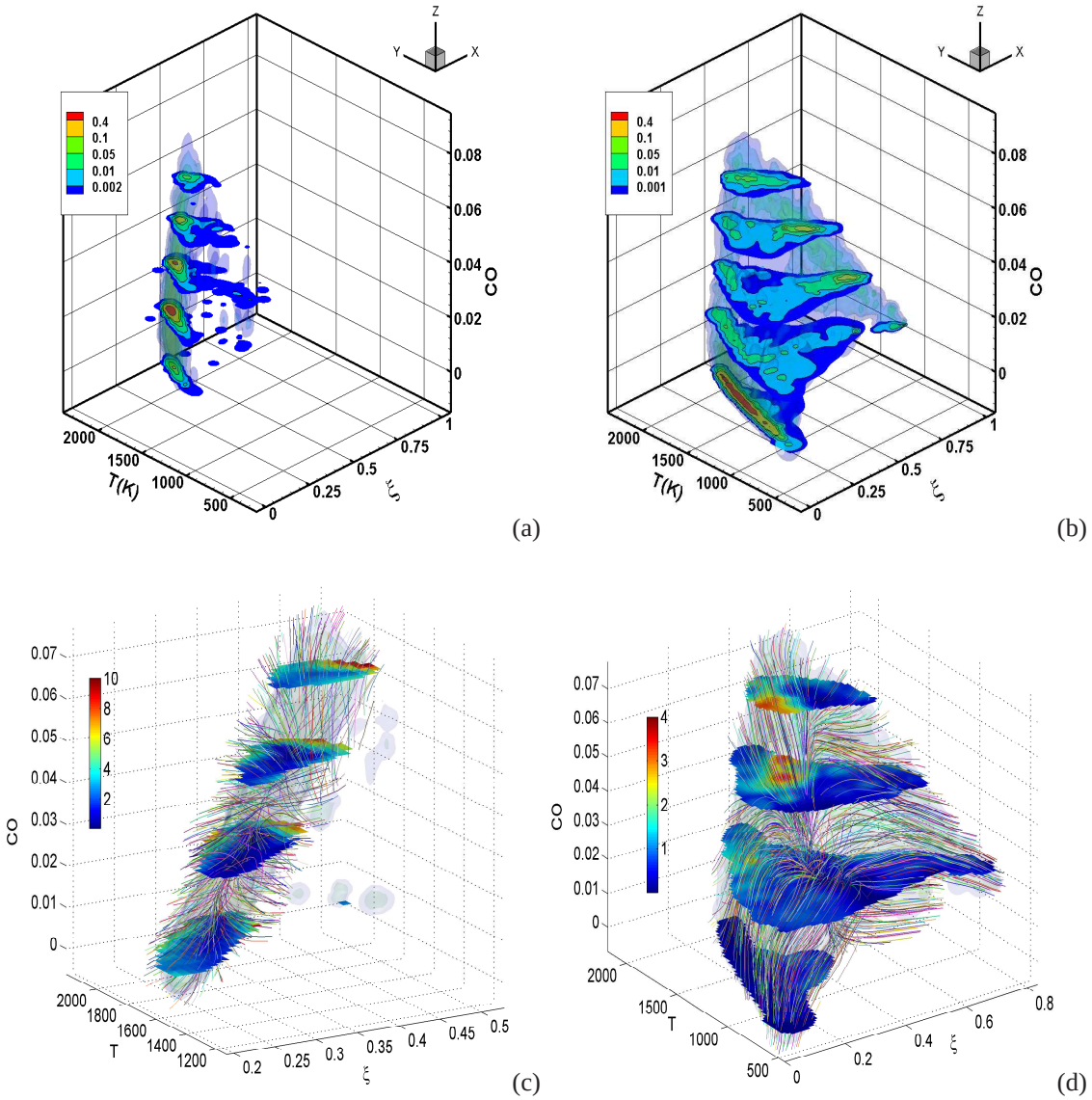

Figure 2.20: FMDF and diffusion velocity streamlines for ξ, T and Y_{CO}. Conditions same as in Fig. 2.17.

Chapter 3

JPDF, conditional diffusion and conditional dissipation in turbulent partially premixed flames

3.1 Introduction

Turbulent mixing and turbulence-chemistry interactions are key process in turbulence combustion. Accurate predictions of turbulent flames depend critically on correct modeling of these process.

The mixing process that evolves the PDF, f_ϕ, of a scalar variable, ϕ, can be studied using the PDF transport equation [47],

$$\begin{aligned} \frac{\partial f_\phi}{\partial t} + \frac{\partial}{\partial x_i}\left[f_\phi\left(U_i + \langle u_i|\hat{\phi}\rangle\right)\right] &= -\frac{\partial}{\partial \hat{\phi}}\left\{f_\phi\left[\langle D\nabla^2\phi|\hat{\phi}\rangle + S(\hat{\phi})\right]\right\} \\ &= D\nabla^2 f_\phi - \frac{1}{2}\frac{\partial^2}{\partial \hat{\phi}^2}\left(f_\phi\langle\chi|\hat{\phi}\rangle\right) - \frac{\partial}{\partial \hat{\phi}}\left[f_\phi S(\hat{\phi})\right], \end{aligned} \tag{3.1}$$

Where U_i, u_i and S are the mean and fluctuating velocities and the reaction rate, respectively. The right-hand side gives two forms of the mixing terms. They involve the conditional scalar diffusion, $\langle D\nabla^2\phi|\phi = \hat{\phi}\rangle$, and the conditional scalar dissipation,$\langle\chi|\phi = \hat{\phi}\rangle = \langle 2D\frac{\partial\phi}{\partial x_i}\frac{\partial\phi}{\partial x_i}|\phi = \hat{\phi}\rangle$, where the brackets denote for an ensemble average. Notice that the chemical source term is treated exactly in the PDF equation, only the

fluctuating velocity and mixing terms are unclosed. The mixing terms (conditional dissipation and conditional diffusion) represent the effects of turbulent mixing on the evolution of the scalar PDF. Therefore, it is of importance to study these mixing terms in the PDF equation.

In applying the pdf equation to variable-density flows, the joint mass density function (JMDF) instead of PDF is often used ad dependent variable, which is defined as $\widetilde{F}_\phi \equiv \rho(\hat{\phi}) f_\phi$. The JMDF is important in the presumed probability density function method and the conditional moment closure. Various probability models such as beta or clipped Gaussian distributions are typically used to represents the joint species distribution.

In the present work we investigate the mixing of mixture fraction, temperature and a species mass fraction in turbulent partially premixed methane flames (Sandia flame D and E). We analyze the JMDF of mixture fraction, temperature and the corresponding mixing terms evolving the JMDF. The knowledge of the JMDF and mixing terms is important for understanding the mixing of multiple reactive scalars and the turbulence-chemistry interaction.

3.2 Experimental data and processing procedures

We use experimental data obtained in piloted turbulent partially premixed methane flames with a 1:3 ratio of CH_4 to air by volume (Sandia flames D and E, see [59, 58, 64] for detail). The measurements employed combined line-image of Raman scattering, Rayleigh scattering, and laser-induced CO fluorescence. Simultaneous measurements of major species (CO_2, O_2, CO, N_2, CH_4, H_2O, and H_2), mixing fraction (obtained from all major species), temperature, and the radial component of scalar dissipation rate and diffusion were made. The mixture fraction is calculated using a variation of Bilger's definition, which has been modified by excluding the oxygen terms.

The length of the imaging line is 6.13 mm with a measurement spacing of 0.2044 mm. The actual measurement resolution is larger (≈ 0.3 *mm*) due to the blurring effects of the optical system and data processing [61]. The overall resolution of the imaging system is capable of resolving 98% of the highest scalar dissipation [41].

In our analysis 6000 line images are used at each measurement location. Due to the limited data size, we employed kernel methods for computing the JMDF, the conditional dissipation rate and conditional diffusion velocity in three dimensions (ξ, T and Y_i) with a resolution of $100\times100\times100$ in the samples space and an oversmooth parameter 1.5. The scalar dissipation and diffusion were computed using 10th-order

central difference scheme. The systematic uncertainty for major species, i.e., CH_4, CO_2, H_2O, O_2 is less than 5%. For CO and H_2, the systematic uncertainty is between 10% to 20%. The statistical uncertainties are estimated using bootstrap method in the context of kernel method. The details about the mean square error (MSE) estimation of kernel density estimator and kernel regression are given in appendix A. The MSE for the JPDF and conditional dissipation rate are discussed in appendix B. The results shows that though the statistical uncertainty not small, are still comparable to the measurement uncertainty, thus, we expect these uncertainties would not change the main trend of these JMDF and mixing terms.

3.3 Results and Discussion

In this section the JMDF, the conditional dissipation rates, and the conditional diffusion of the mixture fraction, temperature and species mass fractions are analyzed . We focus on the radial position at which the mean mixture fraction, $\langle\xi\rangle$, is at or close to the stoichiometric value ($\xi_s = 0.35$) to maximize the probability of sampling the reaction zones. Figure 3.1 shows the responding radial profiles of $\langle\xi\rangle$ for Flame D and Flame E. At $x/D = 7.5, 15$ and 30 the mean stoichiometric mixture fraction is located at $r/D = 1.04, 1.34,$ and 1.78 for the three downstream locations, respectively. In the following discussion, we will omit the corresponding r/D values for convenience unless stated otherwise.

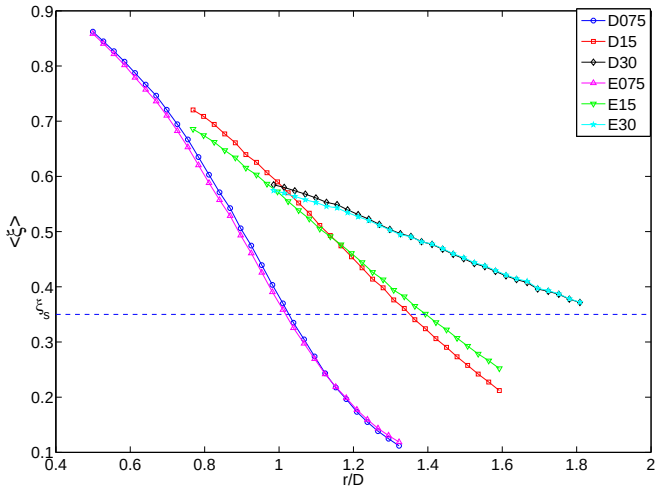

Figure 3.1: Mean mixture fraction $\langle\xi\rangle$ versus radial position at different measurement location in flame D and E, the dash line represent the stoichiometric mixture fraction.

To achieve reasonable statistical convergence for the JMDF and the mixing terms for all the major species, a data sample size much larger than that available is needed. In this study we include one major species at a time, we consider the JMDF of mixture fraction, temperature and one species fraction and the related mixing terms in the PDF transport equation. To improve the statistical convergence, conditional statistics were averaged over 5 pixels in the radial direction while JMDF were averaged over 3 pixels. To fully represent the JMDF and the mixing terms, a three-dimensional scalar space is needed. We present them as functions of three sample-space variables.

The statistical uncertainty and bias for the JMDF are estimated using bootstrap method [65] which analyzed in the way describe in [62]. The maximum r.m.s values of the JMDF are typically less than 10% of the peak JMDF values and the bias is typically less than 15% of the JMDF peak values with MSE (mean square error) less than 25%.

The conditional dissipation rate of a species mass fraction, $\langle \rho D \frac{\partial Y_i}{\partial x_j} \frac{\partial Y_i}{\partial x_j} | \hat{\xi}, \hat{T}, \hat{Y}_i \rangle / \langle \rho \rangle$ represents the effects of turbulent mixing on the evolution of scalar JMDF and is unclosed. We use isocontours to present the dissipation rate. The conditional diffusion of the mixture fraction, temperature, and a species mass fraction, $\langle \frac{\partial}{\partial y}(\rho D \frac{\partial \xi}{\partial y}) | \hat{\xi}, \hat{T}, \hat{Y}_i \rangle / \langle \rho \rangle$, $\langle \frac{\partial}{\partial y}(\rho D_T \frac{\partial T}{\partial y}) | \hat{\xi}, \hat{T}, \hat{Y}_i \rangle / \langle \rho \rangle$ and $\langle \frac{\partial}{\partial y}(\rho D \frac{\partial Y_i}{\partial y}) | \hat{\xi}, \hat{T}, \hat{Y}_i \rangle / \langle \rho \rangle$, appear in the JMDF transport equation as terms transporting the JMDF in the ξ, T and Y_i spaces, respectively. Therefore, they are the three components of the diffusion velocity of the JMDF in the ξ, T and Y_i space. We use streamlines and isocontours to present the direction and the magnitude of the diffusion velocity. The diffusion terms are non-dimensionlized by the filtered scalar dissipation rate, SGS variance and the maximum value of ξ,T and Y_i, respectively.

In the following, we first discuss the mixing of each major species mass fraction using the JMDF, conditional dissipation rates and conditional diffusion for flame D at $x/D = 7.5$. We then discuss the dependence of the mixing on downstream and cross-stream locations. Finally, the Reynolds number dependence of the mixing properties are discussed.

3.3.1 Typical features of JMDF and mixing terms

The JMDF of ξ, T and Y_{CH_4} in flame D at $x/D = 7.5$ (Fig. 3.2a) is concentrated near equilibrium scalar values with a peak on the lean side where the Y_{CH_4} levels are very low. On the rich side, there is a strong correlation between the temperature and the Y_{CH_4} with high temperature corresponding to low Y_{CH_4}. Figure 3.2b shows that the Y_{CH_4} dissipation rate is large on the rich side where the mixture fraction dissipation rate is large. The peak of Y_{CH_4} dissipation rate is located at (0.49, 1640 K, 0.033), approximately coinciding

with the peak of scalar dissipation rate. Previously studies [42, 40] have shown that the ramp-cliff structure is present and has a significant contribution to the dissipation. On the lean side because of very low Y_{CH_4} level, the dissipation rate is small. The figures for diffusion streamlines of ξ, T and Y_{CH_4} for clarity are showed with a perspective different from the plot of JMDF and conditional dissipation rate. At $x/D = 7.5$ (Fig. 3.2c), the streamlines for very rich ($\xi > 0.6$) and lean mixtures ($\xi < 0.2$) generally move along the ridgeline of the JMDF, towards the stoichiometric mixture fraction. For very rich mixtures, the Y_{CH_4} and T depends linearly on mixture fraction, therefore their diffusion is proportional to mixture fraction diffusion, resulting in straight diffusion streamlines along the ridgeline. For very lean mixtures, Y_{CH_4} is close to zero while T depends linearly on mixture fraction, also resulting in straight diffusion streamlines in the horizontal plane. After that, the Y_{CH_4} and T diffusion changes sign near (0.44, 1350 K, 0.025) and (0.24, 1450 K , 0.004) so the streamlines turns near these points and then move towards a stagnation point (0.414, 1300 K, 0.028). Near the peak temperature, ξ diffusion is small because the curvature of the ξ profile is small in this region (center of ramp-cliff structure). The T diffusion and Y_{CH_4} diffusion are negative and positive, respectively, due to the negative and positive curvature of the profiles (as a function of ξ). Consequently, the streamline streamline starting from the equilibrium curve near the $\xi = 0.45$ move towards lower T and higher Y_{CH_4} then converge to the stagnation point. The JMDF is transported by both diffusion and reactions, their combined actions keep the JMDF in the JMDF manifold. Individually they generally transport the JMDF out of the manifold unless one of them is small. Near the peak temperature both the reaction rates and diffusion are large, thus the diffusion streamlines move out of the JMDF manifold. For low temperature, the reaction rate is small resulting in diffusion streamlines move along the JMDF manifold.

The JMDF of ξ, T and Y_{CO_2} at $x/D = 7.5$ (Fig. 3.3a) appears to be largely limited to a two-dimensional manifold and has a shape similar to that of the JMDF of ξ and T due to the strong correlation between T and Y_{CO_2}, since Y_{CO_2} is directly related to the heat release. Consequently, similar to Y_{CH_4}, although there are four scalars in the mixing problem, i.e., ξ, T, Y_{CO_2}, and the co-flow, the mixing is similar to a three-scalar mixing. Thus, mixing for these scalars is a degenerated one. At $x/D = 7.5$ the flame is close to fully burning, with T and Y_{CO_2} not far from the equilibrium values. The JMDF have two peaks with the stronger one on the lean branch. The conditional dissipation rate of Y_{CO_2} (Fig. 3.3b) is small near the peak Y_{CO_2} and increases away from the peak due to the Y_{CO_2} and ξ correlation. There are two maxima on either side of the peak. The diffusion velocity streamline for Y_{CO_2} in flame D at $x/D = 7.5$ are shown in Fig. 3.3c. For very rich ($\xi > 0.6$) and lean ($\xi < 0.2$) mixtures the diffusion streamlines generally move in the direction of the ridgeline of the JMDF, towards the stoichiometric mixture fraction. Because for very rich and lean

mixtures T and Y_{CO_2} depends linearly on the mixture fraction, therefore their diffusion is proportional to the mixture fraction diffusion, resulting in straight diffusion streamlines along the ridgeline of JMDF. Near the peak temperature and Y_{CO_2} the mixture fraction diffusion is small because this region is close to the center of the ramp-cliff structure where the curvature of the profiles are small. The temperature diffusion and Y_{CO_2} diffusion are negative due to the negative curvature of the T and Y_{CO_2} profiles as a function of the mixture fraction and the approximately linear mixture fraction profiles. Consequently, the streamlines starting from near $\xi = 0.45$ move towards lower T and Y_{CO_2} values. As the streamline move towards lower temperatures, the scalar dissipation rate increases as well as the chemical reaction rate, resulting in higher diffusion velocity. The relative large diffusion velocity magnitude occurs near $T = 1600 - 1800K$, $\xi = 0.35 - 0.45$. Below this temperature range T and Y_{CO_2} profiles become broader resulting in lower T and Y_{CO_2} diffusion and there appears to be a stagnation point at (0.42, 1350 K, 0.068). The streamlines starting from the very rich and lean regions moves up along the ridgeline and turn near (0.52, 1650 K, 0.078) and (0.26, 1600 K, 0.076), respectively, towards the stagnation point. The temperature and Y_{CO_2} diffusion changes sign near these points, where the inflection points of the temperature and Y_{CO_2} are located. Below these points the diffusion is strongly influence by both mixing and reaction.

The JMDF for ξ, T and Y_{CO} at $x/D = 7.5$ for flame D (Fig. 3.4a) are not far from the equilibrium values. The JMDF consists of three segment, one on the rich side of the peak Y_{CO} and two on the lean side. They connect four vertices that are not in the same plain; therefore, unlike that of Y_{CH_4} and Y_{CO_2}, the JMDF of ξ, T and Y_{CO} is not limited to a two-dimensional manifold and must be represented in a three-dimensional scalar space, i.e., the mixing problem is "non-degenerated". On the rich side the JMDF ridgeline is largely a straight line, due to the low reaction rates resulting in linear relationships among the scalars. The production rate of Y_{CO} is highest near the peak, and is balanced by (negative) diffusion. Just to the lean side of the peak Y_{CO}, where the consumption rate is highest, Y_{CO} decreases rapidly to reach low values at $\xi = 0.2$. Here the consumption rate is balanced by positive diffusion. Further to the lean Y_{CO} remains low and the temperature decreases linearly with mixture fraction. The structure of Y_{CO} dissipation rate (Fig. 3.4b) is relatively simple compare to other species mass fraction, i.e.,Y_{CH_4} and Y_{CO_2}. There is one peak value on the lean side near the Y_{CO} peak. Here Y_{CO} changes rapidly with ξ and the scalar dissipation rate is large (due to the ramp-cliff structure), resulting in large Y_{CO} dissipation rate. The diffusion streamlines of ξ, T and Y_{CO} (Fig. 3.4c) move largely move towards lower T and Y_{CO} value near the peak Y_{CO}. Here both the reaction rate and the (negative) diffusion are high and largely balance each other. Their combined action transports the JMDF within the JMDF manifold. Thus the diffusion alone transports the JMDF out of the manifold. On the far lean side and

the far rich side, the streamlines stay inside the JMDF manifold. The maximum diffusion magnitude (≈ 4.7) occurs slight to the lean side of the Y_{CO} dissipation peak. On the lean side between 1000K to 1500K, the diffusion streamlines moving towards higher Y_{CO} values but remain at approximately the same temperature values. Due to the high CO consumption rate in these mixtures the streamlines tend to move out of the JMDF manifold. These streamlines then turn towards lower T and Y_{CO} values, and converge to a stagnation point in the interior of the pyramid.

For clarity in the figures involving O_2, the ξ and T axes are plotted differently (Figs. 3.2d&e&f). Due to partially premixing, the JMDF of ξ, T and Y_{O_2} at $x/D = 7.5$(Fig. 3.2b) is similar to the inverted JMDF of ξ, T and Y_{CO_2} with higher Y_{O_2} values for both lean and rich mixtures but low values near ξ_s. The JMDF, although not in a plane, is largely limited to a two-dimensional manifold. The conditional Y_{O_2} dissipation (Fig. 3.2e) and diffusion (Fig. 3.2f) is also similar to the inverted conditional Y_{CO_2} dissipation and diffusion. The mixing scenario involving H_2O (Figs. 3.3d&e&f) and H_2 (Figs. 3.4d&e&f) is again very similar to those involving CO_2 and CO. For the rest of the paper we only show the results of species CH_4, O_2, CO_2 and CO. The results for other species are given in the supplemental materials.

3.3.2 Downstream evolution of JMDF and mixing terms

At $x/D = 15$, close to the equilibrium the JMDFs (Figs. 3.5a&d,6a&6d) are similar to those at $x/D = 7.5$. There is a significant number of local extinction events at this location due to the higher scalar dissipation rate, as reflected by the JMDF in the low temperature regions. For species Y_{CH_4}, Y_{O_2} and Y_{CO_2} (Figs. 3.5a&3.5d&3.6a), the extent of the JMDF is close to a plane in the scalar space. Therefore, the mixing is largely confined to a plane and is similar to a three-scalar mixing scenario. For the JMDF of ξ, T and Y_{CO} (Fig. 3.6d), the burning samples and the samples with lower temperatures, which are extinguished flamelets, form a triangular pyramid-shape JMDF manifold. A plane on the lean side (left) containing three vertices (0.017, 340 K, 0), (0.30, 2020 K, 0.008) and (0.45, 1960 K, 0.07) is formed due to the rising Y_{CO} values resulting from the imbalance between diffusion and the CO consumption rate. A front plane connecting the left plane and the ridgeline on the rich side is also formed. The elevated CO levels due to diffusion and reduced CO consumption results in similar profiles of Y_{CO} and T (hence the profiles are on the front plane). At this downstream location the pyramid is only partially filled, the JMDF values are lower inside the pyramid. At $x/D = 30$, the extinguished samples have largely reignited as a result of the decay of the scalar dissipation rate. The JMDFs (Figs. 3.7a&d,8a&d) are again largely concentrated close to the equilibrium values.

The peak value of the conditional dissipation rate for Y_{CH_4}, Y_{O_2} decreases (Figs. 3.5b&e) as x/D

increases. At $x/D = 15$, the Y_{CH_4} dissipation rate (Fig. 3.5b) has one peak, but some large dissipation rate occur at higher Y_{CH_4} and lower temperature values possibly due to the mixing between extinguished and burning samples. At $x/D = 30$, the peak dissipation rate for Y_{CH_4}, Y_{O_2} (Figs. 3.7b&7e) further decreases. The interesting feature is that move downstream, the peak dissipation rate for Y_{CO_2} first increases (Figs. 3.6b&8b) then decreases, while the trend for Y_{CO} (Figs. 3.6e&8e) is just opposite. A possible explanation for this trend has to do with the water-gas shift reaction, $CO + H_2O \Longleftrightarrow CO_2 + H_2$. At $x/D = 15$, due to local extinction, the backward reaction rate increases. The lower consumption rate of Y_{CO} and higher consumption rate of Y_{CO_2} results in the lower Y_{CO} dissipation rate and higher Y_{CO_2} dissipation rate. Moving further downstream, large amount of samples reignite, the backward reaction rate decrease which results in low consumption rate of Y_{CO_2} and higher consumption rate of Y_{CO}.

The overall diffusion streamline pattern at $x/D = 15$ for Y_{CH_4} (Fig. 3.5c) on the lean side for the burning samples is similar to those in $x/D = 7.5$, with a stagnation point (0.39,1600 K,0.023). The largest magnitude of diffusion velocity has increased to approximately 10. Note that the "center" of diffusion does not correspond to the conditional mean temperature and Y_{CH_4}. On the rich side for the burning part, there are a number of straight streamlines start from very rich region ($\xi > 0.8$) towards another stagnation point (0.52, 1800 K, 0.026). Previous results suggest that this trend is essentially due to the mixing between pilot and the fuel/air streams without reaction[42]. For the extinguished samples the diffusion streamlines starting from both lean and rich mixtures initially move primarily in the direction of mixture fraction towards $\xi \approx 0.4$, with only modest change of T and Y_{CH_4} values. The diffusion streamlines then move largely in the direction of T and Y_{CH_4} towards higher temperature and lower Y_{CH_4}. These trends indicate that the ξ diffusion initially dominates which is due to extinguished flamelet [43]. For the extinguished samples, T and Y_{CH_4} diffusion can occur in the direction of mixture fraction gradient or iso-mixture fraction surface, the latter indicates the interaction between burning and extinguished samples. At $x/D = 30$ the results (Fig. 3.7c) are similar to those at $x/D = 15$ with the maximum diffusion magnitude further increasing to 12. On the rich side, more short straight diffusion lines move towards the JMDF manifold first and then along it which is similar to those in passive scalar mixing [62]. Also the influence of pilot is mush less evident at $x/D = 30$ [43]. The trend of diffusion stream line pattern for Y_{O_2} (Figs. 3.5f&7f) and Y_{CO_2} (Figs. 3.6c&8c) at $x/D = 15$ and $x/D = 30$ are very similar to those involving Y_{CH_4}.

At $x/D = 15$ for Y_{CO} (Fig. 3.6f), the streamline pattern for the burning samples are similar to that at $x/D = 7.5$ with the maximum diffusion magnitude increasing to 7. For the extinguished samples, the streamlines from low temperature and Y_{CO} values on the far lean side first move upward towards higher Y_{CO}

values. Here the reaction rates are low and the streamlines are located within the JMDF manifold (the left plane), which is generated by diffusion. The streamlines then move towards ξ_s, and together with those from the lean side forming the front plane. Since the reaction rate are low, the JMDF is transported in the direction of the streamlines. Near ξ_s the streamlines move towards the stagnation point at higher T and lower Y_{CO}. Again, for each flamelet the diffusion for both the temperature and Y_{CO} is in the opposite direction of the streamlines. The diffusion here, therefore, is along the iso-mixture fraction surface (ξ_s), indicating diffusion among burning and extinguished flamelets. At $x/D = 30$ (Fig. 3.8f), due to reignition, the streamline is again confined in the JMDF which is close to the equilibrium value. In the lean side, a large amount of short streamlines move towards the ridgeline then along it indicate the relative well mixed rich mixtures.

3.3.3 Cross stream dependence of mixing configurations

Moving towards the edge of the flame, the mean mixture fraction deviates from the stoichiometric mixture fraction (ξ_s), resulting in less strong interactions between the turbulence and chemistry. Previous experimental studies shows the radial dependence of the conditional means of major species Y_{CO_2},Y_{CO},Y_{CH_4} in turbulent jet flames is relatively weak[63]. However, the JMDF and the mixing terms at different raidal locations have some distinct characteristics. We mainly focus the results for different radial positions at $x/D = 7.5$ in flame D. At this downstream location the line images cover a wide range of mean mixture fraction, ranging from 0.1 to 0.85 (Fig. 3.1). Figure 3.15-3.21 shows the JMDF and the mixing terms for $r/D = 0.6130,\ 0.9537$ and 1.1240. The mean mixture fraction values at these radial location are 0.7873, 0.4392 and 0.2432, respectively.

At $r/D = 0.9537$ where the mean mixture doesn't deviates much from ξ_s. The shape of JMDF (Figs. 3.17a&d,3.18a&d) is still two dimensional for Y_{CH_4}, Y_{CO_2}, Y_{O_2} and three dimensional for Y_{CO}, with less extension of JMDF on the lean side. The peak Y_{CO_2} and Y_{O_2} dissipation rate on the rich side become much stronger compared to those at radial position where $\langle\xi\rangle = \langle\xi_s\rangle$. The diffusion pattern is almost identical with what we discussed before.

Moving further toward the edge of the flame, at $r/D = 0.6130$, the shape of JMDF (Figs. 3.15a&d,3.16a&d) changes from two-dimensional for Y_{CO_2}, Y_{O_2}, Y_{CH_4} and three dimensional for Y_{CO} to nearly one dimensional because both temperature and species mass fraction is linearly correlated with mixture fraction. The JMDF generally increases with the increase of mixture fraction. The gradient of species dissipation rate (Figs. 3.15b&e, 3.16b&e) is also largely in the direction of mixture fraction. The diffusion streamlines (Figs. 3.15c&f, 3.16c&f) generally move towards the ridgeline of JMDF and then move along it. Therefore, there

are two mixing process, one fast and one slow, which is similar to the mixing of non-reactive scalars.

Moving toward the other edge of the flame, at $r/D = 1.124$, the location of the peak values of JMDFs (Figs. 3.19a&d, 3.20a&d) change from rich side to lean side. The peak of the species conditional dissipation rate (Figs. 3.19b&e, 3.20b&e) on the lean side becomes much stronger which is near $\xi = 0.45$ where the center of ramp-cliff structure is located. The diffusion streamlines (Figs. 3.19c&f, 3.20c&f) on the lean side is very similar to those discussed previously. On the rich side, less straight diffusion streamlines move along the ridgeline towards $\xi = 0.45$. At $r/D = 0.9537$ and 1.1240, the mixing is still strongly influenced by the chemical reaction. Thus, it's still important to model the interaction between turbulence and chemistry at these radial locations.

At $x/D = 15$, the situation for radial dependence of mixing terms is similar to those at $x/D = 7.5$. At $r/D = 0.8825$, the JMDF (Figs. 3.21a&d, 3.22a&d) begin to extend to low temperature regions due to local extinction. The diffusion streamline begin in the extinction region move towards the ridgeline of the JMDFs. At $x/D = 30$ in flame D, the JMDF and mixing terms does not change significantly for the current measurement location which r/D ranging from 0.7689 to 1.5922.

3.3.4 Reynolds number dependence of JMDF and mixing terms

The results for flam E at $x/D = 15$ and 30 (Figs. 3.11-3.14) are qualitatively similar to those for flame D. At $x/D = 7.5$, due to higher Reynolds number there already have a significant extinction samples results in JMDFs (Figs. 3.9a&d, 3.10a&d) extend to very low temperature. An interesting feature at this location is that the peak value of Y_{CH_4}, Y_{CO} dissipation (Fig. 3.9b&10e) is less than those in flame D at $x/D = 7.5$ while the peak value of Y_{O_2} dissipation (Fig. 3.9e) is higher than those in flame D. A possible explanations has to do with the dynamics of turbulence. The velocity ratio between the main jet and pilot jet is approximately the same for flame D and flame E. However, the velocity ratio between pilot jet and coflow increase 50% from flame D to flame E which resulting in more intense mixing between pilot gas and coflow in flame E that producing a higher Y_{O_2} dissipation rate. With the increase of Reynolds number, the scalar dissipation rate decays more quickly which resulting in lower Y_{CH_4} and Y_{CO} dissipation. For the extinguished samples, the temperature and species diffusion can occur in the direction of mixing fraction gradient as well as along iso-mixture fraction surface. At $x/D = 7.5$ in flame E near $\xi = 0.4$ (Figs. 3.9c&f, 3.10c&f) the scalar is close to the center of the ramp-cliff structure where mixture fraction diffusion is small, the streamlines move largely in the direction of temperature and species mass fractions, indicating diffusion among burning and extinguished flamelets. In flame D, the mixing along iso-mixture fraction surface didn't

occur at $x/D = 7.5$.

3.4 Discussion and conclusions

The joint mass density function of mixture fraction, temperature and a species mass fraction, the conditional species mass fraction dissipation rate and the conditional diffusion which evolve the JMDF are studied using the data obtained in turbulent partially premixed flames (Sandia flame D and E). We are interested about the mixing process at the position where the mean mixture fraction is close to the stoichiometric value. At these positions, the mixing processes are strongly influenced by the interaction between turbulence and chemistry thus the main challenge to model in the context of PDF method.

At x/D=7.5 for flame D, the JMDF for all the species are not far from equilibrium values. The peak Y_{CH_4} dissipation rate is near $\xi = 0.5$, $T = 1600 - 1800K$ where the center of ramp-cliff structure is located. The peak Y_{O_2} and Y_{CO} dissipation rate is on the lean side while Y_{CO_2} dissipation rate has two peak values on both lean and rich branch. The diffusion streamlines for Y_{CH_4}, Y_{CO_2}, Y_{O_2} are confined in the two-dimensional region due to the strong correlation between Y_{CH_4}, Y_{CO_2}, Y_{O_2} with the temperature and mixture fraction while the diffusion streamlines for Y_{CO} are in the three-dimensional manifold. For those streamlines start from very rich and lean mixtures generally moves in the ridgeline of the JMDF then turn and move towards a stagnation point which does not correspond to the conditional mean. Those streamlines start from the highest temperature move to the lower temperature regions towards the stagnation point with modest change of mixture fraction.

The mixing configuration of mixing fraction, temperature and a species mass fraction has a strong influence on the mixing of the species mass fraction. Due to its strong correlation with the temperature and mixture fraction, the mixing of ξ, T and Y_{CO_2} (Y_{CH_4}, Y_{O_2}, Y_{H_2O}) can largely represented by a two-dimensional manifold, and therefore is degenerated. On the other hand, the rapid depletion of Y_{CO} (Y_{H_2}) on the lean side results in more complex mixing configuration, and the mixing of ξ, T and Y_{CO} must be represented by a three-dimensional manifold and is non-degenerated.

For $x/D = 7.5$ in flame E, $x/D = 15$ and 30 in flame D and E, significant extinction occur at these location such that the JMDF and mixing terms extends to the low temperature regions. In these regions, the diffusion streamline generally move in the ξ direction towards a intermediate value then move largely in the direction of temperature and species mass fraction. This trend is the evidence suggesting flamelet-flamelet interactions, resulting diffusion along the stoichiometric mixture fraction surface.

For the radial positions where $\langle\xi\rangle$ is much less than ξ_s, the JMDF is largely concentrated in the lean side and the mixing terms is similar to the corresponding lean part for the case where $\langle\xi\rangle \approx \xi_s$. For the position where $\langle\xi\rangle$ is much greater than ξ_s, the manifold of the JMDF is nearly like a straight line in the rich side. The conditional dissipation rate increases with the decrease of temperature and mixture fraction. The diffusion streamlines generally move quickly to the manifold then along it at lower velocities. These mixing patterns are similar to that of non-reactive scalars. Mixing models based on non-reactive scalar can potentially used in these regions.

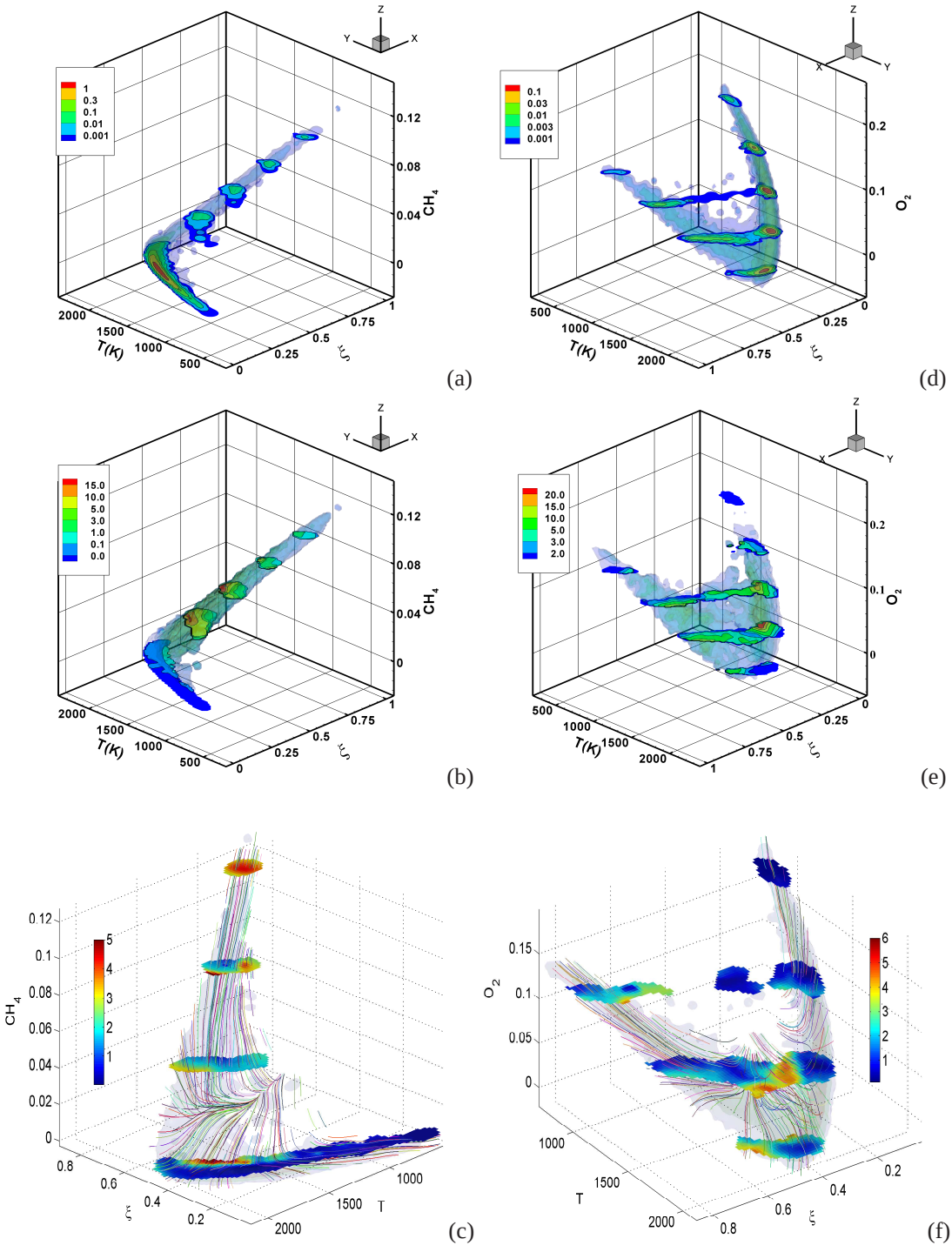

Figure 3.2: (a) JMDF (b) conditional Y_{CH_4} dissipation (c) diffusion velocity streamlines for ξ, T and Y_{CH_4}; (d) JMDF (e) conditional Y_{O_2} dissipation (f) diffusion velocity streamlines for ξ, T and Y_{O_2} at $x/D = 7.5,\ r/D = 1.04$ in flame D.

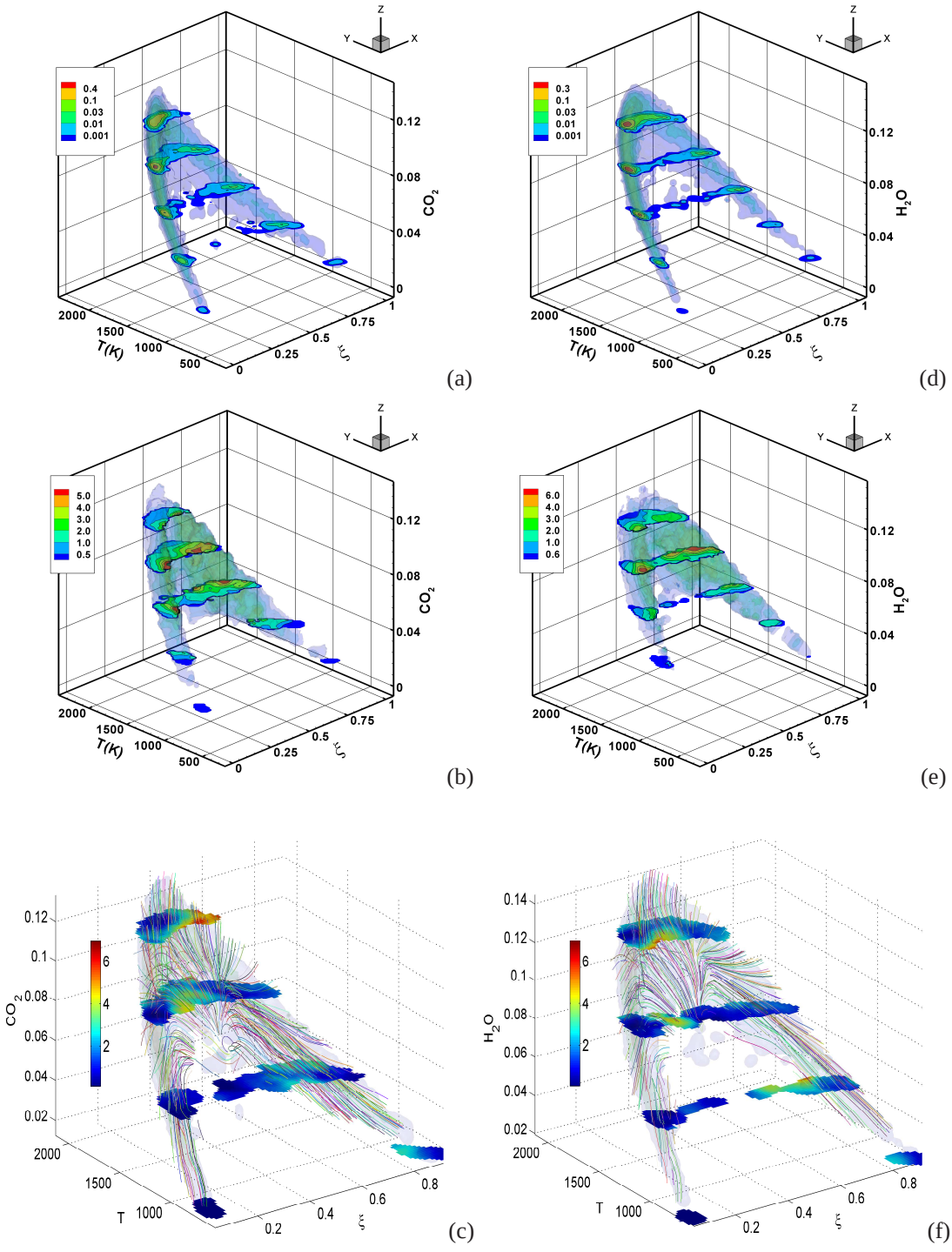

Figure 3.3: (a) JMDF (b) conditional Y_{CO_2} dissipation (c) diffusion velocity streamlines for ξ, T and Y_{CO_2}; (d) JMDF (e) conditional Y_{H_2O} dissipation (f) diffusion velocity streamlines for ξ, T and Y_{H_2O} at $x/D = 7.5$, $r/D = 1.04$ in flame D.

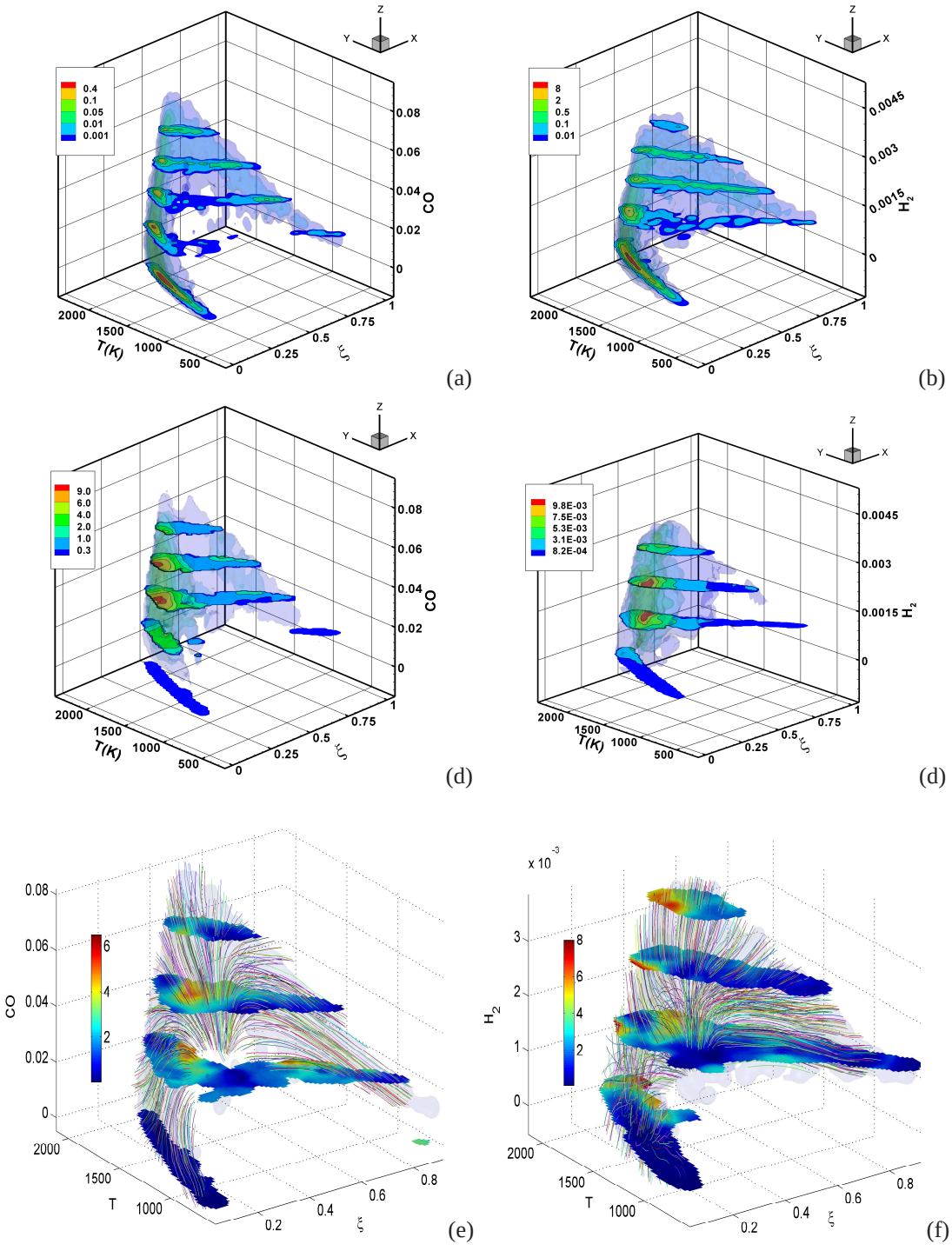

Figure 3.4: (a) JMDF (b) conditional Y_{CO} dissipation (c) diffusion velocity streamlines for ξ, T and Y_{CO}; (d) JMDF (e) conditional Y_{H_2} dissipation (f) diffusion velocity streamlines for ξ, T and Y_{H_2} at $x/D = 7.5$, $r/D = 1.04$ in flame D.

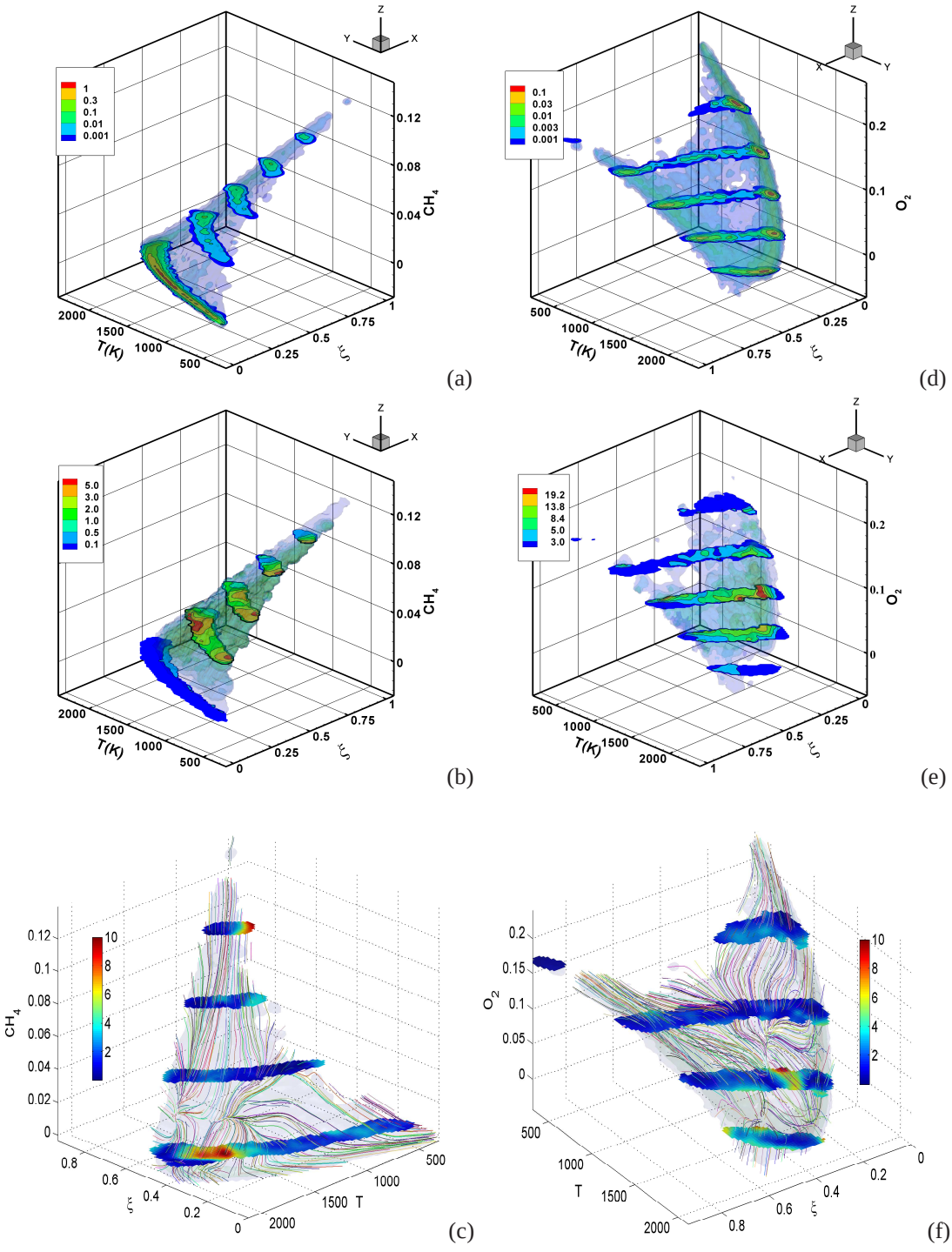

Figure 3.5: (a) JMDF (b) conditional Y_{CH_4} dissipation (c) diffusion velocity streamlines for ξ, T and Y_{CH_4}; (d) JMDF (e) conditional Y_{O_2} dissipation (f) diffusion velocity streamlines for ξ, T and Y_{O_2} at $x/D = 15,\ r/D = 1.34$ in flame D.

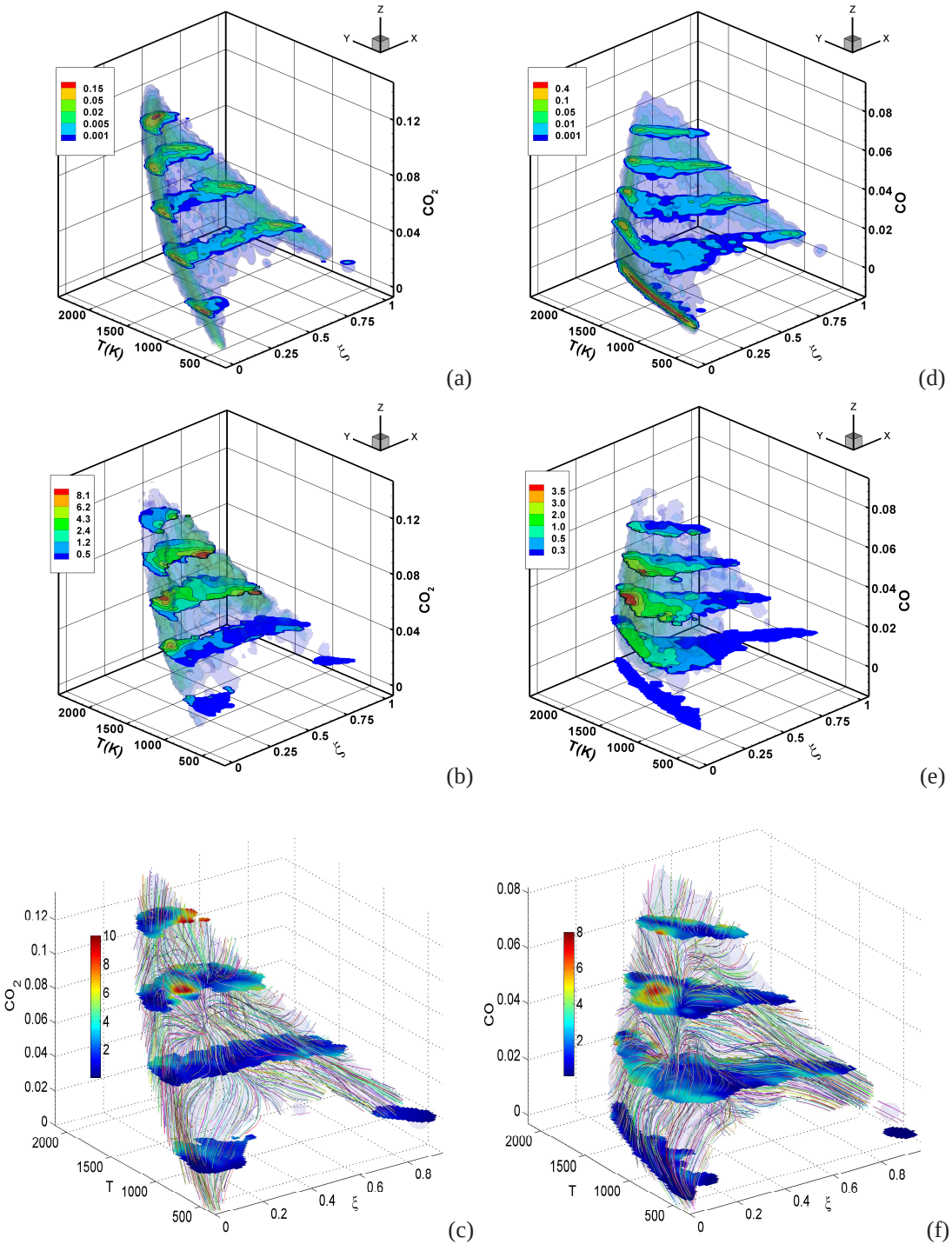

Figure 3.6: (a) JMDF (b) conditional Y_{CO_2} dissipation (c) diffusion velocity streamlines for ξ, T and Y_{CO_2}; (d) JMDF (e) conditional Y_{CO} dissipation (f) diffusion velocity streamlines for ξ, T and Y_{CO} at $x/D = 15,\ r/D = 1.34$ in flame D.

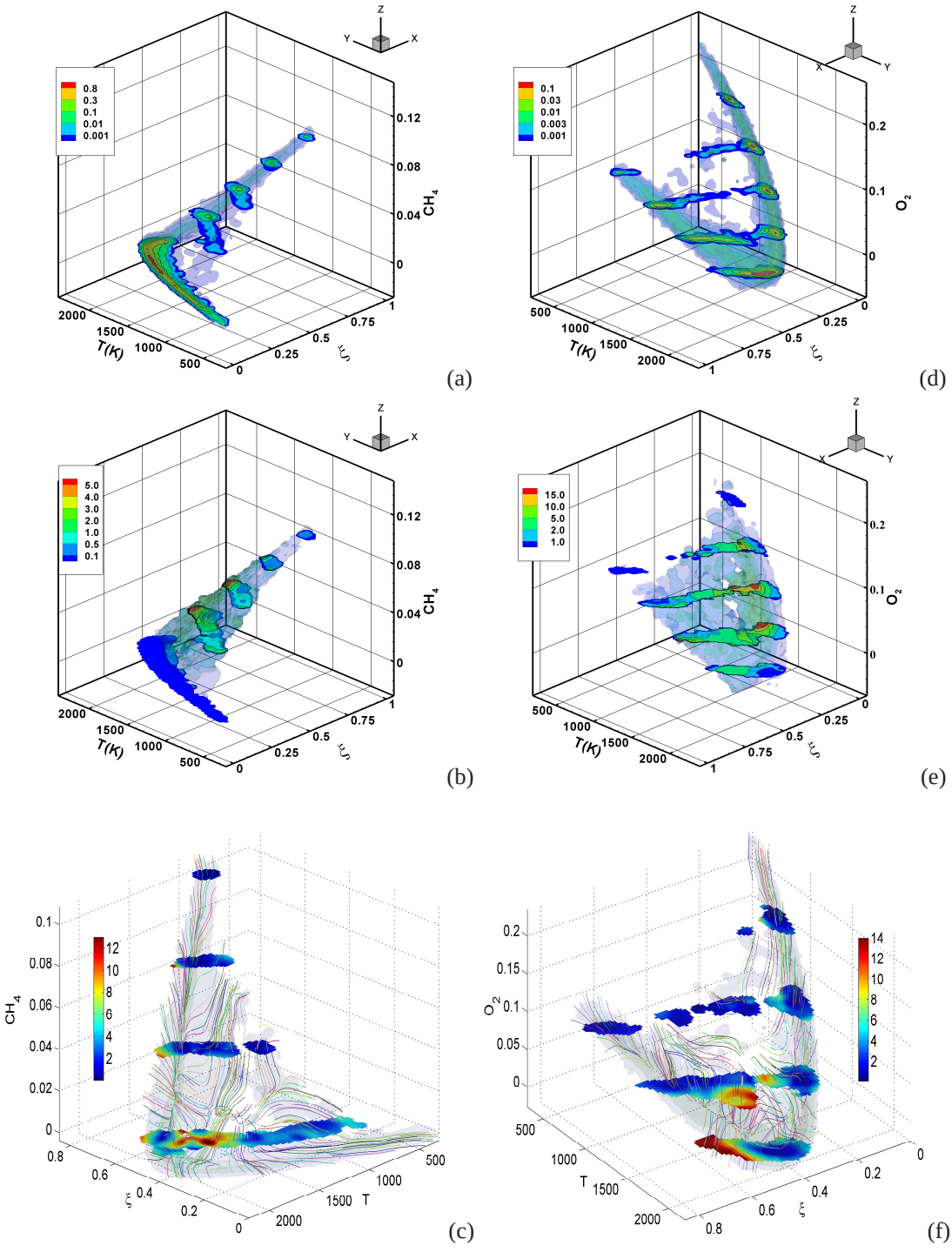

Figure 3.7: (a) JMDF (b) conditional Y_{CH_4} dissipation (c) diffusion velocity streamlines for ξ, T and Y_{CH_4}; (d) JMDF (e) conditional Y_{O_2} dissipation (f) diffusion velocity streamlines for ξ, T and Y_{O_2} at $x/D = 30,\ r/D = 1.78$ in flame D.

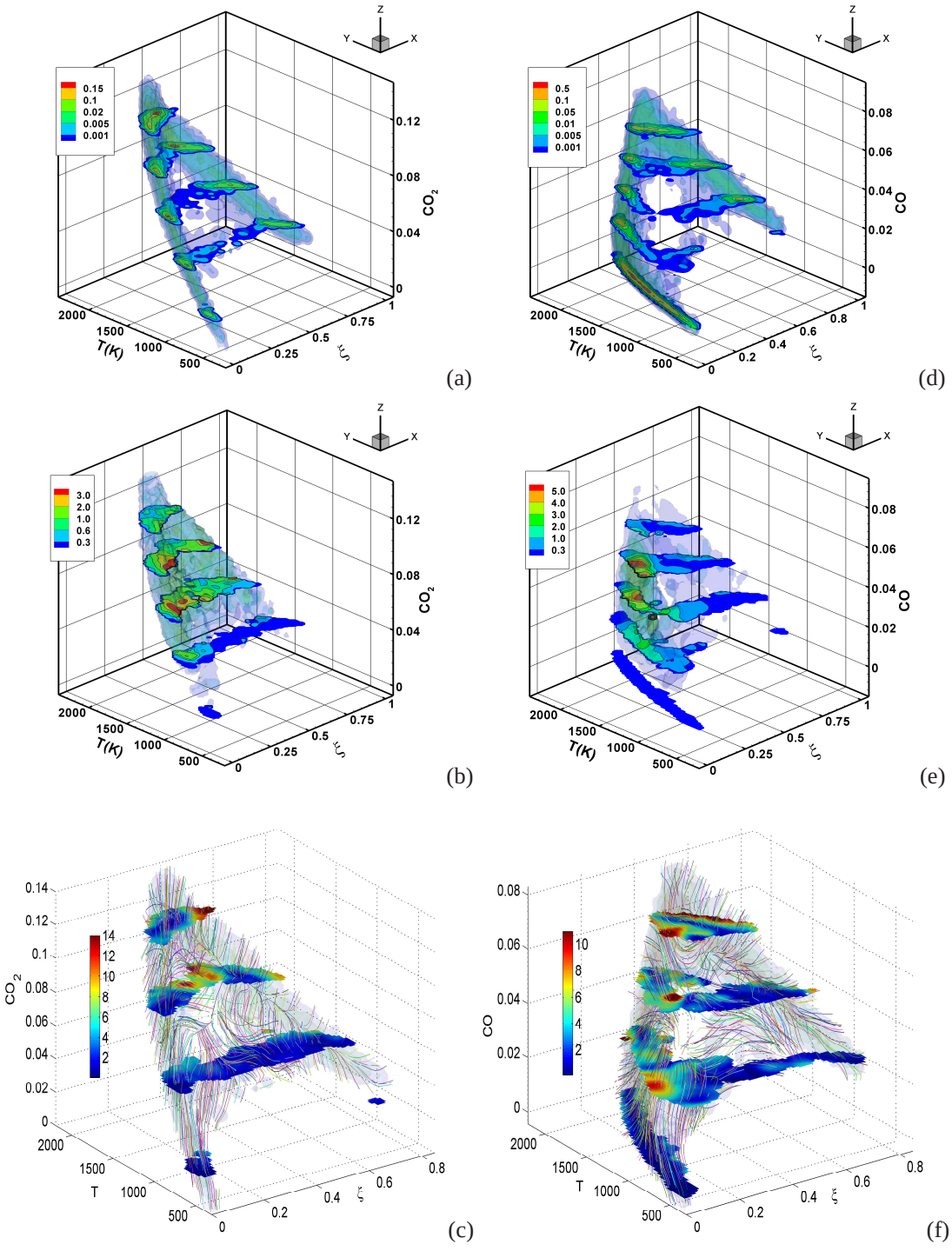

Figure 3.8: (a) JMDF (b) conditional Y_{CO_2} dissipation (c) diffusion velocity streamlines for ξ, T and Y_{CO_2}; (d) JMDF (e) conditional Y_{CO} dissipation (f) diffusion velocity streamlines for ξ, T and Y_{CO} at $x/D = 30,\ r/D = 1.78$ in flame D.

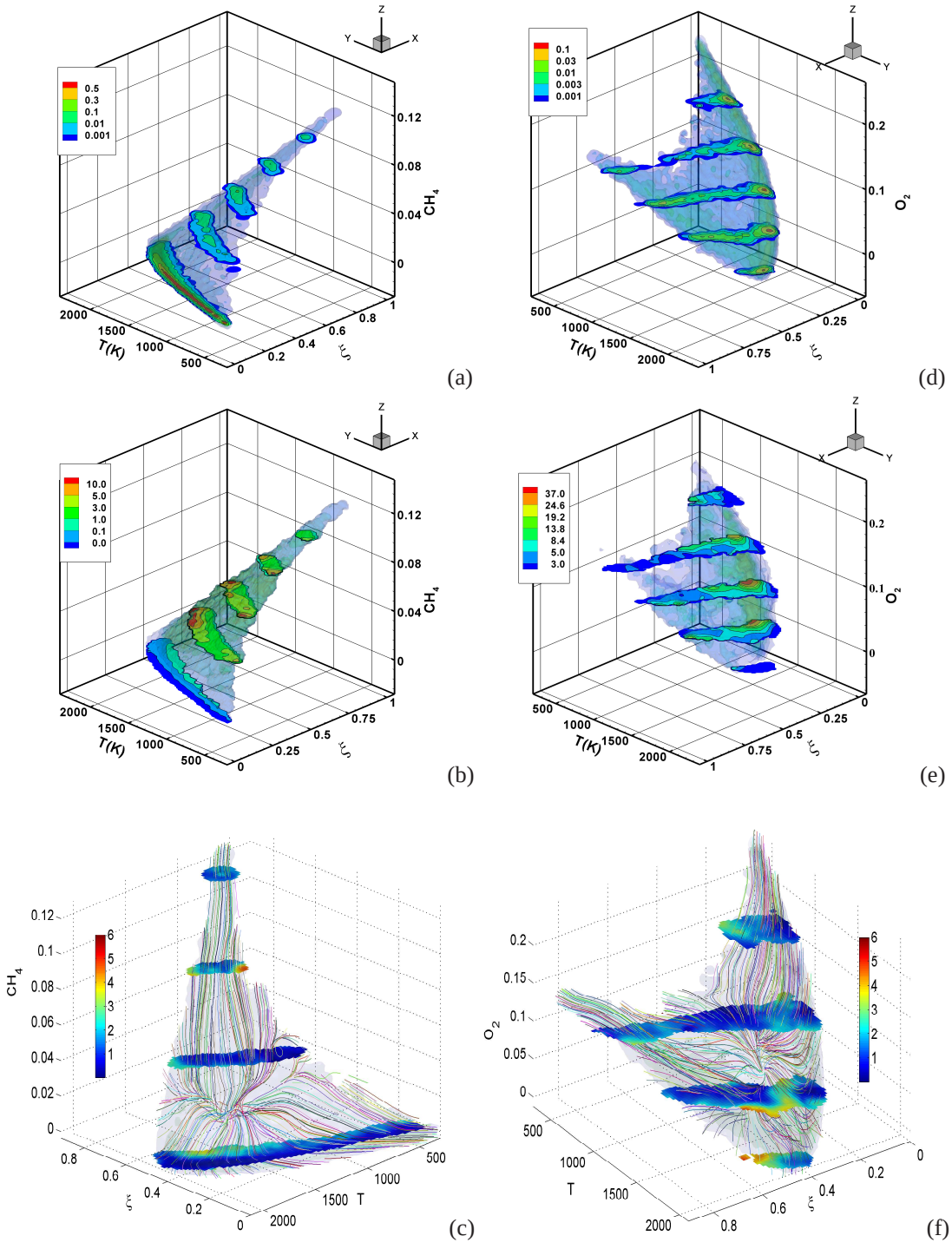

Figure 3.9: (a) JMDF (b) conditional Y_{CH_4} dissipation (c) diffusion velocity streamlines for ξ, T and Y_{CH_4}; (d) JMDF (e) conditional Y_{O_2} dissipation (f) diffusion velocity streamlines for ξ, T and Y_{O_2} at $x/D = 7.5,\ r/D = 1.04$ in flame E.

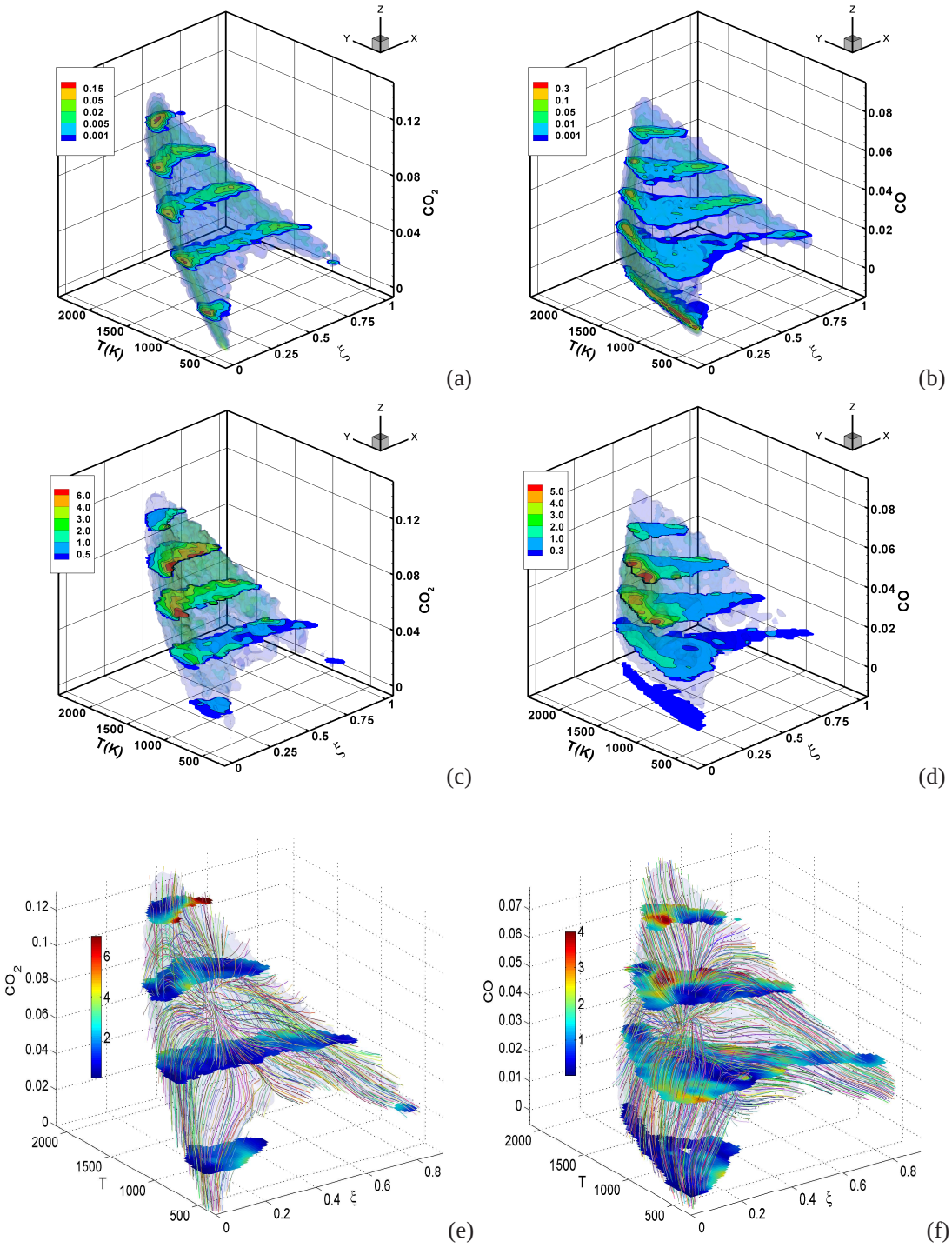

Figure 3.10: (a) JMDF (b) conditional Y_{CO_2} dissipation (c) diffusion velocity streamlines for ξ, T and Y_{CO_2}; (d) JMDF (e) conditional Y_{O_2} dissipation (f) diffusion velocity streamlines for ξ, T and Y_{O_2} at $x/D = 7.5,\ r/D = 1.04$ in flame E.

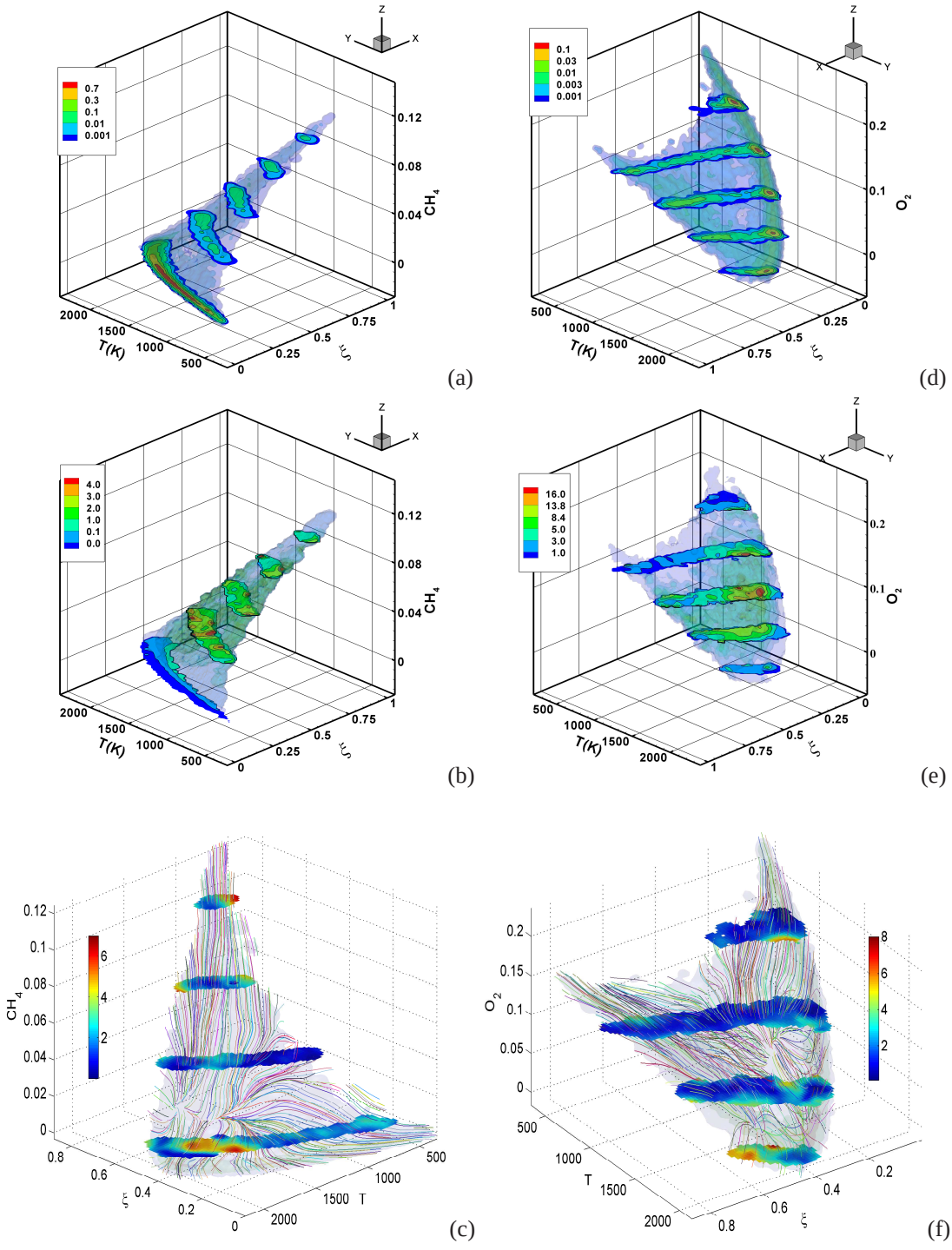

Figure 3.11: (a) JMDF (b) conditional Y_{CH_4} dissipation (c) diffusion velocity streamlines for ξ, T and Y_{CH_4}; (d) JMDF (e) conditional Y_{O_2} dissipation (f) diffusion velocity streamlines for ξ, T and Y_{O_2} at $x/D = 15,\ r/D = 1.34$ in flame E.

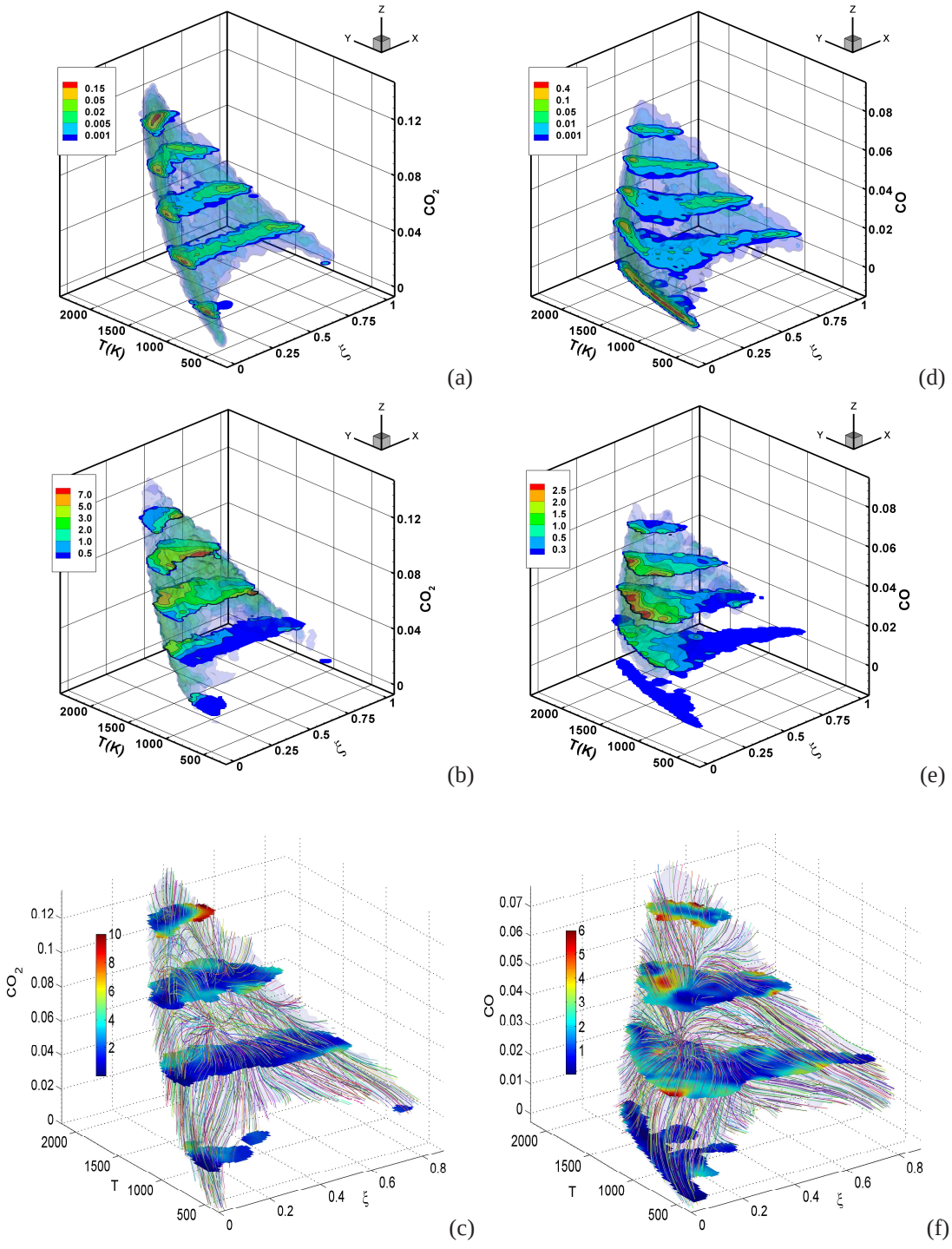

Figure 3.12: (a) JMDF (b) conditional Y_{CO_2} dissipation (c) diffusion velocity streamlines for ξ, T and Y_{CO_2}; (d) JMDF (e) conditional Y_{CO} dissipation (f) diffusion velocity streamlines for ξ, T and Y_{CO} at $x/D = 15,\ r/D = 1.34$ in flame E.

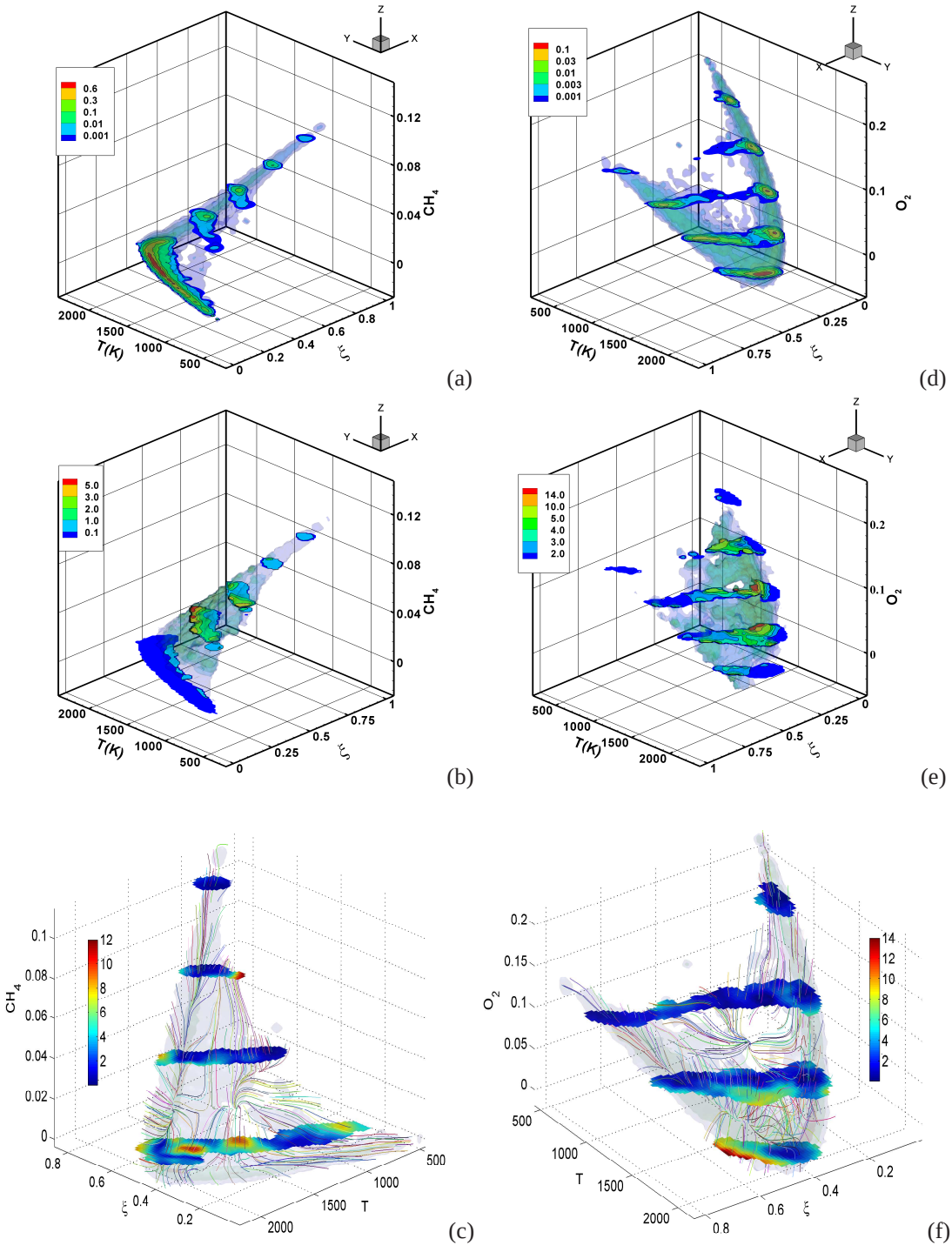

Figure 3.13: (a) JMDF (b) conditional Y_{CH_4} dissipation (c) diffusion velocity streamlines for ξ, T and Y_{CH_4}; (d) JMDF (e) conditional Y_{O_2} dissipation (f) diffusion velocity streamlines for ξ, T and Y_{O_2} at $x/D = 30,\ r/D = 1.78$ in flame E.

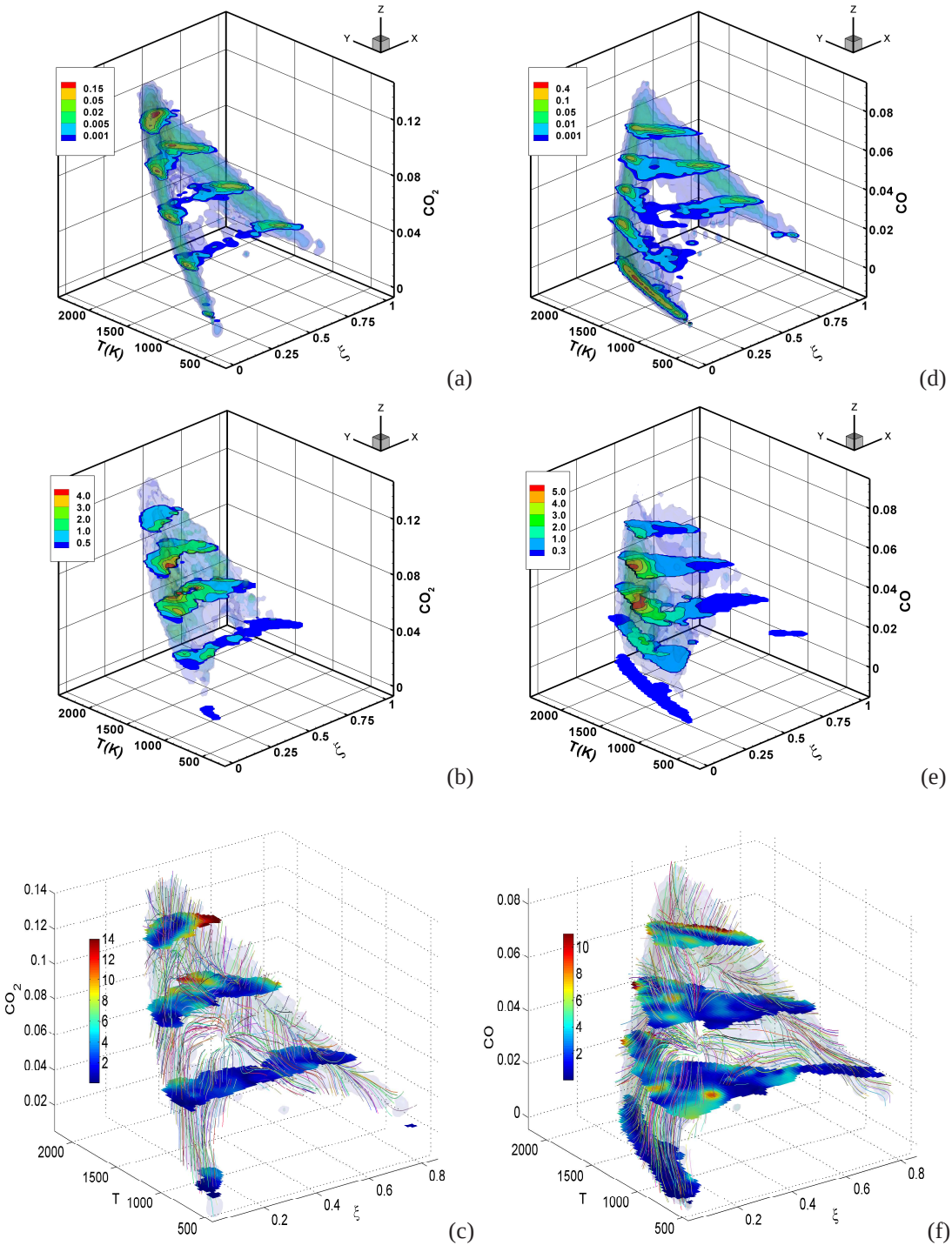

Figure 3.14: (a) JMDF (b) conditional Y_{CO_2} dissipation (c) diffusion velocity streamlines for ξ, T and Y_{CO_2}; (d) JMDF (e) conditional Y_{CO} dissipation (f) diffusion velocity streamlines for ξ, T and Y_{CO} at $x/D = 30,\ r/D = 1.78$ in flame E.

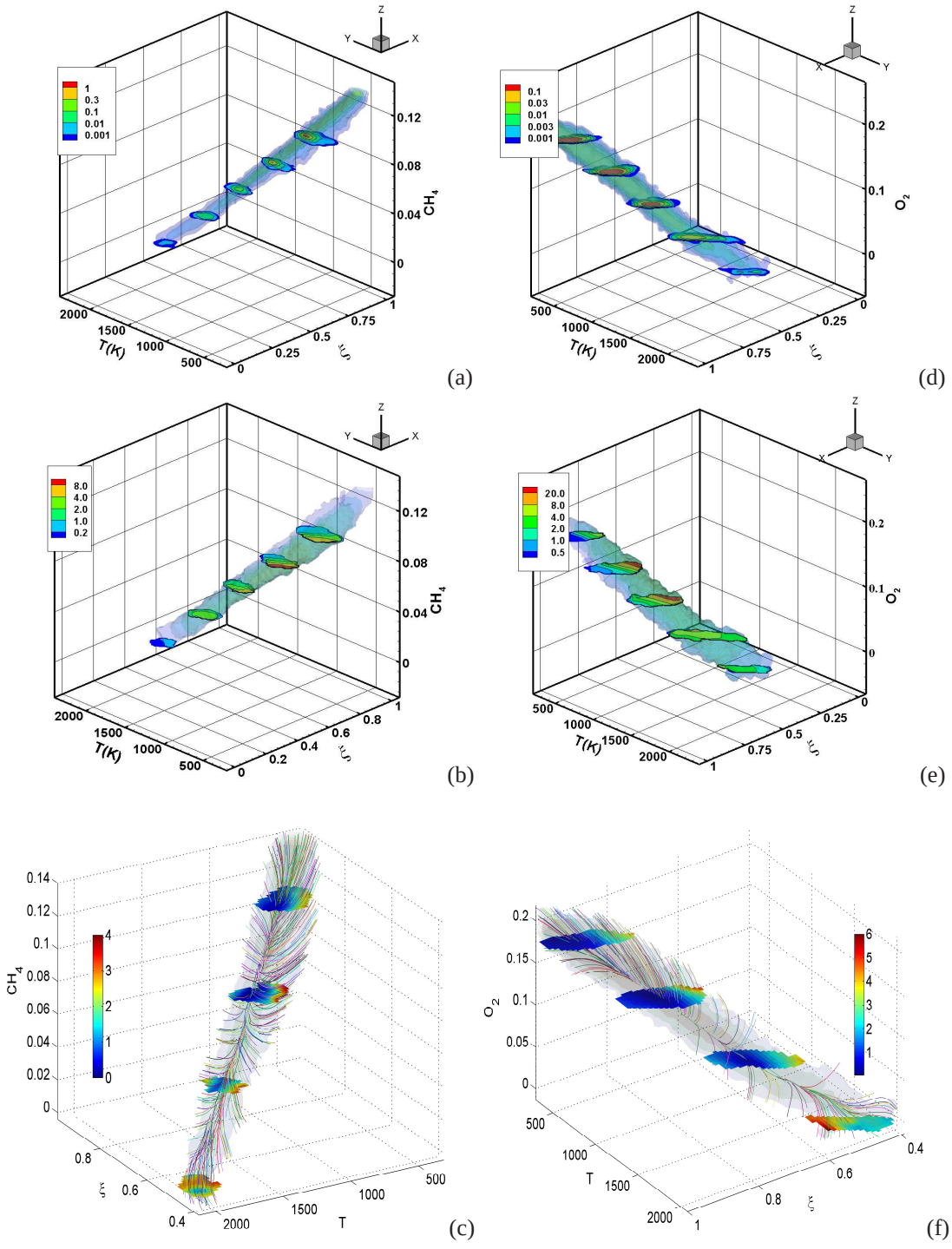

Figure 3.15: (a) JMDF (b) conditional Y_{CH_4} dissipation (c) diffusion velocity streamlines for ξ, T and Y_{CH_4}; (d) JMDF (e) conditional Y_{O_2} dissipation (f) diffusion velocity streamlines for ξ, T and Y_{O_2} at $x/D = 7.5,\ r/D = 0.6130$ in flame D.

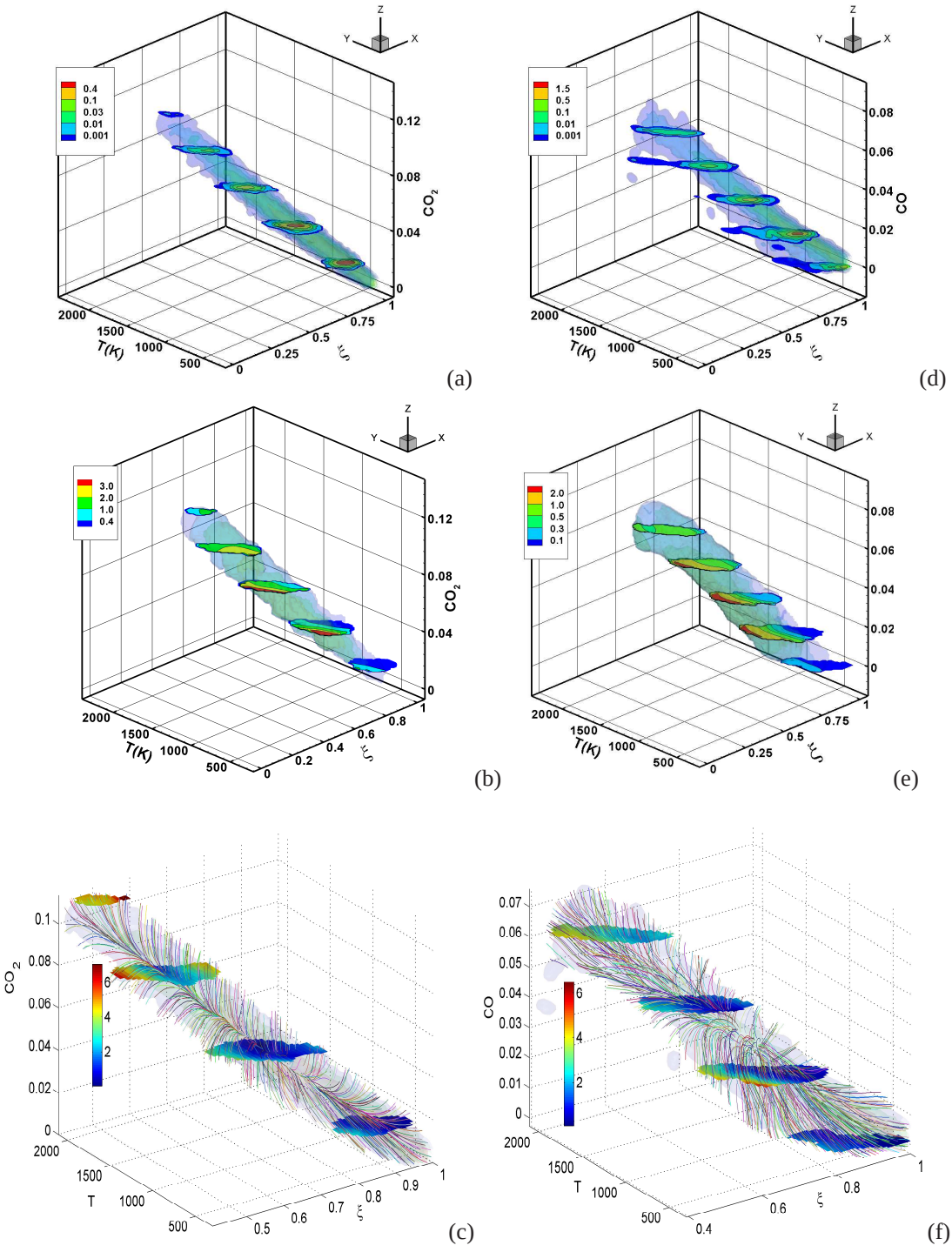

Figure 3.16: (a) JMDF (b) conditional Y_{CO_2} dissipation (c) diffusion velocity streamlines for ξ, T and Y_{CO_2}; (d) JMDF (e) conditional Y_{CO} dissipation (f) diffusion velocity streamlines for ξ, T and Y_{CO} at $x/D = 7.5,\ r/D = 0.6130$ in flame D.

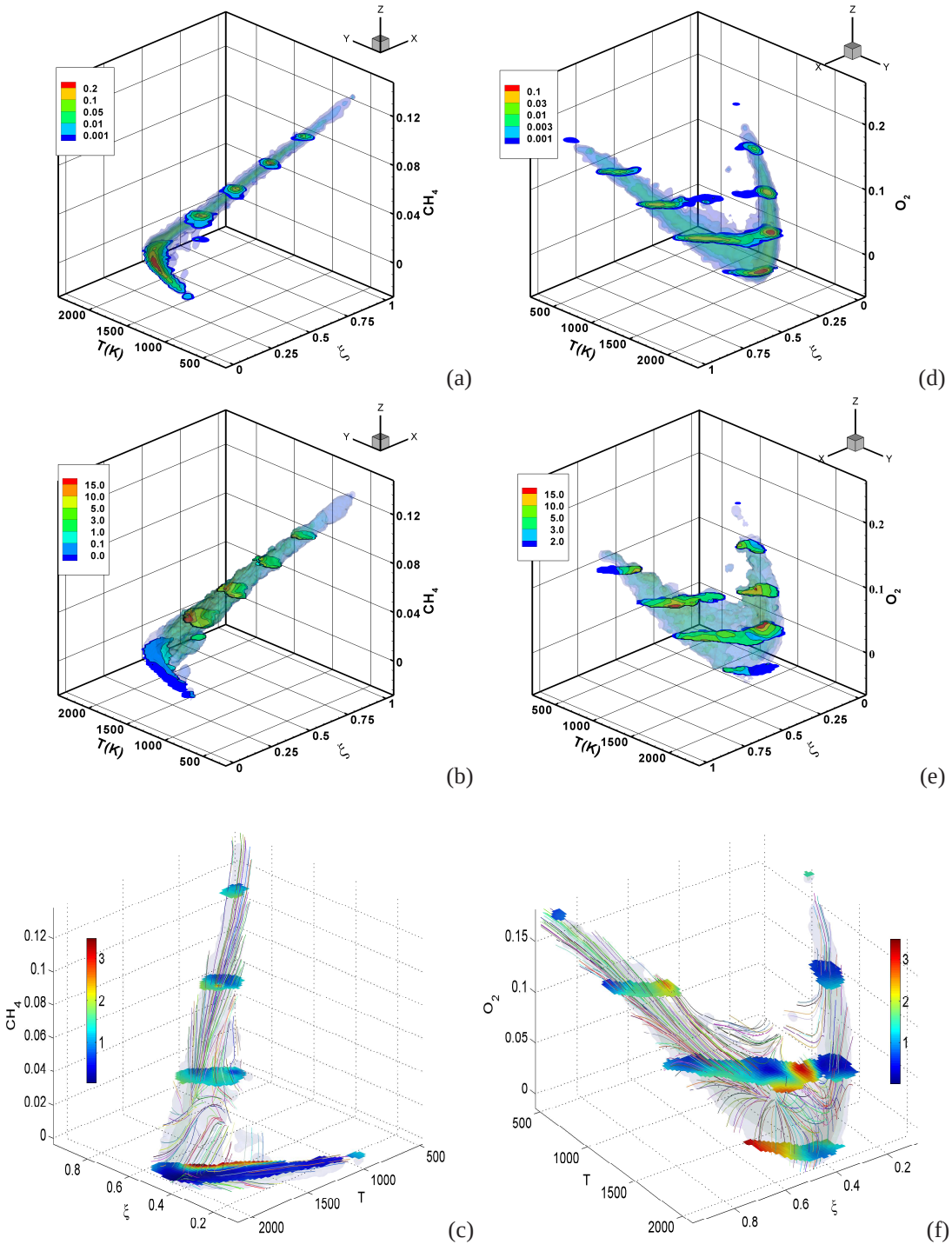

Figure 3.17: (a) JMDF (b) conditional Y_{CH_4} dissipation (c) diffusion velocity streamlines for ξ, T and Y_{CH_4}; (d) JMDF (e) conditional Y_{O_2} dissipation (f) diffusion velocity streamlines for ξ, T and Y_{O_2} at $x/D = 7.5,\ r/D = 0.9537$ in flame D.

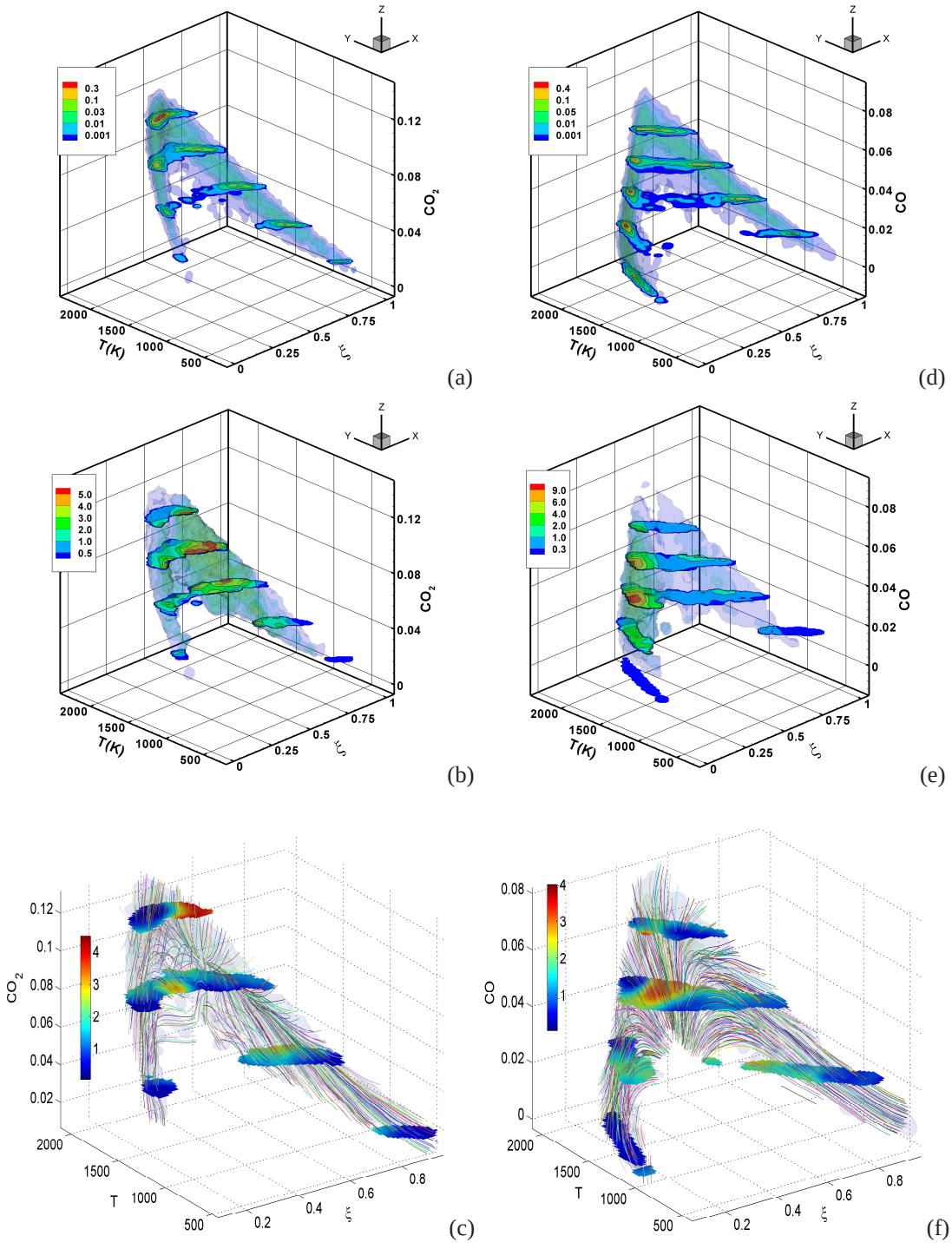

Figure 3.18: (a) JMDF (b) conditional Y_{CO_2} dissipation (c) diffusion velocity streamlines for ξ, T and Y_{CO_2}; (d) JMDF (e) conditional Y_{CO} dissipation (f) diffusion velocity streamlines for ξ, T and Y_{CO} at $x/D = 7.5$, $r/D = 0.9537$ in flame D.

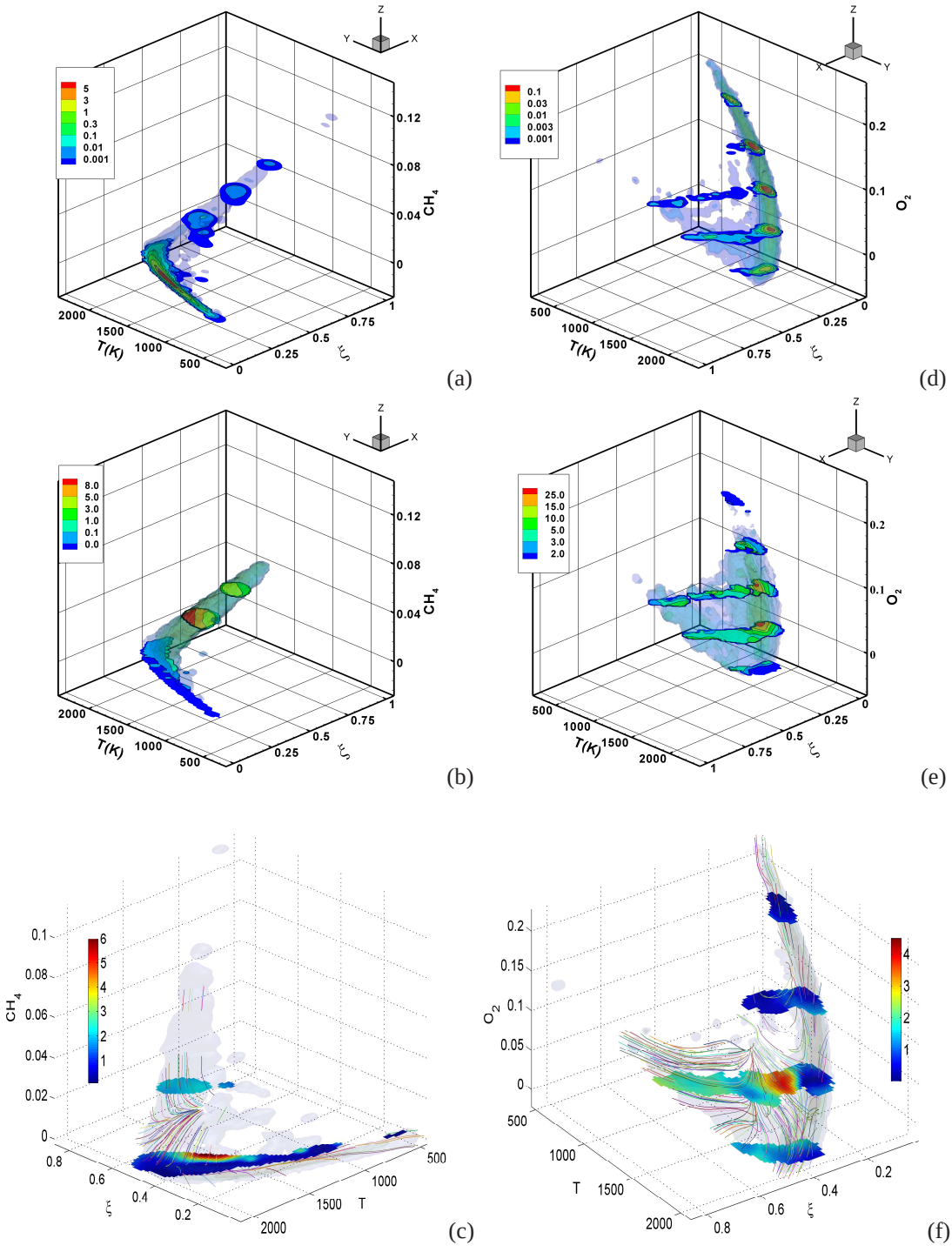

Figure 3.19: (a) JMDF (b) conditional Y_{CH_4} dissipation (c) diffusion velocity streamlines for ξ, T and Y_{CH_4}; (d) JMDF (e) conditional Y_{O_2} dissipation (f) diffusion velocity streamlines for ξ, T and Y_{O_2} at $x/D = 7.5,\ r/D = 1.1240$ in flame D.

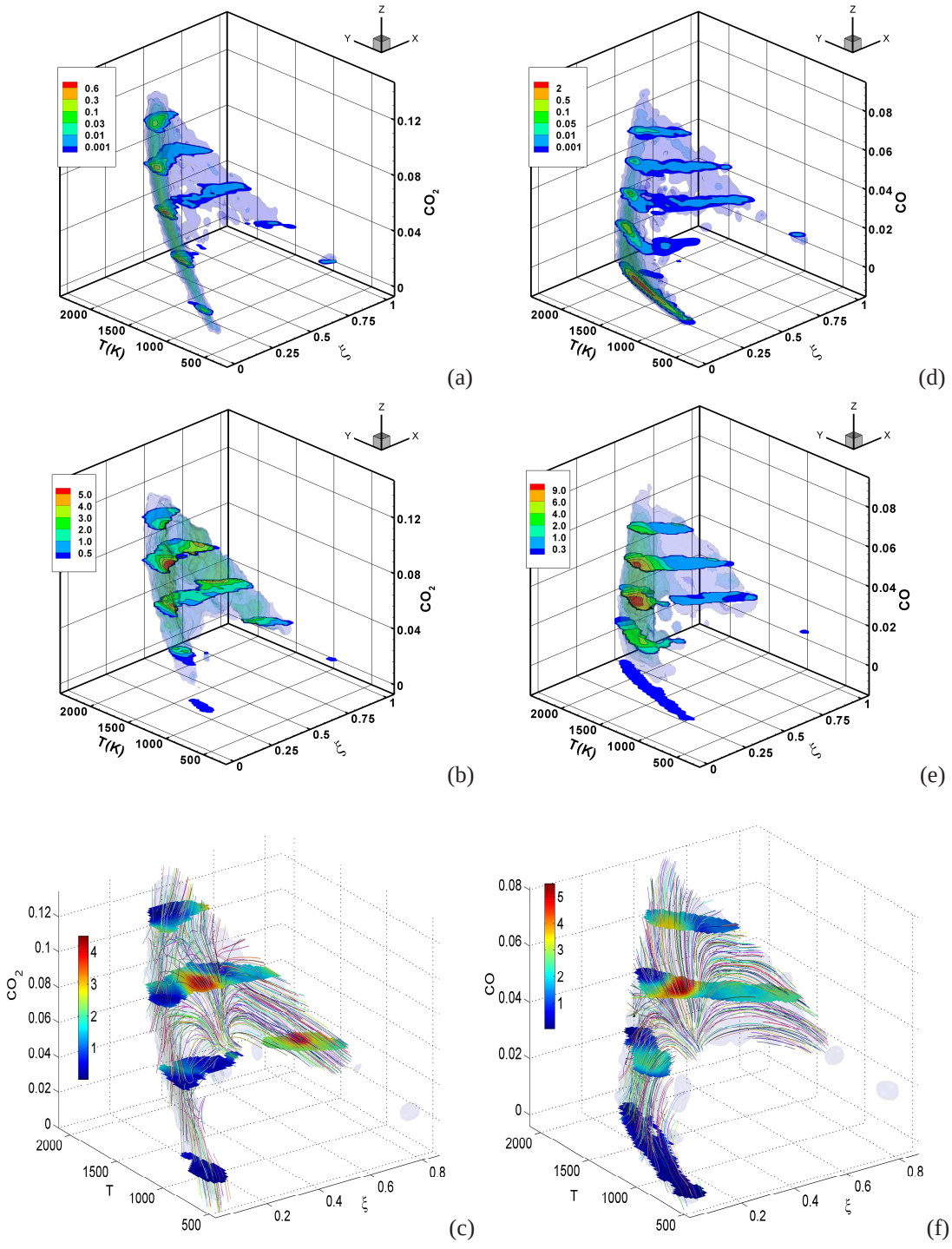

Figure 3.20: (a) JMDF (b) conditional Y_{CO_2} dissipation (c) diffusion velocity streamlines for ξ, T and Y_{CO_2}; (d) JMDF (e) conditional Y_{CO} dissipation (f) diffusion velocity streamlines for ξ, T and Y_{CO} at $x/D = 7.5,\ r/D = 1.1240$ in flame D.

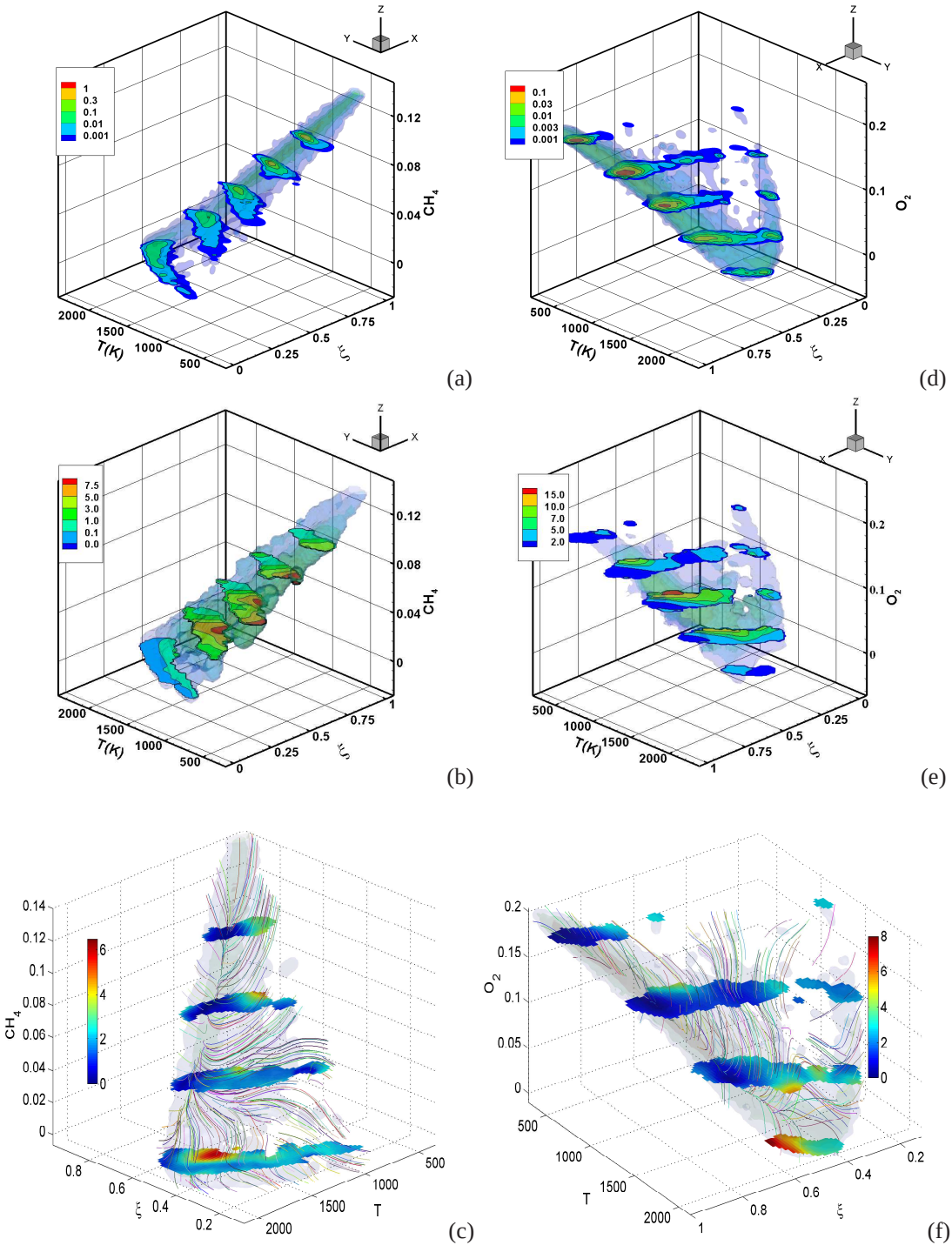

Figure 3.21: (a) JMDF (b) conditional Y_{CH_4} dissipation (c) diffusion velocity streamlines for ξ, T and Y_{CH_4}; (d) JMDF (e) conditional Y_{O_2} dissipation (f) diffusion velocity streamlines for ξ, T and Y_{O_2} at $x/D = 15,\ r/D = 0.8825$ in flame D.

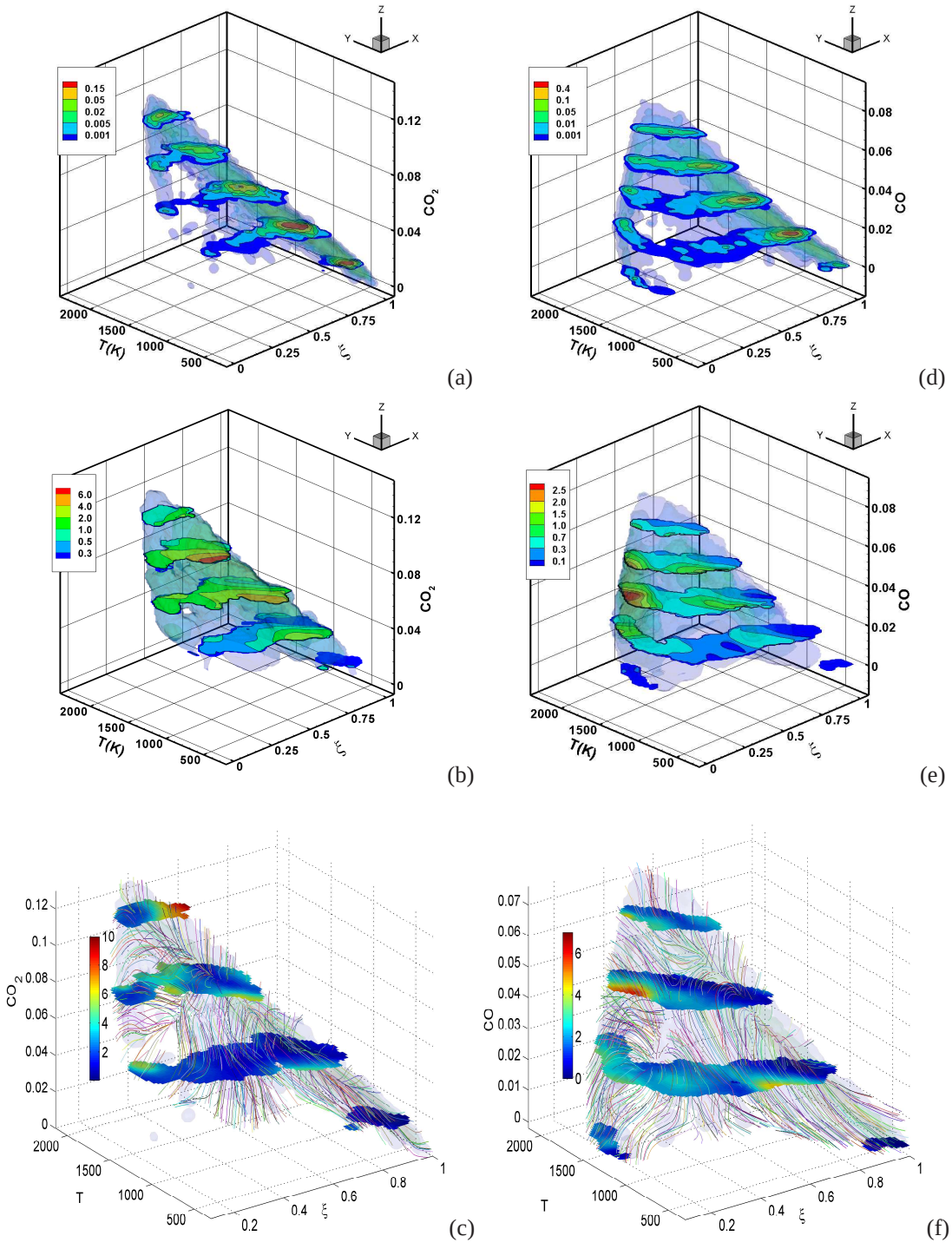

Figure 3.22: (a) JMDF (b) conditional Y_{CO_2} dissipation (c) diffusion velocity streamlines for ξ, T and Y_{CO_2}; (d) JMDF (e) conditional Y_{CO} dissipation (f) diffusion velocity streamlines for ξ, T and Y_{CO} at $x/D = 15,\ r/D = 0.8825$ in flame D.

Chapter 4

Subgrid-scale mixing of reactive scalar perturbations from flamelets in turbulent partially premixed flames

4.1 Introduction

Turbulent flames contain a wide range of length scales as well as structures, which presents a great modeling challenge. Two important and distinct categories of turbulent combustion models are probability density function (PDF) like and flamelet-like [5]. Models in each category are advantageous in predicting different flame structures. Flamelet models are more accurate for predicting flamelet combustion while PDF models in principle can model all flame structures. Current mixing models used in PDF models, however, generally are based on turbulence-controlled mixing, and therefore may be more accurate for non-reactive scalars and distributed reaction zones, and are expected to be less accurate for flamelets, because mixing (diffusion) of reactive scalars in them is enhanced by reaction.

Several approaches have been proposed to improve predictions of flamelet combustion by PDF models. Haworth et at. [66] proposed an approach for partially premixed combustion employing the PDF method for a reduced set of variables (e.g. mixture fraction) combined with a flamelet library. Pope [67] proposed a hybrid approach to explicitly include the flamelet structure into the PDF formalism, combining the chemical source term and the mixing term. The combined term is a unique function of the reaction progress variable

in a premixed laminar flamelet. In this approach the tight coupling between mixing and reaction in flamelets is accounted for using a flamelet library and no longer needs modeling.

Turbulent flames, especially at high Reynolds numbers, however, can contain a range of structures, including flamelets and distributed reaction zones. Even when flamelets are the dominant flame structure, there can be significant deviations from them, which mixing models need to account for. In the present study we investigate reactive scalar mixing in turbulent partially premixed flames to understand the extent of coupling between mixing and reaction when perturbations from flamelets exist, and how mixing may be modeled more accurately. We study perturbations from flamelets burning in non-premixed mode. While under certain conditions premixed-mode burning can occur in partially premixed flames, the fuel stream composition of the Sandia flames supports only flamelets in non-premixed mode.

Since the diffusion in flamelets is strongly coupled to reaction, the degree of coupling of the perturbation diffusion to the reaction term is of interest. We decompose a reactive scalar, say temperature T, into a steady flamelet part, $T^f(Z,\chi_s^f)$, and perturbations from it, T^*, where Z, χ_s^f, and T^f are mixture fraction, the stoichiometric mixture fraction dissipation rate, and a steady flamelet solution, respectively. Following Bilger [68] and Peters [2] the transport equation of T can be written as

$$\begin{aligned}\rho\frac{\partial T^*}{\partial t}+\rho\frac{\partial T^f}{\partial Z}\frac{\partial Z}{\partial t}+\rho u_k\frac{\partial T^*}{\partial x_k}+\rho u_k\frac{\partial Z}{\partial x_k}\frac{\partial T^f}{\partial Z} &= \frac{\partial}{\partial x_k}(\rho D\frac{\partial T^*}{\partial x_k})+\frac{\partial}{\partial x_k}(\rho D\frac{\partial T^f}{\partial x_k})+w_T \qquad (4.1)\\ &= \frac{\partial}{\partial x_k}(\rho D\frac{\partial T^*}{\partial x_k})+\frac{\partial}{\partial x_k}(\rho D\frac{\partial Z}{\partial x_k})\frac{\partial T^f}{\partial Z}+\rho\frac{\chi}{2}\frac{\partial^2 T^f}{\partial Z^2}+w_T,\end{aligned}$$

where D, u_k, and w_T are diffusivity, velocity component, and chemical source, respectively. The third term on the second line of Eq. (4.1) represents the diffusion of T induced by reaction, reflecting the coupling between mixing and reaction. For a suitably defined diffusivity, the terms containing $\frac{\partial T^f}{\partial Z}$ sum to zero, resulting in the transport equation for T^*

$$\rho\frac{\partial T^*}{\partial t}+\rho u_k\frac{\partial T^*}{\partial x_k}=\frac{\partial}{\partial x_k}(\rho D\frac{\partial T^*}{\partial x_k})+\rho\frac{\chi}{2}\frac{\partial^2 T^f}{\partial Z^2}+w_T. \qquad (4.2)$$

The second term on the RHS can also be interpreted as the production (or generation) of T^* due to mixing. When the perturbations are not very large (e.g., with T above local extinction values), this term may be largely balanced by w_T. Thus, the diffusion of T^* depends on the details of the balance. It is likely that some perturbations may not have the structure of the flamelets; therefore their diffusion may not be influenced as strongly by the chemistry. If it is possible to model the diffusion of T^* using mixing models based on

non-reactive scalars, an indirect model for the diffusion of T can be obtained from the first three terms on the RHS of Eq. (4.1) .

In the context of the PDF methods, the mixing process that evolves the mass density function (MDF), F_{ZT}, of Z and T, can be studied using the unclosed mixing terms in the MDF transport equation [47], the conditional mixture fraction diffusion and temperature diffusion, $\left\langle \frac{1}{\rho}\frac{\partial}{\partial x_i}\left(\rho D\frac{\partial Z}{\partial x_i}\right)\middle|\hat{Z},\hat{T}\right\rangle$, $\left\langle \frac{1}{\rho}\frac{\partial}{\partial x_i}\left(\rho D\frac{\partial T}{\partial x_i}\right)\middle|\hat{Z},\hat{T}\right\rangle$, or alternatively, the conditional mixture fraction dissipation, temperature dissipation, and the cross dissipation, $\langle\chi|\hat{Z},\hat{T}\rangle \equiv \left\langle 2D\frac{\partial Z}{\partial x_i}\frac{\partial Z}{\partial x_i}\middle|\hat{Z},\hat{T}\right\rangle$, $\langle\chi_T|\hat{Z},\hat{T}\rangle \equiv \left\langle 2D\frac{\partial T}{\partial x_i}\frac{\partial T}{\partial x_i}\middle|\hat{Z},\hat{T}\right\rangle$, $\langle\chi_{ZT}|\hat{Z},\hat{T}\rangle \equiv \left\langle 2D\frac{\partial Z}{\partial x_i}\frac{\partial T}{\partial x_i}\middle|\hat{Z},\hat{T}\right\rangle$, respectively, where $\hat{Z}$ and $\hat{T}$ are the sample space variables for Z and T, respectively. The angle brackets denote ensemble averages. For convenience, the sample space variable for Z and T are omitted hereafter. To investigate the extent of the coupling between mixing and reaction, the conditional diffusion of the reactive scalar can be decomposed into two terms:

$$\left\langle \frac{1}{\rho}\frac{\partial}{\partial x_i}\left(\rho D\frac{\partial T}{\partial x_i}\right)\middle|Z,T\right\rangle = \left\langle \frac{1}{\rho}\frac{\partial}{\partial x_i}\left(\rho D\frac{\partial T^f}{\partial x_i}\right)\middle|Z,T\right\rangle + \left\langle \frac{1}{\rho}\frac{\partial}{\partial x_i}\left(\rho D\frac{\partial T^*}{\partial x_i}\right)\middle|Z,T\right\rangle. \tag{4.3}$$

The conditional dissipation rate can be decomposed into three terms:

$$\chi_T \equiv \left\langle 2D\frac{\partial T}{\partial x_i}\frac{\partial T}{\partial x_i}\middle|Z,T\right\rangle = \left\langle 2D\frac{\partial T^f}{\partial x_i}\frac{\partial T^f}{\partial x_i}\middle|Z,T\right\rangle + \left\langle 2D\frac{\partial T^*}{\partial x_i}\frac{\partial T^*}{\partial x_i}\middle|Z,T\right\rangle + \left\langle 4D\frac{\partial T^f}{\partial x_i}\frac{\partial T^*}{\partial x_i}\middle|Z,T\right\rangle. \tag{4.4}$$

With flamelet solutions, the first terms on the RHS of Eqs. (4.3) and (4.4) contain the scalar (mixture fraction) dissipation rate (see Eqs. 4.6 and 4.8 below) and do not require modeling of reaction scalar mixing. The dissipation and diffusion of the temperature perturbations still require modeling.

To analyze the diffusion of reactive scalar perturbations from steady flamelet solutions using experimental data, we apply the conditional sampling method we developed previously ([39, 37, 35]) to select instantaneous flame regions that contain flamelets. Our previous studies of subgrid-scale (SGS mixing in the context of large-eddy simulation of turbulent combustion ([39, 37, 35, 38, 36, 40]) have shown that local regions containing flamelets can be selected by conditioning on the SGS scalar variance. The SGS scalar at a fixed location has qualitatively different filtered density function (FDF) shapes and structures depending on the *instantaneous* SGS scalar variance. When the SGS variance is large compared to its mean value, the SGS scalar has bimodal distributions, indicating that the fuel-lean and fuel-rich regions of the SGS fields are highly segregated. There is a ramp-cliff structure separating the two regions, across which there is a large scalar value jump, resulting in a conditional SGS structure resembling that of a counter-flow non-premixed

flame, which is a model for laminar flamelets. Thus, we can use large values of the SGS variance to select SGS scalars containing flamelets. We use the Favre filtered mixture fraction, $\langle Z\rangle_L = \langle \rho Z\rangle_\ell / \langle \rho\rangle_\ell$, and the Favre SGS scalar variance,

$$\langle Z''^2\rangle_L \equiv \frac{1}{\langle \rho\rangle_\ell}\int F_{ZL}(Z;\mathbf{x},t)(Z-\langle Z\rangle_L)^2 dZ = \langle \rho Z^2\rangle_\ell/\langle \rho\rangle_\ell - \langle Z\rangle_L^2, \tag{4.5}$$

as conditioning variables, where $\langle\rangle_\ell$ and $\langle\rangle_L$ denote conventional and Favre filtering with a top-hat filter,respectively. The Favre filtered mixture fraction, $\langle Z\rangle_L$, is set to the stoichiometric mixture fraction, $Z_s(=0.35)$, to maximize the probability of the SGS fields containing reaction zones.

In the present study we analyze the conditionally filtered diffusion and dissipation of the reactive scalar perturbations from steady flamelets using experimental data obtained in the Sandia flames. Knowledge of the mixing properties of the perturbations is an important step in understanding the coupling effects between molecular transport and chemical reaction in turbulent flames. The results are relevant for improving modeling approaches, including the laminar flamelet and the filtered mass density (FMDF) approaches for large-eddy simulation of turbulent combustion.

4.2 Experimental data and processing procedures

We use experimental data obtained in piloted turbulent partially premixed methane jet flames with a 1:3 ratio of CH_4 to air by volume (Sandia flames D and E, see [69, 58] for details). The Reynolds number of flame D and E are 22400 and 33600, respectively. The fuel jet diameter is 7.2 mm. The measurements employed combined line imaging of Raman scattering, Rayleigh scattering, and laser-induced CO fluorescence. Simultaneous measurements of the major species (CO_2, O_2, CO, N_2, CH_4, H_2O, and H_2), the mixture fraction (obtained from all major species), the temperature, and the radial component of scalar dissipation rate were made. In each flame, approximately 6000 line images are available at each measurement location. The mixture fraction is calculated using a variation of Bilger's definition [59], which has been modified by excluding the oxygen terms. The length of the imaging line is 6.0 mm with a pixel spacing of of 0.2 mm.

Measurement noise can contribute to the perturbations obtained using experimental data. The typical uncertainty in the Sandia flame data is 1% for the temperature and the major species except the hydrogen mass fraction, Y_{H_2}, which has an uncertainty of 6%. The perturbations obtained in the present study are generally much larger. More important, the conditional scalar dissipation associated with the perturbations

are consistent with flame behaviors, with a higher dissipation rate corresponding to a lower temperature and vice versa. Thus, the experimental noise does not qualitatively alter the results obtained in the present study.

The steady flamelet library used in the analysis is for the counter-flow configuration generated using the FlameMaster code [70]. The chemistry mechanism is the GRI-Mech 3.0 for methane and air [71], which contains 325 reactions and 53 species. Barlow et al.[63, 72] have shown that it predicts the Sandia flame B (a laminar flame) well. In this work, effects due to radiation are neglected as they are quite small in the Sandia flames.

Calculations of the conditionally filtered variables require spatial filtering of scalar fields. In this work the line images are used to perform one-dimensional filtering. Thus we obtain one component of the variables. For the same filter width one-dimension filter results in a somewhat higher SGS variance than a three-dimensional one, affecting the conditionally filtered scalar diffusion and dissipation. This increase, however, is not sufficiently large to significantly alter the functional forms of the variables. Small-scale anisotropy can also result in differences between the scalar diffusion and dissipation components obtained using one- and three-dimensional data. Given the moderate level of anisotropy in free shear flows, however, we expect the one-dimensional results to be similar to three-dimensional results.

The filter width employed in this work is 3.0 mm, significantly larger than the dissipative (Corrsin) scales (0.065 - 0.106 mm[61]), so that the subgrid scales contain sufficient fluctuations. This filter width is not very small compared to the integral length scales. Nevertheless, given Reynolds number of the Sandia flames, they are preferable than smaller filter sizes, which will not be much larger than the Corrsin scale. Previous studies (e.g., Refs. [39, 35]) have shown that when the filter width is much larger than the dissipation scales the properly scaled conditional statistics are not sensitive to the filter width.

In the present study the dissipation and diffusion terms are calculated using 10th-order explicit central differencing schemes. While the measurement noise affects the conditional mean diffusion obtained from the experimental data, the effects are not amplified by the finite difference scheme because the noise from different samples are uncorrelated and their contributions to the diffusion are canceled when calculating the conditional mean. The noise only enters through the conditioning variable, whose value is the sum of the scalar value and the noise. Thus the measured conditional diffusion is the noise-free diffusion averaged over the PDF of the noise, and therefore depends on the curvature of the conditional diffusion in the scalar sample space (the second derivative). Because significant curvature effects of the conditional mean only occur over large-scale scalar fluctuations, which is much larger than the noise variance, the effects of the noise is negligible.

Previous results [63] as well as our calculations have shown that the Lewis number has strong effects on the laminar flame prediction for the fuel used in the Sandia flames. Barlow et al. [63] have shown that in Sandia flame B, which has a low Reynolds number and is laminar, the measurements are in good agreement with laminar flame calculations with detailed molecular transport (using the Tsuji burner configuration). However, in flame E at $x/d = 45$, the data agree well with the unity Lewis number calculations, where x and d are the distance downstream of the nozzle and the nozzle diameter, respectively. Our comparisons (Fig. 4.1) show that at $x/d = 30$ in flame E, where line images are available for calculating diffusion and dissipation, the measured conditional mean temperature and mass fractions are in good agreement with the unity Lewis number prediction, although not to the same extent as at $x/d = 45$ for Y_{H_2} and Y_{CO_2}. These results suggest that the Lewis number effects in the Sandia flames are quite complex, depending both the Reynolds number and the downstream location. Due to the complexity of the differential diffusion effects in turbulent flames, in the present study we use unity Lewis number in the flamelet calculations and focus on the temperature and Y_{H_2O} at $x/d = 30$ in flame E, which are essentially unaffected by differential diffusion. In addition, at this location the flame is highly turbulent; therefore the SGS mixing is more representative of high-Reynolds-number turbulent flames. We also use the temperature data at $x/d = 15$ in flame E and $x/d = 15$ and 30 in flame D, which are only weakly affected by differential diffusion. The issue of differential diffusion will be addressed in a future study.

4.3 Results

In the present study, due to the limited amount of data available, care must be taken to ensure sufficient convergence for the statistics obtained. Thus, we choose only one SGS variance value much larger than the mean SGS variance when sampling the SGS fields containing flamelets so that a relatively large bin size can be used to ensure sufficient number of samples are obtained. We only analyze the burning samples, as our objective is to examine the mixing process in burning flamelets (local extinction and reignition pose different modeling challenges and are beyond the scope of this work). The flamelet solution at $\chi_s^f = 610/s$ (extinction limit) is used to separate the (nominally) extinguished samples from the burning samples. The line images containing extinguished samples are excluded. The flamelet solution for which the Z-T and Z-Y_{H_2O} profiles are closest to the conditional means obtained from the burning samples is chosen. Figure 4.1 shows that for flame E at $x/D = 30$ the flamelet with $\chi_s^f = 143/s$ closely matches the conditional means of the temperature and Y_{H_2O} for the SGS scalar variance chosen. It also better matches the conditional means of

Y_{CO_2}, and Y_{H_2} than other values of χ_s^f (not shown).

We choose a steady flamelet solution T^f in our analysis instead of the conditional mean $\langle T|Z\rangle$ for two reasons. First, since the goal is to model diffusion in the flamelet regime more accurately, it is natural to use the flamelet solution and model perturbations from it. Second, a flamelet is a physical model for flame structure and a flamelet solution is an exact solution of the flamelet equation. The conditional mean, however, is a statistic and the solution of its equation involve additional assumptions. In particular, assumptions on the conditional reaction term and the covariance of conditional fluctuations are needed. Thus, the equation for the conditional perturbations are more complex than that for the perturbations from a flamelet, making modeling and asymptotic analyses more difficult. In addition, the functional form of the conditional mean obtained experimentally is affected by statistical uncertainty. Thus, for the present study it is more effective to use flamelet solutions than conditional means.

4.3.1 The conditionally filtered diffusion of mixture fraction and temperature perturbations

The conditionally filtered diffusion of the flamelet temperature and that of the temperature perturbations at $x/d = 30$ in flame E, $\langle\langle\frac{1}{\rho}\frac{\partial}{\partial y}(\rho D\frac{\partial T^f}{\partial y})|Z,T\rangle_\ell|\langle Z\rangle_L,\langle Z''^2\rangle_L\rangle$ and $\langle\langle\frac{1}{\rho}\frac{\partial}{\partial y}(\rho D\frac{\partial T^*}{\partial y})|Z,T\rangle_\ell|\langle Z\rangle_L,\langle Z''^2\rangle_L\rangle$ respectively, are shown in Fig. 4.2 along with the mixture fraction diffusion. Because they are transport velocities of the FMDF in the mixture fraction-temperature sample space, we present them as a diffusion velocity in the form of streamlines and magnitudes [43, **?**]. Here the mixture fraction diffusion is non-dimensionalized by the square root of the SGS variance $\langle Z''^2\rangle_L^{1/2}$ and the Favre conditional scalar dissipation rate, $\langle\langle\chi\rangle_L|\langle Z\rangle_L,\langle Z''^2\rangle_L\rangle$ while the temperature diffusion is non-dimensionalized using the peak temperature and the Favre conditional temperature dissipation, $\langle\langle\chi\rangle_L|\langle Z\rangle,\langle Z''\rangle\rangle$. Since $T^f = T^f(Z,\chi_s^f)$, the diffusion of T^f depends on the mixture fraction, the scalar dissipation and diffusion as follows:

$$\left\langle\frac{1}{\rho}\frac{\partial}{\partial y}\left(\rho D\frac{\partial T^f}{\partial y}\right)\Big|Z,T\right\rangle_\ell = \frac{\partial T^f}{\partial Z}\left\langle\frac{1}{\rho}\frac{\partial}{\partial y}\left(\rho D\frac{\partial Z}{\partial y}\right)\Big|Z,T\right\rangle_\ell + \frac{\partial^2 T^f}{\partial Z^2}\left\langle D\frac{\partial Z}{\partial y}\frac{\partial Z}{\partial y}\Big|Z,T\right\rangle_\ell. \tag{4.6}$$

Near the peak temperature the mixture fraction diffusion is small because this region is close to the center of the ramp-cliff structure. The diffusion of T^f is negative due to the negative curvature of the T^f profiles as a function of mixture fraction (Fig. 4.2b). Consequently, the streamlines starting near the peak temperature nearly move vertically towards lower temperatures. As the streamlines move towards lower temperatures, the scalar dissipation increases, resulting in larger diffusion magnitudes. For very lean and

rich mixtures, the dominant term for the diffusion of T^f is the first term on the RHS of Eq. (4.6) so that the diffusion of T^f is proportional to mixture fraction diffusion, which results in long straight streamlines along the direction of ridgeline of the FMDF [42]. This diffusion streamline pattern is very similar to that of the conditionally filtered diffusion of T (Fig. 4.2a) [42], suggesting that the steady flamelet can represent much of the coupling between mixing and reaction. The pattern is, however, very different from that of non-reacting scalar mixing [43], which tends to have streamlines converting to the conditional mean, further highlighting the effects of reaction in inducing diffusion.

Figures 4.2c and 4.2d show the conditionally filtered diffusion of Z and T^* plotted in the $Z-T$ and $Z-T^*$ sample space, respectively. Unlike those in Fig. 4.2b, the diffusion velocity streamlines generally move first towards a manifold close to T^f, which is also close to the ridgeline of the FMDF [43]. The diffusion velocity magnitude decreases as it approaches T^f. The streamlines then move along the manifold at lower velocities. In addition, the magnitude of the diffusion velocity is generally smaller than that of T [43]. Fig. 4.2d further shows that the streamlines largely move towards $T^* = 0$ near the peak temperature, i.e., the dominant effect of diffusion is to reduce T^*. This SGS mixing pattern of the mixture fraction and the temperature perturbations is similar to that of three (non-reactive) scalar mixing in a turbulent coaxial jet [50] and to the temperature mixing in distributed reaction zones [43]. The coaxial jet consists of a center jet, an annular flow, and a co-flow. The spatial relationship among the scalars carried by each stream is similar to the fuel-product-oxidizer relationship in a non-premixed reaction flow. However, the pattern is qualitatively different from the conditionally filtered diffusion of T^f, for which the streamlines move towards lower temperature, not the conditional mean temperature. The diffusion results for Y_{H_2O} is also similar (not shown).

The similarities between the form of the conditionally filtered diffusion of T^* and that of a non-reactive scalar suggest that the former may be modeled using the Interaction by Exchange with the Mean (IEM) model [**?**], which was developed based on non-reactive scalar mixing characteristics. The IEM model for the conditionally filtered temperature perturbation diffusion is

$$\left\langle \frac{1}{\rho}\frac{\partial}{\partial x_i}\left(\rho D\frac{\partial T^*}{\partial x_i}\right)\Big| Z, T^*\right\rangle_\ell = -\frac{T^*}{2\tau_{T^*}}, \tag{4.7}$$

where τ_{T^*} is the mixing time scale for T^*. To examine the trend of the diffusion more clearly in Fig. 4.3 we plot the conditionally filtered diffusion of T^* as a function of T^* at $x/d = 15$ and 30 in flames D and E. The overall linear trend is indeed consistent with the IEM model. Note that the IEM model is qualitatively incon-

sistent with the diffusion of T^f, which is not towards the conditional mean temperature due to the coupling of the diffusion to the reaction. The issue of the choice τ_{T^*} and the comparison between the experiment results and the IEM model will be discussed in section 4.3.

4.3.2 The conditional filtered dissipation rate for temperature perturbations

The conditionally filtered dissipation rate of the flamelet part and its perturbations filtered conditionally on both the mixture fraction and temperature, $\langle\langle 2D\frac{\partial T^f}{\partial y}\frac{\partial T^f}{\partial y}|Z,T\rangle_\ell|\langle Z\rangle_L,\langle Z''^2\rangle_L\rangle$ and $\langle\langle 2D\frac{\partial T^*}{\partial y}\frac{\partial T^*}{\partial y}|Z,T\rangle_\ell|\langle Z\rangle_L,\langle Z''^2\rangle_L\rangle$ are showed in Fig. 4.4. The cross-dissipation term is generally small compared to the other two terms and is not shown. For the flamelet part, its dissipation only depends on the scalar and the scalar dissipation rate:

$$\chi_{Tf} \equiv \left\langle 2D\frac{\partial T^f}{\partial y}\frac{\partial T^f}{\partial y}\Big|Z,T\right\rangle_\ell = \left(\frac{\partial T^f}{\partial Z}\right)^2\left\langle 2D\frac{\partial Z}{\partial y}\frac{\partial Z}{\partial y}\Big|Z,T\right\rangle_\ell . \tag{4.8}$$

The conditionally filtered temperature dissipation rate of the flamelet part has two peak values, one on the lean side near $Z = 0.3$ and one on the rich side near $Z = 0.5$ and (Fig. 4.4b), where the conditionally filtered scalar dissipation rate is generally large at lower temperatures [42]. Near the peak temperature $\frac{\partial T^f}{\partial Z}$ is approximately zero, which results in a lower dissipation rate of T^f. Because the tight coupling between T^f and Z, χ_{Tf} can be obtained from the conditionally filtered scalar dissipation rate.

Figure 4.4c shows the conditionally filtered dissipation rate of T^*. Unlike $\langle\chi_{Tf}|Z,T\rangle_\ell$ (Fig. 4.4b) and $\langle\chi_T|Z,T\rangle_\ell$ (Fig. 4.4a), there is generally one peak near $Z = 0.45$ at a lower temperature where the maximum gradient in the ramp-cliff structure is located. Thus, the dependence of $\langle\chi_{T^*}|Z,T\rangle$ on T and Z has some similarities to that of a nonreactive scalar and temperature in distributed reaction zones [42]. Compared to Fig. 4.4b, the dissipation rate of T^* is almost an order of magnitude smaller than that of T^f, indicating that the dominant contributions of the conditional filtered temperature dissipation rate come from the flamelet structure and that the mixing of T^* may pose a lesser modeling challenge.

4.3.3 Asymptotic analysis of the perturbations from flamelets

The similar functional forms of SGS diffusion and dissipation of reactive scalar perturbations to those of a non-reactive scalar suggests that they may be modeled in a similar way. To further understand the reactive scalar perturbations, such as their dynamics and time and length scales, we perform perturbation analysis of the flamelet equation. We will consider two possible limiting forms of the perturbations, whose

length scales are small and large compared to the reaction zone width, respectively. While these forms only represent the perturbations in flames under limiting conditions, they nevertheless can help us understand the nature and behaviors of the perturbations. Consistent with our objective of examining mixing in burning flamelets and perturbations from them, in the analysis we assume that χ_s^f is far from the extinction limit (high Damköhler number).

Starting from the transport equation for reactive scalars ϕ_i,

$$\rho\frac{\partial\phi_i}{\partial t}+\rho u_k\frac{\partial\phi_i}{\partial x_k}-\frac{\partial}{\partial x_k}\left(\rho D\frac{\partial\phi_i}{\partial x_k}\right)=w_i, \tag{4.9}$$

with the coordinate transformation using $Z_2=x_2, Z_3=x_3, t^*=t$, and replacing the coordinate x_1 by Z, we obtain

$$\begin{aligned}\frac{\partial}{\partial t} &= \frac{\partial}{\partial t^*}+\frac{\partial Z}{\partial t}\frac{\partial}{\partial Z}, \quad \frac{\partial}{\partial x_1}=\frac{\partial Z}{\partial x_1}\frac{\partial}{\partial Z}\\ \frac{\partial}{\partial x_k} &= \frac{\partial}{\partial Z_k}+\frac{\partial Z}{\partial x_k}\frac{\partial}{\partial Z}, \quad (k=2,3)\end{aligned} \tag{4.10}$$

one obtains the flamelet equation (Peters 1984)

$$\rho\frac{\partial\phi_i}{\partial t^*} = \rho D\nabla Z\cdot\nabla Z\frac{\partial^2\phi_i}{\partial Z^2}+w_i+R \tag{4.11}$$

$$R = -\rho(u_2\frac{\partial\phi_i}{\partial Z_2}+u_3\frac{\partial\phi_i}{\partial Z_3})+\frac{\partial(\rho D)}{\partial x_2}\frac{\partial\phi_i}{\partial Z_2}-\frac{\partial(\rho D)}{\partial x_3}\frac{\partial\phi_i}{\partial Z_3} \tag{4.12}$$

$$+ \rho D\left[\left(\frac{\partial Z}{\partial x_k}\right)^2\frac{\partial^2\phi_i}{\partial Z^2}+2\frac{\partial Z}{\partial x_2}\frac{\partial^2\phi_i}{\partial Z\partial Z_2}+2\frac{\partial Z}{\partial x_3}\frac{\partial^2\phi_i}{\partial Z\partial Z_3}+\frac{\partial^2\phi_i}{\partial Z_2^2}+\frac{\partial^2\phi_i}{\partial Z_3^2}\right]. \tag{4.13}$$

Introducing stretched coordinates

$$\zeta=\frac{Z-Z_s}{\varepsilon}, \quad \tau=\frac{t^*}{\varepsilon^2}, \tag{4.14}$$

the reactive scalars and the reaction rate are expanded into leading-order, first-order, and higher order terms

$$\nabla\phi_i=\nabla\phi_i^0+\varepsilon\nabla\phi_i^1+O(\varepsilon^2), \quad w_i=w_i^0+\left(\frac{\partial w_i}{\partial\phi_j}\right)^0\varepsilon\phi_j^1+O(\varepsilon^2), \tag{4.15}$$

where a superscript denotes the order. Since perturbations from flamelets are caused by perturbations in the

mixture fraction gradient, we expand the latter as

$$\nabla Z = \nabla Z^0 + \varepsilon \nabla Z^1 + O(\varepsilon^2). \tag{4.16}$$

Substituting Eqs. (4.14-4.16) into the flamelet equation and using the mixture fraction transport equation,

$$\rho \frac{\partial Z}{\partial t} + \rho u_k \frac{\partial Z}{\partial x_k} - \frac{\partial}{\partial x_k}\left(\rho D \frac{\partial Z}{\partial x_k}\right) = 0, \tag{4.17}$$

we obtain the leading-order equation

$$\rho \frac{\partial \phi_i^0}{\partial \tau} = \rho \frac{\chi^0}{2} \frac{\partial^2 \phi_i^0}{\partial \zeta^2} + \varepsilon^2 w_i^0, \tag{4.18}$$

and the equation for the first-order perturbation

$$\begin{aligned} \rho \frac{\partial \phi_i^1}{\partial \tau} &= \rho \frac{\chi^0}{2} \frac{\partial^2 \phi_i^1}{\partial \zeta^2} + \rho \frac{\chi^1}{2} \frac{\partial^2 \phi_i^0}{\partial \zeta^2} + \varepsilon^2 \left(\frac{\partial w_i}{\partial \phi_j}\right)^0 \phi_j^1 - \rho D \sum_{k=2}^{3} 2 \frac{\partial Z^0}{\partial x_k} \frac{\partial^2 (\phi_i^0 + \varepsilon \phi_i^1)}{\partial \zeta \partial Z_k} \\ &= \rho \frac{\chi^0}{2} \frac{\partial^2 \phi_i^1}{\partial \zeta^2} + \rho \frac{\chi^1}{2} \frac{\partial^2 \phi_i^0}{\partial \zeta^2} + \varepsilon^2 \left(\frac{\partial w_i}{\partial \phi_j}\right)^0 \phi_j^1 - \varepsilon \rho D \sum_{k=2}^{3} 2 \frac{\partial Z^0}{\partial x_k} \frac{\partial^2 \phi_i^1}{\partial \zeta \partial Z_k}, \end{aligned} \tag{4.19}$$

where $\chi^0 = 2D\nabla Z^0 \cdot \nabla Z^0$ and $\chi^1 = 4D\nabla Z^0 \cdot \nabla Z^1$ are the flamelet dissipation rate and the dissipation perturbation, respectively. The terms on the RHS of Eq. (4.19) are the diffusion of the perturbation, production of the perturbation due to the scalar dissipation rate perturbation, the reaction source term, and the curvature term, respectively. The curvature term containing ϕ_i^0 vanishes because there are no curvature effects in the (leading-order) equation for ϕ_i^0. The perturbation ∇Z^1 must be of order one in order for ϕ_i^1 to be of the same order: $\varepsilon \nabla Z^1 \sim \nabla Z^0 \frac{\ell_R}{\ell} \sim \varepsilon \nabla Z^0$, where ℓ and ℓ_R are the length scale of ∇Z^0 and the reaction zone width, respectively. We further decompose ∇Z^1 and χ^1 into $\nabla Z^1 = \nabla Z^{1f} + \nabla Z^{1*}$ and $\chi^1 = \chi^{1f} + \chi^{1*}$, where ∇Z^{1f}, χ^{1f}, ∇Z^{1*}, and χ^{1*} represent the slow variations of ∇Z and χ (or the first-order corrections to ∇Z^0 and χ^0, respectively) inside the reaction zone and the perturbations from the flamelet ($\nabla Z^0 + \varepsilon \nabla Z^1$, $\chi^0 + \varepsilon \chi^1$), respectively. Correspondingly, ϕ_i^{1f} and ϕ_i^{1*} are the first-order correction to ϕ_i^0 and the perturbations resulting from χ^{1*}, respectively. In the following we consider two limiting cases of χ^{1*} with its length scales, ℓ_1, much smaller and larger than the reaction zone width respectively.

1. Perturbations with $\ell_1 \ll \ell_R$

For the case $\ell_1 \ll \ell_R$, the perturbations could potentially result in a greater curvature of the mixing

fraction field. However, the curvature of the perturbed mixture fraction field ($Z = Z^0 + \varepsilon(Z^{1f} + Z^{1*})$) must remain of order ε for the leading-order expansion to be valid. The curvature without the fluctuations ∇Z^{1*} is $\frac{\ell_R}{\ell} \sim \varepsilon$. When ∇Z^{1*} has fluctuations of scale $\ell_1 \ll \ell_R$ the curvature is

$$\frac{\varepsilon(|\nabla Z^{1*}|/|\nabla Z^0|)\ell_1}{\ell_1} = \varepsilon\frac{|\nabla Z^{1*}|}{|\nabla Z^0|}, \tag{4.20}$$

where $\varepsilon|\nabla Z^{1*}|\ell_1$ is the change of scalar difference over the length ℓ_1 due to ∇Z^{1*}; therefore $\varepsilon(|\nabla Z^{1*}|/|\nabla Z^0|)\ell_1$ is the displacement of the iso-mixture fraction contour. If ∇Z^{1*} is of order one or less, the curvature induced by ∇Z^{1*} is of the same order to or smaller than the curvature of the Z^0 field, i.e., $\varepsilon\frac{|\nabla Z^{1*}|}{|\nabla Z^0|} \leq \varepsilon$. Thus, for $|\nabla Z^{1*}| \ll |\nabla Z^0|$, i.e., for a perturbation gradient much smaller than the flamelet gradient, the flamelet structure is preserved, even when scalar fluctuations are present in the reaction zone.

For isotropic ∇Z^1 perturbations, the orders of magnitude of the diffusion term and the curvature term in Eq. (4.19) can be estimated as

$$\rho\frac{\chi^0}{2}\frac{\phi_i^{1*}}{\ell_1^2\nabla Z^0\cdot\nabla Z^0/\varepsilon^2} = \varepsilon^2\rho D\frac{\phi_i^{1*}}{\ell_1^2} \tag{4.21}$$

and

$$\varepsilon\rho D\nabla Z^0\frac{\phi_i^{1*}}{\ell_1\nabla Z^0\ell_1/\varepsilon} = \varepsilon^2\rho D\frac{\phi_i^{1*}}{\ell_1^2}, \tag{4.22}$$

respectively. Thus, the two terms are of the same order of magnitude. The reaction term, on the other hand, is smaller, as will be shown below.

For $\ell_1 \ll \ell_R$, the variables χ^0, $\frac{\partial^2\phi_i^0}{\partial\zeta^2}$, and $\frac{\partial Z^0}{\partial x_k}$ in Eq. (4.19) can be considered as independent of ζ. Fourier transform the first order equation, we have

$$\rho i\omega\widehat{A_i} = -\rho\frac{\chi^0}{2}\widehat{A_i}k_\zeta^2 + \frac{1}{2}\rho\overline{\frac{\partial^2\phi_i^0}{\partial\zeta^2}}\widehat{\chi^{1*}} + \varepsilon^2\overline{\left(\frac{\partial w_i}{\partial\phi_j}\right)^0}\widehat{A_j} + \rho D\sum_{m=2}^{3}\frac{\partial Z^0}{\partial x_m}\varepsilon\widehat{A_i}k_\zeta k_m \tag{4.23}$$

$$\left[\rho i\omega\delta_{ij} + \rho\frac{\chi^0}{2}k_\zeta^2\delta_{ij} - \varepsilon^2\overline{\left(\frac{\partial w_i}{\partial\phi_j}\right)^0} - \varepsilon\rho D\sum_{m=2}^{3}\frac{\partial Z^0}{\partial x_m}(k_\zeta k_m)\right]\widehat{A_i} = \frac{1}{2}\rho\overline{\frac{\partial^2\phi_i^0}{\partial\zeta^2}}\widehat{\chi^{1*}} \tag{4.24}$$

where $\widehat{A_i} = \widehat{A_i}(\omega, k_\zeta, k_2, k_3)$ and $\widehat{\chi^{1*}} = \widehat{\chi^{1*}}(\omega, k_\zeta, k_2, k_3)$ are the Fourier transforms of ϕ_i^{1*} and χ^{1*} respectively, and ω, k_ζ, k_2, k_3 are the angular frequency, wavenumber in the ζ direction, and wavenumber in the x_2 and x_3 directions, respectively. An overbar denotes the spatially averaged value in the reaction zone. The terms in the bracket on the LHS can be inverted to obtain the transfer function of the system described by Eq. (4.24)

which is a frequency-wavenumber filter of first and second orders, respectively, acting on the production (or forcing) term $\frac{1}{2}\rho\widehat{\frac{\partial^2\phi_i^0}{\partial\zeta^2}}\chi^{1*}$. The reaction term does not depend on the wavenumber, and consequently is small compared to the second term (diffusion) for small-scale perturbations, because for $k_\zeta > \frac{\varepsilon}{\Delta Z_R}$,

$$\frac{\chi^0}{2}k_\zeta^2 > \frac{\chi^0}{2}\frac{\varepsilon^2}{(\Delta Z_R)^2} \approx \varepsilon^2\frac{\chi^0}{2}\frac{\phi^0}{Z_s(1-Z_s)\Delta Z_R}\frac{Z_s(1-Z_s)}{\Delta Z_R\phi^0} \approx \rho\frac{\chi^0}{2}\frac{\partial^2\phi^0}{\partial\zeta^2}\frac{Z_s(1-Z_s)}{\phi^0\Delta Z_R} \tag{4.25}$$

$$\approx \varepsilon^2 w^0\frac{Z_s(1-Z_s)}{\phi^0\Delta Z_R} \approx \varepsilon^2\left(\frac{\partial w}{\partial\phi}\right)^0\frac{Z_s(1-Z_s)}{\Delta Z_R} \approx \varepsilon^2\left(\frac{\partial w}{\partial\phi}\right)^0, \tag{4.26}$$

i.e., the reaction term does not significantly alter the filter function at high wavenumbers. The perturbation ϕ_i^{1*} is essentially proportional to the filtered production term, with the filter function largely determined by the mixture fraction field, and the length scale determined by ∇Z^{1*}. Therefore, it is expected to have diffusion characteristics, such as the functional form of the conditionally filtered diffusion and the SGS mixing time scale, that are similar to a non-reactive scalar. This type of perturbations are likely to occur in high-Reynolds number flames where the dissipation length scales are smaller than the reaction zone width.

2. Perturbations with $\ell_1 \gg \ell_R$

For $\ell_1 \gg \ell_R$, χ^{1*} is independent of ζ in the reaction zone, and is only a function of time. Thus the perturbations essentially causes the flamelet to become unsteady or quasi-steady. For isotropic ∇Z^1 perturbations, the orders of magnitude of the diffusion term and the curvature term in Eq. (4.19) can be estimated as

$$\rho\frac{\chi^0}{2}\frac{\phi_i^{1*}}{\ell_R^2\nabla Z^0\cdot\nabla Z^0/\varepsilon^2} = \varepsilon^2\rho D\frac{\phi_i^{1*}}{\ell_R^2} \tag{4.27}$$

and

$$\varepsilon\rho D\nabla Z^0\frac{\phi_i^{1*}}{\ell_R\nabla Z^0\ell_1/\varepsilon} = \varepsilon^2\rho D\frac{\phi_i^{1*}}{\ell_R\ell_1}, \tag{4.28}$$

respectively. The curvature term therefore is much smaller and is neglected in the following analysis.

The Fourier transform of Eq. (4.19) is

$$\rho i\omega\widehat{A}(k,\omega) = -\rho\frac{\chi^0}{2}\widehat{A}k_\zeta^2 + \frac{1}{2}\rho\widehat{\frac{\partial^2\phi^0}{\partial\zeta^2}}\widehat{\chi^{1*}}(\omega) + \varepsilon^2\widehat{\left(\frac{\partial w_i}{\partial\phi_j}\right)^0} * \widehat{A}_j. \tag{4.29}$$

The spatial variations of ϕ_i^{1*} is now determined by $\frac{\partial^2\phi^0}{\partial\zeta^2}$ and $\left(\frac{\partial w_i}{\partial\phi_j}\right)^0$. Since both terms are limited to the reaction zone, so is the diffusion term. Thus, the length scales of these terms are of the order of

the reaction width. The order of magnitudes of the diffusion and reaction terms are estimated as $\rho\frac{\chi_0}{2}\phi_i^{1*}$ and $\varepsilon^2\frac{w_i^0\phi_j^{1*}}{\phi_j^0}$, respectively, and therefore, are of the same order. This shows that the diffusion is strongly influenced by reaction. The temporal variations of ϕ_i^{1*} is largely determined by χ^{1*} through a first-order filter.

The diffusion term in Eq. (4.19) is largely limited to the reaction zone, and therefore can be estimated as $\rho\frac{\chi^0}{2}\frac{\partial^2\phi_i^{1*}}{\partial Z^2}\sim-\rho\frac{\chi^0}{2}\frac{\phi_i^{1*}}{Z_s(1-Z_s)\Delta Z_R}$, which can be expressed in the same form as the IEM model:

$$-C\frac{\chi^0}{2}\frac{\phi_i^{1*}}{Z_s(1-Z_s)\Delta Z_R}=-C\frac{\phi_i^{1*}}{2\tau_{\phi_i^{1*}}}, \tag{4.30}$$

where $\tau_{\phi_i^{1*}}=\frac{Z_s(1-Z_s)\Delta Z_R}{\chi^0}$ and C are the SGS mixing time for ϕ_i^{1*} and the model coefficient respectively. Since the estimate should also be valid for nearly steady flamelet, we show in Fig. 4.5 the perturbation diffusion from the steady flamelet (differences between the dominant flamelet and other flamelets) near the peak temperature. The overall functional form is indeed consistent with the IEM model. Thus, while the diffusion of T^f has qualitatively different characteristics than that of a non-reactive scalar, the perturbation diffusion has similarities to the latter.

The above asymptotic analysis suggests that the diffusion of the reactive scalar perturbations, whether in the form of small-scale random fluctuations or unsteady flamelets, has the form of non-reactive scalars, but with different mixing times. To examine which form of the perturbations are more consistent with those observed in the Sandia flames, in Fig. 4.3 we compare the experimental results of the conditionally filtered diffusion of T^* $(=\varepsilon T^{1*})$ near the peak temperature to the prediction of the IEM model using $\tau_T^*=\tau_{\phi_i^{1*}}$ (Eq. 4.30). The results at $x/d=15$ and 30 in flames D and E cover two Reynolds numbers, two SGS variance values (the SGS variance at the same downstream locations are approximately equal for the two flames), and four scalar dissipation rate values, and therefore are good test cases for the scaling of the mixing time scale. The approximately linear trend of the experimental results is consistent with the IEM model. Perhaps more important, the magnitude of the measured diffusion is consistent with the IEM model having the mixing time given by Eq. (4.30) and a C value of 2.5 for all the cases. The significance of these results is that the mixing time appears to scale with $\tau_{\phi_i^{1*}}$ while the numerical value of C is not important. Using the time scale of SGS mixture fraction, on the other hand, would require different C values for the model to fit the data for the different cases. The overall similarity of the experimental results to the flamelet solutions suggests that the perturbation diffusion is consistent with predictions based on unsteady or quasi-steady flamelets.

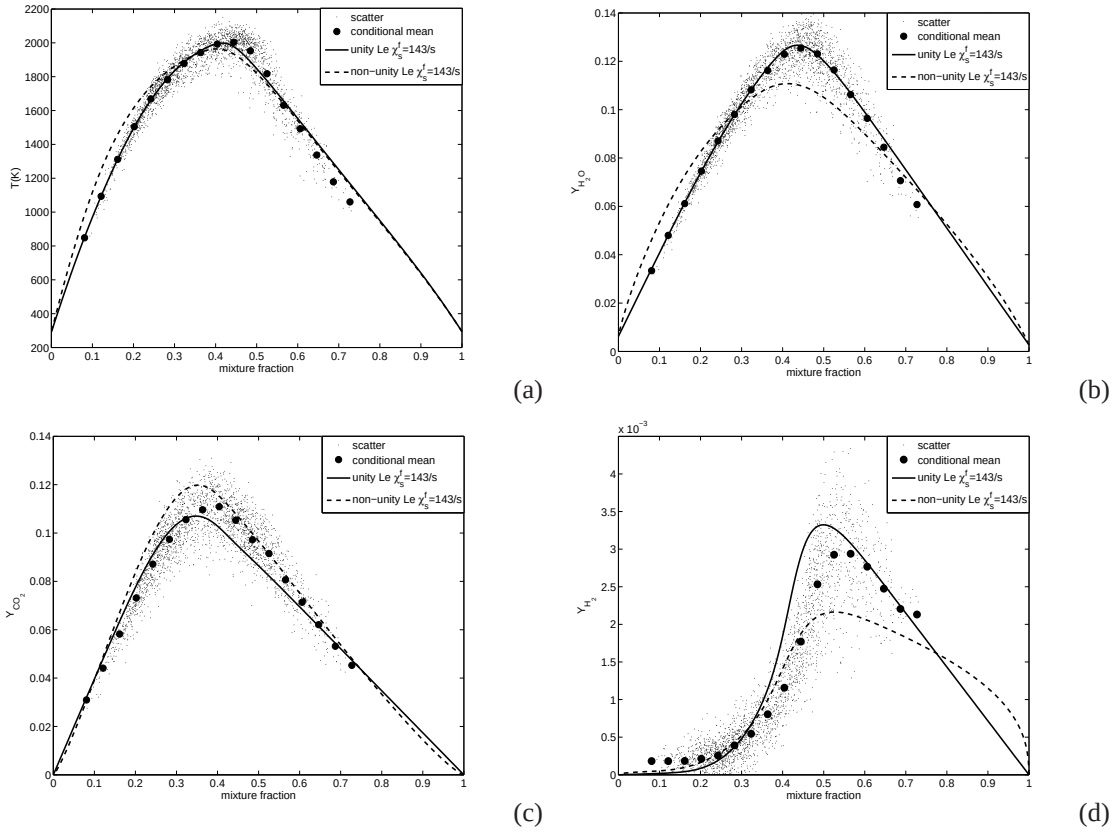

Figure 4.1: Measured conditionally filtered mean of (a) temperature and (b) Y_{H_2O} (c) Y_{CO_2} (d) Y_{H_2} at $x/d = 30$ in flame E compared with flamelet calculations with and without the unity Lewis number assumption.

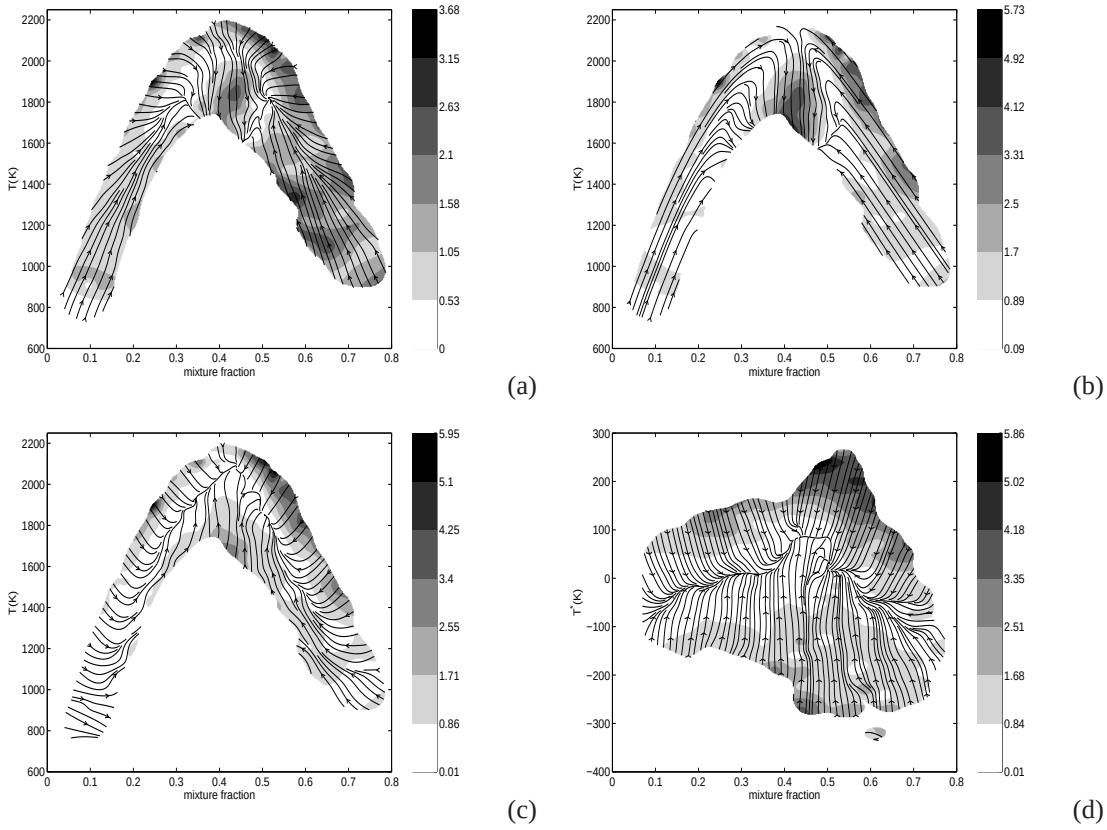

Figure 4.2: (a) Conditionally filtered mixture fraction diffusion and temperature diffusion; (b) the flamelet part; (c) Conditionally filtered temperature perturbation diffusion conditional on temperature and (d) Conditionally filtered temperature perturbation diffusion conditional on temperature perturbation. All figures are for flame E at $x/d = 30$.

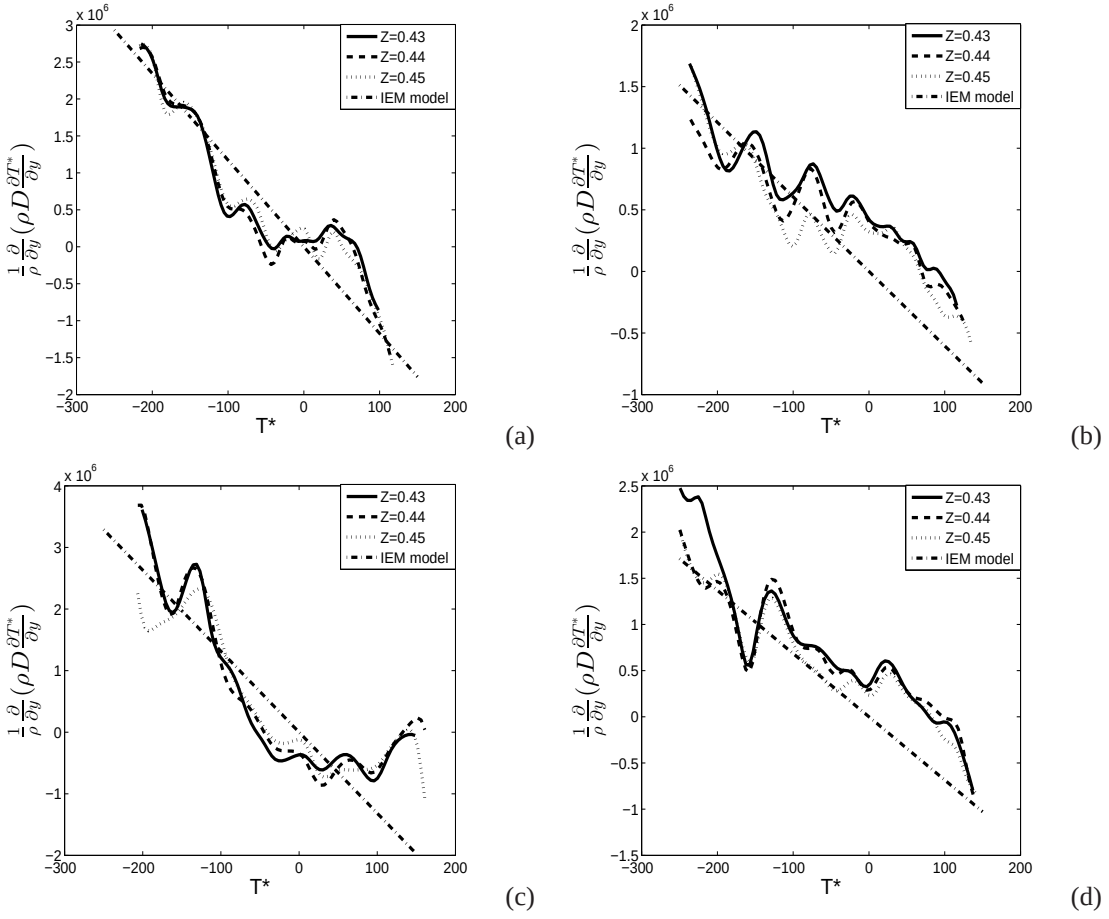

Figure 4.3: Conditionally filtered temperature perturbation diffusion near the peak temperature in flame E compared with the mixing time scale given in Eq. 4.30 and a C_ϕ value of 2.5 (a) at $x/d = 15$, (b) $x/d = 30$ in flame D and (c)$x/d = 15$, (d) $x/d = 30$ in flame E.

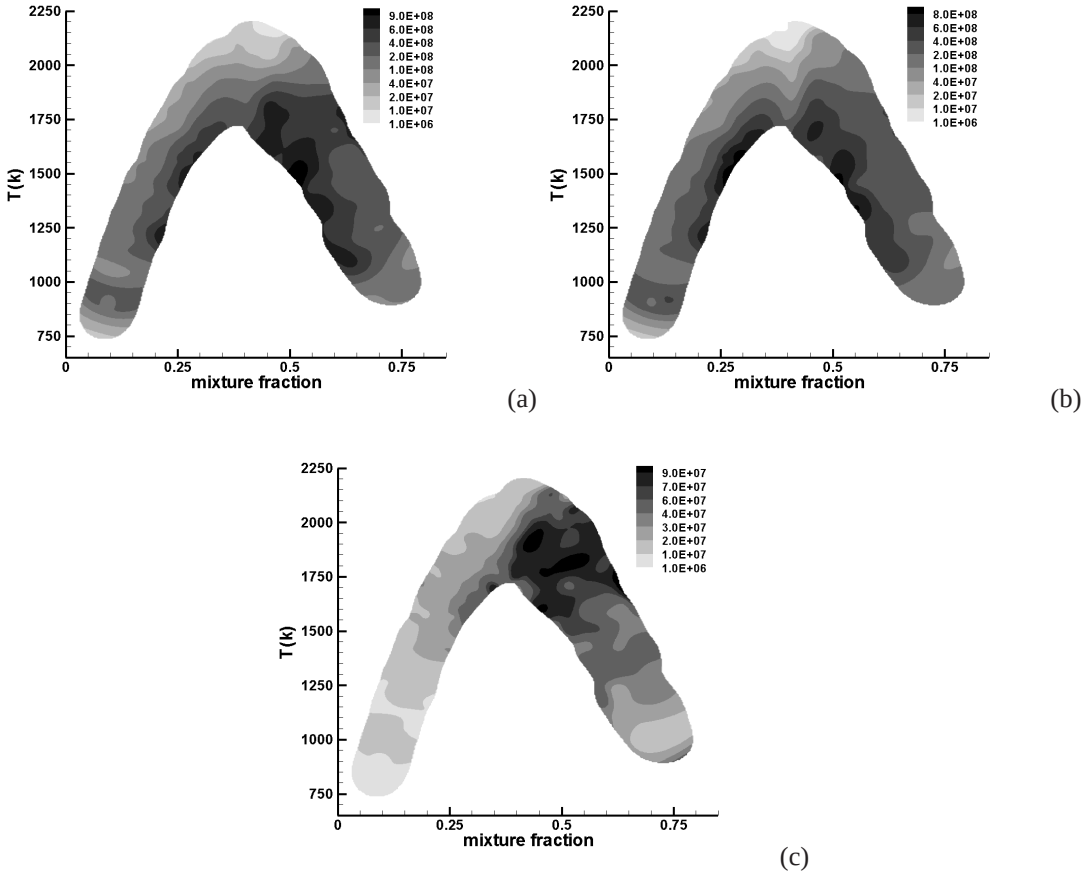

Figure 4.4: Conditionally filtered dissipation rate of (a) T and (b) T^f and (c) T^* at $x/d = 30$ in flame E.

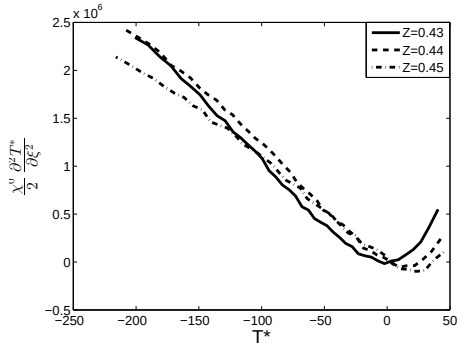

Figure 4.5: Conditionally filtered temperature perturbation diffusion near the peak temperature from flamelet solutions with $\chi_s^f = 143/s$

Chapter 5

DNS study of three scalar mixing in temporally developing plane jets

5.1 Introduction

A direction numerical simulation (DNS) is a numerical experiment in which the Navier-Stokes equations are numerically solved without any turbulence models. Currently, it's the only approach that provides detailed temporally and spatially resolved information of the flow and scalar field. Although the computational cost of DNS is very high, it's a very useful tool in fundamental research in turbulence. It can be used to give significant insight of turbulence in canonical configurations. Also, it's useful in testing model, i.e., a priori evaluation of scalar PDF and mixing models.

There already have extensive studies about turbulent mixing based on two-scalars. However, in many applications such as reactive flows, at least three scalar (two reactants and one product) are involved. The mixing process is multiscalar and more complex. Recently Cai et al.[50] has studied the non-reactive three-scalar mixing in a turbulent coaxial jet. In this flow a central jet and an annulus flow, consisting of acetone-doped air and ethylene, are mixed with the co-flow air, thus two of the scalars (the central jet and the co-flow air) are separated by the third (annulus flow); therefore better approximates the mixing process in a non-premixed turbulent reactive flow. Previous numerical and experimental studies also found the upstream conditions, such as velocity ratio between the central jet and off-central jet, have a great impact on the turbulent structure and mixing properties in turbulent coaxial jets [52, 53, 54, 55, 56, 57]. In order to investigate

the effects of upstream conditions on the scalar mixing, the temporally developing plane jets which evolve three scalars was performed using direct numerical simulation.

5.2 Numerical implementation

The DNS code currently developed is written in Fortran 90 and parallelized with MPI in 3 Cartesian coordinates. The code solves the compressible, reacting Navier-Stokes equations which include the following equations for continuity, momentum, energy, and species mass fractions, respectively [73].

$$\frac{\partial \rho}{\partial t} = -\frac{\partial(\rho u_i)}{\partial x_i}, \tag{5.1}$$

$$\frac{\partial(\rho u_i)}{\partial t} = -\frac{\partial(\rho u_j u_i)}{\partial x_i} - \frac{\partial P}{\partial x_i} + \frac{\partial \tau_{i,j}}{\partial x_i}, \tag{5.2}$$

$$\frac{\partial(\rho e_o)}{\partial t} = -\frac{\partial(\rho e_o u_i)}{\partial x_i} - \frac{\partial(P u_i)}{\partial x_i} + \frac{\partial(\tau_{i,j} u_j)}{\partial x_i} - \frac{\partial q_i}{\partial x_i}, \tag{5.3}$$

$$\frac{\partial(\rho Y_k)}{\partial t} = -\frac{\partial(\rho Y_k u_i)}{\partial x_i} - \frac{\partial j_{k,i}}{\partial x_i} + \omega_k, \tag{5.4}$$

where ρ, u_i, t, x_i, P, $\tau_{i,j}$, Y_k, ω_k are density, velocity, time, position, pressure, viscous stress tensor, mass fraction, and reaction rate of species k, respectively. Moreover, e_o, q_i and $j_{k,i}$ stand for the specific total energy, heat flux vector, and the species diffusion flux vector, respectively. The total energy, viscous stress tensor and the heat flux vector are given by:

$$e_o = \frac{1}{2}u_i u_i + h - \frac{P}{\rho}, \quad q_i = -\lambda \Delta T + \sum_k h_k j_{k,i}, \tag{5.5}$$

$$\tau_{i,j} = \mu\left(\frac{\partial u_i}{\partial x_j} + \frac{\partial u_j}{\partial x_i} - \frac{2}{3}\delta_{i,j}\frac{\partial u_i}{\partial x_i}\right) \tag{5.6}$$

where λ, T, h and h_k are the thermal conductivity, temperature, specific enthalpy of the mixture and species, respectively. The above equations are closed with constitutive relations for species diffusivity, a thermodynamic relation linking enthalpy and temperature and ideal gas equation of state.

The current code is based on finite difference method. Spatial derivative are approximated on a rectangular cartesian uniform mesh using explicit eight-order central difference with tenth-order filter to remove high wave number errors [74]. Explicit fourth-order, four-stage Runge-Kutta method is implemented to approximate the temporal derivatives [74]. 3D Navier-Stokes characteristic boundary conditions [75, 76] are employed at open boundaries.

5.3 Code validation

To validate the code, previous experimental and DNS results are compared with the current DNS results for spatially developing non-reacting round jet, temporally developing non-reacting and reacting plane jet. For reacting jet, a mixture-averaged formulation is used for the species diffusion flux $J_{k,i} = -\rho D_k \frac{\partial Y_k}{\partial x_i} - \frac{\rho D_k Y_k}{M} \frac{\partial M}{\partial x_i}$, where M and are the gas mixture molecular weight, and the mixture-average diffusion coefficient for species k, respectively [73, 77]. In appendix C, the the Navier-Stokes characteristic boundary conditions are also tested through a two-dimensional single vortex test case and a three-dimensional spherical pressure wave test case.

5.3.1 Spatially developing non-reacting round jet

Direct numerical simulation of spatially developing non-reacting round jet with Reynolds number 4700 was carried out. The simulation was performed in a Cartesian mesh with $768 \times 576 \times 576$ grid points in the axial, and two lateral directions, respectively. The physical domain size is $Lx = 21D$, $Ly = Lz = 14D$, where D is the jet diameter. A hyperbolic tangent velocity profile was specified at the inlet:

$$u_{in} = \frac{U_1 + U_2}{2} + \frac{U_1 - U_2}{2} tanh(\frac{r}{2\theta}) \tag{5.7}$$

where U_1, U_2, r and $\theta = 0.05D$ are the jet velocity, coflow velocity, radius, and momentum thickness. The coflow velocity was set to be 5% of the value of inlet jet velocity. The convective Mach number and CFL number was set to be 0.3, and 0.15, respectively. To achieve fast transition to turbulence, synthesized isotropic turbulence was added to the inlet velocity [78]. The root mean square magnitude of the disturbance was set to be 1% of the mean velocity at the inlet boundary. The simulation was performed for 20 convective time scales ($\frac{L_x}{U_1+U_2}$). After two convective time scales, sampling are started for calculating statistics.

Fig. 5.1 shows the instantaneous image of the vorticity magnitude. In the region of $x/D < 3$ the flow is almost laminar. Further downstream, the coherent vortex start to roll up, merge and then breakup due to three-dimensional instability. After $x/D \approx 7$, the jet potential core ends and the flow becomes fully turbulent. Fig. 5.2 shows some one point velocity statistics from current simulation which are compared with experimental and numerical results from Wygnanski and Fiedler [79] (WF), Hussein et al.[80] (HCG), Panchapakesan and Lumley [81] (PL), and DNS data from Picano and Casciola [82] (PC), Boersma et al. [83] (BBN) and Wang et al. [84] (Wang). All of these experimental data are measured in the self-similar

region of the jet.

Figure 5.2a shows the centerline mean velocity. For a self-similar round jet, it can be modeled as

$$U_m = \frac{U_1 - U_2}{\Delta U_c} = \frac{1}{B_u}(\frac{x}{d} - \frac{x_o}{d}) \tag{5.8}$$

where B_u is a constant for centerline velocity decay rate, ΔU_c is the centerline mean velocity excess the local coflow, x_o is the virtual origin of the jet. The constant of B_u for centerline velocity decay rate here is 5.9, Hussein et al. obtained 5.8, Wygnanski et al. obtained 5.4, Panchapakesan et al. obtained 6.06 and Wang et al. obtained 5.5, Boersma et al. obtained 5.9 which is the same value obtained here. In the present simulation the distance of virtual original of the jet is kind of smaller than the value in Wang et al. [84] which might be caused by the different method for generating inlet disturbance. It turns out that the digital filtering technique [85] used in Wang et al. [84] gives a slightly faster transition to turbulence.

Figures 5.3b-d show the axial, radial and azimuthal Reynolds stress profiles across the jet near $x/D = 18D$ where the flow is not affected by the boundary and the turbulent flow field are resolved more sufficiently. Although the curves from present simulation are not smooth enough, all the Reynolds stress profiles show reasonably good agreement with previous results which validate the current DNS code. The

discrepancy between them might be caused by short sampling time.

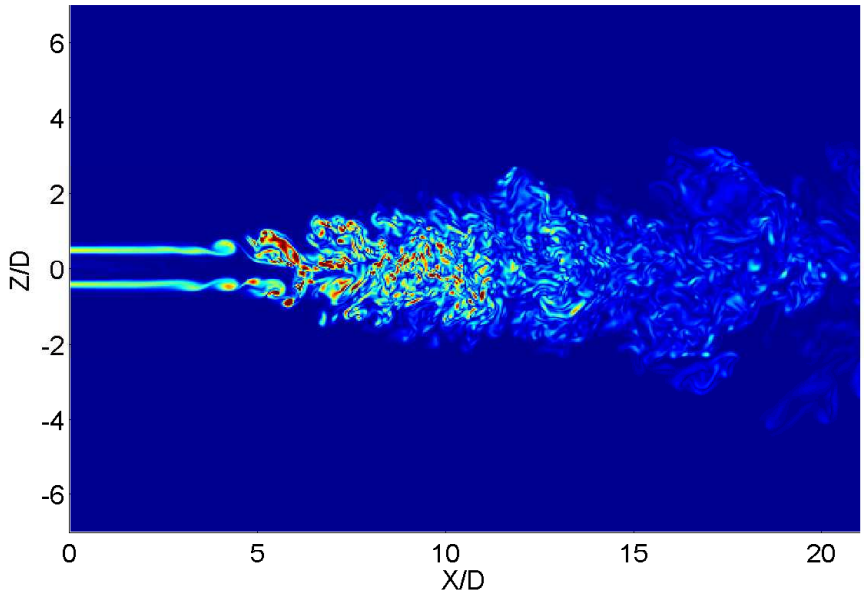

Figure 5.1: Instantaneous contour plot of vorticity magnitude at plane y=0

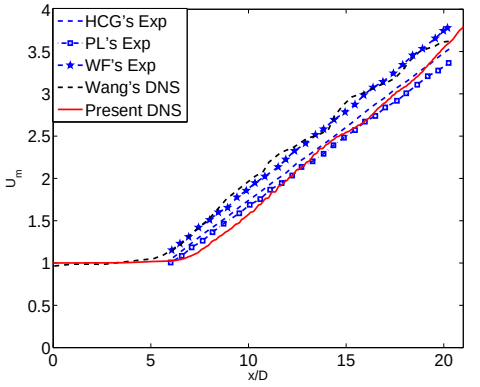

(a)

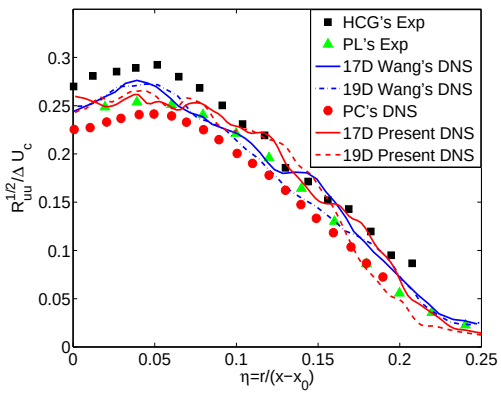

(b)

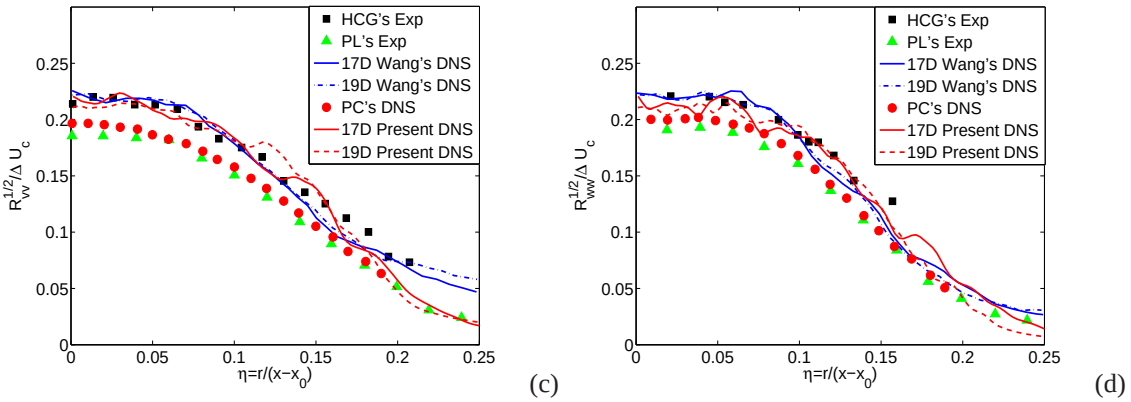

Figure 5.2: Present DNS compared to previous experimental and DNS results: (a) Axial mean velocity variation along the jet centerline, (b) axial Reynolds stress, (c) Radial Reynolds stress, and (d) Azimuthal Reynolds stress profiles across the jet.

5.3.2 Temporally developing non-reacting plane jet

Numerical simulation of spatially developing jets can be very expensive both in terms of computational time and memory due to the large computational domain. Instead, a temporal simulation of a plane jet can be used to limit the computational cost. In the current test case, a temporally developing non-reacting plane jet with Reynolds number 4700 was simulated. The domain size of the computational box is $Lx = 6H$, $Ly = 7H$, $Lz = 4H$, where H is the plane jet width. The grid number in each direction is $Nx = 432$, $Ny = 504$, $Nz = 288$. The DNS was started by using a hyperbolic-tangent velocity profile with isotropic turbulent velocity fluctuations superimposed on the mean field and filtered outside of the jet. The turbulence intensity is 5% of the initial velocity difference between the central stream and the surrounding flow. The flow is periodic in the streamwise and spanwise direction, while non-reflecting outflow boundary conditions are set in the cross-stream condition. The self-similar regime is obtained at 20 jet times. The statistics were calculated from a single instantaneous field where spatial averaging was taken in the two homogenous directions (x and z). Figure 5.3 shows the one point statistics at the self-similar region from present DNS at 20 jet times compared to previous experimental from Gutmark Wagnansky [86], Ramparian and Chandrasekhara [87], Thomas and Prakash [88],and the DNSs results from Stanley et al. [89], da Silva et al. [90, 91, 92]. Although there is some scatter between the experiment and simulations, the mean streamwise velocity and Reynolds stress profiles form the present DNS agree with the data available very well which again validate the current

DNS code.

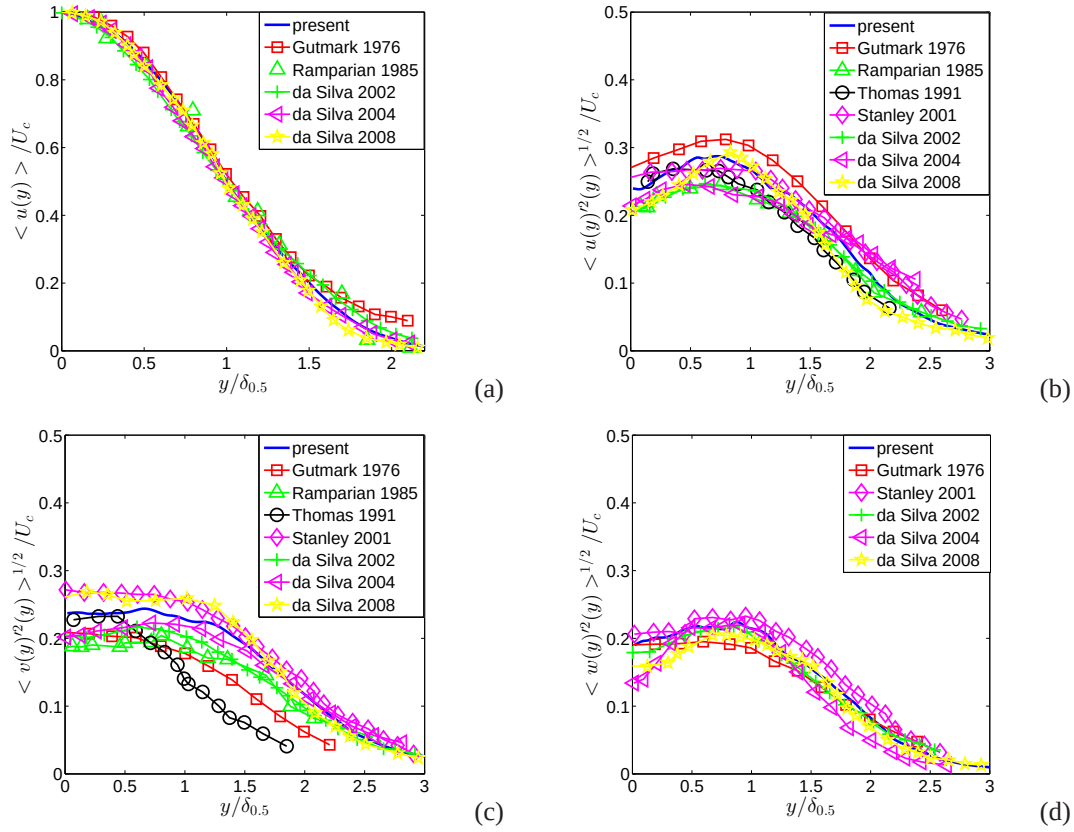

Figure 5.3: One point statistics at the self-similar region from present DNS compared to previous experimental and DNS results: (a) Mean streamwise velocity, (b) streamwise Reynolds stress, (c) normal Reynolds stress, (d) spanwise Reynolds stress.

5.3.3 Temporally developing plane jet flame

Direct numerical simulation of turbulent temporally developing plane $CO/H2$ jet with skeletal mechanism at Reynolds number of 4478 are performed to compare with previous DNS results [77]. Figure 5.4 shows the current DNS configuration. The fuel is comprised of 50% CO, 10% H_2 and 40% O_2 by volume while the oxidizer streams comprised of 25% $O2$ and 75% $N2$. The initial temperature of both streams is set to 500K. The streamwise velocity filed is set with $\Delta U/2$ in the central fuel stream and $-\Delta U/2$ for the oxidizer stream. Hyperbolic tangent profiles are used to smooth transitions between the fuel and oxidizer. The combustion is initialized with a laminar flamelet solution at an initial scalar dissipation rate $\chi = 0.75\chi_q$ where χ_q is the extinction scalar dissipation rate. To trigger the evolution of shear-generated

turbulent, isotropic turbulent fluctuations are superimposed on the fuel stream with turbulent intensity set to be 5% of the mean velocity. The domain size of the computational box is $Lx = 12H$, $Ly = 14H$, $Lz = 8H$. The grid number in each direction is $Nx = 432$, $Ny = 504$, $Nz = 288$.

Figure 5.5a shows the scalar dissipation field at 40 jet times which are plot on a logarithmic scale to visualize its wide dynamic range. The high dissipation regions are organized into thin sheet-like structures with lengths far exceeding their thickness which consistent with the observation in [77]. The pdf of the log normalized dissipation conditional on stoichiometric mixture fraction $(log_{10}\chi_{st} - \mu_{\chi_{st}})/\sigma_{\chi_{st}}$ are plotted along with log-normal gaussian distribution in Fig. 5.5b. The χ distribution after 20 jet times is nearly log-normal, with slightly departure from the Guassian in the form of negative skewness which consistent with nonreactive measurements. Figure 5.6 shows the mean mixture fraction, mean temperature and r.m.s. of mixture fraction at 20 and 45 jet times from current DNS and compared to previous DNS from Hawkes et al. [77] and Krisman et al. [93]. There are some discrepancy of the r.m.s of mixture fraction at 45 jet times in Fig. 2.8(d) which might be due to the relative small number of samples in x-z plane and insufficient grid resolution. Overall,

the present results matches the results from Krisman et al. [93] very well.

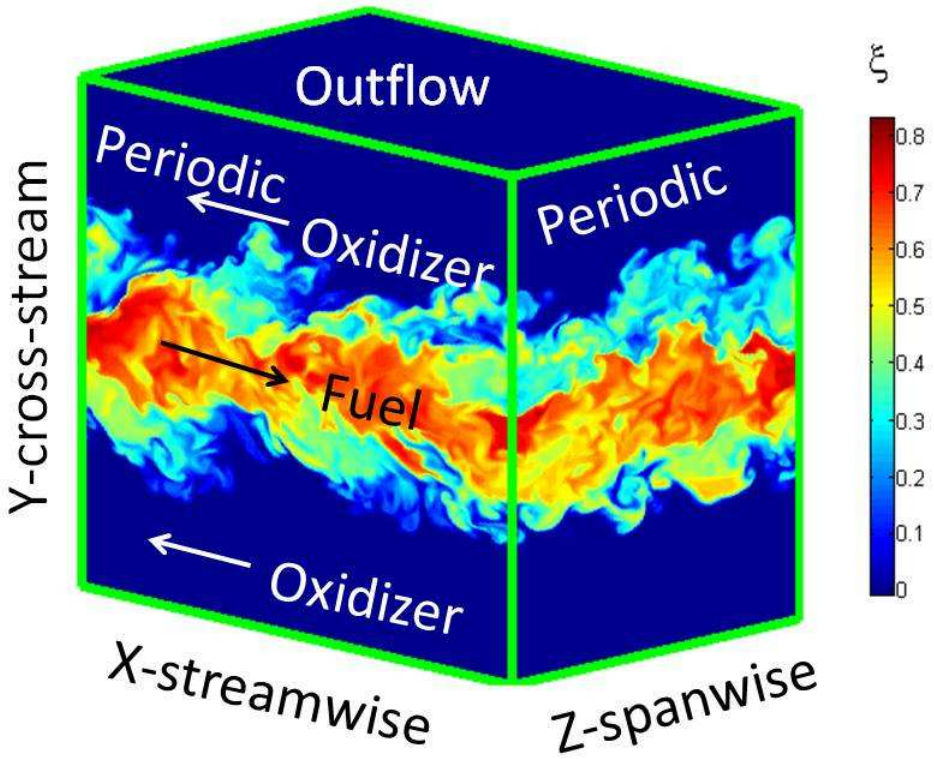

Figure 5.4: DNS configuration of temporally developing plane jet flame

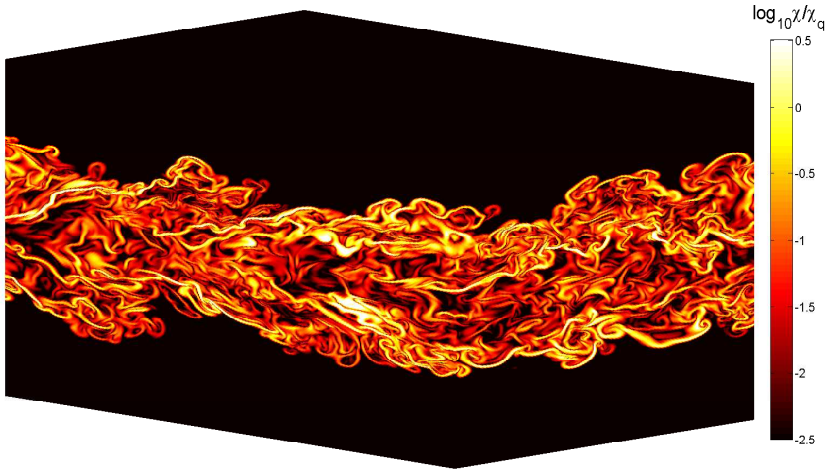

(a)

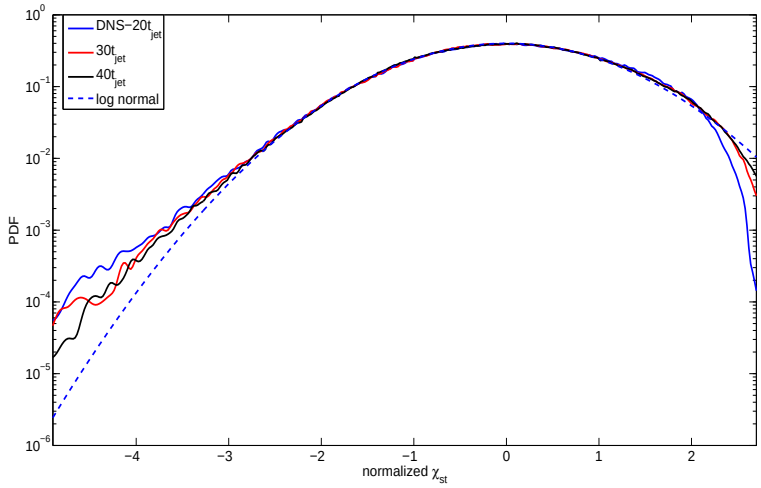

(b)

Figure 5.5: (a) Logarithm of χ/χ_q at 40 jet times in streamwise and spanwise cuts (b) Pdf of the normalized logarithm of χ at $Z = Z_{st}$.

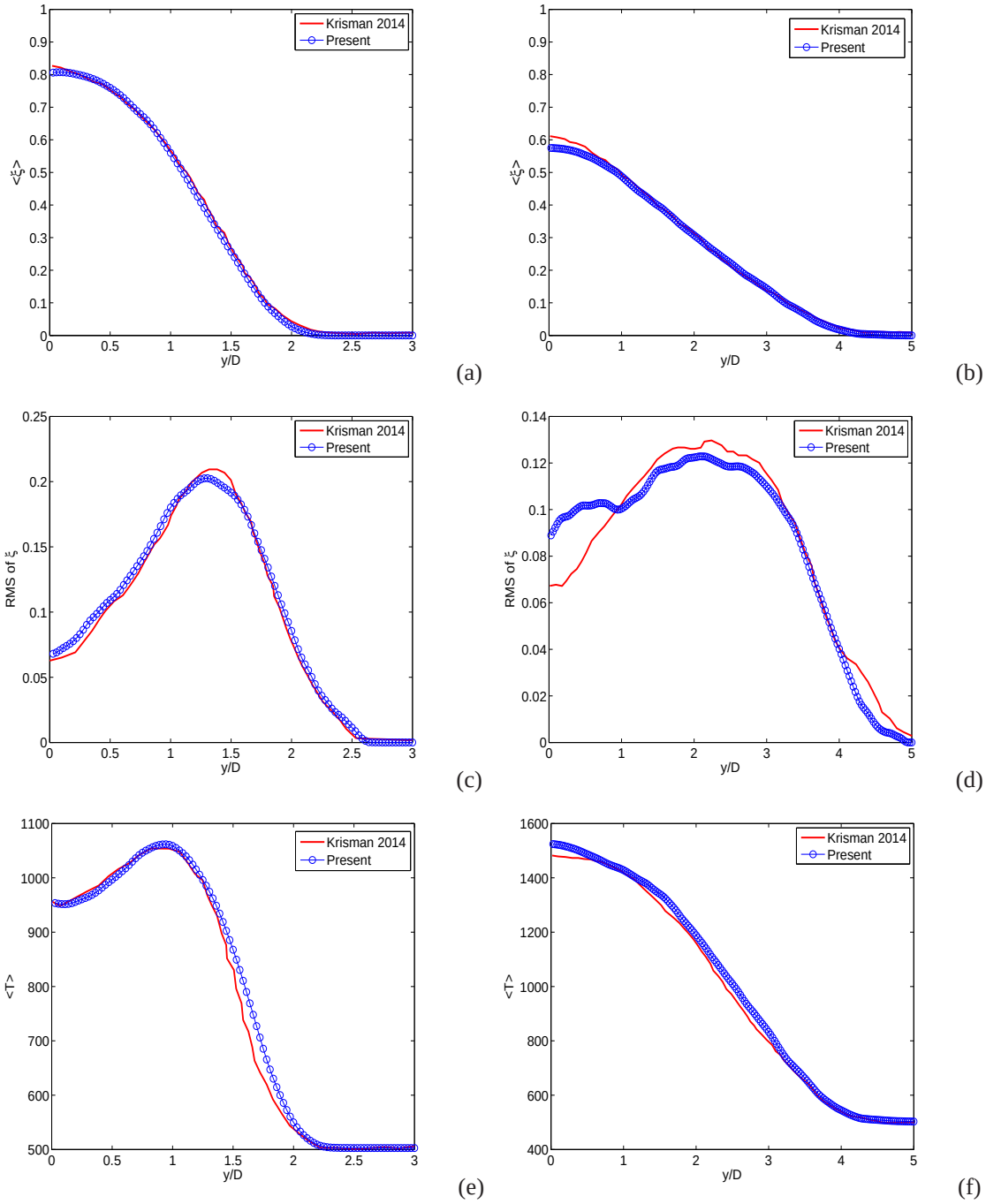

Figure 5.6: Present DNS compared to Hawkes's DNS: (a,b) mean mixture fraction, (c,d) RMS mixture fraction, (e,f) mean temperature cross-stream profiles at 20 and 40 jet times.

To conclude, in this section different test cases are simulated and the statistics from current code

show good agreement with previous experiment and DNS results. This completes the validation of the current DNS code.

5.4 DNS configuration of three scalar mixing in temporally developing plane jets

The flow configuration is a temporally developing plane jet which consists of five streams: a central jet, two off-central jets surround the central jet, and the two coflows surround the off-central jets and the mean shear is in the cross-stream direction. Figure 5.7 shows the initial profiles for the three scalars and streamwise velocity. The periodic boundary condition is implemented in the streamwise and spanwise direction while the outflow boundary condition is used in the cross-stream direction which is the same as in Fig. 5.4. This temporal configuration limits the use of very large domains which allows the study of the scalar mixing in turbulent jets with relatively high Reynolds number. Moreover, the two statistically homogeneous directions (streamwise and spanwise direction) maximize the data available for statistical analysis.

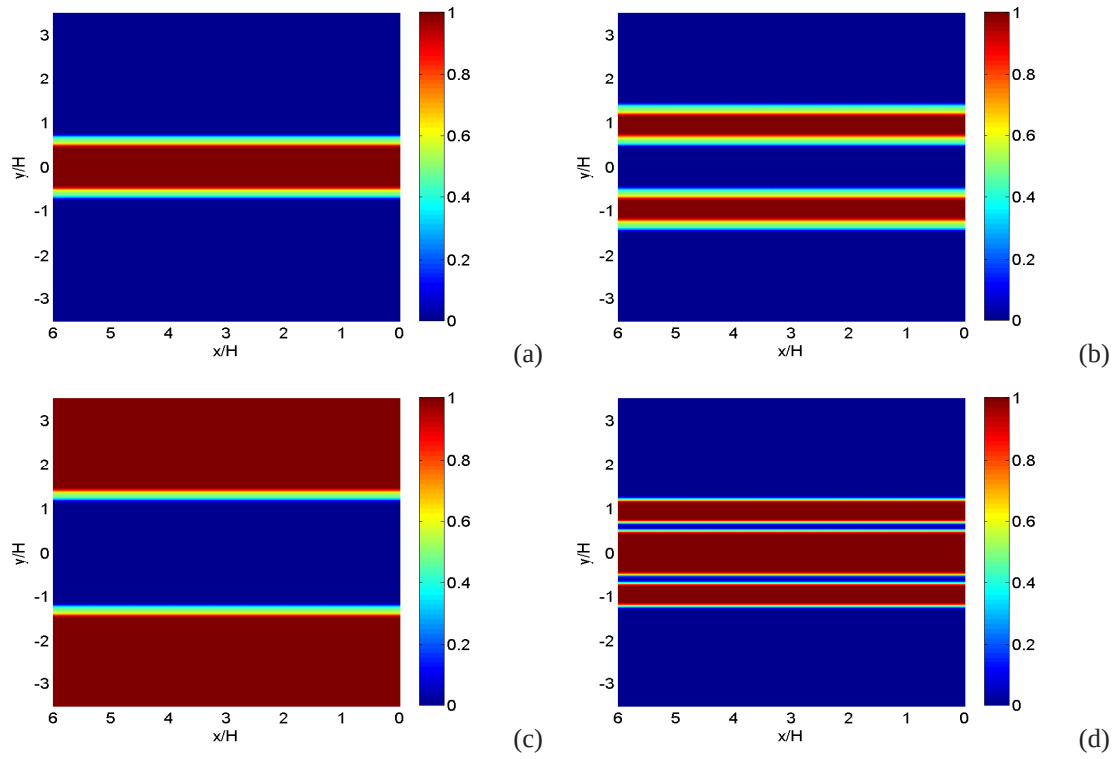

Figure 5.7: Initial profile of (a) ϕ_1 (b) ϕ_2 (c) ϕ_3 (d) normalized streamwise velocity

Re ($\Delta UH/\nu$)	10000	L_x/H	6	Nx	864	δ_U/H	0.13
Sc (ν/D)	0.7	L_y/H	7	Ny	1008	δ_ϕ/H	0.29
Ma ($\Delta U/c$)	0.3	L_z/H	4	Nz	576	$u'/\Delta U$	5%

Table 5.1: Simulation parameters of the four DNS cases.

Case number	1	2	3	4
Velocity ratio $(U_1-U_3)/(U_2-U_3)$	1.0	2.0	1.0	2.0
Length ratio $H/(2H_{off})$	1.0	1.0	0.5	0.5

Table 5.2: Velocity and length ratios between the central and off-central jet of the four parametric DNS cases.

In order to get smooth transitions between different streams, the jet walls with wall thickness ($H_w = 0.2H$) are placed between the central jet and off-central jet and between the off-central jet and coflow, where H_w and H are wall thickness and the central-jet width, respectively. Table 5.1 gives the physical and geometric parameters used in all the cases. To study the influence of the upstream conditions, we vary the velocity and length ratio between the central jet and off-central jet. Table 5.2 summarize the different flow configurations studied. *Lx*, *Ly*, and *Lz* are the domain lengths in *x*, *y* and *z* directions, respectively. The *x*, *y* and *z* correspond to the streamwise, cross-stream and spanwise direction. *Nx*, *Ny* and *Nz* are the grid numbers in *x*, *y* and *z* directions, respectively. The grid is uniform in all three directions with grid resolution $\delta x = \delta z = \delta y \approx 0.007H$. U_1, U_2, U_3 are the velocity for central jet, off-central jet, and coflow, respectively. ΔU, c are the characteristic velocity ($\Delta U = U_1 - U_3$) and speed of sound, respectively. δ_U, δ_ϕ are the initial thickness of scalar profile and velocity profile, respectively. In order to accelerate the jet development, isotropic turbulent fluctuations u' are added in the initial flow field. The jet time scale t_{jet} and reference time t_{ref} are defined as $t_{jet} = H/\Delta U$ and $t_{ref} \equiv 10\ t_{jet}$, respectively. t_{ref} will be used to normalize the scalar dissipation rate and scalar diffusion in the following section.

5.5 DNS assessment

Figure 5.8 shows the normalized planar averaged one dimensional spectra for streamwise velocity and kinetic energy dissipation at several instants for case 1. The velocity spectrum (fig.5.8a) has a -5/3 region which spans nearly two decades in the wave number space. The power law region is followed by a smooth decay at high wave numbers where the maximum resolved $k\eta$ is about 1.5, indicating the dissipative scales are being well resolved according to [23]. The dissipation spectrum shows (fig.5.8b) a peak which marks the start of the dissipation region. This is consistent with the ones obtained by [90, 94]. To further test the

resolution, figure 5.9 shows the profile of the length scale ratio between the kolmogorov scale and the grid resolution for case 1. The smallest value at several instants is approximately 0.6 which also indicates good resolution [23]. The Schmidt number ($Sc \equiv \frac{\nu}{D}$) of scalar in current simulation is set to be 0.7 which is close to unity, indicating the smallest scalar length scale (Bachelor scale) is similar to the kolmogorov scale. Hence in the current DNS simulations, all the scalar length scales are also resolved. These results indicate that the present turbulent plane jet simulations are accurate for both large and small scales.

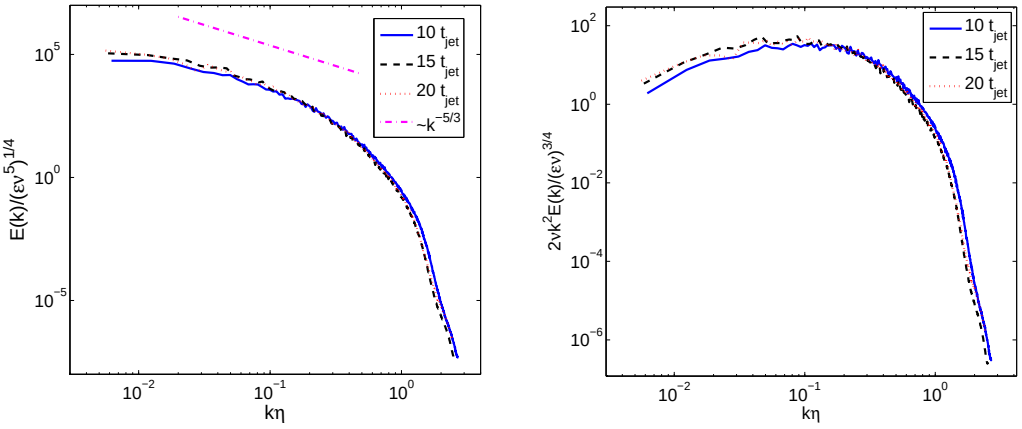

Figure 5.8: One dimensional spectra for (a) streamwise velocity (b) turbulent kinetic energy dissipation for case 1.

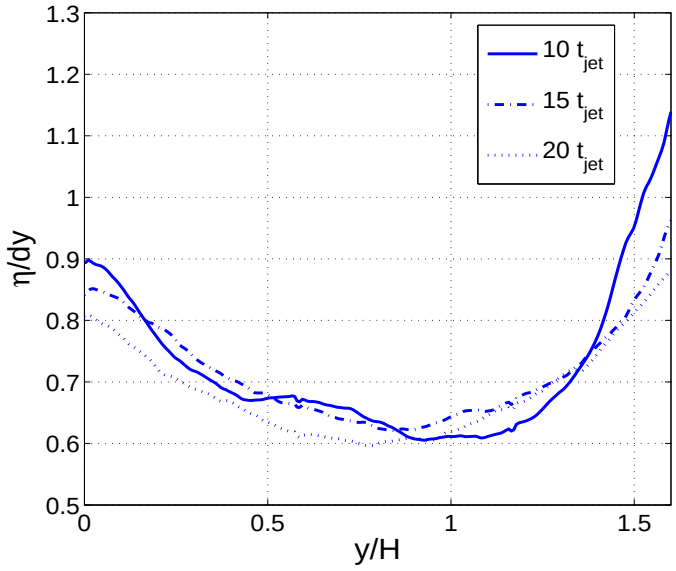

Figure 5.9: Length ratio between Kolmorogov scale ($\eta = (\nu^3/\varepsilon)^{1/4}$) and grid resolution for case 1.

5.6 Time evolution at the jet center plane (y=0)

Figure 5.10 shows the time evolution of the mean, root mean square (r.m.s) of ϕ_1 and ϕ_2 ($\left\langle \phi'^2 \right\rangle$) at $y = 0$ for case 1 and case 2. These statistics generally didn't change until $5t_{jet}$. The shear layers develop rather quickly after $5t_{jet}$ and the r.m.s of ϕ_1 and ϕ_2 are similar before 12 jet times, indicating no co-flow present on the center plane, i.e. $\phi_1 + \phi_2 \approx 1$. After 12 jet times, σ_1 and σ_2 gradually differ from each other, suggesting co-flow starts to reach the center plane. The fluctuation intensities at the center plane, $\sigma_1/\langle\phi_1\rangle$ and $\sigma_2/\langle\phi_2\rangle$ are showed in fig. 5.11. $\sigma_1/\langle\phi_1\rangle$ rises rapidly due to the increase of σ_1 as well as the decrease of $\langle\phi_1\rangle$, while $\sigma_2/\langle\phi_2\rangle$ drops rapidly due to the increase of $\langle\phi_2\rangle$. After 12 jet times, the $\sigma_2/\langle\phi_2\rangle$ profiles for all the cases overlap indicating a self-similar sate of ϕ_2.

The mean and r.m.s. value of the scalars measure the evolution of the individual scalar, but not the extent of mixing between three scalars. The correlation coefficient, $\rho = \left\langle \phi_1' \phi_2' \right\rangle / (\sigma_1 \sigma_2)$ can characterize the extent of mixing. The correlation coefficient between ϕ_1 and ϕ_2 would be negative 1 in the absence of co-flow ϕ_3. In fig 5.12a, before 12 jet times, ρ is close to negative one. After that ρ increases but still remain negative value (-0.9) at 20 t_{jet}. Another measure of extent of mixing between ϕ_1 and ϕ_2 is the segregation parameter, $\alpha = \left\langle \phi_1' \phi_2' \right\rangle / (\langle\phi_1\rangle \langle\phi_2\rangle)$. When ϕ_1 and ϕ_2 don't mixing with each other at all, $\alpha = -1$. The evolution of alpha is in 5.12b. It drops rapidly after $5t_{jet}$ due to the negative $\left\langle \phi_1' \phi_2' \right\rangle$ and very small value of $< \phi_2 >$. After $5t_{jet}$, α increases slowly due to the increase of $\langle\phi_2\rangle$.

Figure 5.13 shows the evolution of the scalar JPDF of ϕ_1 and ϕ_2 at the jet center plane for case 1. The JPDF should be confined to a triangle domain in the $\phi_1 - \phi_2$ sample space with vertices at (0, 0), (0, 1) and (1, 0) which corresponds to pure co-flow, pure center jet and pure off-central jet, respectively. At 10 t_{jet}, the JPDF are large concentrated along the mixing line connecting (0, 1) and (1, 0). As the jet developed further to 15 t_{jet} , the co-flow is present on the center plane, bending the JPDF towards (0, 0). After 30 t_{jet}, ϕ_1 and ϕ_2 are largely confined within 0.3 and 0.4, indicating the two scalars are well mixed, and the mixing becomes binary again, i.e., mixing between ϕ_3 and the mixture of ϕ_1 and ϕ_2. The JPDF evolution at the jet center plane shows that the most unique mixing of the scalars occur before 30 jet times, which shows the properties of both binary mixing and multi-scalar mixing. This is consistent with [50], in which they found the unique mixing occurs at the near field corresponding the early jet times for the temporally developing jet.

Figure 5.14 shows the central jet convection distance defined as $\int_0^t U_c dt$ where U_c is the mean center plane streamwise velocity. At 10 and 20 jet times, the convection distances are about 4.92H and 8.5H, respectively. Since the most unique part of three-scalar mixing of axial jet is the near field [50], we focus on

the results at 10 and 20 t_{jet} at which the turbulent jet is well developed and the convection distance is less than 10H.

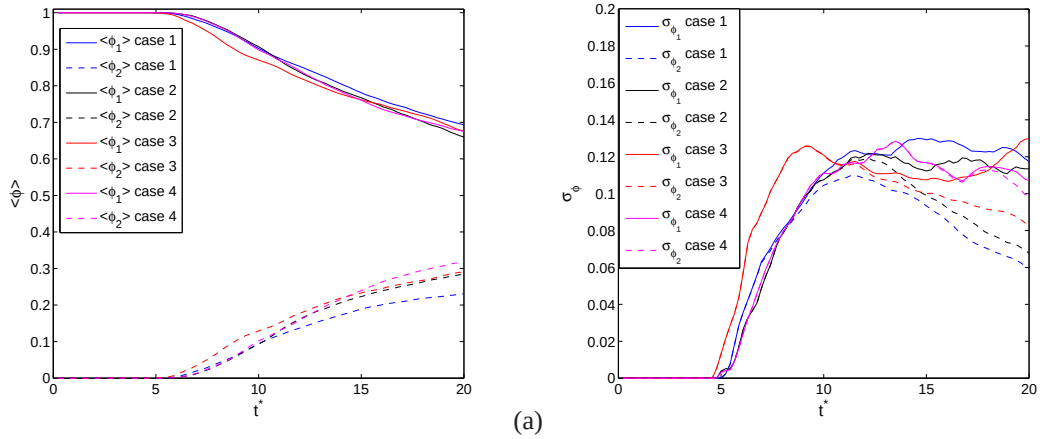

(a) (b)

Figure 5.10: Evolution of (a)mean, (b) std of ϕ_1 and ϕ_2 at center plane for case 1 and case 2.

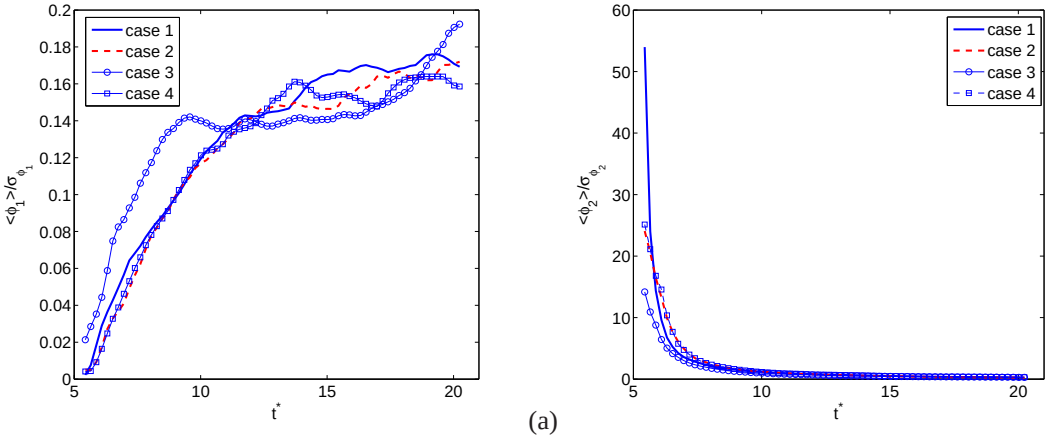

(a) (b)

Figure 5.11: Evolution of fluctuation intensity of (a) ϕ_1 and (b) ϕ_2 at center plane for case 1 and case 2.

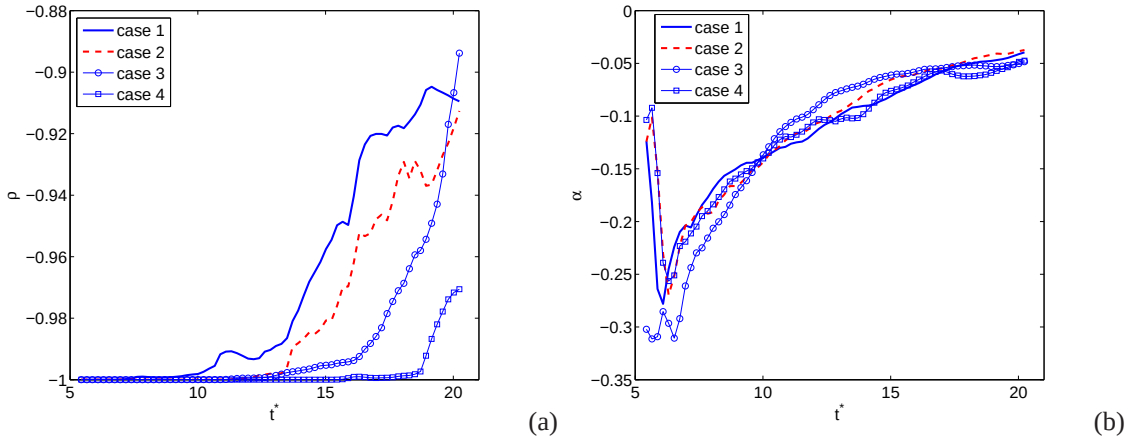

(a) (b)

Figure 5.12: Evolution of (a)correlation coefficient, (b)segregation parameter between (a)ϕ_1 and (b)ϕ_2 at center plane for case 1 and case 2.

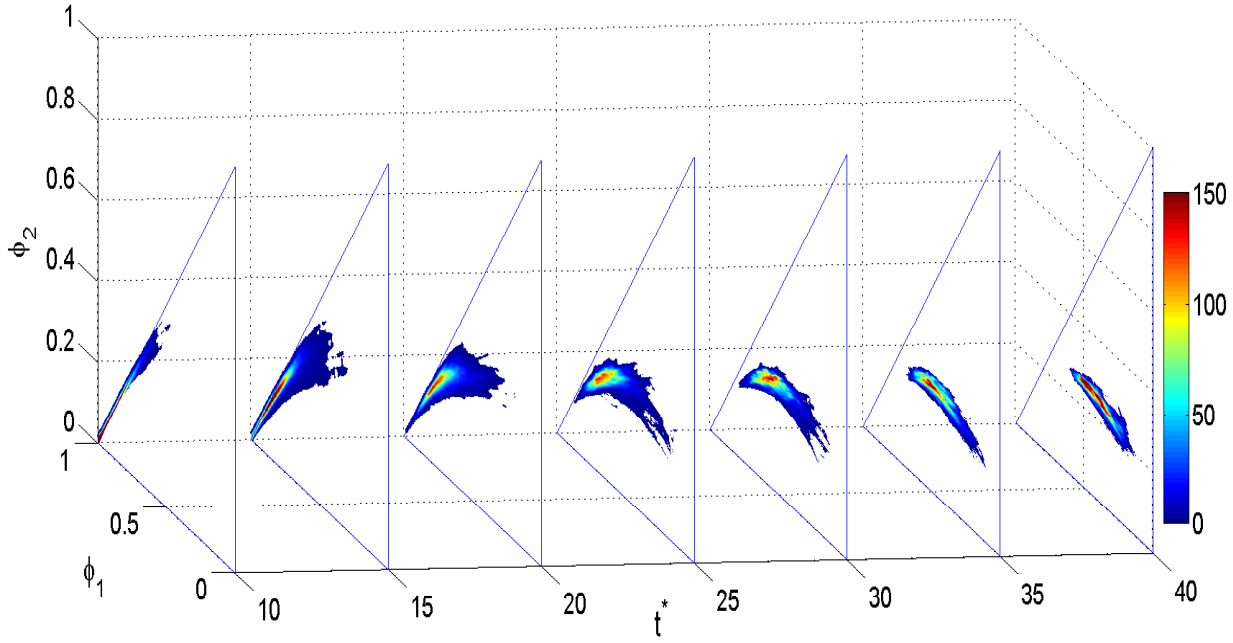

Figure 5.13: Evolution of JPDF of ϕ_1 and ϕ_2 at center plane for case 1

.

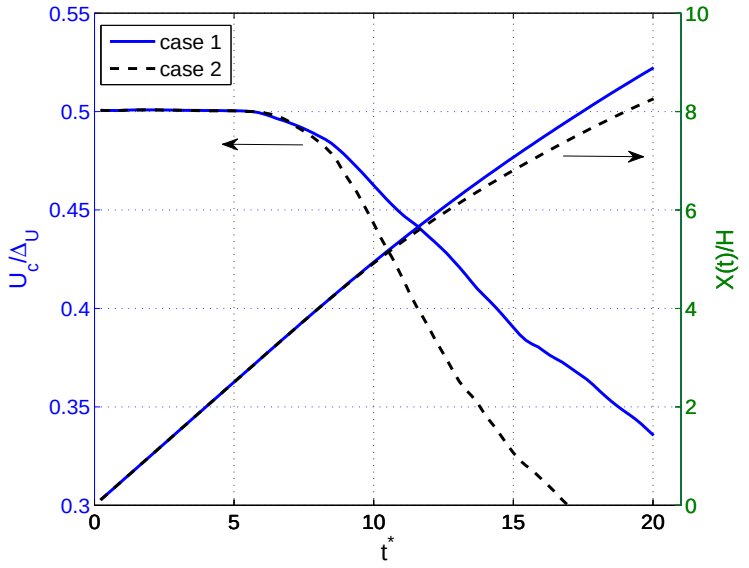

Figure 5.14: Evolution of streamwise velocity and convection distance at center plane for case 1 and case 2.

5.7 Cross-stream profile

The mean profiles of ϕ_1 and ϕ_2 at 10 t_{jet} and 20 t_{jet} are shown in figure 5.15. At 10 t_{jet}, the profiles of $\langle\phi_1\rangle$ for all the cases are very similar. The peak $\langle\phi_1\rangle$ is approximately 0.88 at the center plane. The profiles of $\langle\phi_2\rangle$ have off-central peaks. Near the center plane ($y/H < 0.5$), $\langle\phi_2\rangle$ profiles for all the cases are nearly identical. Away from the center plane ($y/H > 0.5$), the $\langle\phi_2\rangle$ profiles for different cases start to differ from each other with case 4 has the largest peak value and case 1 has the smallest peak value. At 20 t_{jet} , the non-zero parts of $\langle\phi_1\rangle$ and $\langle\phi_2\rangle$ (fig.5.15b) extend to large y/H as the jet spreads. $\langle\phi_1\rangle$ profiles are still similar for all the cases with the peak value decreases to 0.78 at the center plane, while $\langle\phi_2\rangle$ profiles start to differ from different cases. The mean profiles indicate that the velocity and length ratio between the central and off-central jet have more influence on the mixing of ϕ_2 than that of ϕ_1.

The profiles of the r.m.s. of ϕ_1 (σ_1) for all the cases (figs. 5.16a&b) show an off-central peak. The peak position is close to $y/H = 0.65$ for case 1 and 3, and $y/H = 0.75$ for case 1 and 3 at 10 t_{jet}. With the jet further developed the peak σ_1 for case 1, 2, and 3 decreases significantly, while the peak value for case 4 slightly increases. Because of larger off-central jet velocity for case 1 and 3, the inward velocity fluctuations that bring the ϕ_2 to the center plane is probably larger than the velocity fluctuations that bring ϕ_1 away from

the center which results in the peak σ_1 shift to the center. For case 2 and 4, the velocity fluctuations in the ϕ_2 stream is small, the velocity fluctuations in ϕ_1 stream generally take ϕ_1 out of the center, which results in the peak σ_1 move towards ϕ_2 stream. On the jet center plane, the mean shear vanishes which results in zero production of the scalar variance; therefore the mean advection and turbulent transport are responsible for the non-zero r.m.s values and generally the turbulent transport of scalar variance (figs. 5.18a&b) is much greater than the mean advection (not shown).

The r.m.s. profiles of ϕ_2 (σ_2) (fig 5.16c&d) generally has two off-central peaks located at each side of the maximum of $\langle\phi_2\rangle$ at 10 t_{jet}. This reflects the domination contribution of production of the scalar variance. The minimum point between the peaks is approximately at the location of maximum value of the mean profile where the production is zero. With the jet further developed (20 t_{jet}), the peak closer to the center plane almost vanishes for the all cases which might be due to the zero production of the variance and non-zero scalar dissipation rate of ϕ_2. The peak σ_2 for case 4 is significant larger than the value for other cases. At this time instant, ϕ_2 is relatively well mixed for case 1, 2, and 3, and σ_2 decays with time. However, because of the lower velocity and large width of the off-central jet in case 4, the development of the shear layer between the off-central jet and co-flow is not as quick as other cases. At 20 jet times, the shear layer for case 4 is fully developed and σ_2 near $y/H = 1.5$ still does not decay at this time instant.

Figure 5.17 shows the fluctuation intensity profiles for ϕ_1 and ϕ_2. $\sigma_1/\langle\phi_1\rangle$ generally increases with y/H. For $y/H < 0.7$, $\sigma_1/\langle\phi_1\rangle$ increases slowly with y/H and the profiles for all the cases are similar. Beyond $y/H = 0.7$, $\sigma_1/\langle\phi_1\rangle$ increases rapidly for case 2 and 4 due to the small value of $\langle\phi_1\rangle$, while the value for $y/H < 1$ slightly decrease with y/H at 10 t_{jet} (fig. 5.17c). Beyond $y/H < 1$, $\sigma_2/\langle\phi_2\rangle$ increases with y/H. With the jet further developed, $\sigma_2/\langle\phi_2\rangle$ almost remains the same for $y/H < 1$ (fig. 5.17d). For $y/H > 1$, $\sigma_2/\langle\phi_2\rangle$ increase greatly with y/H, suggesting the higher intensity of the mixing process.

The normalized turbulent transport ($-\frac{\partial\left\langle v'\phi'^2\right\rangle}{\partial y}$) and production rate of scalar variance ($-2\left\langle v'\phi\right\rangle\frac{\partial\langle\phi\rangle}{\partial y}$) are shown in figure 5.17 and 5.18, where v' are the fluctuating velocity in the cross-stream direction. The derivative with respect to x and z vanishes because streamwise and spanwise are homogeneous directions. The mean advection and diffusion of scalar variance are very small compare to production rate hence are not shown. The turbulent transport for $\left\langle\phi_1'^2\right\rangle$ generally have a negative minimum value near the location of peak $\left\langle\phi_1'^2\right\rangle$ (figs. 5.18a&b) where the production rate has a positive maximum value. The ratio of peak magnitude between the production and turbulent transport of $\left\langle\phi_1'^2\right\rangle$ is greater than two, indicating the dominant contribution of variance budget comes from the production rate. The turbulent transport of $\left\langle\phi_2'^2\right\rangle$ generally has local minimum values located near the peak $\left\langle\phi_2'^2\right\rangle$ (figs. 5.18c&d) as well as local maximum values near the

minimum value of $\left\langle \phi_2'^2 \right\rangle$. The production rate of the variance of ϕ_2 generally have two peaks near the two edges of the shear layer. At 10 t_{jet}, the magnitude of the two peaks are comparable while at 20 t_{jet}, the peak located at $y/H > 1$ has a larger magnitude than that of the peak at $y/H < 1$, indicating the mixing between the off-central jet and coflow is more intense than that between the central jet and off-central jet.

The profiles of covariance between ϕ_1 and ϕ_2 are showed in figure 5.20. $\left\langle \phi_1' \phi_2' \right\rangle$ are largely negative for case 4 at 10 t_{jet}, while positive $\left\langle \phi_1' \phi_2' \right\rangle$ are found for other cases. The absolute value of the negative peak is much larger than the value of the positive peak, indicating more strong mixing between central and off-central jet than those between off-central jet and coflow at this time instant. The y/H value corresponding for the starting point of positive $\left\langle \phi_1' \phi_2' \right\rangle$ are 0.886, 1.039, 1.039 for case 1, 2, and 3 respectively. In the absence of co-flow, ϕ_1 and ϕ_2 sum up to unity such that the increase of ϕ_2 leads to the decrease of ϕ_1 by the same amount, resulting in negative covariance. So the positive covariance indicate the existence of ϕ_3. With the jet further developed, $\left\langle \phi_1' \phi_2' \right\rangle$ shows positive value for all the cases (fig. 5.20b).

The cross-stream profiles of correlation coefficient ρ between ϕ_1 and ϕ_2 shows a similar trend (fig. 5.21). At 10 t_{jet} and small y/H, the correlation coefficient is close to negative 1 where there is no ϕ_3 and the mixing in essentially binary (between ϕ_1 and ϕ_2). Beyond certain y/H, the correlation start to increase due to the present of ϕ_3. The corresponding y/H values for the correlation to reach 0.9 are 0.49, 0.69, 0.69, and 0.96 for case 1, 2, 3, and 4, respectively. At $y/H = 1.5$, the correlation coefficient for case 4 is close to zero while the value for other cases is greater than 0.3 which indicate the mixing between the coflow and the off-central jet is much weaker for case 4 than those for other cases (fig 5.21a). With the jet further developed, the difference between correlation coefficient for different cases becomes small (fig. 5.21b). Beyond $y/H = 2$, the correlation coefficient approaches unity where the coflow is mixed with the mixture of ϕ_1 and ϕ_2. Because the fluid carry ϕ_1 and ϕ_2 from center to the coflow side, the structure for ϕ_1 and ϕ_2 away from the center is very similar, resulting in large positive correlation.

The profiles of the segregation parameter α between ϕ_1 and ϕ_2 are shown in figure 5.22. The profiles generally have a small negative value for small y/H due to the negative correlation between ϕ_1 and ϕ_2. For large y/H, α become positive because of the positive correlation and high scalar fluctuation intensity. To clearly illustrate the trend near the center plane, figures 5.22c&d show the α profiles for $y/H < 1.2$. The α profile first decreases with y/H for case 2 and 4 at 10 t_{jet} due to the more negative value of covariance between ϕ_1 and ϕ_2. At 20 t_{jet}, the profile of α also decreases with the increase of y/H for case 4, indicating the mixing rate of ϕ_2 is less than the value for other cases.

The mean scalar dissipation rate ($\langle \chi_1 \rangle$, $\langle \chi_2 \rangle$) and the mean cross-dissipation rate ($\langle \chi_{12} \rangle$) normalized

by the jet reference time ($t_{ref} \equiv 10 t_{jet}$) are shown in figure 5.23. The dissipation rate for ϕ_1 (figs. 5.23a&b) generally has one peak value located at the position corresponding to the peak r.m.s of ϕ_1. The dissipation rate profiles would be expected to be similar to the scalar variance profile if the time scale for the spectral transfer of the scalar variance is constant and there is no turbulent transport for scalar dissipation. At 20 t_{jet}, the ratio of the peak χ_1 to the center plane $\langle \chi_1 \rangle$ is 2.46, 1.97, 1.84, and 3.30 for the four cases, respectively. The corresponding peak to center plane ϕ_1 variance is 2.2, 2.48, 2.39, and 4.42, respectively. Although the peak to center plane dissipation and variance ratios are different, they are comparable, suggesting the time scale for spectral transfer varies across the jet does not vary too much.

The mean dissipation rate for $\langle \chi_2 \rangle$ has two peaks at 10 t_{jet} (fig. 5.23c). For case 1 and case 3, the peak value of χ_2 located at $y/H > 1$ is greater than the peak value located at $y/H < 1$, indicating the mixing of ϕ_2 is more intense between the off-central jet and the co-flow. While for case 2 and 4 the mixing of ϕ_2 is more intense between the central jet and off-central jet. With the jet further developed, $\langle \chi_2 \rangle$ generally has one peak in the coflow side (fig. 5.23d) and the peak $\langle \chi_2 \rangle$ of case 4 is much larger than the value for other cases, suggesting strong mixing between off-central jet and coflow and relatively well mixing between central jet and off-central jet.

The cross dissipation $\langle \chi_{12} \rangle$ profiles are very similar to the profiles of covariance (fig. 5.23e&f). $\langle \chi_{12} \rangle$ is generally negative on the jet center plane. Away from the central plane, the magnitude increase and reach a maximum before decreasing. At 10 t_{jet}, much of the $\langle \chi_{12} \rangle$ is negative for all the cases, indicating the binary mixing nature of ϕ_1 and ϕ_2. With the jet further developed, the y/H value for positive $\langle \chi_{12} \rangle$ extends which is due to present of ϕ_3.

Figure 5.24 shows the scalar mixing time scale ($\left\langle \phi'^2 \right\rangle / \langle \chi \rangle$) normalized by the jet reference time. Generally the mixing time scales for ϕ_1 and ϕ_2 are comparable. The peak value of the mixing time scale for ϕ_2 are slightly larger than those for ϕ_1 indicating the mixing rate is a little higher for ϕ_1. This trend is different from the results in [62], possibly due to the different jet geometry and influence of noise in Rayleigh scattering. In their experiment, around jet instead of slot jet was used.

Figures 5.25-5.27 show the instantaneous contour plot of ϕ_1, ϕ_2, ϕ_3 at 10 t_{jet} at the plane $z/H = 2$. Near the center plane ($y/H = 0$), the distribution of ϕ_1 is similar for all the cases (fig. 5.25). Away from the center plane, ϕ_1 extends to more regions for case 1 and case 3 compare to that of case 2 and case 4, indicating the high velocity ratio between central and off-central jet generally results in high rate of mixing of ϕ_1. This is also true for ϕ_2 with ϕ_2 level much smaller for case 1 and 3 than that of case 2 and 4. Especially for case 4, near the outside edge of the off-central jet, there have many regions with pure ϕ_2, indicating the mixing rate

of the co-flow and off-central jet is very small (fig 5.26). This can also been observed by figure 5.27. At the coflow edge, there are more fine structures for case 1 and 3 than that for case 2 and 4. Compare between case 1 and 3, the ϕ_2 level is slightly smaller for case 1. This is because reducing the width of off-central jet will result in reducing the initial length scale of ϕ_2, hence increasing the mixing rate of ϕ_2.

The instantaneous contour plot of the cross dissipation rate ($\chi_{12},\ \chi_{13},\ \chi_{23}$) at 10 t_{jet} are shown in figures 5.28-5.30. To visualize its large dynamics range, we show the normalized log scale of cross dissipation rate, i.e. $log(|\chi_{12}|t_{ref}+1)\times sign(\chi_{12})$. Plus one is used to make the small dissipation regions show zero level in the figure. The figure shows that the high cross-dissipation regions are generally organized into very thin sheet-like structures with lengths far exceeding their thickness. For case 1 and case 2, negative cross-dissipation with high magnitude largely occur between the central jet and off-central jet region indicating binary mixing between ϕ_1 and ϕ_2, while the large positive cross-dissipation appears at the off-central jet edge. For case 3, the positive χ_{12} region is very limited, while for case 4 almost all the χ_{12} is positive. For cross-dissipation rate χ_{13}, the value is almost negative with regions of high magnitude located at the shear layer between off-central jet and coflow. For case 4, χ_{13} is near zero for all the region which indicate no mixing between ϕ_1 and ϕ_3. The contour of χ_{23} are also consistent with χ_{12} and χ_{13} (fig. 5.30). It generally have large negative value near the ϕ_2 and ϕ_3 shear layer towards the co-flow and large positive value towards the center plane due to the present of ϕ_1. For case 1, there are more positive χ_{23} regions than other cases, indicating the high mixing rate between ϕ_3 and the mixture of ϕ_1 and ϕ_2. For case 4, the positive χ_{23} region is very limited, indicating binary mixing between ϕ_2 and ϕ_3.

The instantaneous contour plot of scalar and scalar cross-dissipation rate at 20 t_{jet} are shown in figures 5.31-5.36. The ϕ_1 distribution is similar for all the cases (fig. 5.31) while there are some difference for ϕ_2 distribution. For case 1 and case 2, ϕ_2 is relatively well mixed while for case 3 and case 4 there still have large regions with high ϕ_2 level. Notice that, at 10 t_{jet} ϕ_2 is less well mixed for case 2 than that for case 3. It seems the relative large initial length scale of ϕ_2 in case 3 can still affect the mixing rate of ϕ_2 in the later stage. Figure 5.33 shows that ϕ_3 extends to the center plane for case 1 and 2, while for case 3 and 4 there is still no co-flow near the center plane. The contour of cross-dissipation χ_{12} (fig 5.34) is similar for all the cases with negative value located at $y/H<1$ and positive value near the out edge of the off-central jet. High negative of χ_{13} (fig 5.35) has extends to the center plane for case 1, 2 and 3 which indicates the regions of mixing between ϕ_1 and ϕ_3. At the center plane for case 4, χ_{13} is still close to zero which is similar to χ_{23} in figure 5.36d.

In the next chapter, the scalar JPDF, the conditional diffusion, the conditional dissipation rates, and

the the conditional cross-dissipation rate for ϕ_1 and ϕ_2 at 10 and 20 jet times will be discussed in detail.

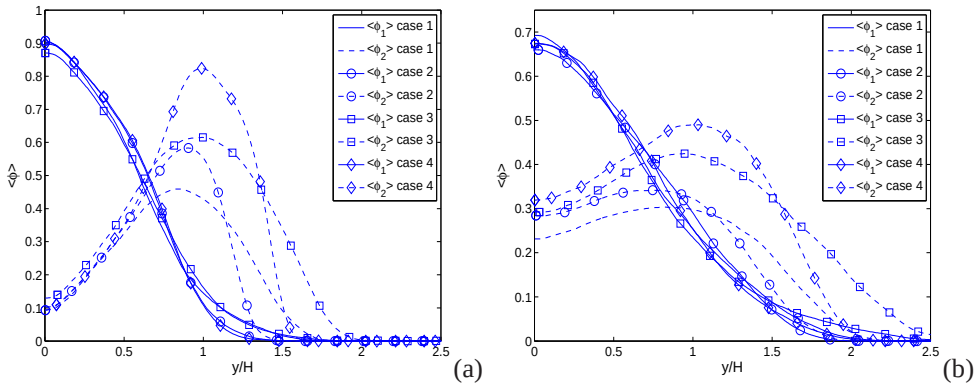

Figure 5.15: Cross-stream profiles of the mean scalars at (a) 10 t_{jet} and (b) 20 t_{jet}.

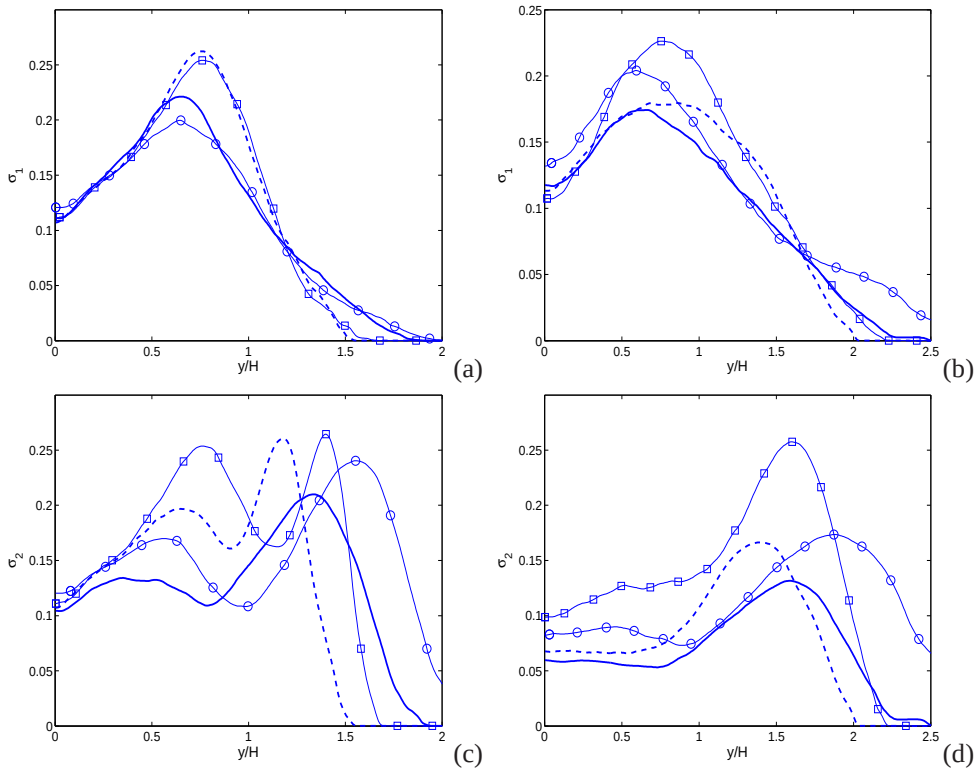

Figure 5.16: Cross-stream profiles of the r.m.s. scalar fluctuations at (a,c) 10 t_{jet} and (b,d) 20 t_{jet}. The solid line represents case 1. Dashed line represents case 2. Solid line with circle represents case 3. Solid line with square represents case 4.

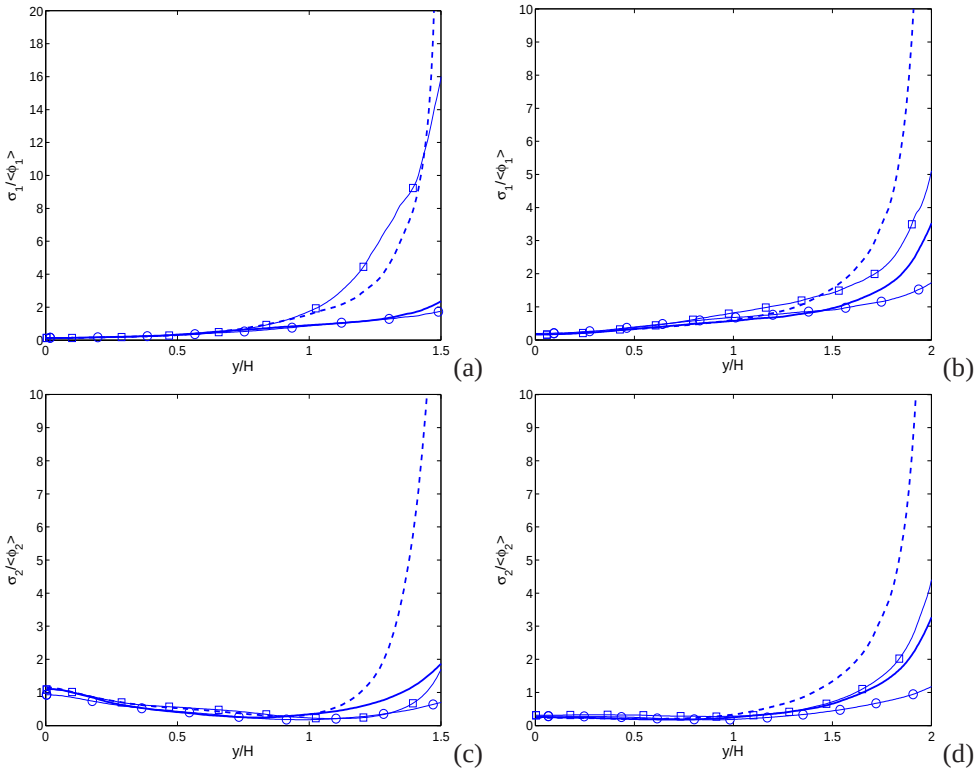

Figure 5.17: Cross-stream profiles of the fluctuation intensities at (a,c) 10 t_{jet} and (b,d) 20 t_{jet}. Symbols same as in Fig. 5.16.

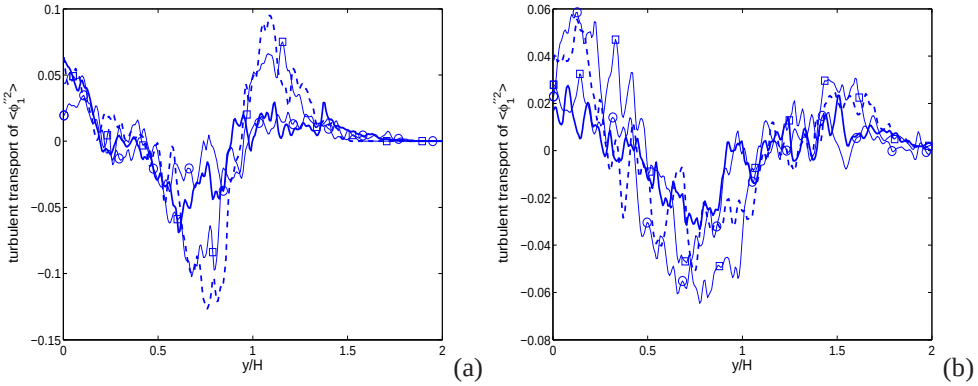

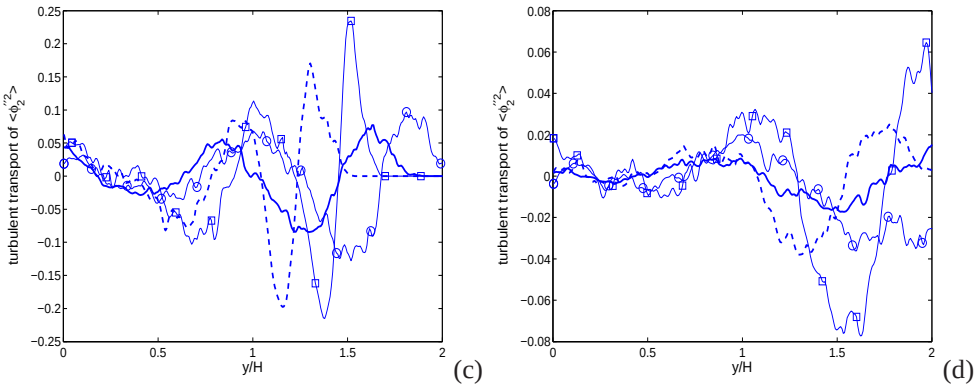

Figure 5.18: Turbulent transport of scalar variance at (a,c) 10 t_{jet} and (b,d) 20 t_{jet}. Symbols same as in Fig. 5.16.

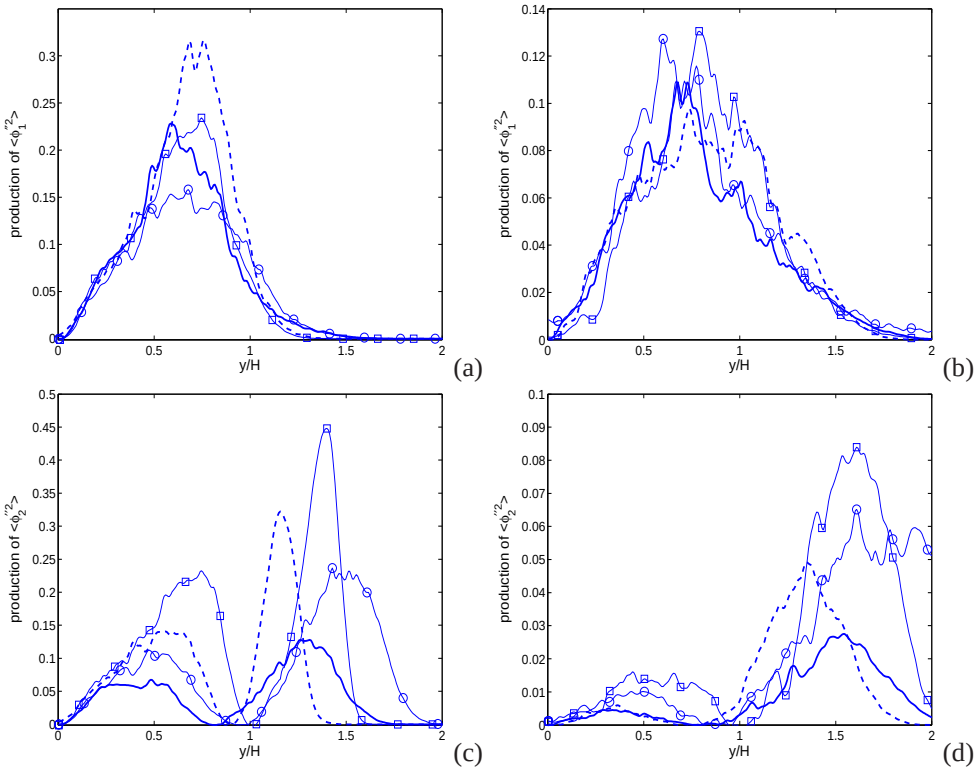

Figure 5.19: Production rate of scalar variance at (a,c) 10 t_{jet} and (b,d) 20 t_{jet}. Symbols same as in Fig. 5.16.

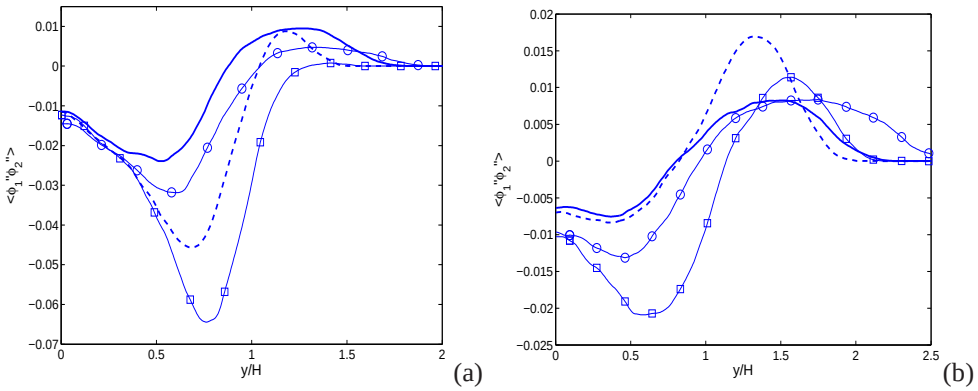

Figure 5.20: Cross-stream profiles of the co-variance of ϕ_1 and ϕ_2 at (a) 10 t_{jet} and (b) 20 t_{jet}. Symbols same as in Fig. 5.16.

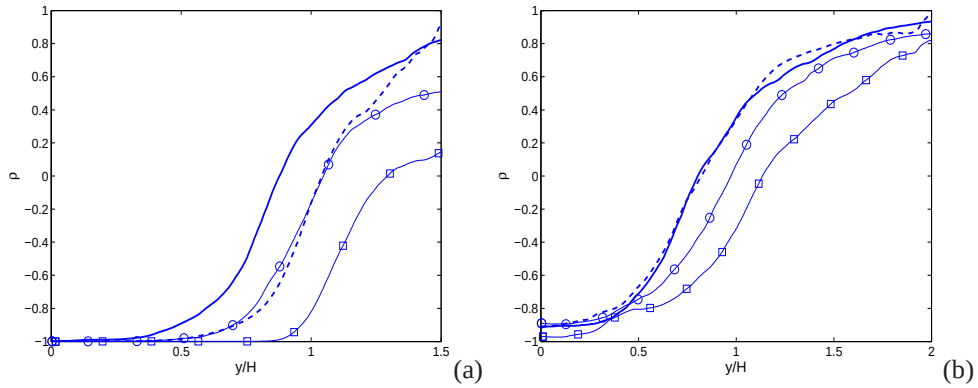

Figure 5.21: Cross-stream profiles of correlation coefficient between ϕ_1 and ϕ_2 at (a) 10 t_{jet} and (b) 20 t_{jet}. Symbols same as in Fig. 5.16.

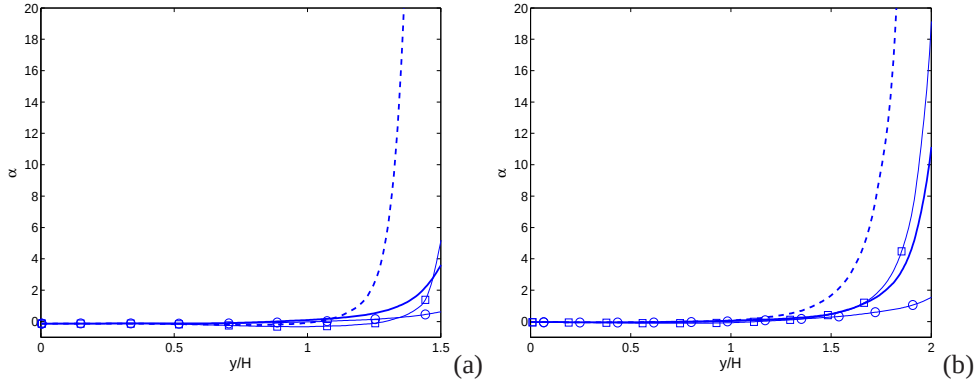

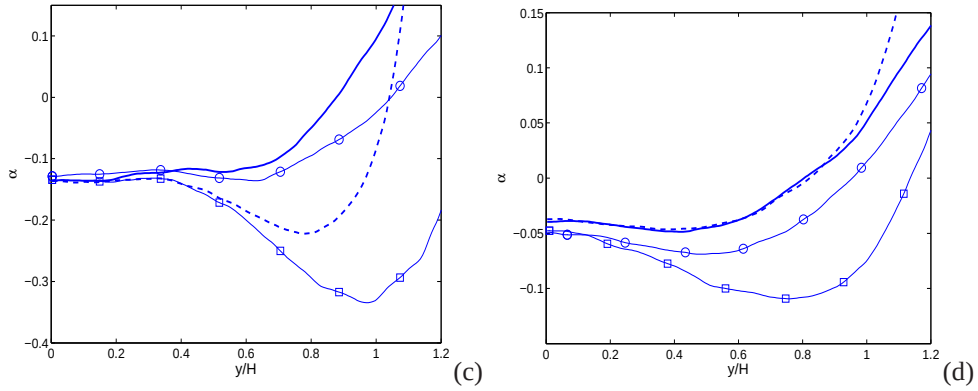

Figure 5.22: Cross-stream profiles of the segregation parameter between ϕ_1 and ϕ_2 at (a,c) 10 t_{jet} and (b,d) 20 t_{jet}. Symbols same as in Fig. 5.16.

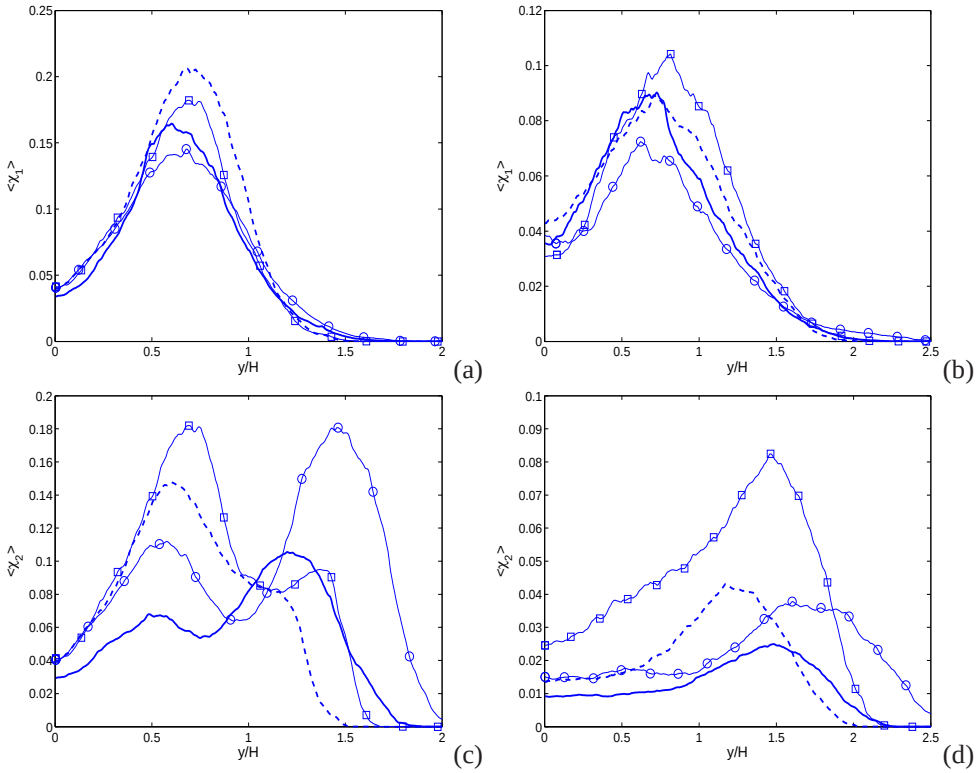

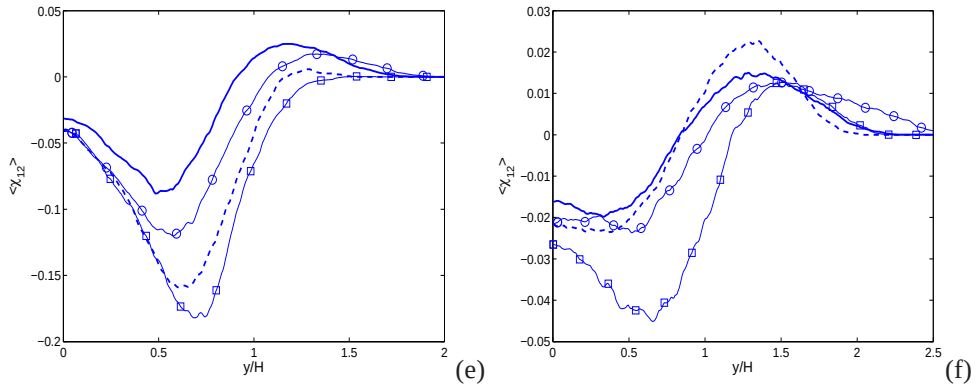

Figure 5.23: Cross-stream profiles of mean scalar dissipation rate and the mean cross-dissipation rate at (a,c,e) 10 t_{jet} and (b,d,f) 20 t_{jet}. Symbols same as in Fig. 5.16.

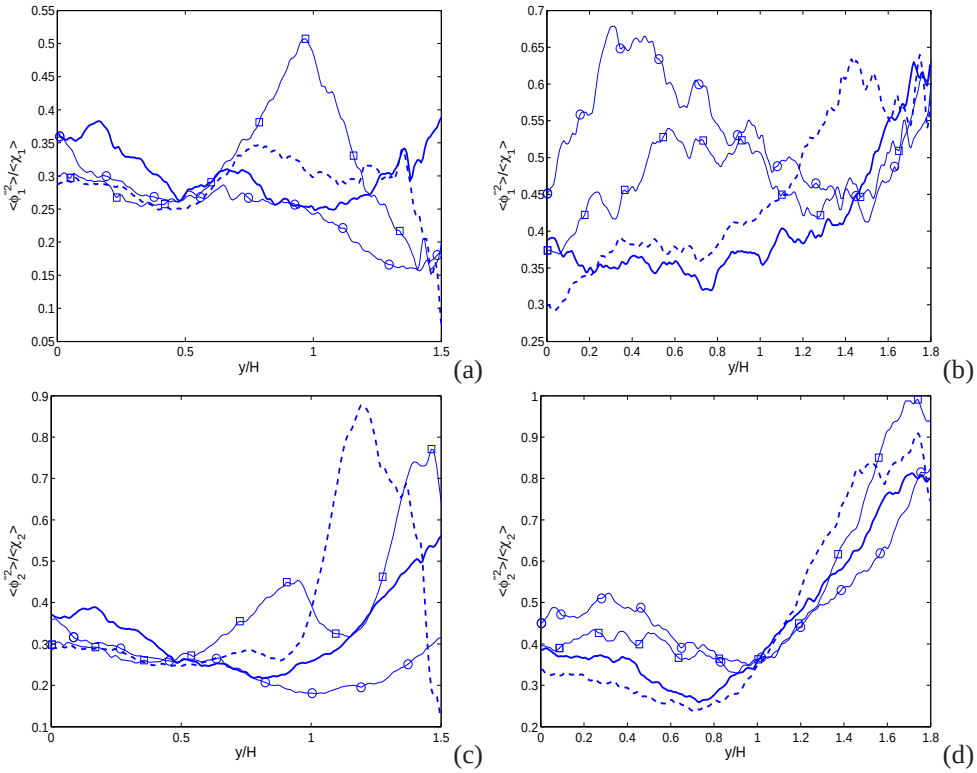

Figure 5.24: Cross-stream profiles of scalar mixing time scale at (a,c) 10 t_{jet} and (b,d) 20 t_{jet}. Symbols same as in Fig. 5.16.

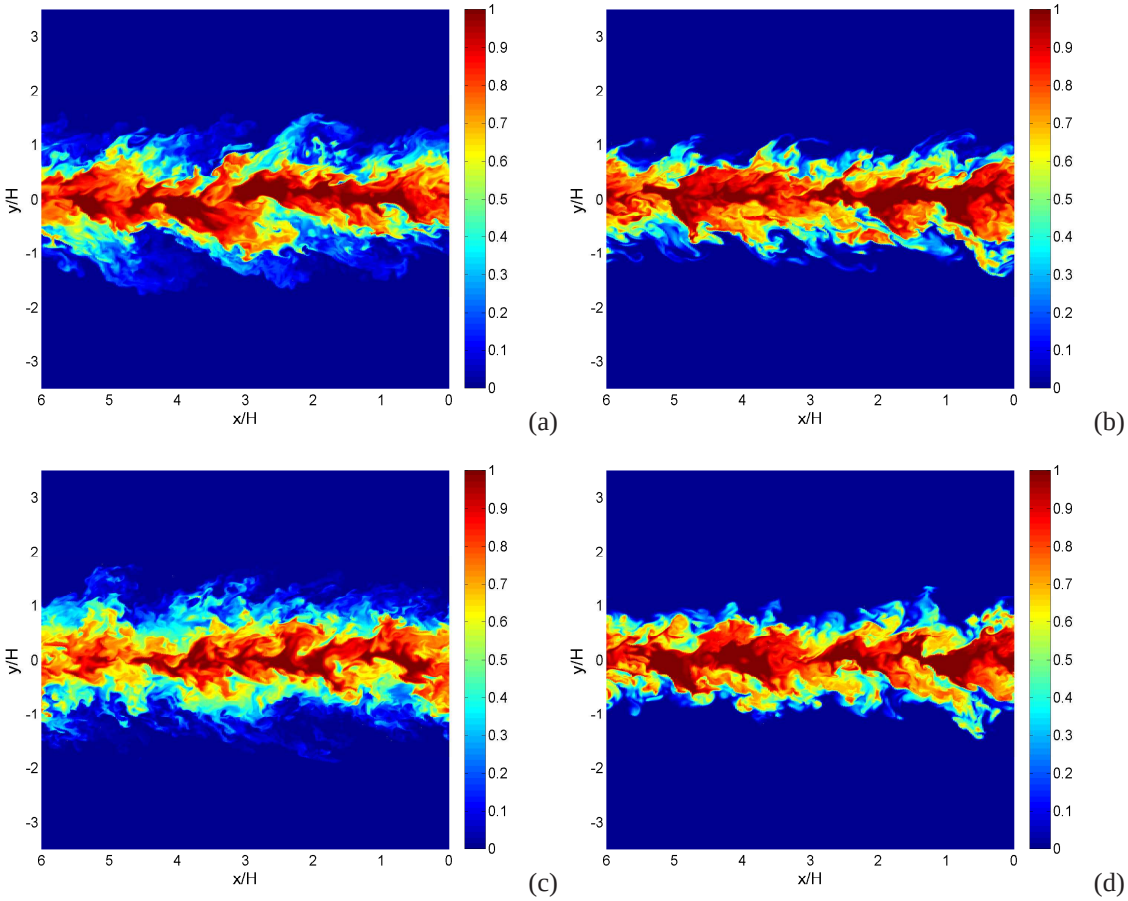

Figure 5.25: ϕ_1 contours at 10 t_{jet} ($z/H = 2$) for (a) case 1, (b) case 2, (c) case 3, and (d) case 4.

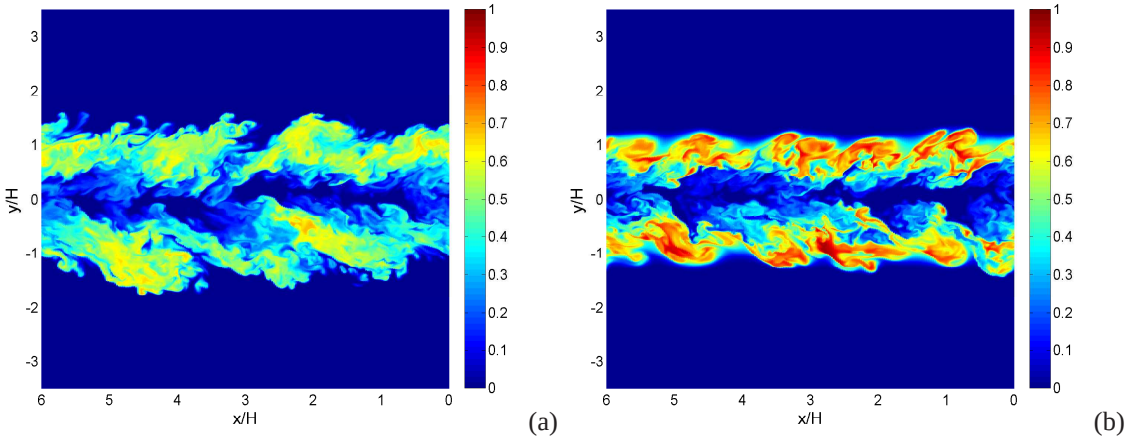

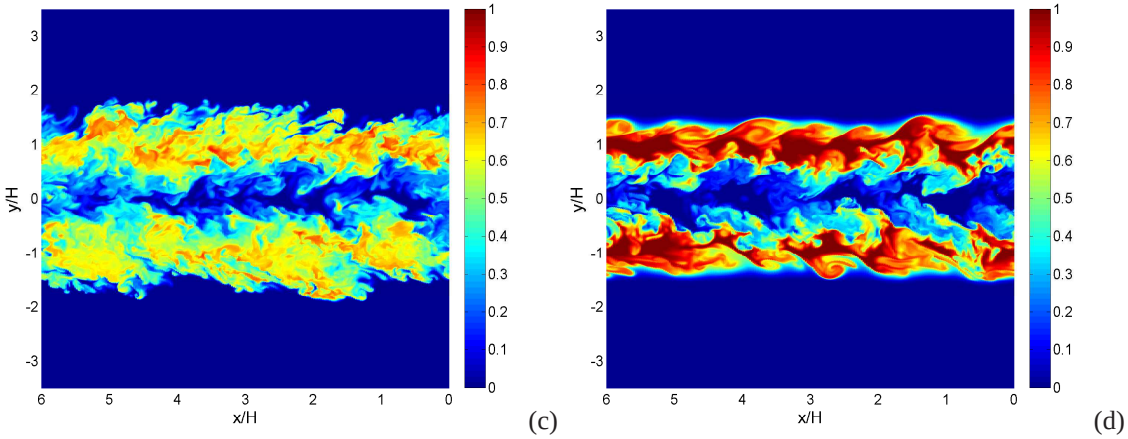

Figure 5.26: ϕ_2 contours at 10 t_{jet} ($z/H = 2$) for (a) case 1, (b) case 2, (c) case 3, and (d) case 4.

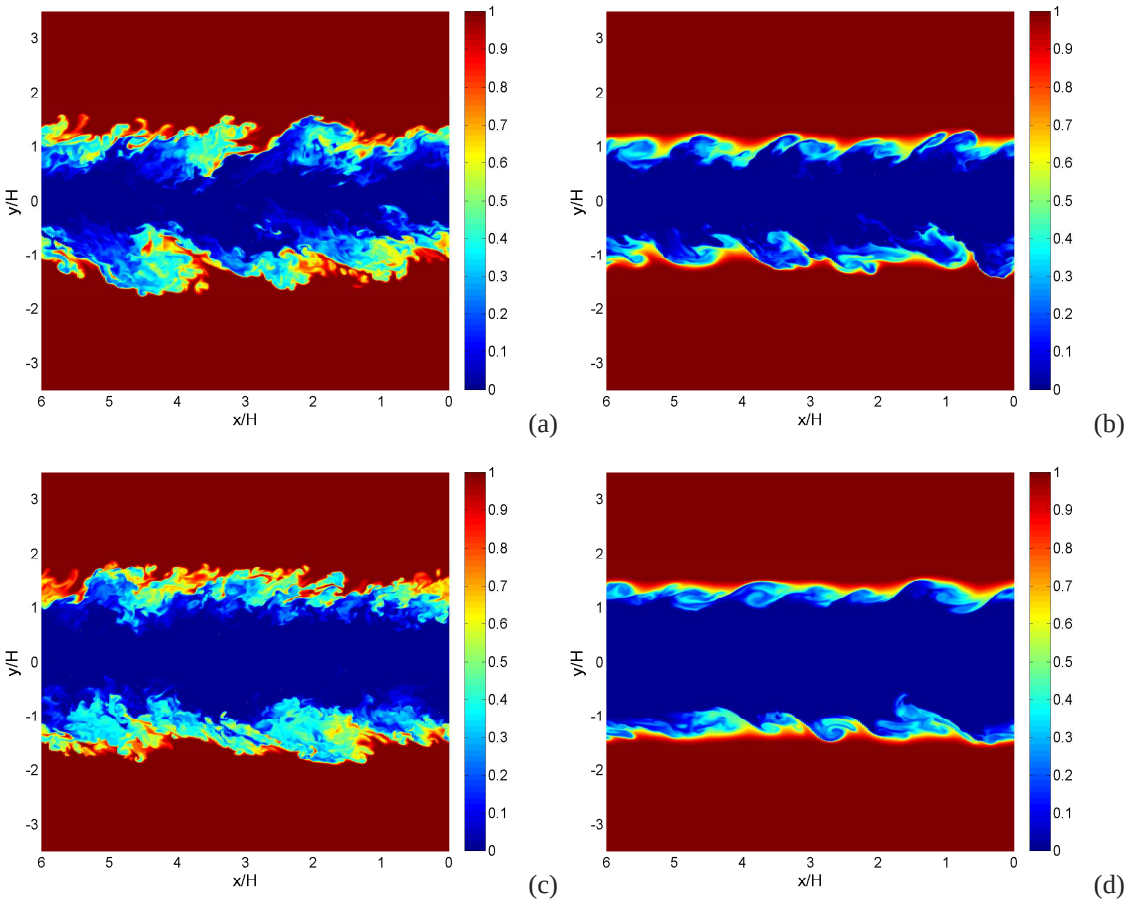

Figure 5.27: ϕ_3 contours at 10 t_{jet} ($z/H = 2$) for (a) case 1, (b) case 2, (c) case 3, and (d) case 4.

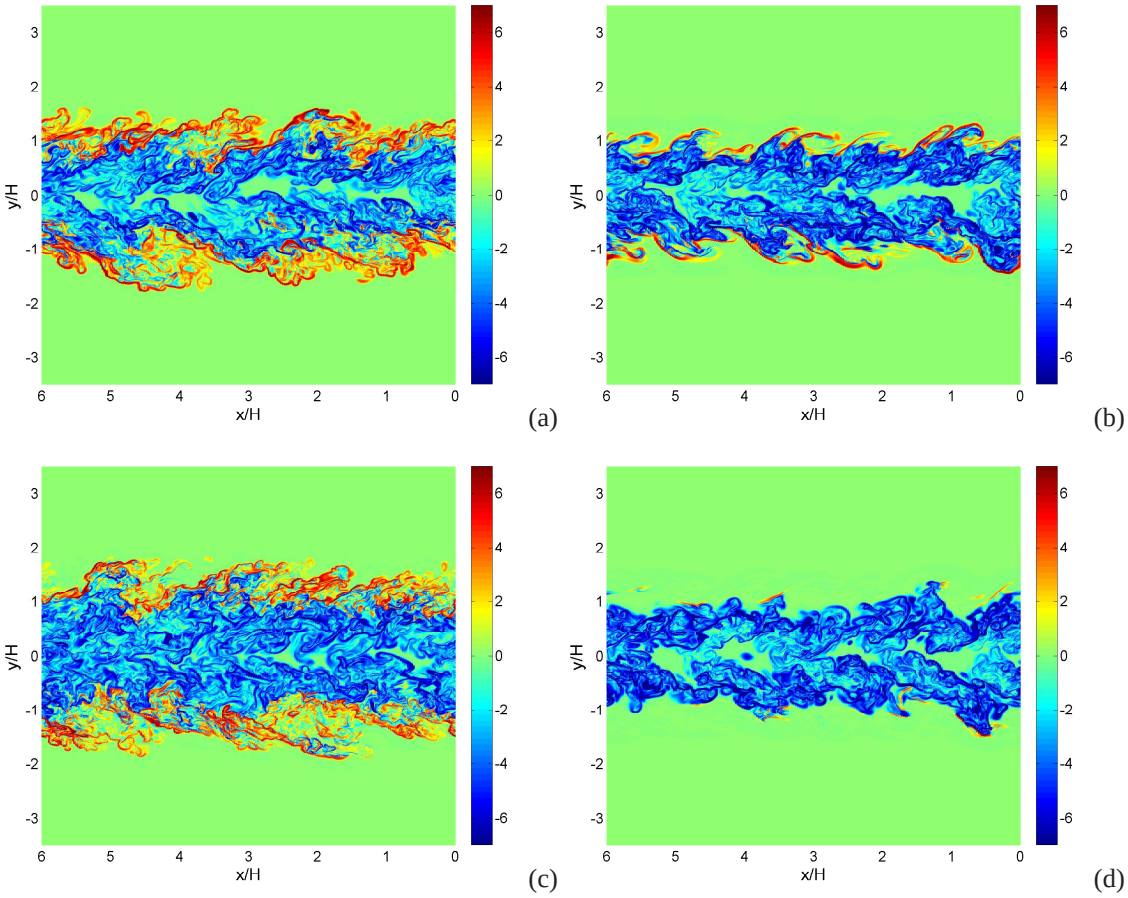

Figure 5.28: Cross-dissipation (χ_{12}) contours (log scale) at 10 t_{jet} ($z/H = 2$) for (a) case 1, (b) case 2, (c) case 3, and (d) case 4.

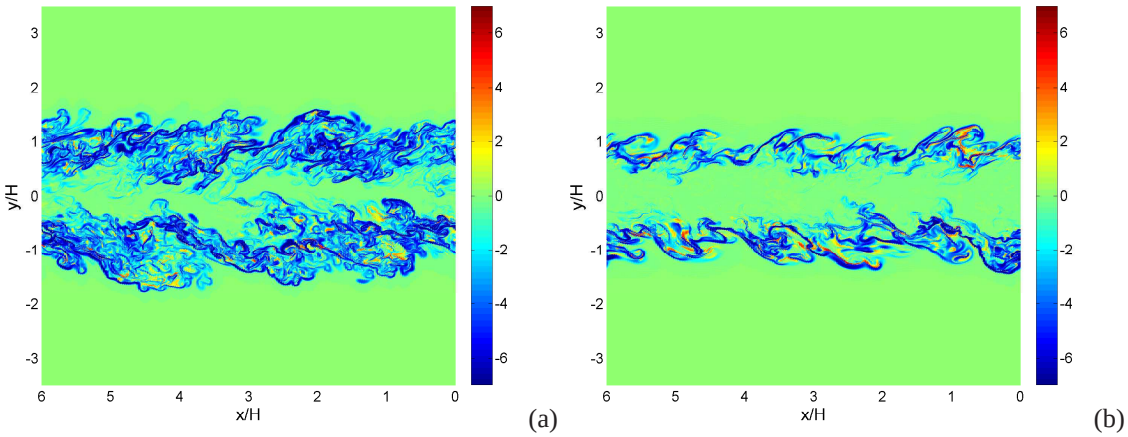

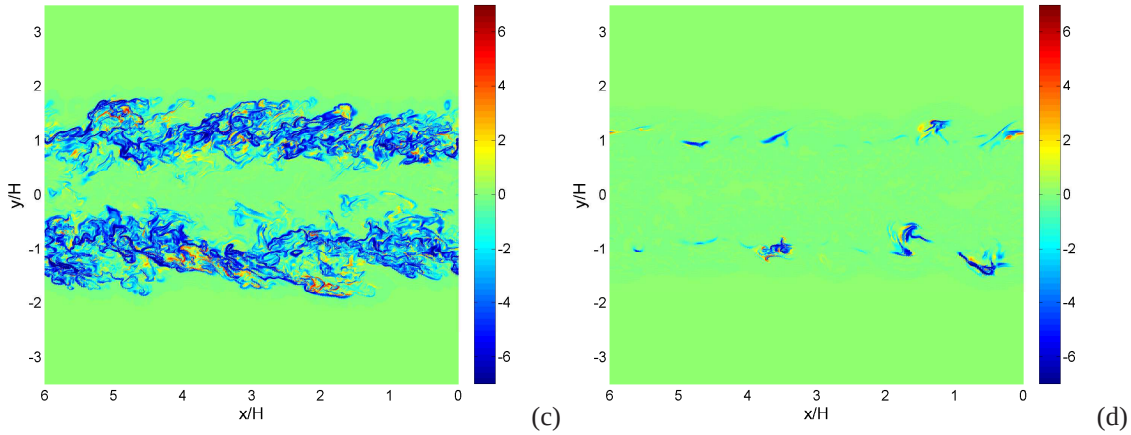

Figure 5.29: Cross-dissipation (χ_{13}) contours (log scale) at 10 t_{jet} ($z/H = 2$) for (a) case 1, (b) case 2, (c) case 3, and (d) case 4.

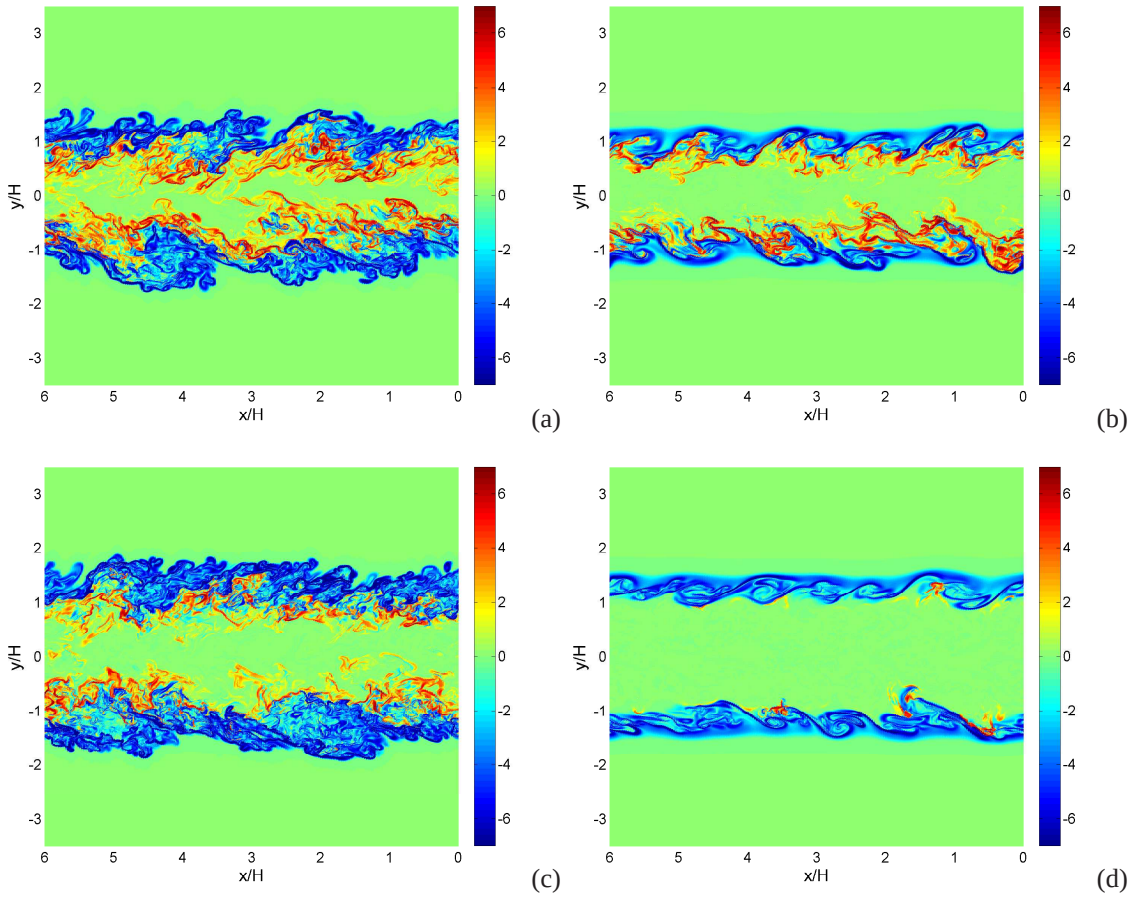

Figure 5.30: Cross-dissipation (χ_{23}) contours (log scale) at 10 t_{jet} ($z/H = 2$) for (a) case 1, (b) case 2, (c)

case 3, and (d) case 4.

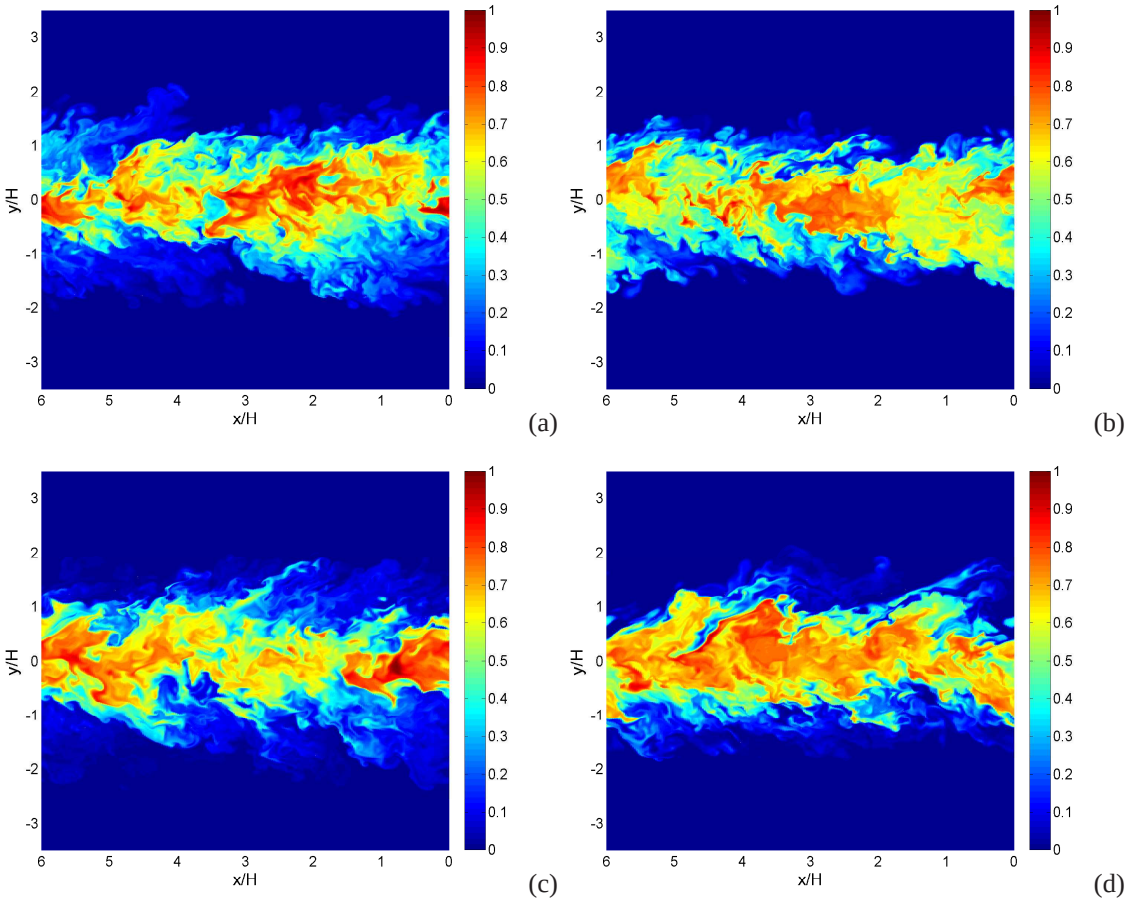

Figure 5.31: ϕ_1 contours at 20 t_{jet} ($z/H = 2$) for (a) case 1, (b) case 2, (c) case 3, and (d) case 4.

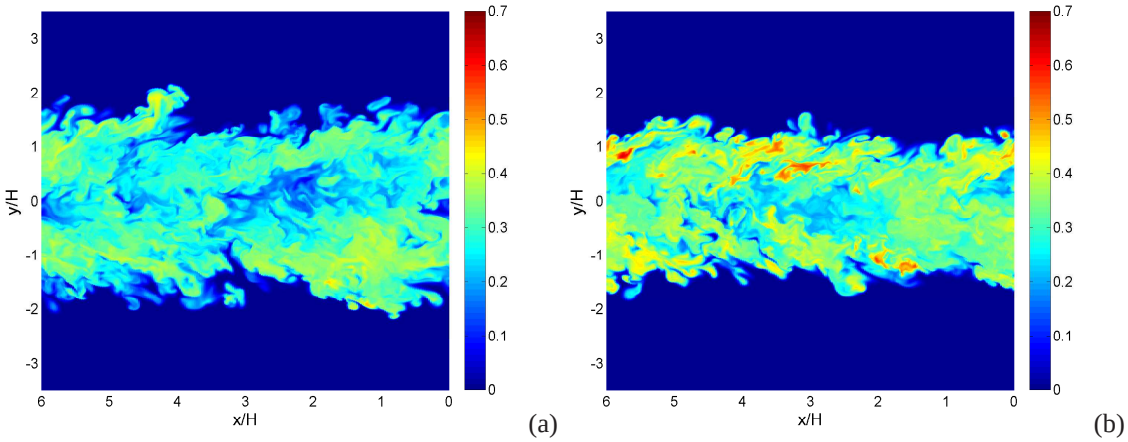

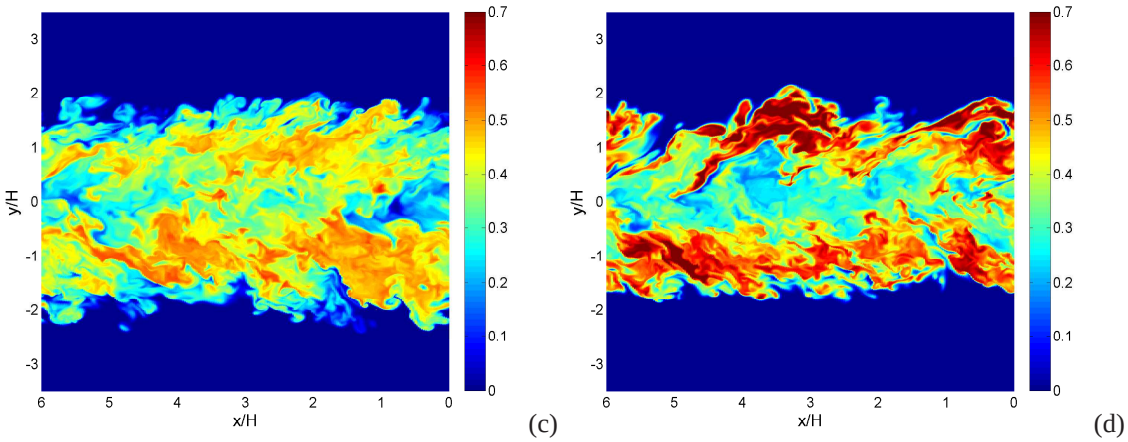

Figure 5.32: ϕ_2 contours at 20 t_{jet} ($z/H = 2$) for (a) case 1, (b) case 2, (c) case 3, and (d) case 4.

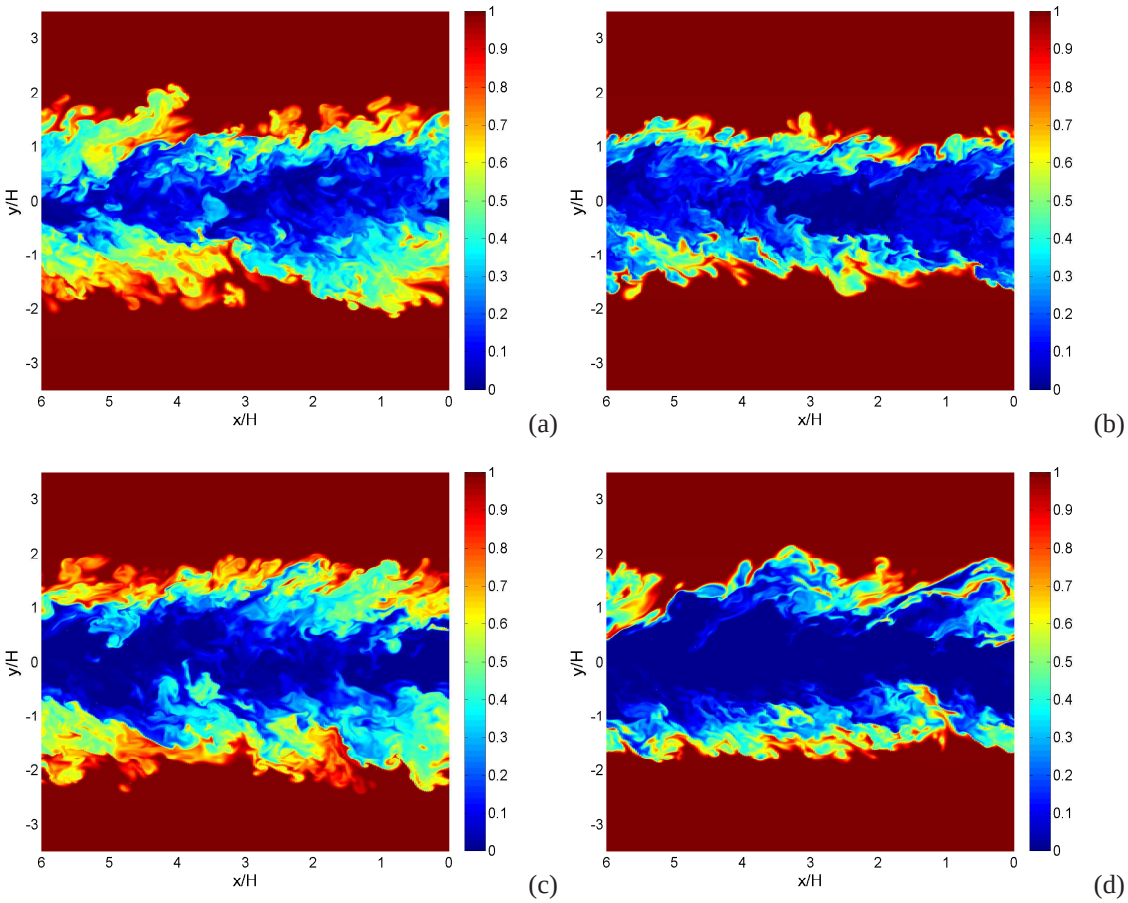

Figure 5.33: ϕ_3 contours at 20 t_{jet} ($z/H = 2$) for (a) case 1, (b) case 2, (c) case 3, and (d) case 4.

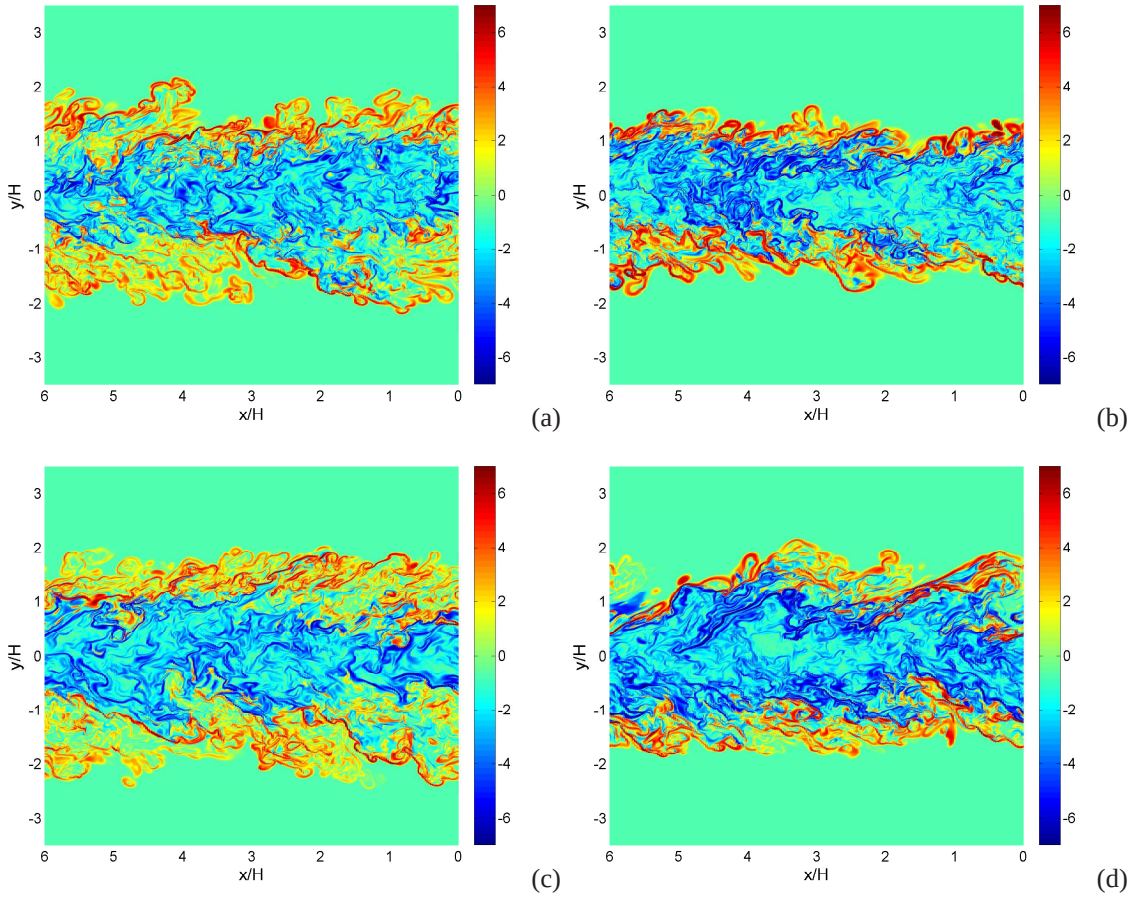

Figure 5.34: Cross-dissipation (χ_{12}) contours (log scale) at 20 t_{jet} ($z/H = 2$) for (a) case 1, (b) case 2, (c) case 3, and (d) case 4.

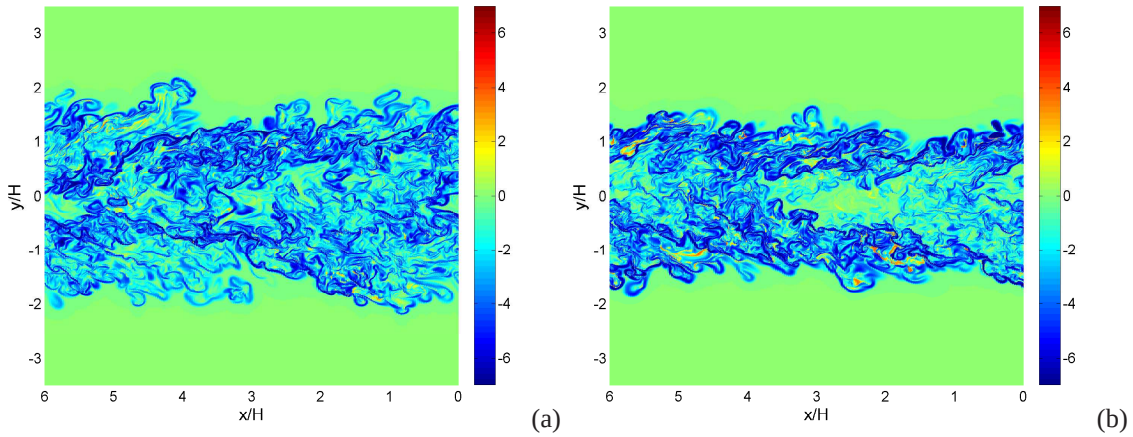

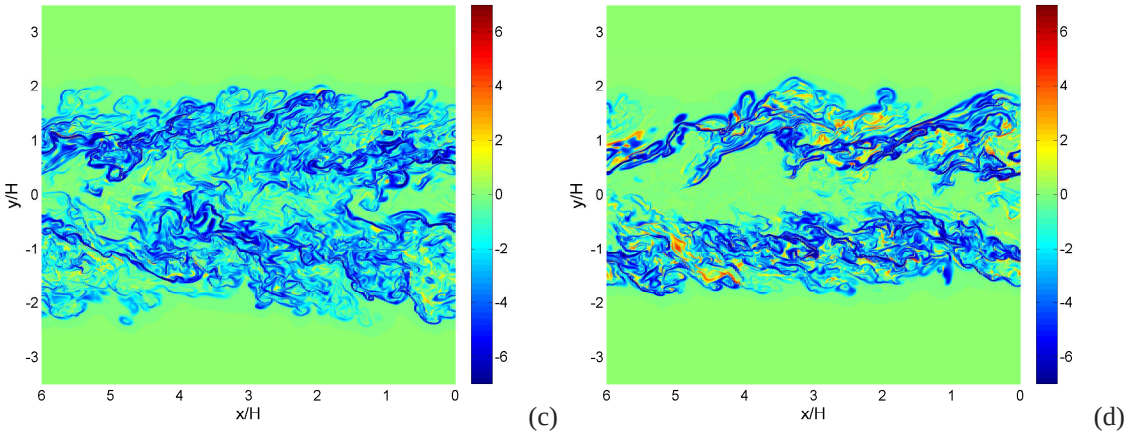

Figure 5.35: Cross-dissipation (χ_{13}) contours (log scale) at 20 t_{jet} ($z/H = 2$) for (a) case 1, (b) case 2, (c) case 3, and (d) case 4.

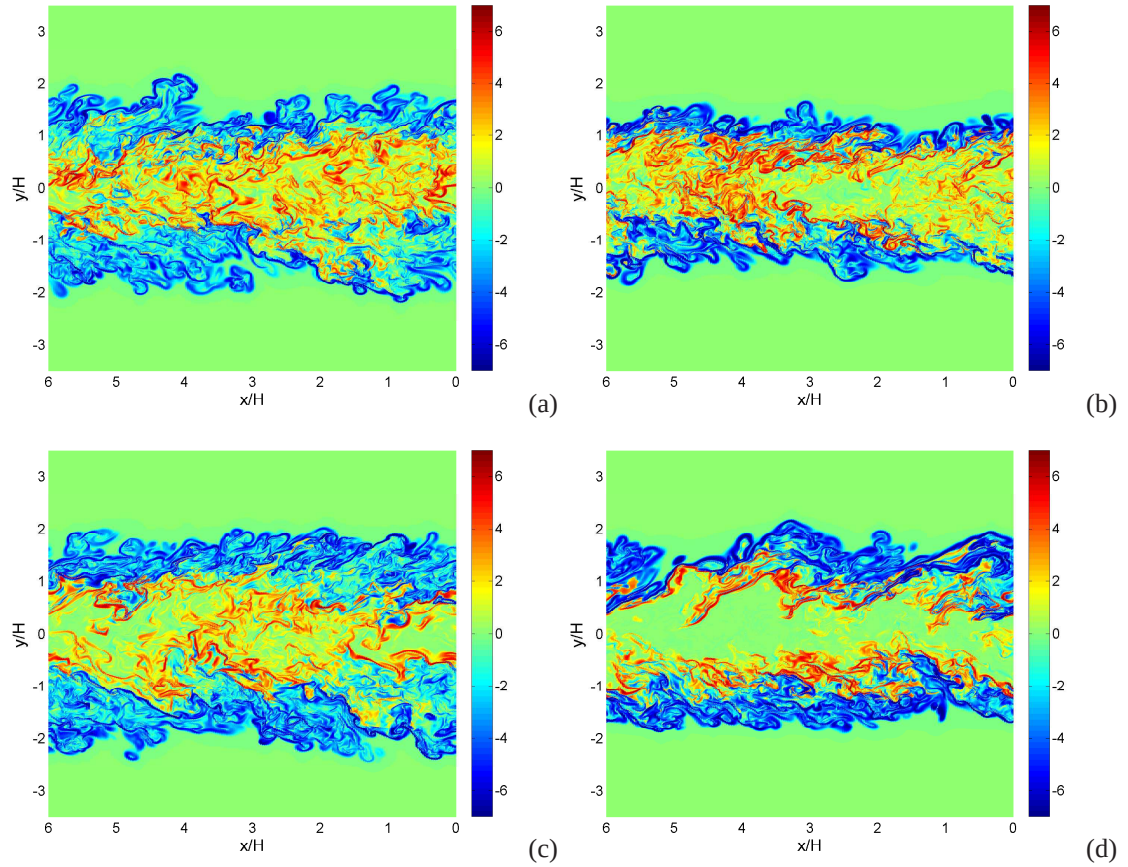

Figure 5.36: Cross-dissipation (χ_{23}) contours (log scale) at 10 t_{jet} ($z/H = 2$) for (a) case 1, (b) case 2, (c) case 3, and (d) case 4.

Chapter 6

JPDF, conditional diffusion, and conditional dissipation in temporally developing plane jets

In this chapter, the scalar JPDF, the conditional diffusion, the conditional dissipation rate, and the conditional cross-dissipation rate of ϕ_1 and ϕ_2 at 10 and 20 jet times will be discussed in detail in the context of the scalar PDF transport equation. Equation 6.1 shows the JPDF transport equation. The mixing terms $\left\langle D\nabla^2\phi_1|\hat{\phi_1},\hat{\phi_2}\right\rangle$ and $\left\langle D\nabla^2\phi_2|\hat{\phi_1},\hat{\phi_2}\right\rangle$ transport the JPDF in the scalar scale, which represents the two components of diffusion velocity. We will present the conditional diffusion as the diffusion velocity, represented by streamlines and magnitudes. The mixing terms can also in forms of the conditional dissipation $\left\langle \chi_1|\hat{\phi_1},\hat{\phi_2}\right\rangle = \left\langle 2D(\partial\phi_1/\partial x_i)(\partial\phi_1/\partial x_i)|\hat{\phi_1},\hat{\phi_2}\right\rangle$, $\left\langle \chi_2|\hat{\phi_1},\hat{\phi_2}\right\rangle = \left\langle 2D(\partial\phi_2/\partial x_i)(\partial\phi_1/\partial x_i)|\hat{\phi_1},\hat{\phi_2}\right\rangle$ and the conditional cross dissipation $\left\langle \chi_{12}|\hat{\phi_1},\hat{\phi_2}\right\rangle = \left\langle 2D(\partial\phi_1/\partial x_i)(\partial\phi_2/\partial x_i)|\hat{\phi_1},\hat{\phi_2}\right\rangle$ (Eqn. 6.1), which is similar to the diffusivity of JPDF in scalar space. To better compare the mixing terms for difference cases, we normalize the conditional diffusion and dissipation terms using the jet reference time.

$$
\begin{aligned}
& \frac{\partial f_{\phi_1,\phi_2}}{\partial t} + \frac{\partial}{\partial x_i}\left[f_{\phi_1,\phi_2}\left(U_i + \left\langle u_i \middle| \hat{\phi_1}, \hat{\phi_2} \right\rangle\right)\right] \\
= & -\frac{\partial}{\partial \hat{\phi_1}}\left(f_{\phi_1,\phi_2}\left\langle D\nabla^2\phi_1 \middle| \hat{\phi_1}, \hat{\phi_2} \right\rangle\right) - \frac{\partial}{\partial \hat{\phi_2}}\left(f_{\phi_1,\phi_2}\left\langle D\nabla^2\phi_2 \middle| \hat{\phi_1}, \hat{\phi_2} \right\rangle\right) \\
= & \nabla^2 f_{\phi_1,\phi_2} - \frac{1}{2}\frac{\partial^2}{\partial \hat{\phi_1}^2}\left(f_{\phi_1,\phi_2}\left\langle \chi_1 \middle| \hat{\phi_1}, \hat{\phi_2} \right\rangle\right) - \frac{1}{2}\frac{\partial^2}{\partial \hat{\phi_2}^2}\left(f_{\phi_1,\phi_2}\left\langle \chi_2 \middle| \hat{\phi_1}, \hat{\phi_2} \right\rangle\right) \\
& -\frac{\partial^2}{\partial \hat{\phi_1}\hat{\phi_2}}\left(f_{\phi_1,\phi_2}\left\langle \chi_{12} \middle| \hat{\phi_1}, \hat{\phi_2} \right\rangle\right)
\end{aligned} \tag{6.1}
$$

6.1 JPDF and mixing terms at 10 jet times

The JPDF and the conditional diffusion at three cross-stream locations (10 t_{jet}) are shown in figures 6.1-6.6. The white, green, and pink contour of the JPDF represents the boundary within which the JPDF integrates to the value of 90%, 95%, and 99%. At $y/H = 0.625$ for case 4, the JPDF is along the straight mixing line connecting (0,1) and (1,0), indicating the mixing the essentially binary (fig. 6.1d). The diffusion lines for case 4 are also long the mixing line of ϕ_1 and ϕ_2 towards the mean value (0.5, 0.5) which represents by the white circular marker (fig. 6.2d). The diffusion magnitude is generally large away from the mean value. This trend is essentially consistent with the prediction by the IEM model. For case 2 and 3, although the mixing is still largely binary, the JPDF becomes wider and begins to extend towards (0,0), indicating there is some ϕ_3 mixed with ϕ_2. Along the ϕ_1, ϕ_2 mixing line, the JPDF extends to (0,1) for case 2 while for the case 4 the JPDF extends to (0.15,0.85). The trend of the diffusion streamlines are similar to case 4 (fig. 6.2b&c) near the ϕ_1, ϕ_2 mixing line. Away from the mixing line, the direction of the diffusion streamlines become more and more towards ϕ_1 direction. For case 1, the JPDF extends further towards (0,0), indicating more ϕ_3 in the mixture. Moreover, the trend of the diffusion lines for case 1 are very different from other cases. The diffusion magnitude is generally large for very high and lower ϕ_2 level. There is a manifold correspond to the very low diffusion magnitude region and the diffusion streamlines generally move towards the low diffusion magnitude region with high velocity and then move along the manifold until reach the stagnation point (fig. 6.2a). Notice that the stagnation point does not correspond to $(\langle\phi_1\rangle, \langle\phi_2\rangle)$ which is different from the IEM prediction.

Moving further away from the center plane ($y/H = 0.925$), the JPDF further extends towards the coflow side for case 1, 2 and 3. For case 4, the JPDF is still largely on the ϕ_1, ϕ_2 mixing line with the peak located at (0.1) indicating the mixture is largely pure ϕ_2. The peak JPDF for case 2 is located along the mixing

line connecting (0,1) and (0,0), indicating the mixing is largely between ϕ_2 and ϕ_3. Compare between case 1 and case 3, the JPDF extends to higher ϕ_2 value in case 3 than that in case 1, indicating relatively better mixing for the three scalars in case 1. The trend of the diffusion streamlines for case 1 and 3 are similar with high diffusion magnitude located at the low ϕ_2 region which is similar to the mixing of mixture fraction and temperature away from the reaction zone. Near the peak ϕ_2 region, the diffusion is largely in the direction of ϕ_2 towards the stagnation point. For case 2, the diffusion magnitude is also large near the peak of ϕ_2. For case 3, the diffusion trend is similar to that for $y/H = 0.625$.

Moving even further away from the center plane ($y/H = 1.125$), the JPDF are largely extended to the coflow side. For case 2 and 4, the peak regions of JPDF are concentrated along the ϕ_2, ϕ_3 mixing line, indicating the mixing is largely between ϕ_2 and ϕ_3. For case 1, there generally has no samples on the ϕ_1 and ϕ_2 mixing line and the peak JPDF is near the (0.0) while for case 3 there still have some samples on the ϕ_1 and ϕ_2 mixing line and the peak value is located at (0, 0.55). The trend of diffusion streamlines for case 3 and 4 are very similar with the JPDF extends to wider regions for case 2. For case 1, the lower diffusion magnitude region is approximately at $\phi_2 = 0.4$ and the diffusion lines are largely in the direction of ϕ_2, indicating the mixing between ϕ_2 and ϕ_3 is more intense than the mixing between ϕ_2 and ϕ_1. The conditional diffusion for case 3 is similar to that at $y/H = 0.925$ with slightly increasing of the diffusion magnitude.

These results show that at 10 t_{jet}, the mixing for case 2 and 4 at different cross-stream locations is largely between ϕ_2 and ϕ_1 or between ϕ_2 and ϕ_3, which is essentially similar to two-scalar mixing. For case 1 and 3, the mixing is essentially evolving three scalars away from the center plane. The higher velocity of the off-central jet can increase the mixing rate between ϕ_1 and ϕ_2 as well as the mixing between ϕ_2 and ϕ_3, which makes the mixing between ϕ_1 and ϕ_3 occur earlier than that for the lower off-central jet velocity. The larger width of the off-central jet makes the JPDF extend to higher ϕ_2 level because ϕ_3 need to travel longer distance to reach ϕ_1. The diffusion streamlines generally move towards the manifold correspond to the low diffusion magnitude regions with high velocity, and then move along the manifold with lower velocity until reach the stagnation point. Generally the stagnation point is different from ($\langle\phi_1\rangle$, $\langle\phi_2\rangle$) which is against the IEM model.

The conditional dissipation rate and cross-dissipation rate at 10 jet times for different cross-stream locations are shown in figures 6.7-6.15. At $y/H = 0.625$, the dissipation rate for ϕ_1 is generally large and has the peak value near the $\langle\phi_1\rangle$ and low ϕ_2 regions (fig. 6.7). For case 4 the peak $\langle\chi_1|\phi_1,\phi_2\rangle$ is located on the ϕ_1, ϕ_2 mixing line at (0.4,0.6), suggesting intense mixing between (1, 0) and (0, 1) (fig. 6.7d). The conditional dissipation rate for ϕ_2 at this location is similar to ϕ_1 for case 1, 2, and 3 because the mixing is largely between

ϕ_1 and ϕ_2. The peak value of $\langle\chi_2|\phi_1,\phi_2\rangle$ is smaller than that of ϕ_1 for case 2 and 3 (figs. 6.8c&d), while for case 4 even the magnitude is the same indicating pure mixing between ϕ_1 and ϕ_2 (fig. 6.8d). For case 1 at this location, the JPDF already extends to the coflow side, the conditional dissipation rates of ϕ_2 has two peak values at (0.65, 0.2) and (0.1, 0.3) (figs. 6.8a). The former peak is much stronger than the latter peak which indicate the mixing between ϕ_2 and ϕ_1 is more intense than the mixing between ϕ_2 and ϕ_3 at this location. The mean cross dissipation rate of ϕ_1 and ϕ_2 for case 2, 3, and 4 are largely negative which is due to the anti-correlation between ϕ_1 and ϕ_2 (figs.6.9b-d). For case 1 there has positive mean cross-dissipation rate near (0.18, 0.33) because of mixing between ϕ_3 and the mixture of ϕ_1 and ϕ_2 (fig 6.9a).

At $y/H = 0.925$, there has ϕ_3 present which is transported by the turbulent fluctuations in the cross-stream direction. The peak dissipation rate of ϕ_1 is located near $\phi_1 = 0.4$ and low ϕ_2 for case 1, 2, and 3, while for case 4 the peak is still located on the mixing line (fig, 6.10). For the dissipation rate of ϕ_2, it shows two peaks for all the cases. For case 2 and 3 the peak with much higher value is near the mixing line of ϕ_1 and ϕ_2, while for case 1 the stronger peak is near ϕ_2 and ϕ_3 mixing line. For case 3 the two peaks are equally strong. This suggest that at $y/H = 0.925$, the mixing between the central jet and off-central jet is more intense that of the off-central jet and coflow for case 2 and 4, while for case 1 the situation reverses. For the cross-dissipation rate (fig. 6.12), for case 1 and 3 there has more negative values, while for case 2 and 4 $\langle\chi_{12}|\phi_1,\phi_2\rangle$ is still largely positive. The higher velocity ratio between central jet and off-central jet generally reduce the mixing rate between ϕ_2 and ϕ_3, resulting in the delaying of mixing between ϕ_3 and $\phi_1 - \phi_2$ mixtures.

Moving further away from the center plane ($y/H = 1.125$), the JPDF are largely towards (0, 0) for case 1, 2 and 3. At fixed ϕ_1, the dissipation rate of ϕ_1 is generally large towards lower ϕ_2. For case 4, the higher χ_1 region is still located on the $\phi_1 - \phi_2$ mixing line. The dissipation rate of ϕ_2 at this location shows one peak for case 1 and 3 which is largely due to the mixing between ϕ_2 and ϕ_3. Although $\langle\chi_{12}|\phi_1,\phi_2\rangle$ has two peak for case 2, the peak value near $\phi_1 = 0$ is much higher than the one near the $\phi_1 - \phi_2$ mixing line. For case 4, the dissipation rates for χ_1 and χ_2 are still similar. The cross-dissipation rate has a positive peak at the same location corresponding to the peak χ_2 for case 1, 2, and 3. For case 4, the cross-dissipation is negative on the $\phi_1 - \phi_2$ mixing line and close to zero near $\phi_2 - \phi_3$ mixing line.

6.2 JPDF and mixing terms at 20 jet times

With the jet further developed ($20\,t_{jet}$), there is already coflow ϕ_3 near the center plane ($y/H = 0.025$) for case 1, 2, and 3 as reflected by the JPDF extend away from $\phi_1 - \phi_2$ mixing line (figs. 6.51a-c) and the

diffusion streamlines generally move towards the a manifold with higher magnitude and then move along the manifold with small magnitude (figs. 6.52a-c). For case 4, the JPDF is still largely on the $\phi_1 - \phi_2$ mixing line (fig. 6.53d) and the diffusion lines move along the mixing line towards the mean value (6.54d). Moving away from the center plane ($y/H = 0.525$), the JPDF extend further away from the center plane for all the cases (fig. 6.53). For case 1 and 2, the peak of JPDF for case 3 and 4 are located on the mixing line while the peak shifts to the co-flow side for case 1 and 2, indicating the mixing has progressed much further for case 1 and 2. The conditional diffusion are largely in the direction of ϕ_1 for case 1, 2 and 3 indicating relatively well mixing of ϕ_2 (fig. 6.54). Moving further away from the center plane ($y/H = 1.025$), almost pure co-flow ϕ_3 begin to appear for all the cases (fig 6.55). The JPDF has one peak value for case 1 and 3 while for case 2 and 4, the JPDF is bimodal. For case 4, the peaks of the JPDF are near (0.6, 0.4) and (0, 0.6) which is on the $\phi_1 - \phi_2$ mixing line and $\phi_2 - \phi_3$ mixing line, indicating high mixing rate between the central jet and off-central jet, and between the off-central jet and co-flow. The conditional diffusion is generally large at low ϕ_2 and very large or small ϕ_1 levels, this shows some similarity for the conditional diffusion of mixture and temperature in Sandia flames.

The conditional dissipation rate and cross-dissipation rate for ϕ_1 and ϕ_2 at 20 h_{jet} are shown in figures 6.57-6.65. The conditional dissipation rate for ϕ_1 is similar to those at 10 t_{jet} with higher value located at median ϕ_1 and low ϕ_2 (figs. 6.57&6.60&6.63). The conditional dissipation rate for ϕ_2 at $y/D = 0.025$ is similar to those for ϕ_1 for all the cases (fig. 6.58). Moving away from the center plane ($y/H = 0.525$), $\langle \chi_2 | \phi_1, \phi_2 \rangle$ shows two peaks for case 1 and 2 (Fig. 6.61). Moving further away from the center plane ($y/H = 1.025$), the conditional dissipation rate for ϕ_2 has one peak value near the co-flow (0, 0) (Fig. 6.64). For the cross-dissipation rate, at $y/H = 0.025$ $\langle \chi_{12} | \phi_1, \phi_2 \rangle$ is largely negative for all the cases (fig. 6.59), indicating high mixing rate between ϕ_1 and ϕ_2. Moving away from the center plane ($y/H = 0.525$), there is positive value for the cross-dissipation rate for case 1, 2 and 3. Moving further away from the center plane ($y/H = 1.025$), the cross-dissipation rate are largely positive for case 1 and 2, indicating mixing between ϕ_3 and the mixture of ϕ_1 and ϕ_2 (figs. 6.65a&b). For case 3 and 4, the regions corresponding to positive and negative cross-dissipation are comparable (figs. 6.65c&d).

The conditional dissipation, and conditional cross-dissipation rates for ϕ_1 and ϕ_2 studied here show some similarities to those for the mixture fraction and temperature in turbulent flames [50, 42]. The conditional dissipation rate for ϕ_1 is similar to the conditional filtered dissipation rate of mixture fraction with higher value at median mixture fraction and lower temperature. The conditional dissipation rate for ϕ_2 is similar to the conditional filtered dissipation rate of the temperature which shows two peaks in the branch of

lean and rich mixtures. These similarities indicate that some of the mixing properties of non-reactive scalar are also present in reactive flows. These properties can be used to test and improve mixing models without the complication from chemistry[50].

The results on the conditional diffusion also give insights for mixing models. The diffusion manifold in scalar samples space provides a diffusion path. The diffusion of mixtures that are close in scalar space but separated in physical space must take a detour. Such mixing path presents a challenge test for mixing models since most mixing models only depend on sample space variables and do not take into account the physical-space scalar structure. The most popular mixing model, IEM model depend only on the scalar-space variable which make all the samples move directly towards the mean value. This is not consistent with current DNS results with the curved streamlines in scalar space .

The comparison from four cases shows that the JPDF and the mixing terms are strongly affected by the velocity ratio and width ratio between the central jet and off-central jet. In the early stage of the jet development, lower velocity and larger width of off-central jet (case 4) generally result in binary mixing, i.e., mixing between ϕ_1 and ϕ_2 or between ϕ_2 and ϕ_3. There even has spots of pure ϕ_2 near the shear layer at 10 jet times for case 4 which shows the disadvantage of this configuration when considering the scalar mixing activity. On the contrary, a multiscalar mixing regime quickly established for case 1 which has a higher velocity and low width of the off-central jet. Overall the results show high quality of mixing favored by the configuration in case 1.

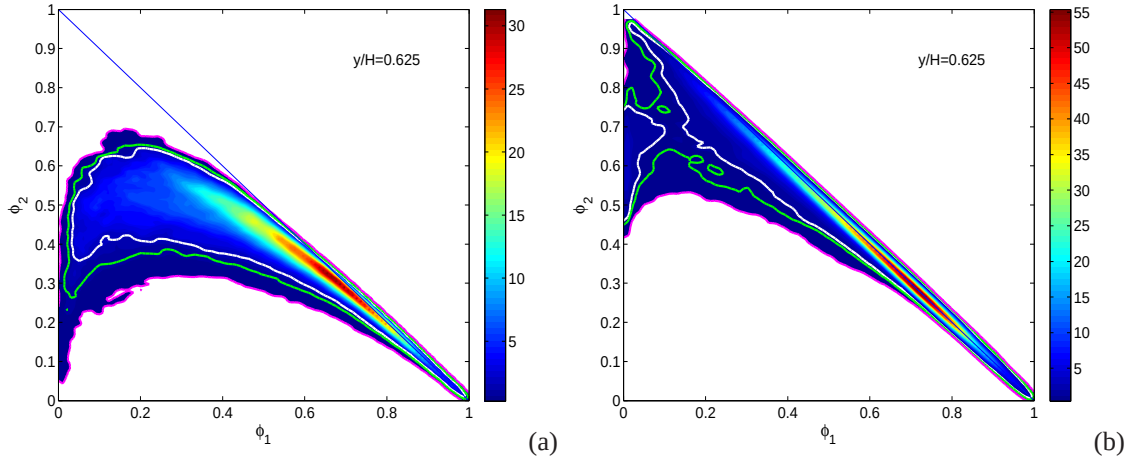

(a) (b)

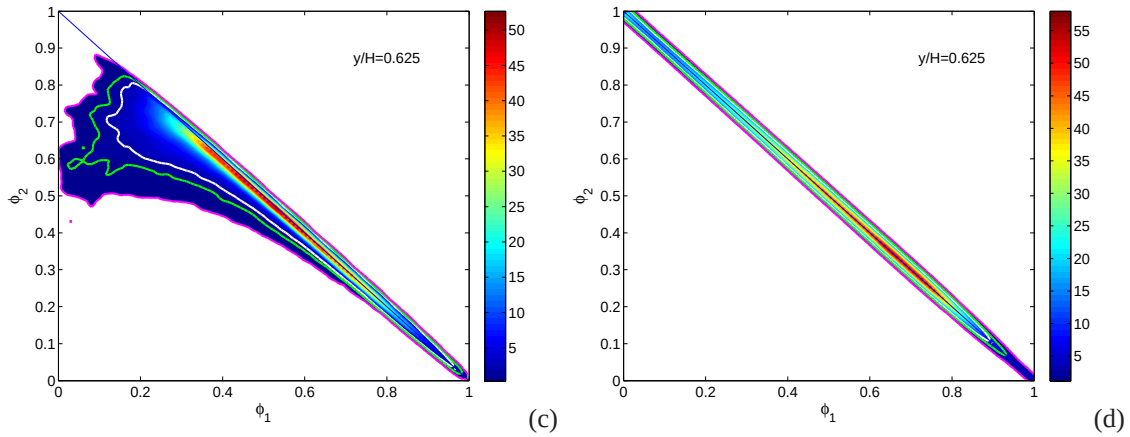

Figure 6.1: Scalar JPDF at 10 t_{jet}, $y/H = 0.625$ for (a) case 1, (b) case 2, (c) case 3, and (d) case 4.

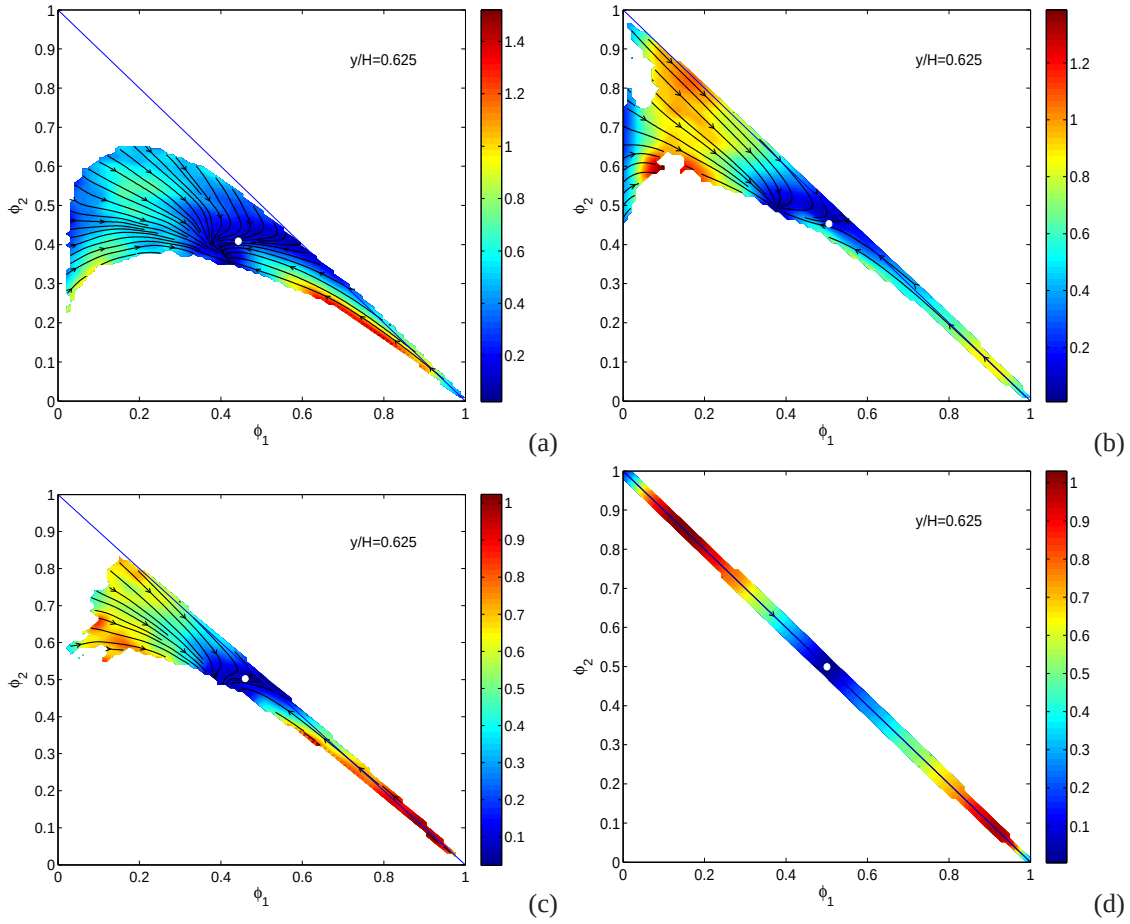

Figure 6.2: Conditional diffusion at 10 t_{jet}, $y/H = 0.625$ for (a) case 1, (b) case 2, (c) case 3, and (d) case 4.

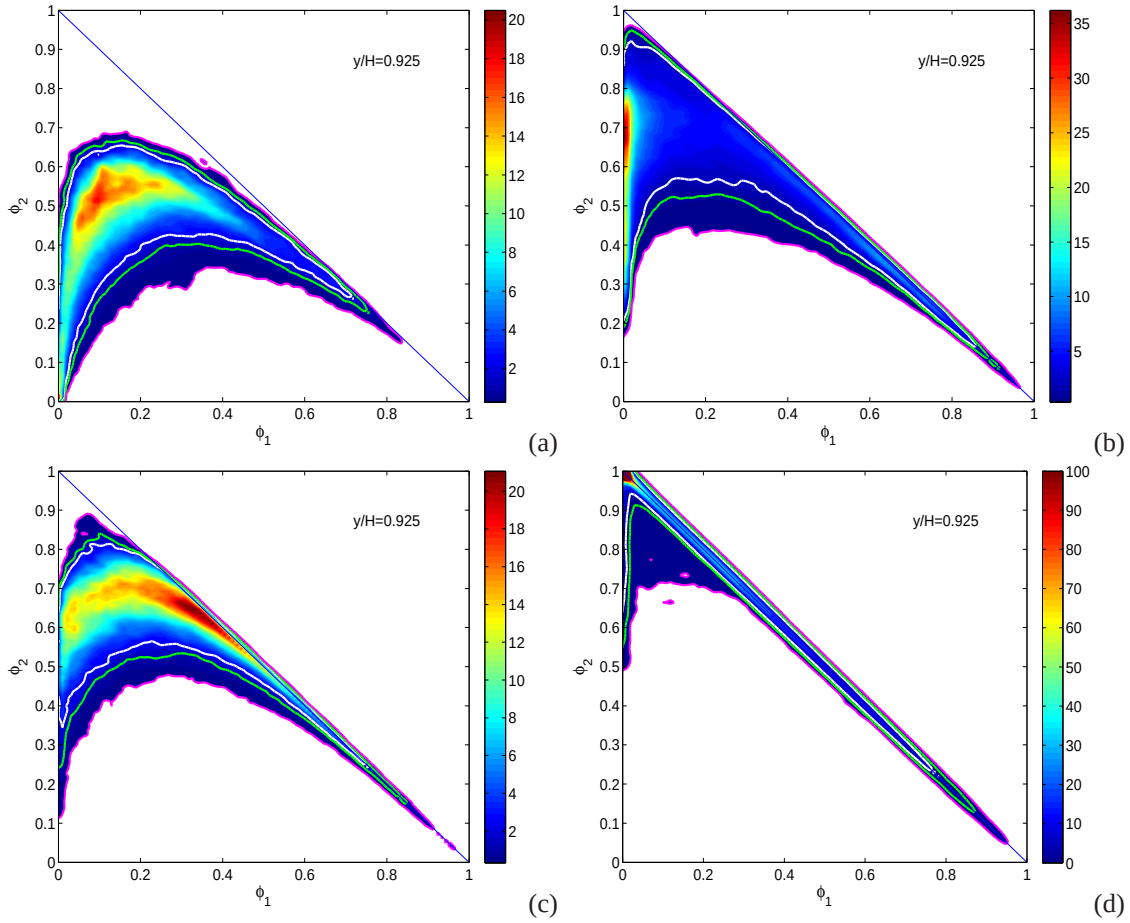

Figure 6.3: Scalar JPDF at 10 t_{jet}, $y/H = 0.925$ for (a) case 1, (b) case 2, (c) case 3, and (d) case 4.

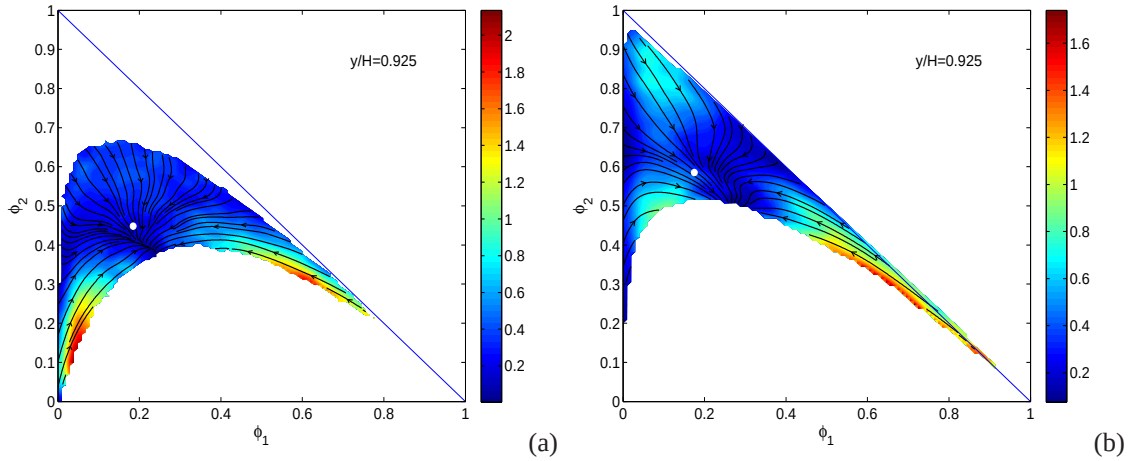

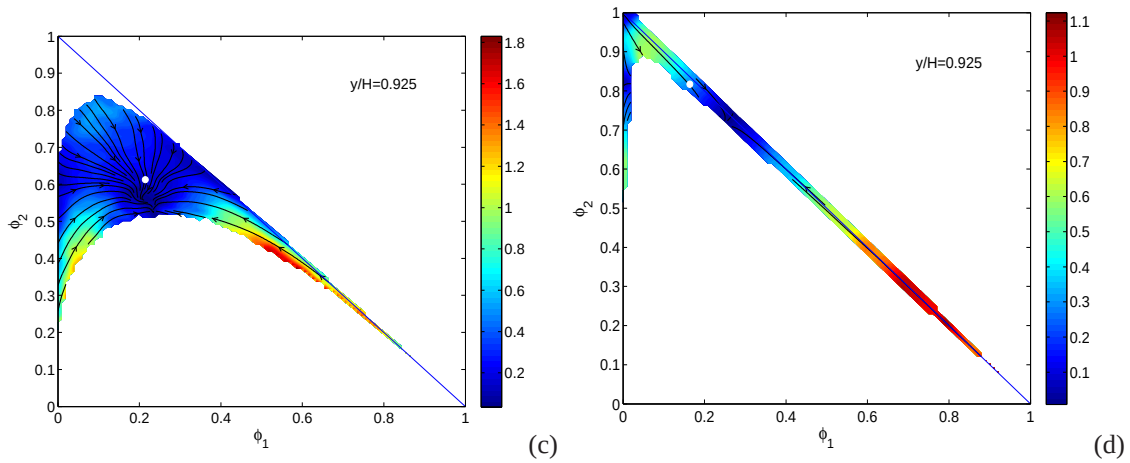

Figure 6.4: Conditional diffusion at 10 t_{jet}, $y/H = 0.925$ for (a) case 1, (b) case 2, (c) case 3, and (d) case 4.

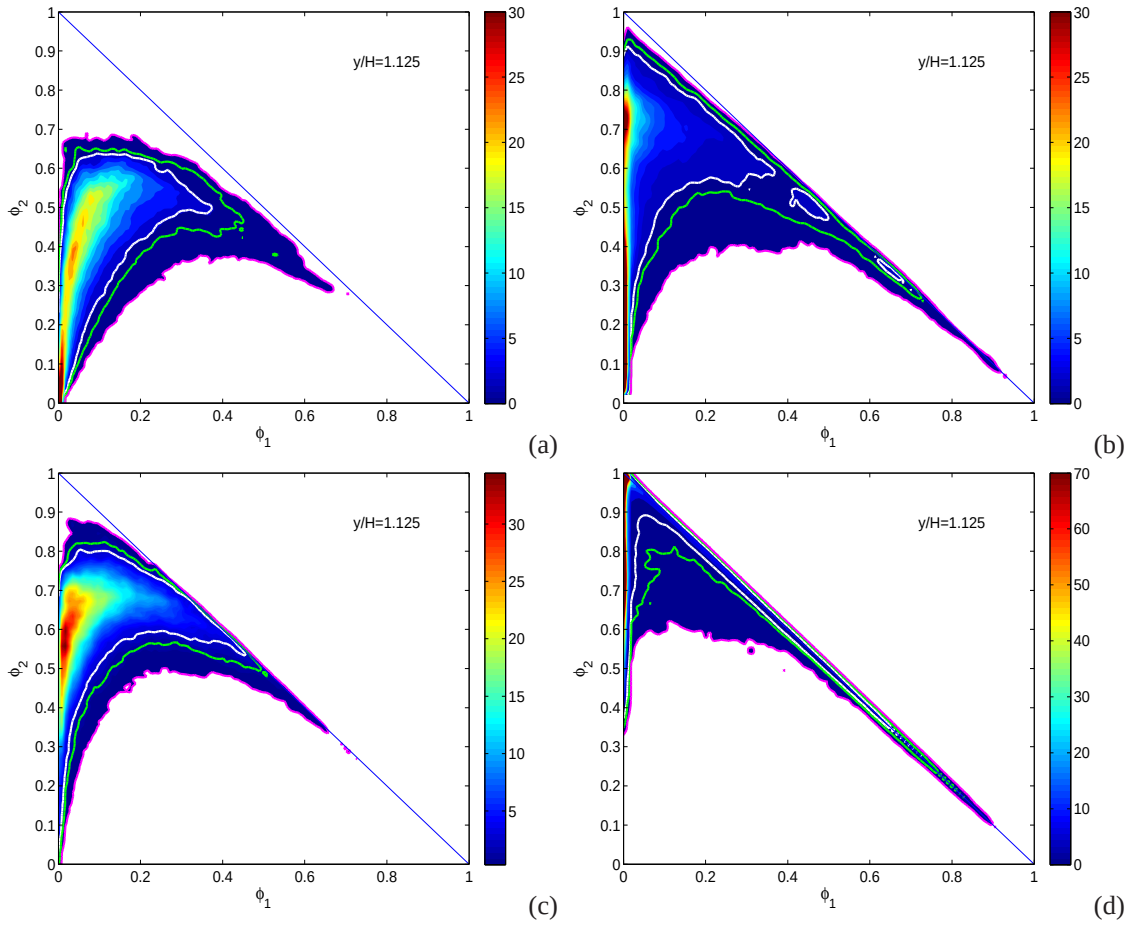

Figure 6.5: Scalar JPDF at 10 t_{jet}, $y/H = 1.125$ for (a) case 1, (b) case 2, (c) case 3, and (d) case 4.

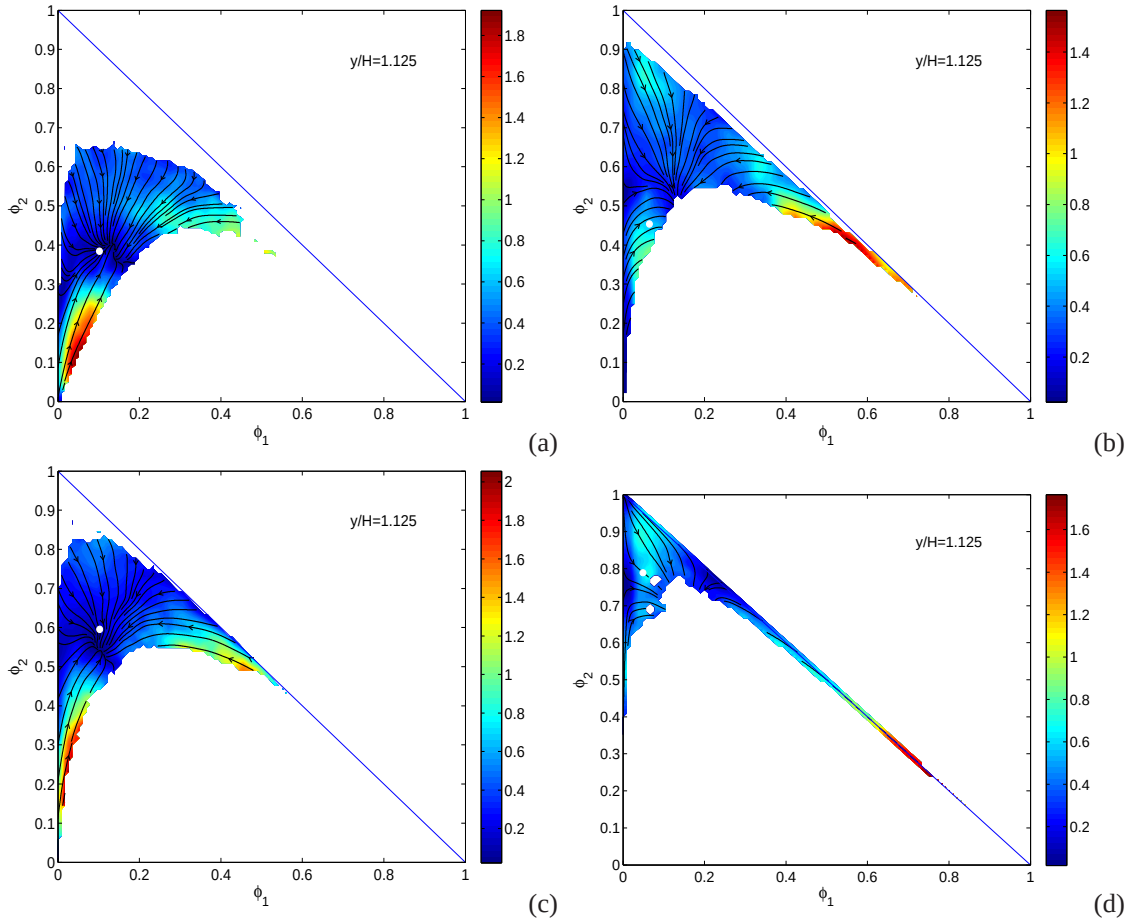

Figure 6.6: Conditional diffusion at 10 t_{jet}, $y/H = 1.125$ for (a) case 1, (b) case 2, (c) case 3, and (d) case 4.

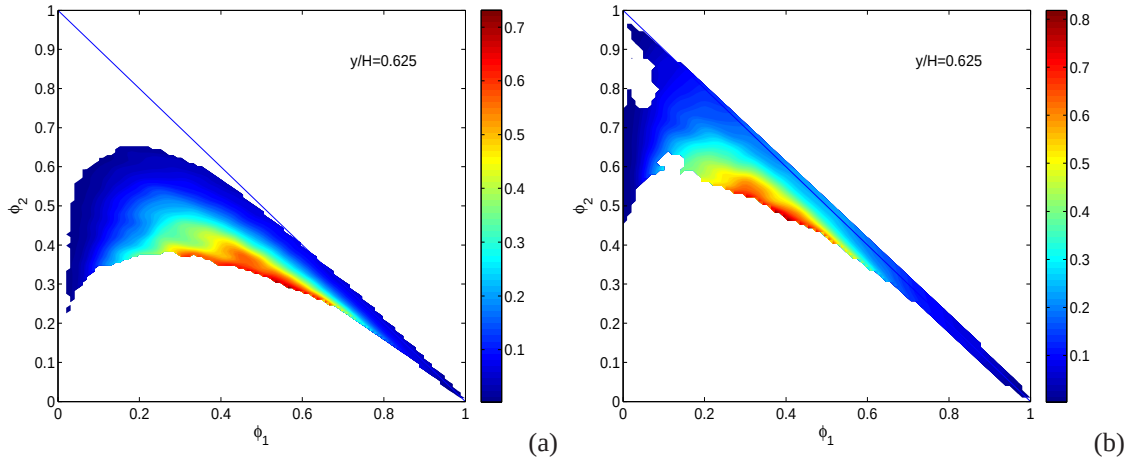

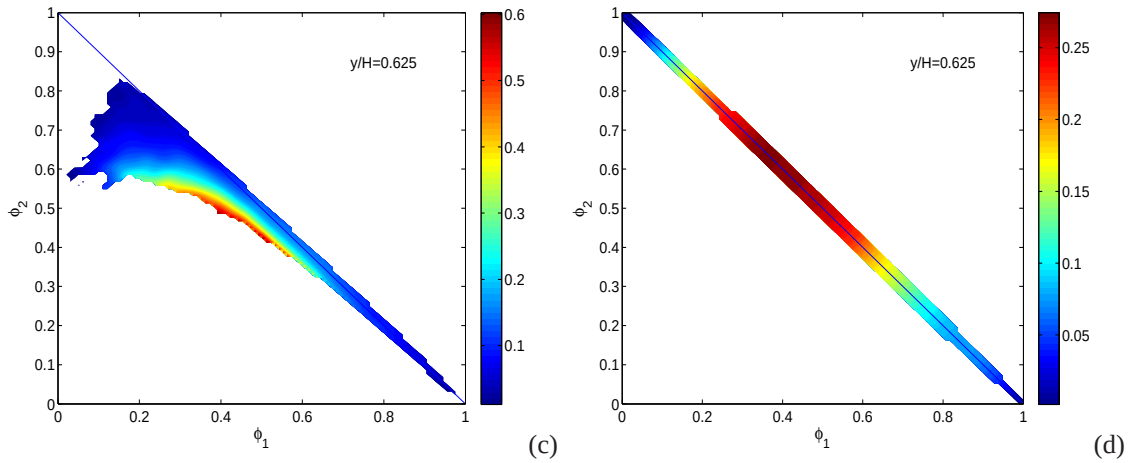

Figure 6.7: Conditional scalar dissipation rate for ϕ_1 at 10 t_{jet}, $y/H = 0.625$ for (a) case 1, (b) case 2, (c) case 3, and (d) case 4.

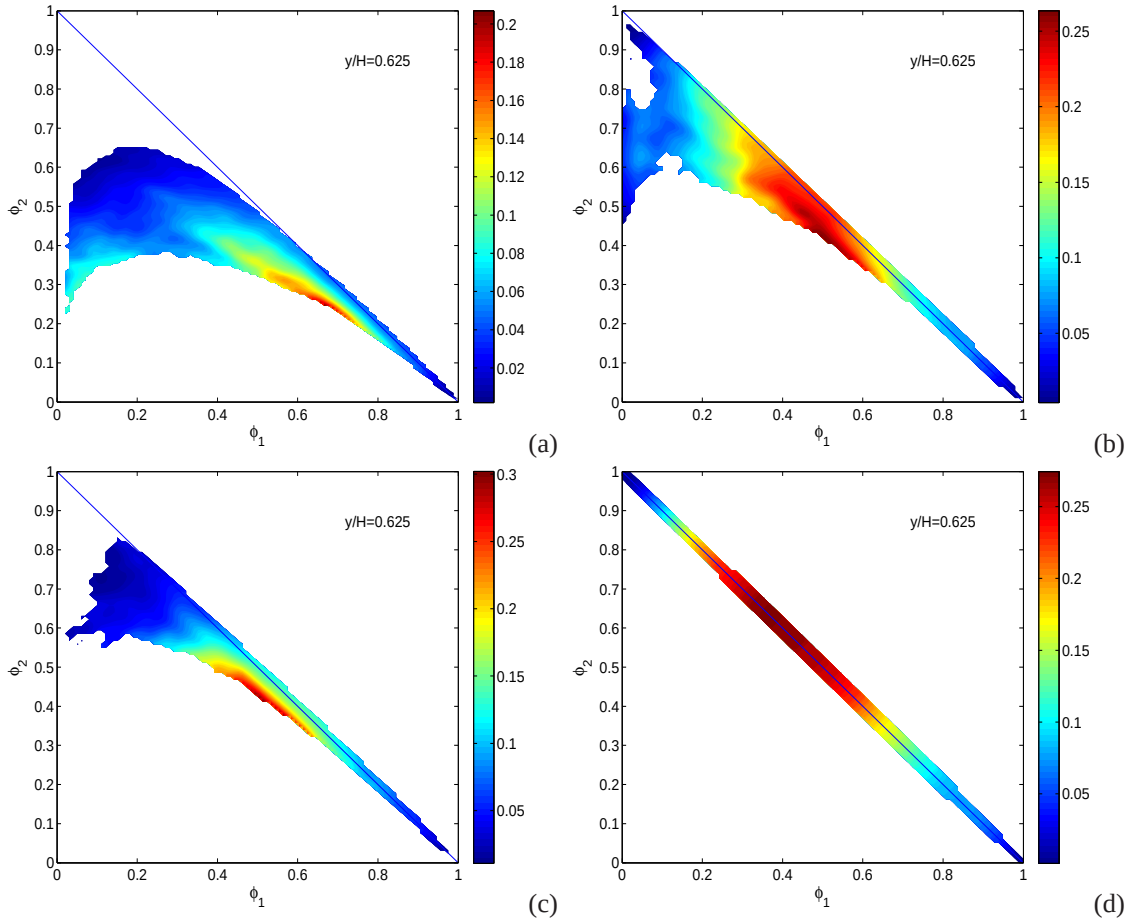

Figure 6.8: Conditional scalar dissipation rate for ϕ_2 at 10 t_{jet}, $y/H = 0.625$ for (a) case 1, (b) case 2, (c)

case 3, and (d) case 4.

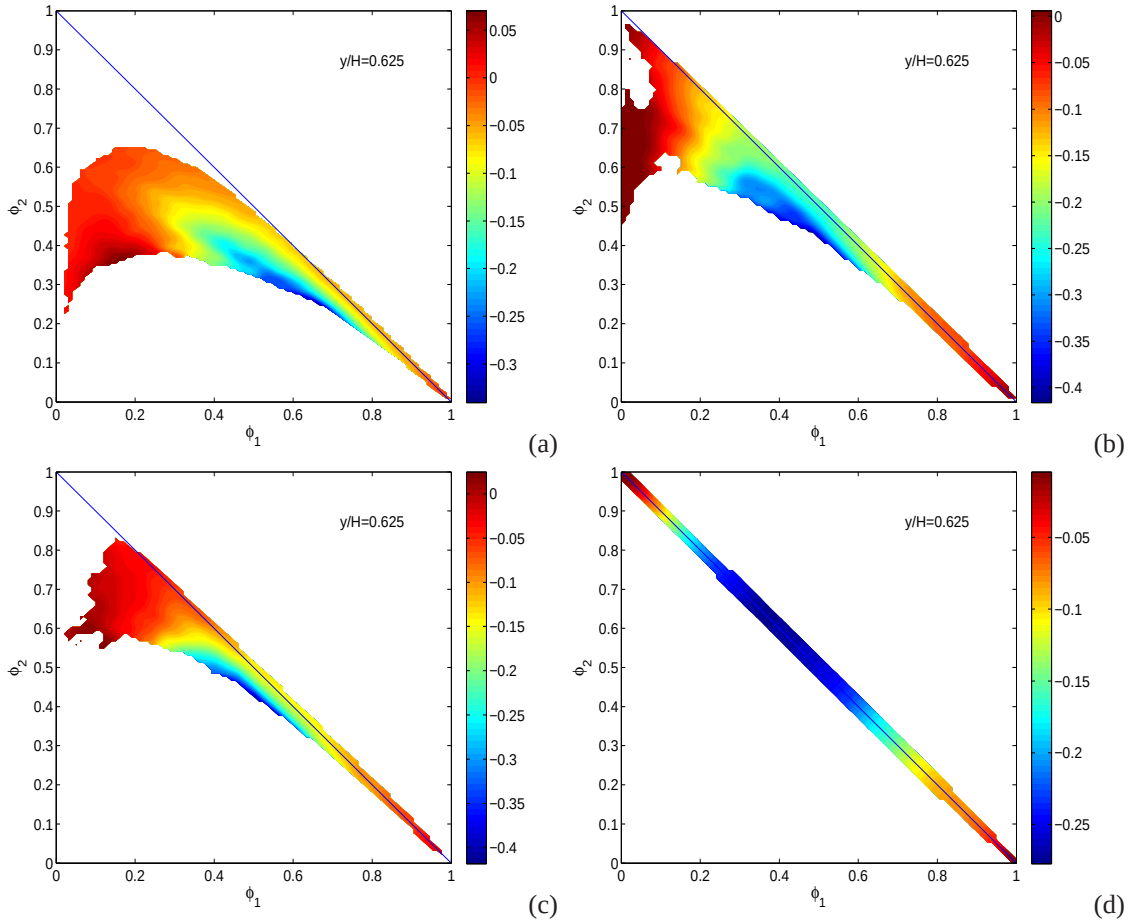

Figure 6.9: Conditional cross-dissipation rate χ_{12} at 10 t_{jet}, $y/H = 0.625$ for (a) case 1, (b) case 2, (c) case 3, and (d) case 4.

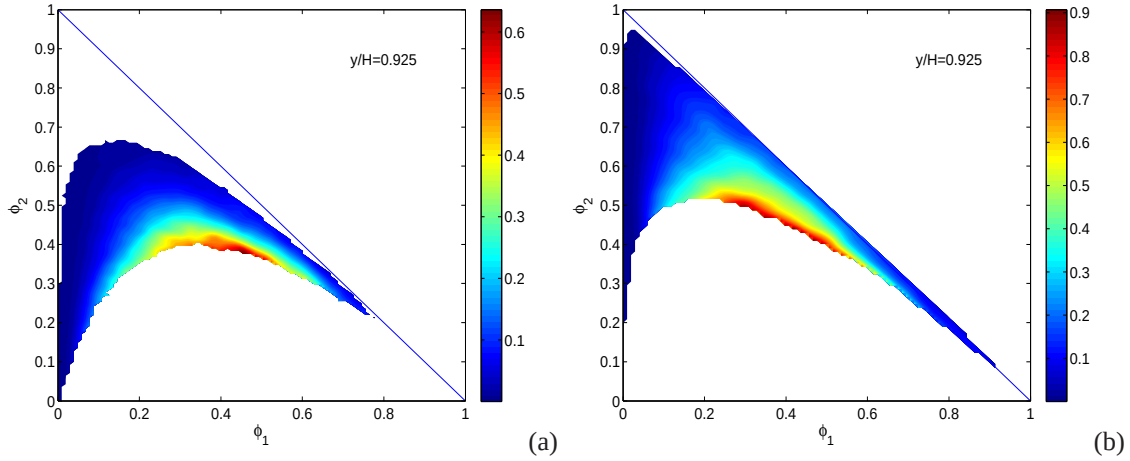

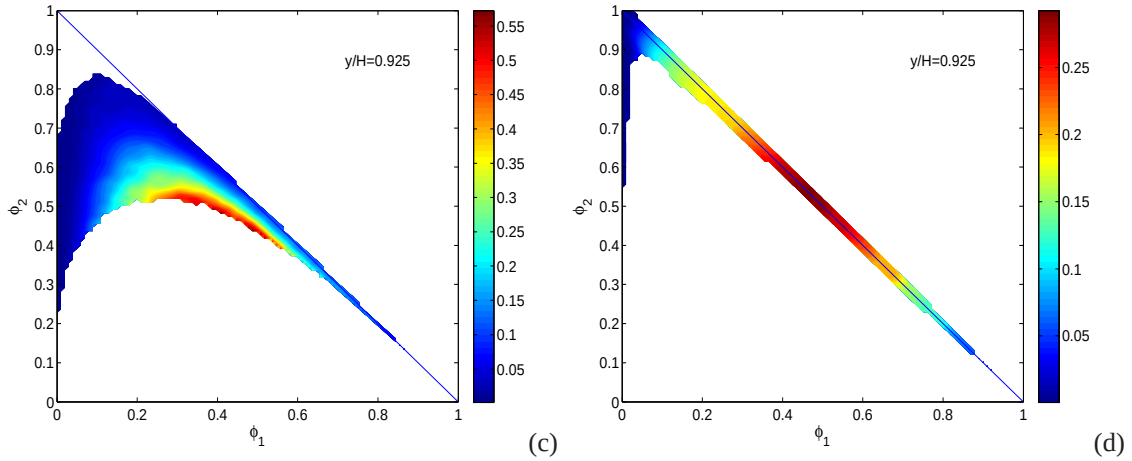

Figure 6.10: Conditional scalar dissipation rate for ϕ_1 at 10 t_{jet}, $y/H = 0.925$ for (a) case 1, (b) case 2, (c) case 3, and (d) case 4.

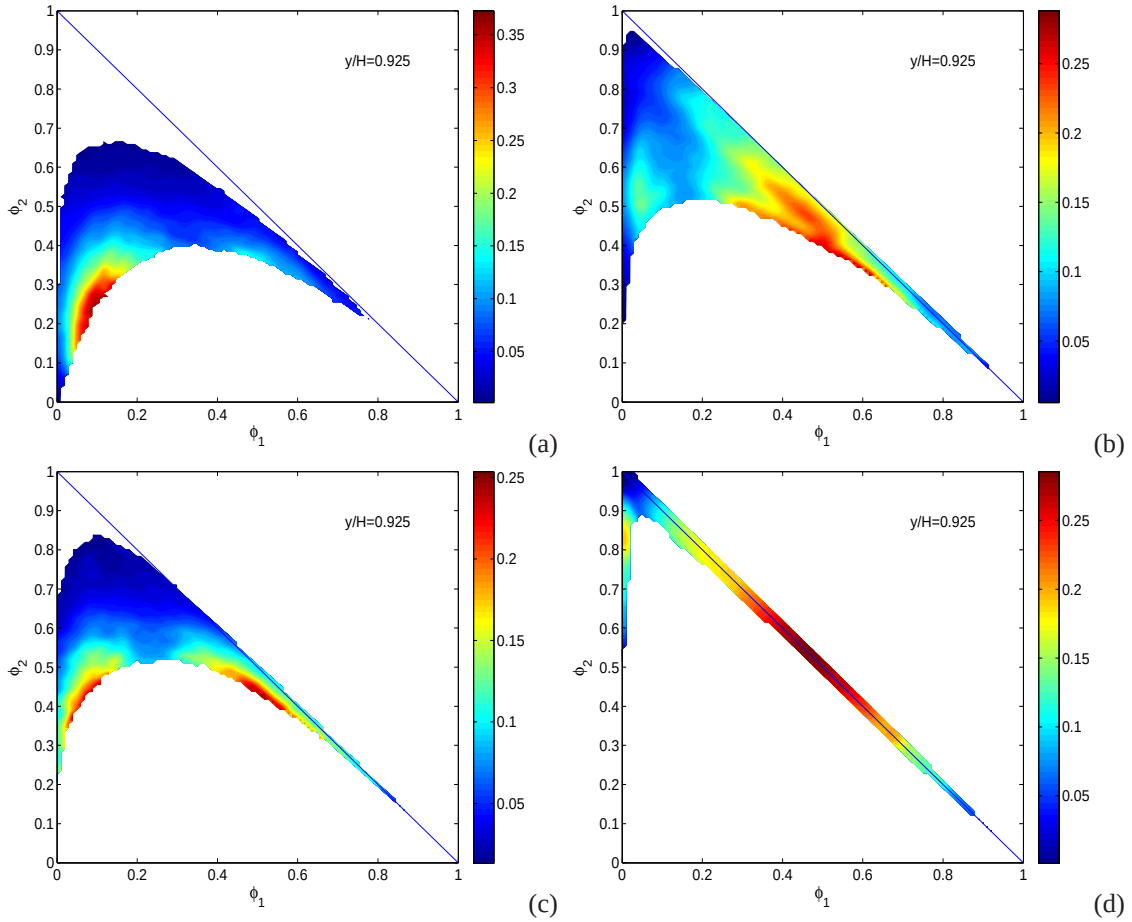

Figure 6.11: Conditional scalar dissipation rate for ϕ_2 at 10 t_{jet}, $y/H = 0.925$ for (a) case 1, (b) case 2, (c)

case 3, and (d) case 4.

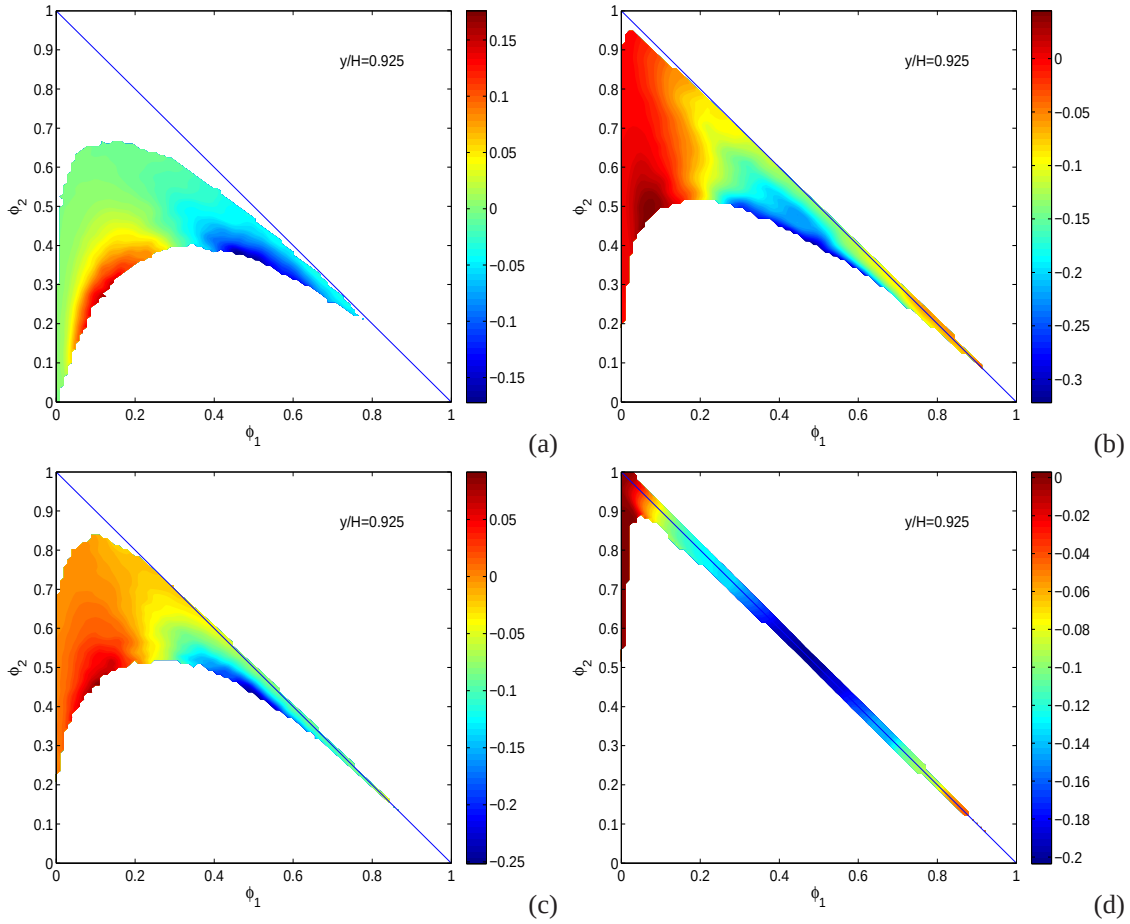

Figure 6.12: Conditional cross-dissipation rate χ_{12} at 10 t_{jet}, $y/H = 0.925$ for (a) case 1, (b) case 2, (c) case 3, and (d) case 4.

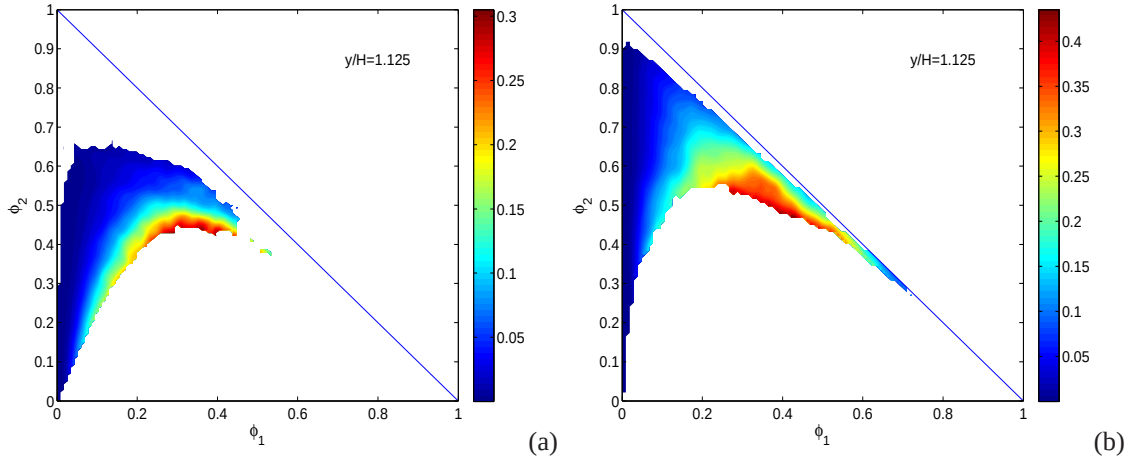

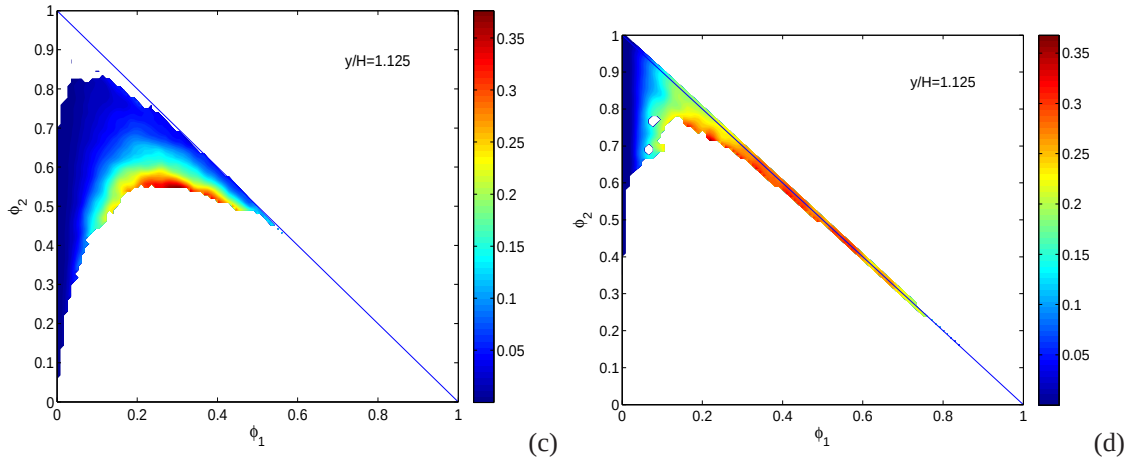

Figure 6.13: Conditional scalar dissipation rate for ϕ_1 at 10 t_{jet}, $y/H = 1.125$ for (a) case 1, (b) case 2, (c) case 3, and (d) case 4.

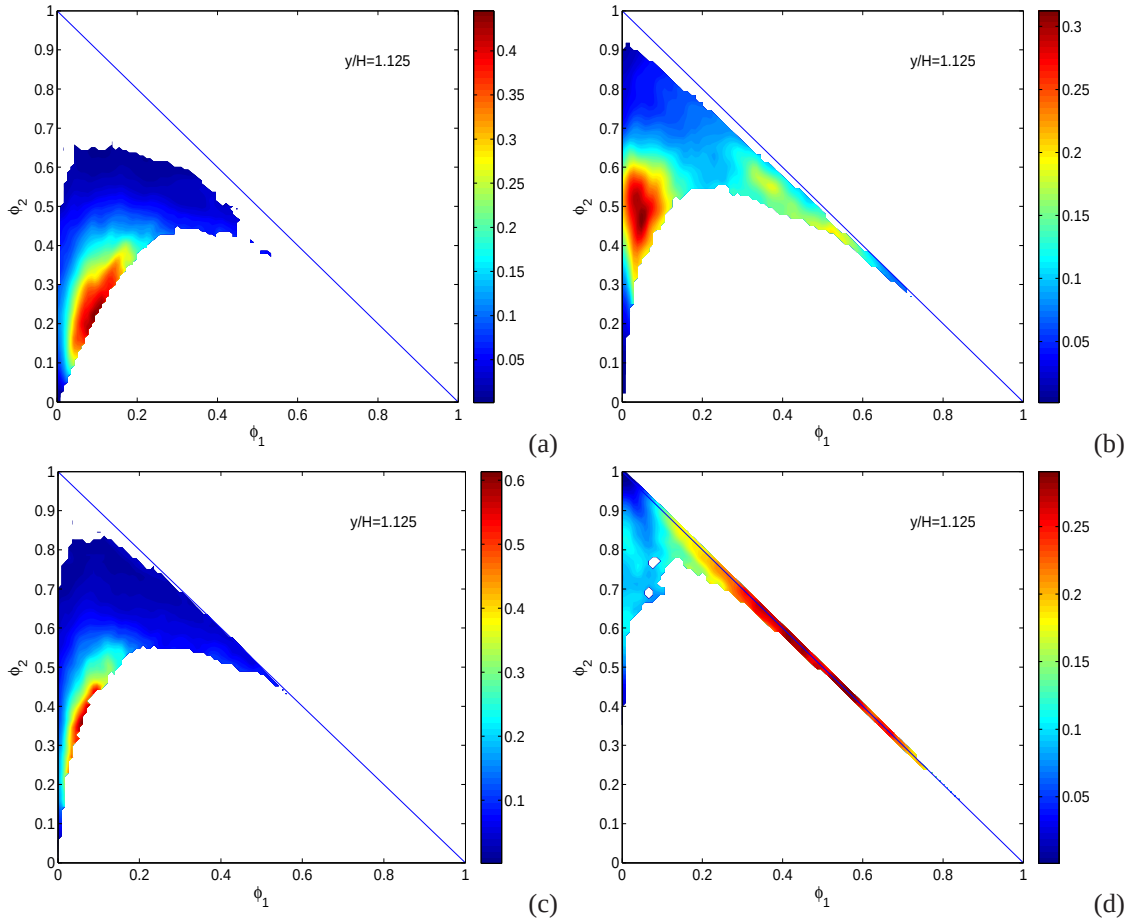

Figure 6.14: Conditional scalar dissipation rate for ϕ_2 at 10 t_{jet}, $y/H = 1.125$ for (a) case 1, (b) case 2, (c)

case 3, and (d) case 4.

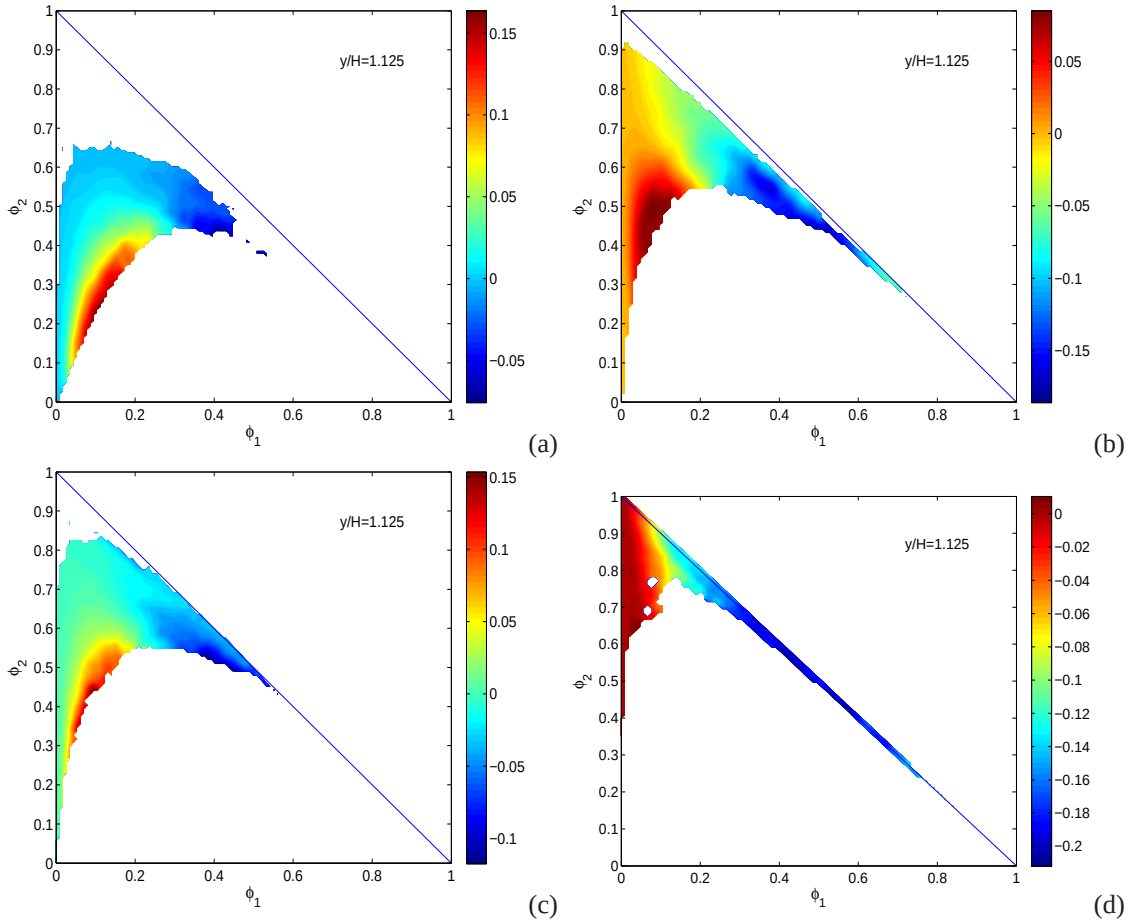

Figure 6.15: Conditional cross-dissipation rate χ_{12} at 10 t_{jet}, $y/H = 1.125$ for (a) case 1, (b) case 2, (c) case 3, and (d) case 4.

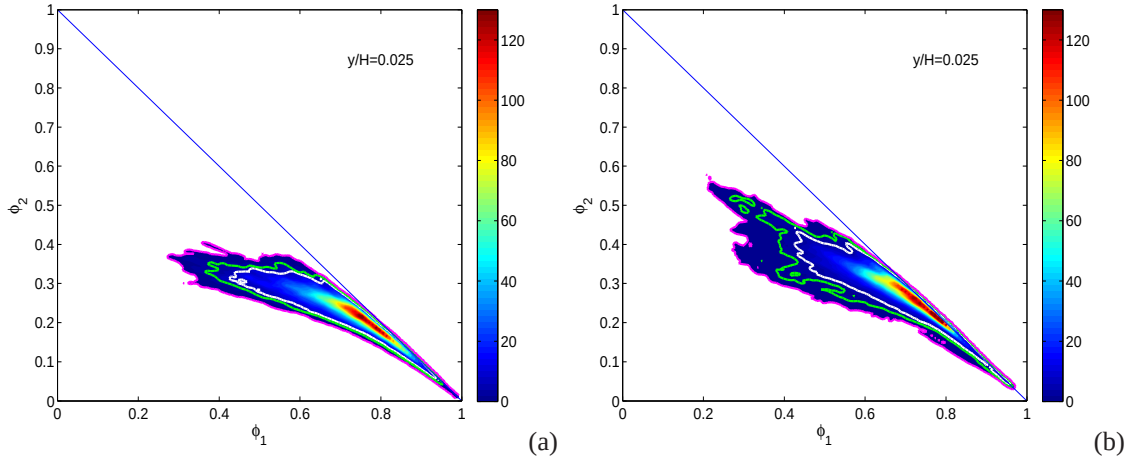

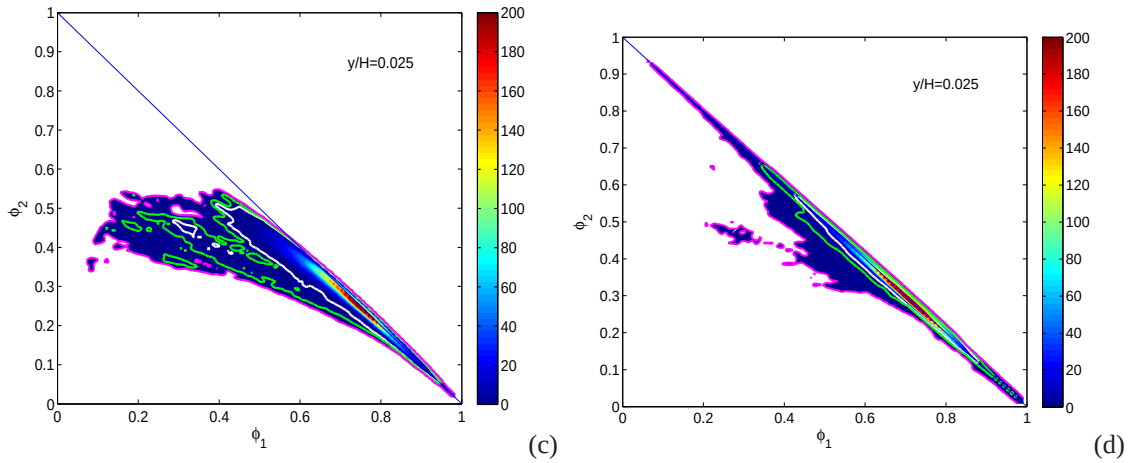

Figure 6.16: Scalar JPDF at 20 t_{jet}, $y/H = 0.025$ for (a) case 1, (b) case 2, (c) case 3, and (d) case 4.

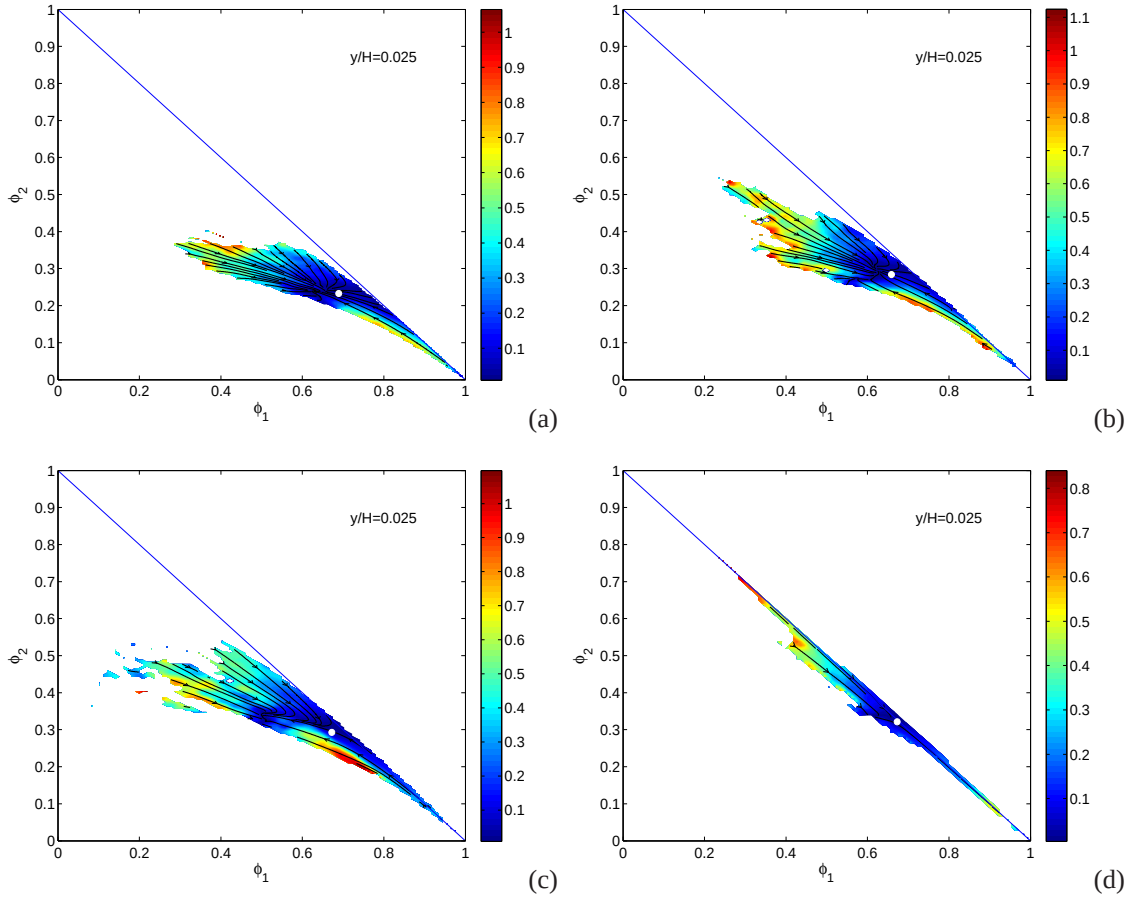

Figure 6.17: Conditional diffusion at 20 t_{jet}, $y/H = 0.025$ for (a) case 1, (b) case 2, (c) case 3, and (d) case 4.

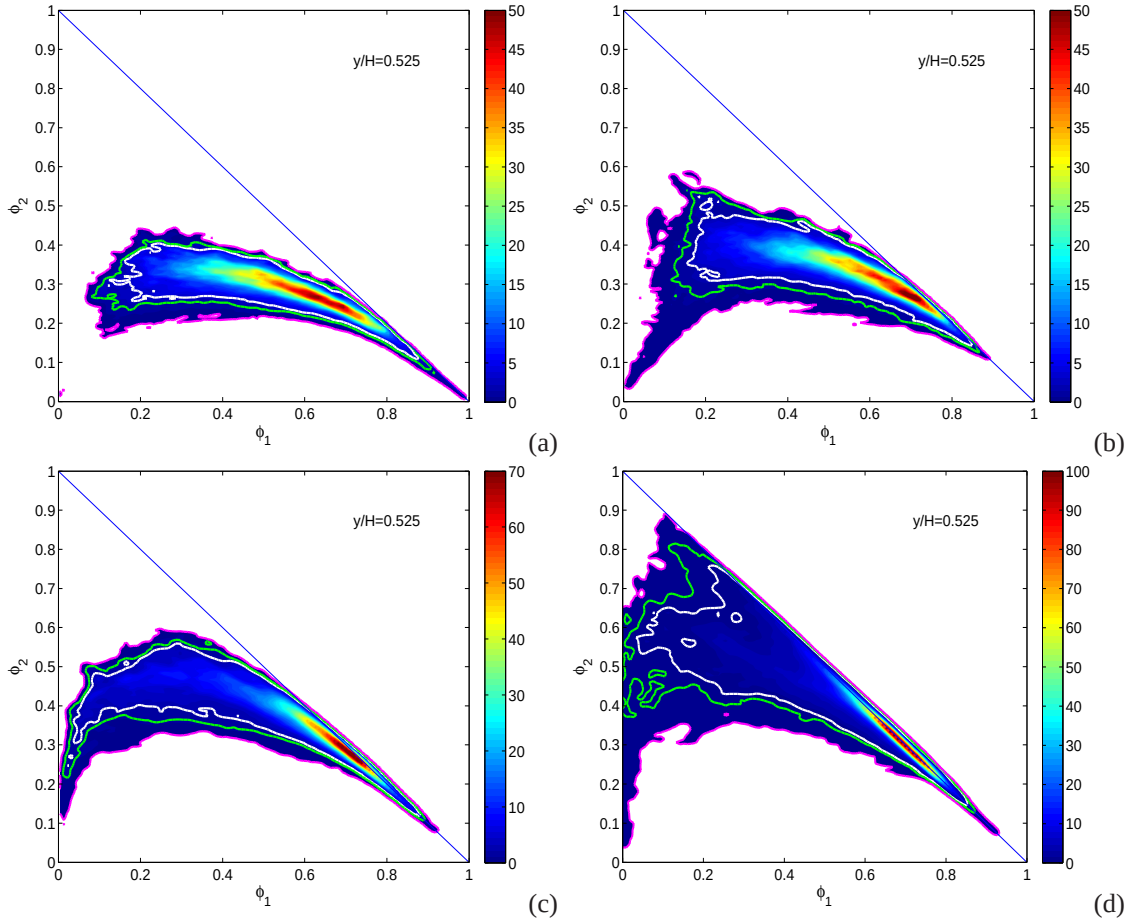

Figure 6.18: Scalar JPDF at 20 t_{jet}, $y/H = 0.525$ for (a) case 1, (b) case 2, (c) case 3, and (d) case 4.

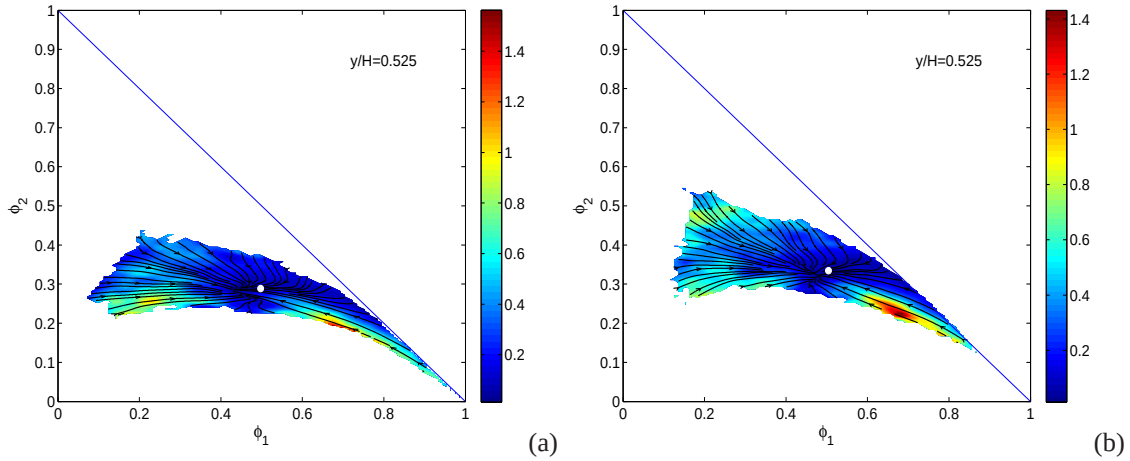

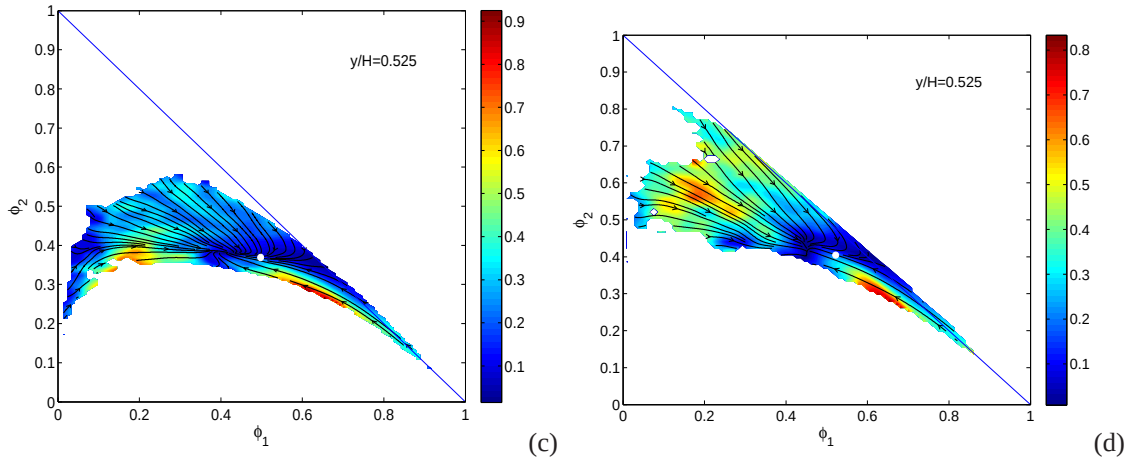

Figure 6.19: Conditional diffusion at 20 t_{jet}, $y/H = 0.525$ for (a) case 1, (b) case 2, (c) case 3, and (d) case 4.

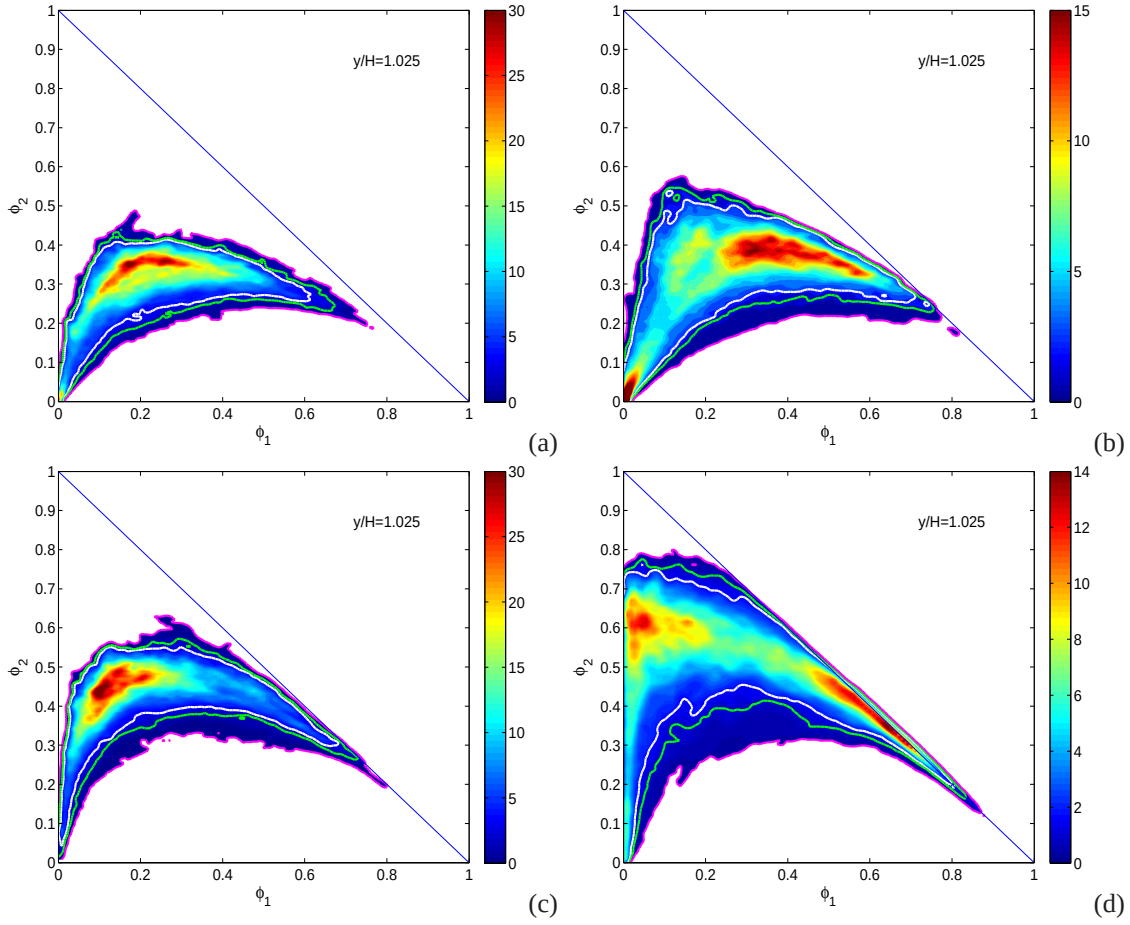

Figure 6.20: Scalar JPDF at 20 t_{jet}, $y/H = 1.025$ for (a) case 1, (b) case 2, (c) case 3, and (d) case 4.

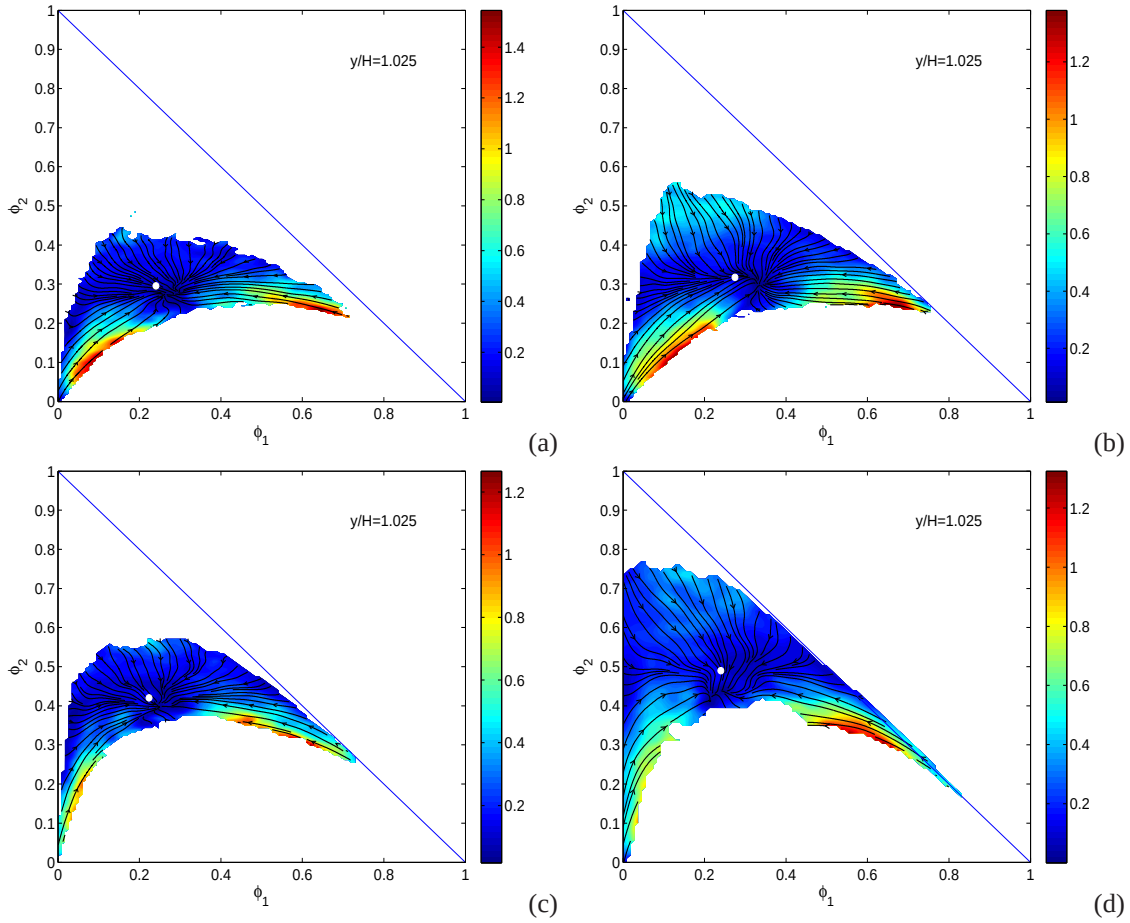

Figure 6.21: Conditional diffusion at 20 t_{jet}, $y/H = 1.025$ for (a) case 1, (b) case 2, (c) case 3, and (d) case 4.

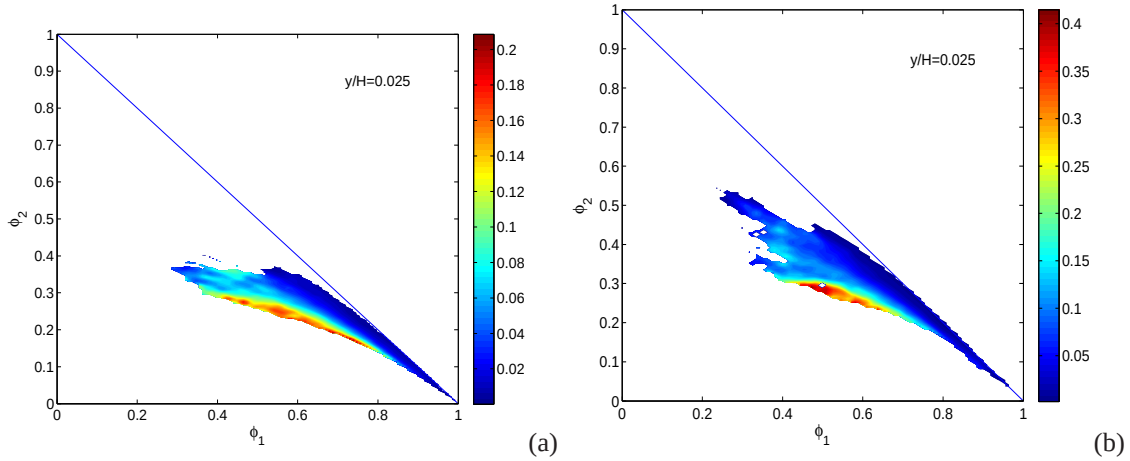

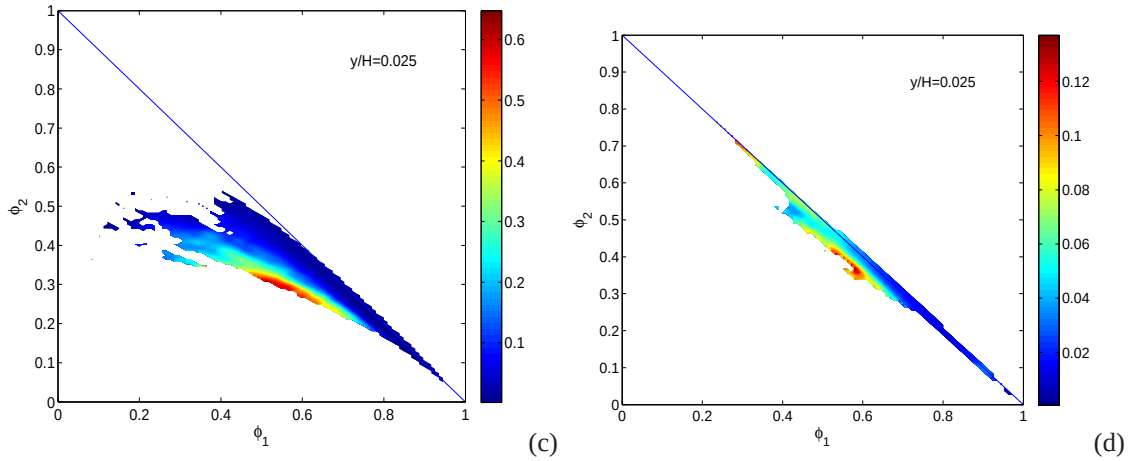

Figure 6.22: Conditional scalar dissipation rate for ϕ_1 at 20 t_{jet}, $y/H = 0.025$ for (a) case 1, (b) case 2, (c) case 3, and (d) case 4.

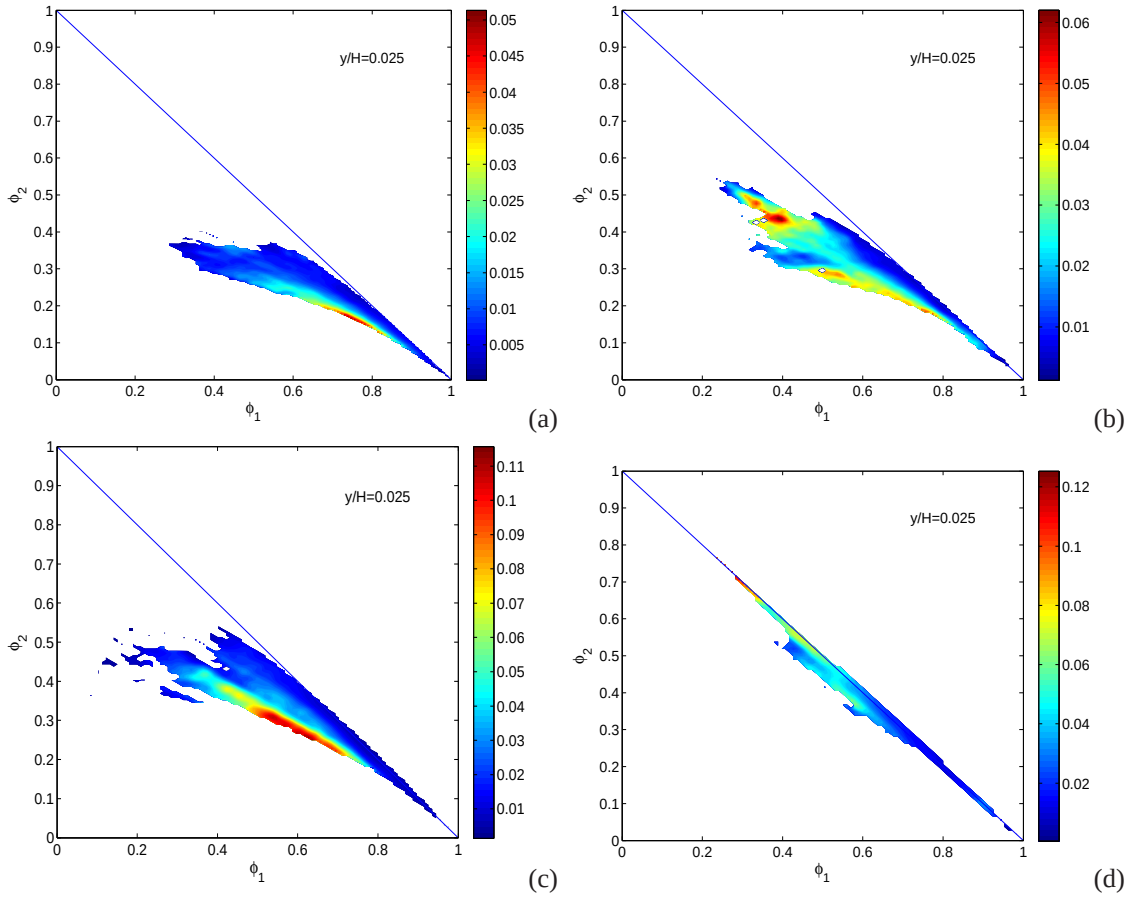

Figure 6.23: Conditional scalar dissipation rate for ϕ_2 at 20 t_{jet}, $y/H = 0.025$ for (a) case 1, (b) case 2, (c)

case 3, and (d) case 4.

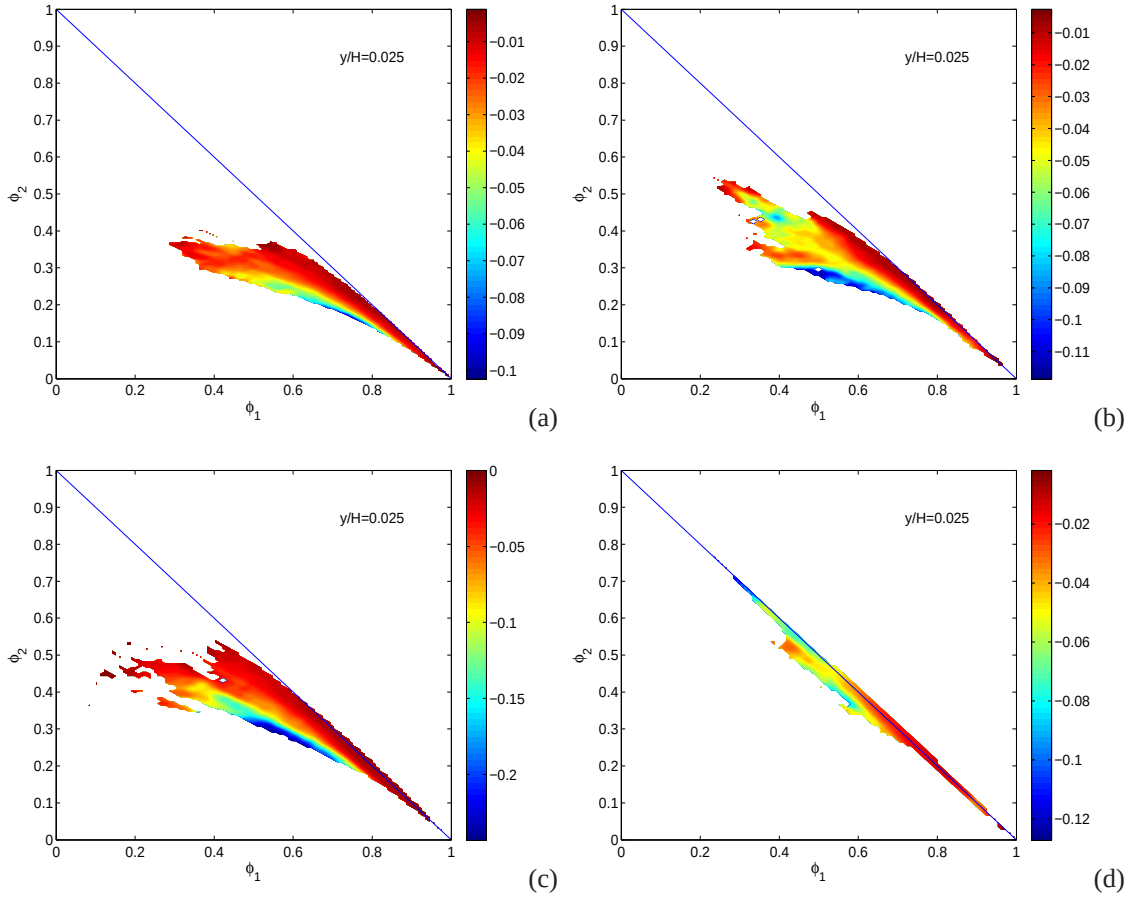

Figure 6.24: Conditional cross-dissipation rate χ_{12} at 20 t_{jet}, $y/H = 0.025$ for (a) case 1, (b) case 2, (c) case 3, and (d) case 4.

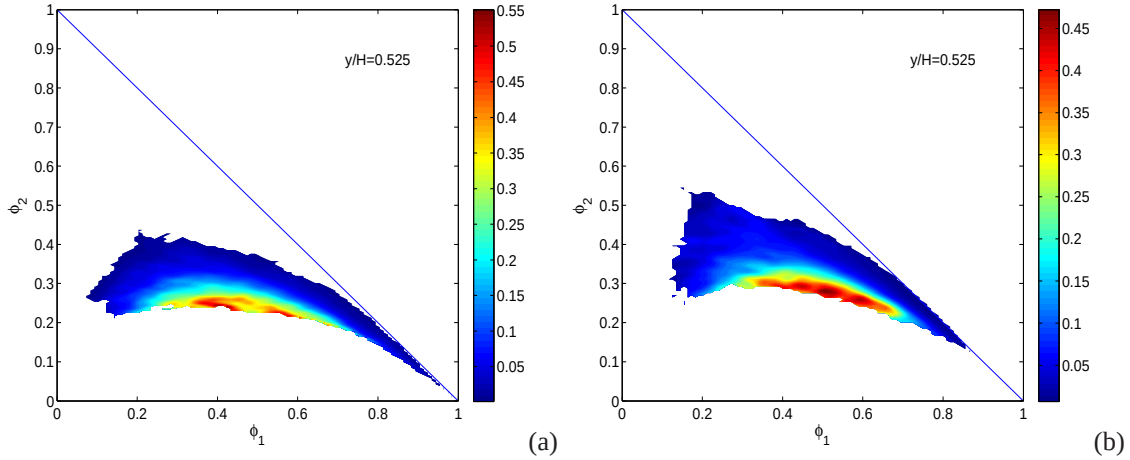

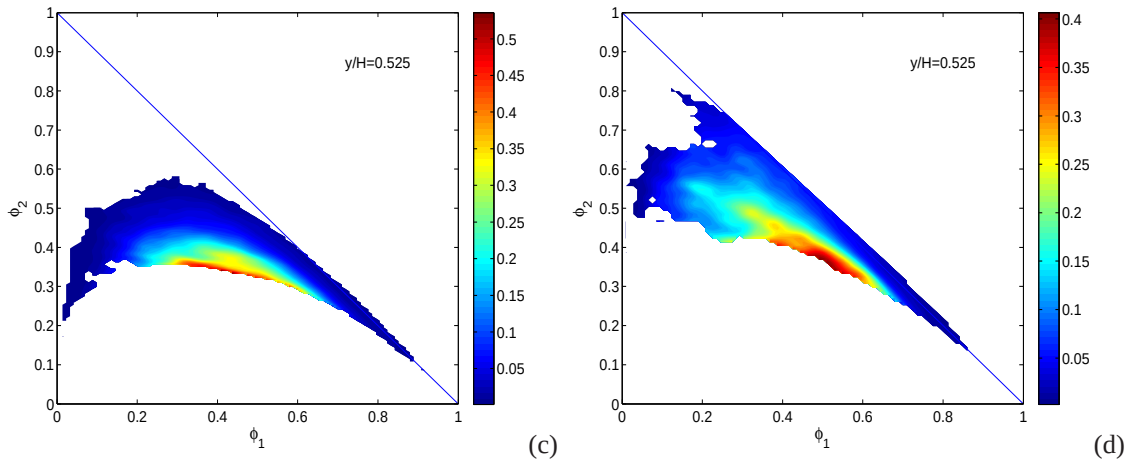

Figure 6.25: Conditional scalar dissipation rate for ϕ_1 at 20 t_{jet}, $y/H = 0.525$ for (a) case 1, (b) case 2, (c) case 3, and (d) case 4.

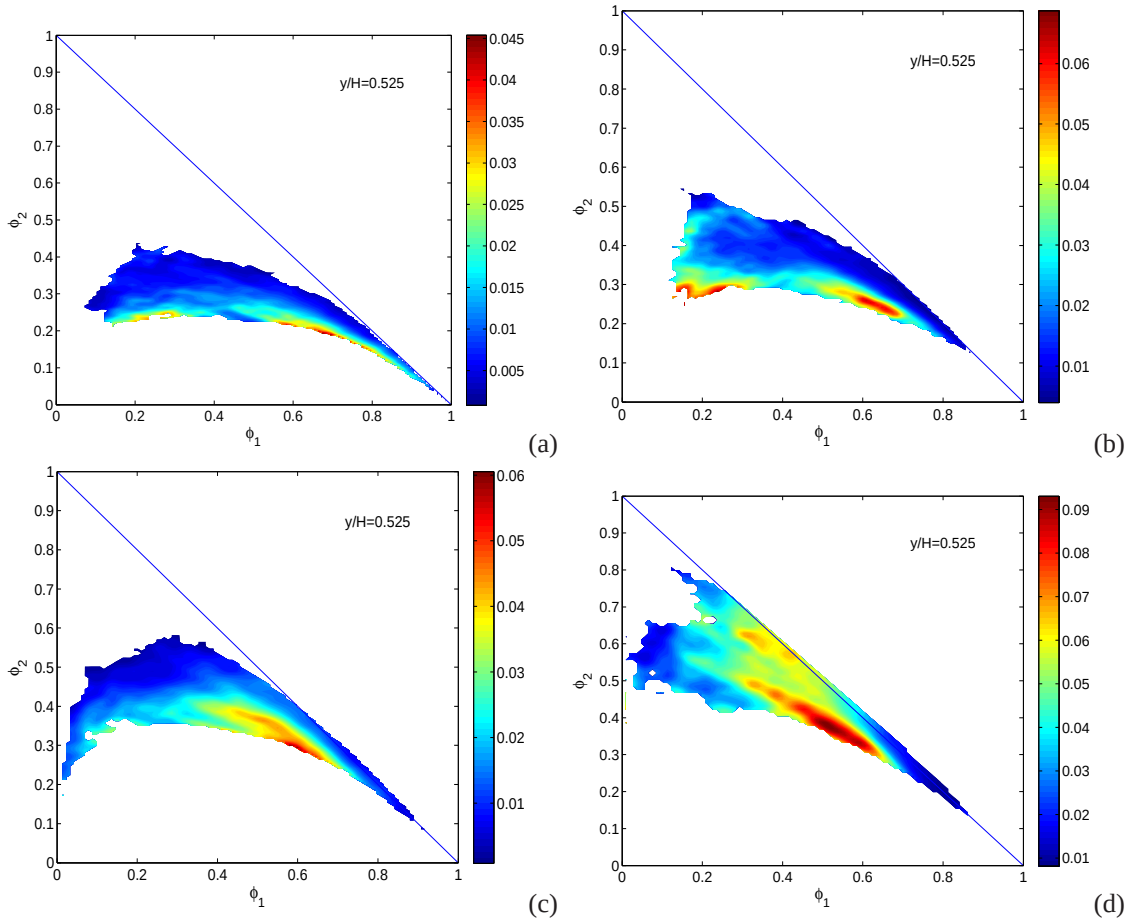

Figure 6.26: Conditional scalar dissipation rate for ϕ_2 at 20 t_{jet}, $y/H = 0.525$ for (a) case 1, (b) case 2, (c)

case 3, and (d) case 4.

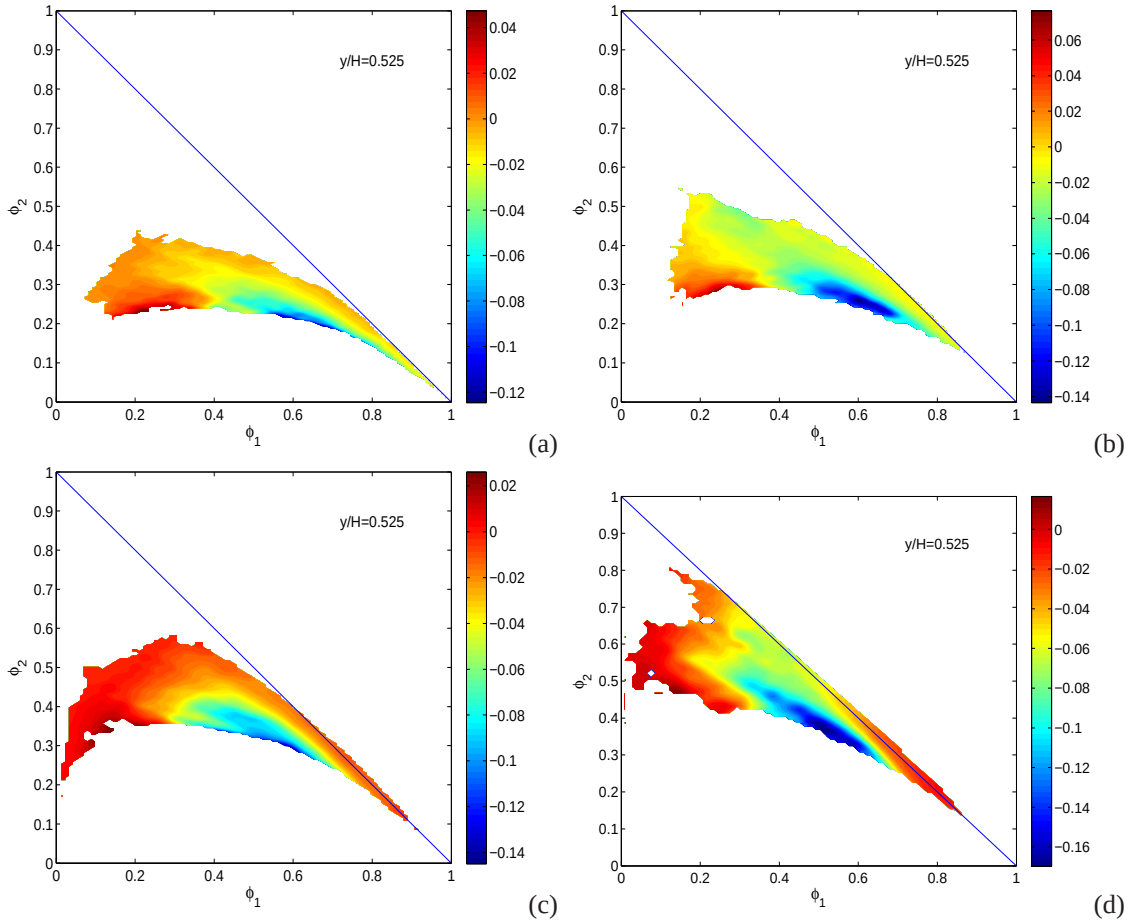

Figure 6.27: Conditional cross-dissipation rate at 20 t_{jet}, $y/H = 0.525$ for (a) case 1, (b) case 2, (c) case 3, and (d) case 4.

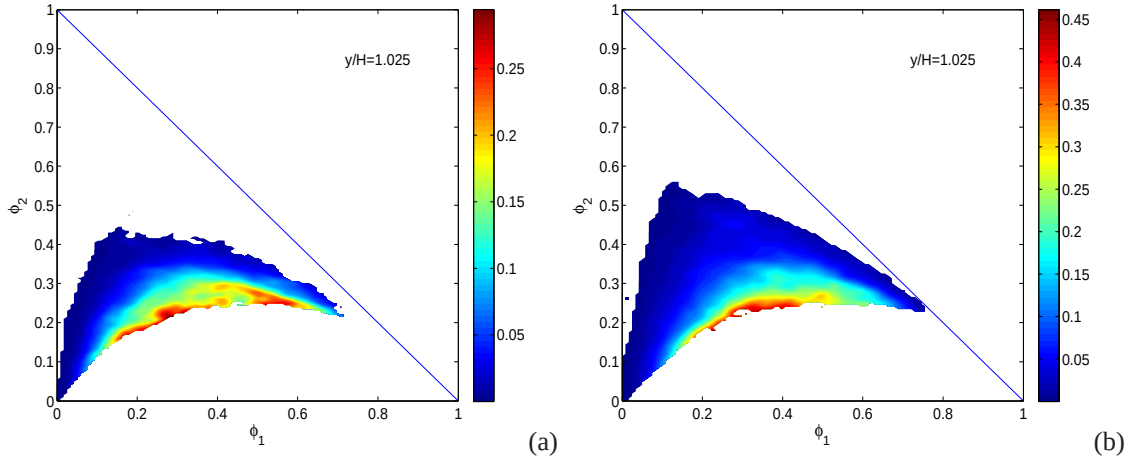

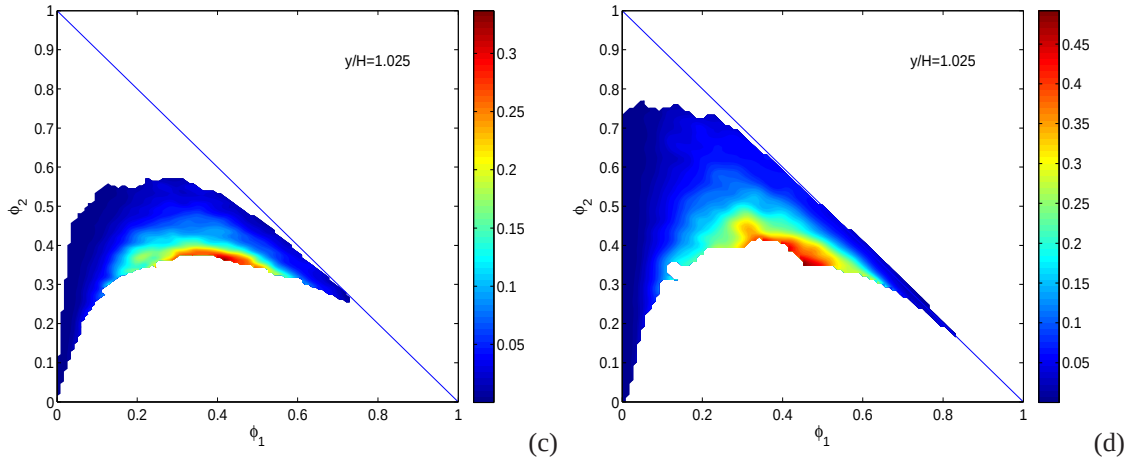

Figure 6.28: Conditional scalar dissipation rate for ϕ_1 at 20 t_{jet}, $y/H = 1.025$ for (a) case 1, (b) case 2, (c) case 3, and (d) case 4.

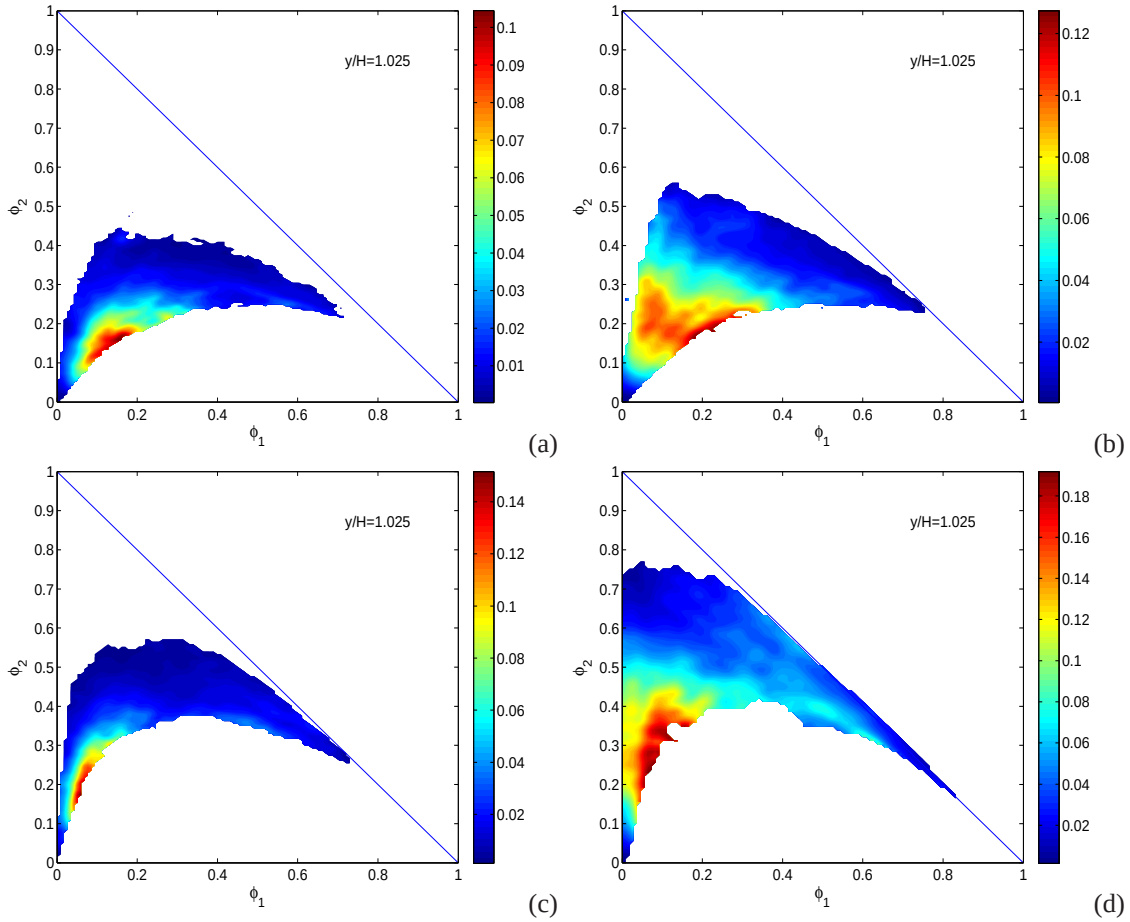

Figure 6.29: Conditional scalar dissipation rate for ϕ_2 at 20 t_{jet}, $y/H = 1.025$ for (a) case 1, (b) case 2, (c)

case 3, and (d) case 4.

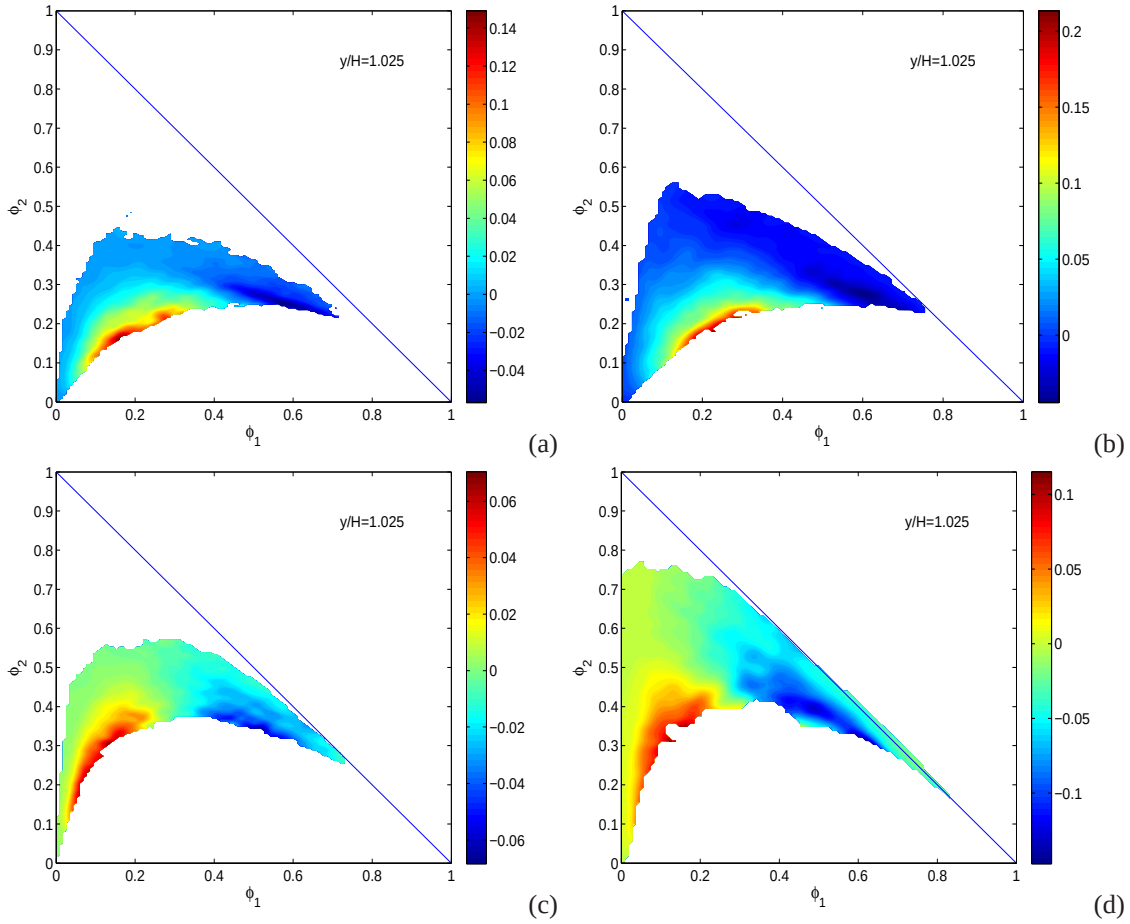

Figure 6.30: Conditional cross-dissipation rate χ_{12} for ϕ_2 at 20 t_{jet}, $y/H = 1.025$ for (a) case 1, (b) case 2, (c) case 3, and (d) case 4.

Chapter 7

Summary and conclusions

In the first part of this work, SGS mixing of mixture fraction, temperature, and species mass fractions are investigated using the filtered mass density function and the conditionally filtered diffusion from turbulent partially premixed flames (Sandia flames D and E).

The results shows the SGS mixing regimes for the mixture fraction have a strong influence on the SGS mixing of species mass fractions. For small SGS variance, the FMDF is unimodal. For samples close to equilibrium the diffusion streamlines generally converge to a manifold and then move towards a stagnation point. At lower temperatures, the streamlines converge to another manifold and stagnation point at approximately 1600K, due to the SGS mixing between burning and extinguished samples. For large SGS variance, the FMDF is bimodal. The diffusion streamline pattern is consistent with burning and extinguished flamelets. Some SGS mixing among these flamelets appear to be along the iso-mixture fraction surface (flamelet-flamelet interaction).

The mixing configuration of the mixture fraction, temperature and a species mass fraction, which results from the turbulence-chemistry interaction, has a strong influence on the SGS mixing of the species mass fraction. Due to its strong correlations with the temperature, the SGS mixing of Y_{CO_2} (and Y_{H_2O}) is similar to that of temperature. Thus, the SGS mixing of ξ, T, and Y_{CO_2} can largely be represented by a two-dimensional manifold, and therefore is degenerated. On the other hand, the rapid depletion of Y_{CO} on the lean side results in a more complex mixing configuration, and the SGS mixing of ξ, T, and Y_{CO} must be represented by a three-dimensional manifold and is non-degenerated.

The present study shows that both the SGS mixing regimes and the SGS mixing configurations have a strong influence on the SGS mixing of the species mass fractions. The results present a challenging test for

SGS mixing models.

In the second part of the work, we use data obtained in turbulent partially premixed flames (Sandia flames) to study SGS mixing of temperature perturbations from steady flamelets. The Favre filtered mixture fraction and Favre filtered SGS scalar variance were used as conditioning variables for analyzing the conditionally filtered dissipation and diffusion of temperature perturbations. We focus on the temperature and Y_{H_2O} in flame E at $x/d = 30$ where the Reynolds number is high and the differential diffusion effects for these variables are negligible. We chose the flamelet with $T^f(Z,\chi_s^f)$ closest to the conditionally filtered temperature $\left\langle \langle T|Z\rangle_L \,|\, \langle Z\rangle_L, \left\langle Z''^2\right\rangle_L \right\rangle$ for the burning samples. Due to the limited amount of data available, we obtained results for one large SGS variance value. If other values are chosen, the dissipation rate χ_s for flamelets that match the conditional mean values will vary. Since $\left\langle Z''^2\right\rangle_L$ is a fluctuations in a turbulent flame, so does χ_s, allowing the analysis to account for the scalar dissipation rate fluctuations.

The results show that for large SGS variance, the streamline representing the conditionally filtered diffusion of mixture fraction and reactive scalar perturbations for the nearly fully burning samples generally converge quickly to a manifold close to $\phi^f(Z,\chi_s^f)$, along which they continue at lower velocities, i.e., the dominant effect of the diffusion is to reduce ϕ^*. The conditionally filtered dissipation rate of reactive scalar perturbations is generally much smaller than the value from the flamelet part. The peak value is near $\xi = 0.4 - 0.45$ at lower temperature where the maximum gradient in the ramp-cliff structure is located. These mixing patterns are very similar to those of three non-reactive scalar mixing in a turbulent coaxial jet. Further analysis shows that the functional form of the diffusion is well described by the IEM model.

Our perturbation analysis of the flamelet equation shows that for perturbations having length scales smaller than the reaction zone width, the reactive scalar diffusion are largely controlled by the mixture fraction field, thus having the characteristics of non-reactive scalar mixing. This type of perturbations probably requires high Reynolds numbers so that the scalar dissipation length scale is smaller than the reaction zone width. For perturbations with length scales larger than the reaction width, which are consistent with unsteady or quasi-steady flamelets, the conditionally filtered diffusion has the same form as non-reactive scalar mixing, with the mixing time scale depending on Z_s and ΔZ_R. The IEM model predictions based on this mixing time scale are in good agreement with the experimental results for a range of SGS conditions, suggesting that the perturbations for the conditions studied are consistent with unsteady or quasi-steady flamelets.

The present study suggest that mixing models that are based on non-reactive scalars can potentially model the mixing of the reactive scalar perturbations from flamelets accurately. Because the mixing models do not need to model the flamelet part, the total reactive scalar diffusion (the flamelet part plus the

perturbations) can be modeled more accurately. Since most current mixing models already perform well for distributed reaction zones, the results in the present study can be useful for developing a unified mixing model that can predict all combustion regimes, including distributed reaction zones and flamelets accurately.

In the third part of the work, three-scalar mixing in temporally developing plane jets using direct numerical simulation (DNS). The flow configuration consists of five streams: a central jet, two off-central jets surround the central jet, and two coflows surround the off-central jets. The mixing process of the flow are analyzed in detail using joint probability density functions (JPDF), conditional diffusion, and conditional dissipation rate. The results show that the mixing process is greatly affected by length and velocity ratio between the central and off-central jet, with high quality of mixing favored by high initial velocity gradients and high ratios between the central and off-central jet widths. The scalar JPDF and the conditional dissipation rates obtained in current simulations show some similarities to these of mixture fraction and temperature in turbulent flames. The present study, therefore, provide a basis for understanding the multiscalar mixing in reactive flows.

Appendices

Appendix A Mean square error (MSE) estimation of kernel density estimator and kernel regression

A.1 MSE estimation of kernel density estimator

Given $x_1, x_2, ..., x_n$ independent and identically distributed variables which have a distribution of $f(x)$, the kernel density estimator on the kernel K and bandwidth h is defined as

$$K_n(y) = \frac{1}{nh}\sum_{i=1}^{n} K(\frac{y-x_i}{h}) \tag{1}$$

The mean square error (MSE) of the estimator is defined as $MSE(y) = E([K_n(y) - f(y)]^2)$ which could be separated into bias term and variance term:

$$\begin{aligned} MSE(y) &= E([K_n - E(K_n) + E(K_n) - f]^2) = E(K_n^2) - E^2(K_n) + (E(K_n) - f)^2 && (2)\\ Bias &= E(K_n) - f, \quad Variance = E(K_n^2) - E^2(K_n) && (3) \end{aligned}$$

Substitute the kernel estimator and transform the variable through $x_i = y - hu,\ dx_i = -hdu$, the bias and variance terms can be calculated by

$$\begin{aligned} Bias &= E(K_n) - f = \frac{1}{nh}\int \sum K(\frac{y-x_i}{h}) f(x_i) dx_i - f \\ &= \frac{1}{nh}\sum \int hK(u) f(y-hu) du = \int K(u) f(y-hu) du - f && (4)\\ E(K_n^2) &= \int \{\frac{1}{nh}\sum K(\frac{y-x_i}{h})\}^2 dx_i \\ &= \frac{1}{n^2h^2}\int \sum K^2(\frac{y-x_i}{h}) f(x_i) dx_i + \frac{n^2-n}{n^2h^2}[\int K(\frac{y-x_i}{h}) f(x_i) dx_i]^2 && (5)\\ E^2(K_n) &= [\frac{1}{nh}\int \sum K(\frac{y-x_i}{h}) f(x_i) dx_i]^2 = \frac{1}{h^2}[\int K(\frac{y-x_i}{h}) f(x_i) dx_i]^2 && (6)\\ Variance &= E(K_n^2) - E^2(K_n) = \frac{1}{nh}\int K^2(u) f(y-hu) du - \frac{1}{n}[\int K(u) f(y-hu) du]^2 && (7) \end{aligned}$$

If sampling from the distribution of $K_n = \frac{1}{nh}\sum K(\frac{y-x_i}{h})$, and get n iid random variables $x_1^*, x_2^*, ..., x_n^*$, the kernel estimator of the sampling variable is $K_n^* = \frac{1}{nh}\sum K(\frac{y-x_i^*}{h})$, and we could use the $Bias(K_n^*)$ and $Variance(K_n^*)$ as the estimator for $Bias(K_n)$ and $Variance(K_n)$ [65, 95]. Typically, sampling from the distribution of K_n is needed. Fortunately, when the kernel function is Gaussian type, the $Bias(K_n^*)$ and $Variance(K_n^*)$

have analytical forms. Notice that the samples $x_1^*, x_2^*, ..., x_n^*$ are from the distribution of $K_n = \frac{1}{nh}\sum K(\frac{y-x_i}{h})$, thus $K_n = f$ is substitute in eqns. 4-7 for calculating the bias and variance. The calculation procedures are showed in eqns.8-13. After getting the expression for $\int K(u)K_n(y-hu)du$ and $\int K^2(u)K_n(y-hu)du$, the final expressions for $Bias(K_n^*)$ and $Variance(K_n^*)$ are showed in eqns. 14-15.

$$\begin{aligned}
\int K(u)K_n(y-hu)du &= \int \frac{1}{\sqrt{2\pi}}\exp(-\frac{u^2}{2})\frac{1}{nh}\sum K(\frac{y-hu-x_i}{h})du \\
&= \frac{1}{nh}\sum\int \frac{1}{\sqrt{2\pi}}\exp(-\frac{u^2}{2})\frac{1}{\sqrt{2\pi}}\exp(-\frac{(y-hu-x_i)^2}{2h^2})du \\
&= \frac{1}{nh}\sum\phi_i \qquad (8) \\
\phi_i &= \int \frac{1}{2\pi}\exp[-\frac{u^2}{2}-\frac{(y-x_i)^2}{2h^2}-\frac{u^2}{2}+\frac{2hu(y-x_i)}{2h^2}]du \\
&= \frac{1}{2\sqrt{\pi}}\exp[-\frac{(y-x_i)^2}{4h^2}] \qquad (9)
\end{aligned}$$

$$\begin{aligned}
\int K(u)K_n(y-hu)du &= \frac{1}{nh}\sum\frac{1}{2\sqrt{2\pi}}\exp[-\frac{(y-x_i)^2}{4h^2}] \\
&= \frac{1}{n\sqrt{2}h}\sum\frac{1}{\sqrt{2\pi}}\exp[-\frac{1}{2}(\frac{y-x_i}{\sqrt{2}h})^2] \\
&= \frac{1}{n\lambda_1}\sum K(\frac{y-x_i}{\lambda_1}) \qquad (\lambda_1 = \sqrt{2}h) \qquad (10)
\end{aligned}$$

$$\begin{aligned}
\int K^2(u)K_n(y-hu)du &= \int \frac{1}{2\pi}\exp(-u^2)\sum K(\frac{y-hu-x_i}{h})du \\
&= \frac{1}{nh}\sum\int \frac{1}{2\pi}\exp(-u^2)\frac{1}{\sqrt{2\pi}}\exp[-\frac{(y-hu-x_i)^2}{2h^2}]du \\
&= \frac{1}{nh}\frac{1}{2\pi}\frac{1}{\sqrt{2\pi}}\sum\phi_i \qquad (11) \\
\phi_i &= \int \exp(-u^2)\exp[-\frac{(y-x_i)^2}{2h^2}-\frac{u^2}{2}+\frac{2hu(y-x_i)}{2h^2}]du \\
&= \sqrt{\frac{2\pi}{3}}\exp[-\frac{(y-x_i)^2}{3h^2}] \qquad (12)
\end{aligned}$$

$$\begin{aligned}\int K^2(u)K_n(y-hu)du &= \frac{1}{nh}\frac{1}{2\sqrt{3}\pi}\sum \exp[-\frac{(y-x_i)^2}{3h^2}] \\ &= \frac{1}{2\sqrt{\pi}}\frac{1}{n\sqrt{\frac{3}{2}}h}\sum\frac{1}{\sqrt{2\pi}\sqrt{\frac{3}{2}}h}\exp[-\frac{1}{2}(\frac{y-x_i}{\sqrt{\frac{3}{2}}h})^2] \\ &= \frac{1}{2\sqrt{\pi}}\frac{1}{n\lambda_2}\sum K(\frac{y-x_i}{\lambda_2}) \qquad (\lambda_2=\sqrt{\frac{3}{2}}h) \end{aligned} \tag{13}$$

$$Bias(K_n^*) = \frac{1}{n\lambda_1}\sum K(\frac{y-x_i}{\lambda_1}) - \frac{1}{nh}\sum K(\frac{y-x_i}{h}) \qquad (\lambda_1=\sqrt{2}h) \tag{14}$$

$$\begin{aligned} Variance(K_n^*) &= \frac{1}{nh}\frac{1}{2\sqrt{\pi}}\frac{1}{n\lambda_2}\sum K(\frac{y-x_i}{\lambda_2}) - \frac{1}{n}[\frac{1}{n\lambda_1}\sum K(\frac{y-x_i}{\lambda_1})]^2 \\ &= \frac{1}{2\sqrt{\pi}nh}\frac{1}{n\lambda_2}\sum K(\frac{y-x_i}{\lambda_2}) - \frac{1}{n}[\frac{1}{n\lambda_1}\sum K(\frac{y-x_i}{\lambda_1})]^2 \qquad (\lambda_2=\sqrt{\frac{3}{2}}h) \end{aligned} \tag{15}$$

A.2 MSE estimation of kernel regression

Let X and Y be two random variables whose relationship can be modeled as $Y = m(X) + \sigma(X)\varepsilon$ with $E\varepsilon = 0, var(\varepsilon) = 1$. If the $(p+1)th$ derivative of $m(x)$ at the point x_o exists, $m(x)$ can be approximated locally by a polynomial function of order p:

$$m(x) \approx m(x_o) + m'(x_o) + ... + m^{(p)}(x_o)(x-x_o)^p/p! \tag{16}$$

for x in a neighborhood of x_o [96, 97]. A local polynomial regression can be implemented to minimize the following:

$$\sum_{i=1}^{n}\{Y_i - \sum_{j=0}^{p}\beta_j(x_i-x_o)^j\}^2 K(\frac{x_i-x_o}{h}), \qquad j!\beta_j = m^{(j)}(x_o) \tag{17}$$

For convenience, the matrix form is used for the following derivation. Let W stand by the diagonal matrix with entries $W_i \equiv K(x_i-x_o)/h$. Let X be a design matrix whose $(l,j)th$ element is $(x_l-x_o)^{j-1}$ and let

$y = (Y_1, Y_2, .., Y_n)^T$, $\beta = (\beta_o, ..., \beta_p)^T$, then problem could be written in matrix form as

$$min\{E = (y - X\beta)^T W (y - X\beta)\} \tag{18}$$

To minimize the above equation, take the derivative with respect to β:

$$\begin{aligned} E &= y^T Wy - \beta^T X^T Wy - y^T WX\beta + \beta^T X^T WX\beta & (19)\\ \frac{dE}{d\beta} &= -X^T Wy - (y^T WX)^T + X^T WX\beta + (X^T WX)^T\beta \\ &= -2X^T Wy + 2X^T WX\beta & (20) \end{aligned}$$

Set $\frac{dE}{d\beta} = 0$, we have $\hat{\beta} = (X^T WX)^{-1} X^T Wy$. The variance of $\hat{\beta}$ is $var(\hat{\beta}) = E(\hat{\beta}\hat{\beta}^T) - E(\hat{\beta})E(\hat{\beta}^T)$. Equations 21-24 show the derivation for $var(\hat{\beta})$.

$$\begin{aligned} \hat{\beta}\hat{\beta}^T &= (X^T WX)^{-1} X^T Wy[(X^T WX)^{-1} X^T Wy]^T \\ &= (X^T WX)^{-1} X^T Wy(X^T Wy)^T (X^T WX)^{-1} \\ &= (X^T WX)^{-1} X^T Wyy^T WX(X^T WX)^{-1} & (21)\\ E(\hat{\beta}\hat{\beta}^T) &= (X^T WX)^{-1} X^T WE(yy^T) WX(X^T WX)^{-1} & (22)\\ E(\hat{\beta})E(\hat{\beta}^T) &= (X^T WX)^{-1} X^T WE(y)E(y^T) WX(X^T WX)^{-1} & (23)\\ var(\hat{\beta}) &= (X^T WX)^{-1} X^T \sum X(X^T WX)^{-1}, \quad \sum \equiv w[E(yy^T) - E(y)E(y^T)]w & (24) \end{aligned}$$

Because $E(y_i y_j) - E(y_i)E(y_j) = 0$ and $E(y_i^2) - E(y_i)E(y_i) = \sigma^2(x_i)$, matrix $\sum$ is a diagonal matrix with diagonal component $\sum_{ii} = K^2(\frac{x_i - x_o}{h})\sigma^2(x_i)$. To estimate the variance, $\sigma^2(x_i)$ need to be estimated and then substitute to the above equation to get $var(\hat{\beta})$. Here the residual variance is used to estimate $\sigma^2(x_i)$ (eqn. 25).

$$\sigma^2(x_i) = \{y_i - \hat{m}(x_i)\}^2, \text{ where } \hat{m}(x_i) \text{ is the kernel regression at } x = x_i \tag{25}$$

For estimating the bias of kernel regression, the results for the kernel regression at several bandwidth are used to fit a model for the expectation of $\hat{m}(x;h)$ as a function of h. For zero-order kernel regression($p =$

0), we fit the $\hat{m}(x;\alpha)$ using a linear function, where α is the coefficient that the test bandwidth over the original bandwidth (eqn. 26).

$$\hat{m}(x_o;\alpha) = c_o + k\alpha \tag{26}$$

In application, we change α from 0.2 to 2 for fitting purpose, then the Bias term could be estimated by:

$$Bias \approx \hat{m}_o(x_o,1) - c_o = k \tag{27}$$

which is essentially the slope of the linear function.

A.3 Testing MSE estimation of kernel density estimator

The samples are generated based on the joint PDF in eqn. 28. The kernel density estimation from these samples are in good agreement with the true joint PDF (fig.1). The mean square error estimation (fig.2b) using bootstrap method also agrees very well with the real mean square error (figs.2a) which validate the method for estimating the uncertainty of kernel density estimator.

$$f_{xy}(X,Y) = \frac{1}{5}\frac{1}{2\pi}(e^{-\frac{X^2+Y^2}{2}} + e^{-\frac{(X-1)^2+(Y-1)^2}{2}} + e^{-\frac{(X-1)^2+(Y+1)^2}{2}} + e^{-\frac{(X+1)^2+(Y-1)^2}{2}} + e^{-\frac{(X+1)^2+(Y+1)^2}{2}}) \tag{28}$$

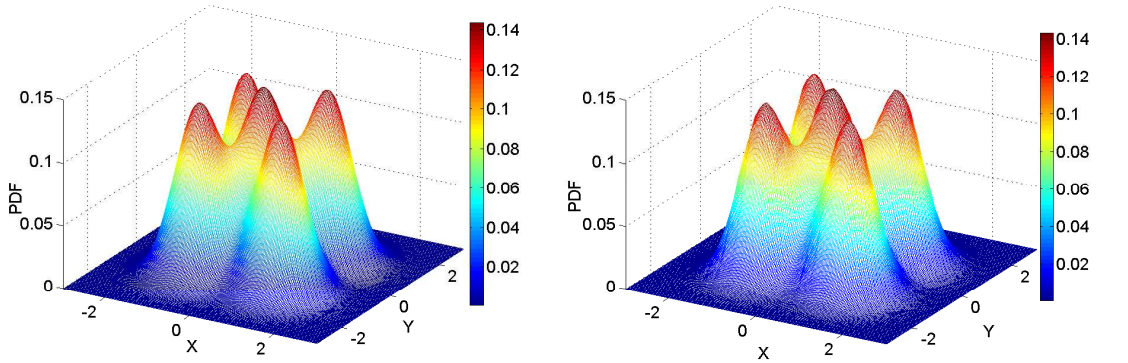

(a) (b)

Figure 1: (a)Multi-normal PDF, (b) kernel density estimation

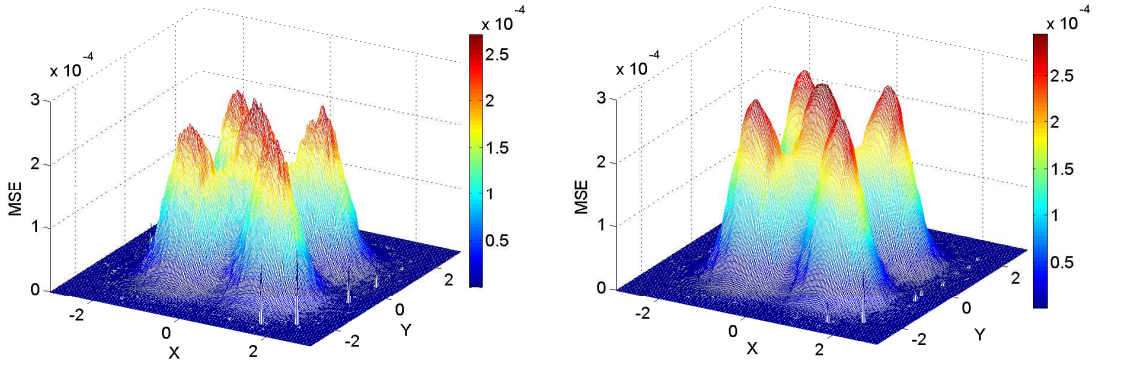

Figure 2: (a)Real mean square error, (b) estimated mean square error

A.4 Testing MSE estimation of kernel regression

The samples are generated base on $y = x + 2exp(= 16x^2) + \varepsilon$, where x is from the uniform distribution and ξ is from the standard normal distribution (fig. 3a). Figure 3b shows the kernel regression result which is almost identical with the true regression function. Figure 2 shows the bias and variance estimation using the method in [96, 97]. The estimated bias and variance agree very well with the real bias and variance, hence the method for estimating the bias and variance of kernel regression is validated.

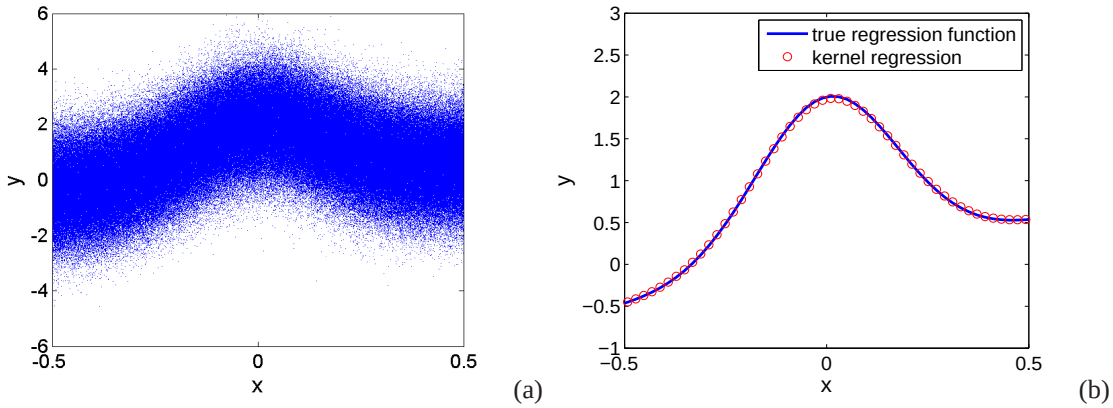

Figure 3: (a) Random samples, (b) true regression function and kernel regression

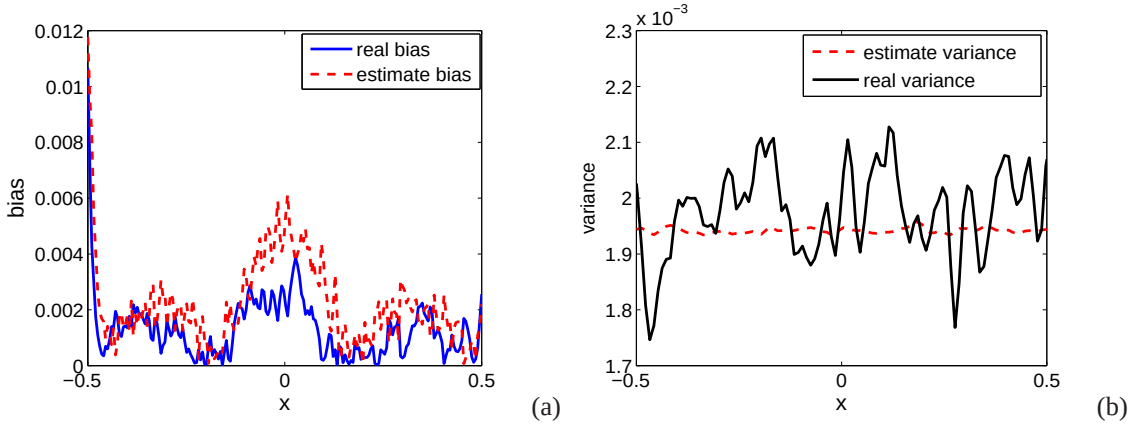

Figure 4: (a) Real bias and bias estimation, (b) real variance and variance estimation

Appendix B Statistical uncertainty estimation using bootstrap method

The root mean square (r.m.s) and bias for the JMDF are estimated using the bootstrap method [65] in the context of kernel density estimator. The structure of the r.m.s and the magnitude of bias is similar to its JMDF with large values near the JMDF ridgeline and small values near the boundary. For flame D, the maximum r.m.s values of the JMDF is generally less than 10% of the JMDF peak value at $x/D = 7.5$ and 30 and rises slightly at $x/D = 15$ due to the extend of JMDF in the extinction region. The magnitude of bias is comparable to the r.m.s at $x/D = 7.5$. At $x/D = 15$ and 30 the bias dominant the mean square error except for Y_{CO_2}, its peak value is generally two or three times as the peak value of r.m.s. The combined error (MSE) is typically less than $20\% - 30\%$ of the JMDF peak value. For flame E, the conclusion is similar to those in flame D. Figure 5 shows the r.m.s and magnitude of bias of the JMDF of ξ, T and Y_{CO} at $x/D = 7.5$ and 15 in flame D. In conclusion, the estimated r.m.s and bias of the JMDF are comparable to the systematic uncertainty in the species data [61].

The r.m.s and bias for the conditional dissipation rate and conditional diffusion velocity are estimated using the method described in appendix A. The r.m.s uncertainty of the conditional dissipation rate is typically less than 10% of the peak dissipation value for all the species and locations. However, unlike the case for JMDF, the bias term dominates the statistical uncertainty for all the cases. The maximum magnitude of the bias is generally two or three times larger than the peak value of r.m.s, which make the peak value of MSE as large as 30% of the peak dissipation rate. Though the MSE is not small, it is not sufficiently large to significantly alter the structure of the conditional dissipation rate because the peak value is often five to ten times larger than the mean value. Figure 6 shows the r.m.s and the magnitude of bias of the conditional dissipation rate of Y_{CO} at $x/D = 7.5$ and 15 in flame D. The statistical uncertainty for the conditional diffusion is almost the same as those for conditional dissipation rate, with bias dominates the MSE. The peak MSE is about 30% of the peak diffusion velocity magnitude.

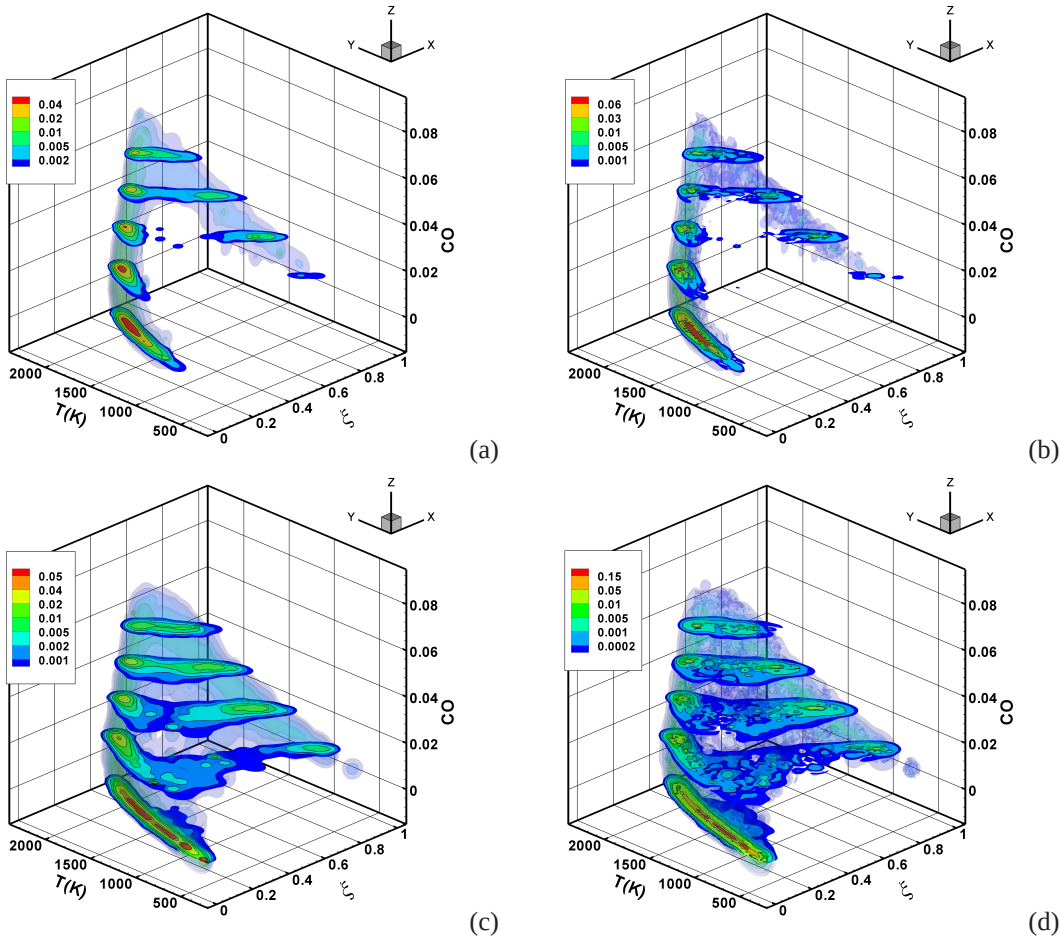

Figure 5: Estimated r.m.s (a,c) and magnitude of bias (b,d) for the JMDF of ξ, T and Y_{CO} at $x/D = 7.5,\ r/D = 1.04$ (a,b) and $x/D = 15,\ r/D = 1.34$ (c,d) in flame D.

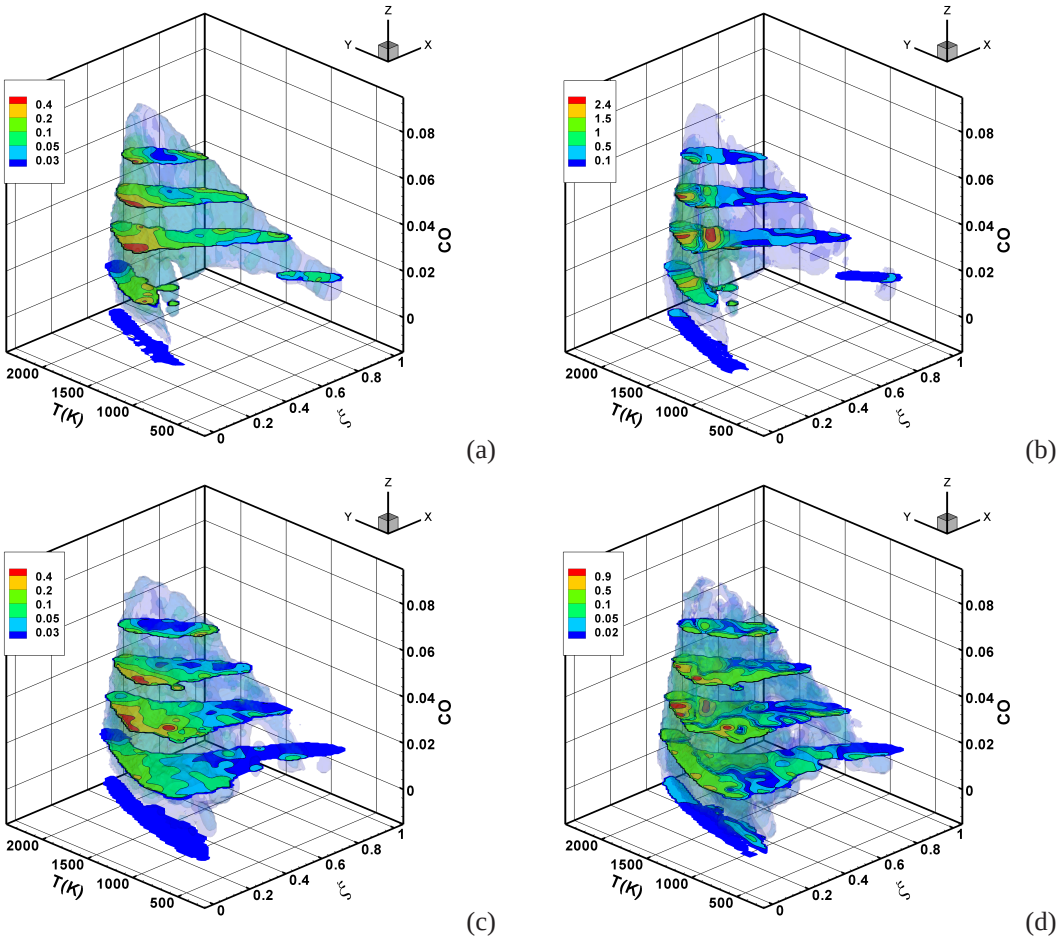

Figure 6: Estimated r.m.s (a,c) and magnitude of bias (b,d) for the conditional dissipation of Y_{CO} at $x/D = 7.5,\ r/D = 1.04$ (a,b) and $x/D = 15,\ r/D = 1.34$ (c,d) in flame D.

Appendix C Testing for Navier-Stokes characteristic boundary conditions

Navier-Stokes characteristic boundary conditions (NSCBC) usually assume that the incoming acoustic wave amplitudes are imposed at the flow boundary which can be regarded as locally one dimensional [76]. Recently Lodato et al. [75] extend the NSCBC to include transverse terms (3DNSCBC) which they showed a drastic reduction of flow distortion and numerical refection under 3DNSCBC. Here we tested both NSCBC and 3DNSCBC to ensure the boundary treatment is correct for current code.

The first test case is a two-dimensional compressible vortex convected through a non-reflecting outflow boundary which is typical test use to evaluate boundary conditions for turbulent flow simulations. The initial flow field can be expressed in terms of stream functions as,

$$\Psi = C_v exp\left(-\frac{r^2}{2R_v^2}\right) + U_0 x_2, \tag{29}$$

$$P(r) = P_\infty exp\left[-\frac{\gamma}{2}\left(\frac{C_v}{cR_v}\right)^2 exp\left(-\frac{r^2}{2R_v^2}\right)\right] \tag{30}$$

where C_v, R_v, U_0, P_∞, T_0, c, γ and r are vortex strength, vortex radius, speed of the uniform flow field along x_1, reference pressure, reference temperature, speed of sound, heat capacity ratio, and the radial distance from the reference frame, respectively. For the present test, C_v and R_v were set at $0.005m^2/s$, and 10% of the domain size. U_0,P_∞, T_0 were set to be $200m/s$, 1 atm, and 300 K, respectively, with corresponding Mach number 0.575 [75]. The computational domain is a square of dimension $0.0130m \times 0.013m$ with uniform inlet velocity at the left boundary, and non-reflecting outflow for other three boundaries.

Figures 7&8 show the results obtained by NSCBC and 3DNSCBC. The quantities for comparison are the pressure, the longitudinal velocity and the velocity gradient tensor invariant defined as $Q = -\frac{1}{2}\frac{\partial u_i}{\partial x_j}\frac{\partial u_j}{\partial x_j}$. The frame have been taken in three different times with time increasing from top to bottom. The pressure is normalized by the reference pressure and the initial pressure at the center of the vortex $(P(\mathbf{x},t) - P_\infty)/(P(\mathbf{0},0) - P_\infty)$. In figures 7&8 it's clear that the pressure, longitudinal velocity and vorticity contours undergo significant distortion for NSCBC at the boundary and even the pressure field far away from the boundary is contaminated. For 3DNSCBC, only the pressure contours show some notable distortions at the boundary when the vortex leave the domain.

The second test case is a three dimensional flow configuration for spherical pressure wave passing

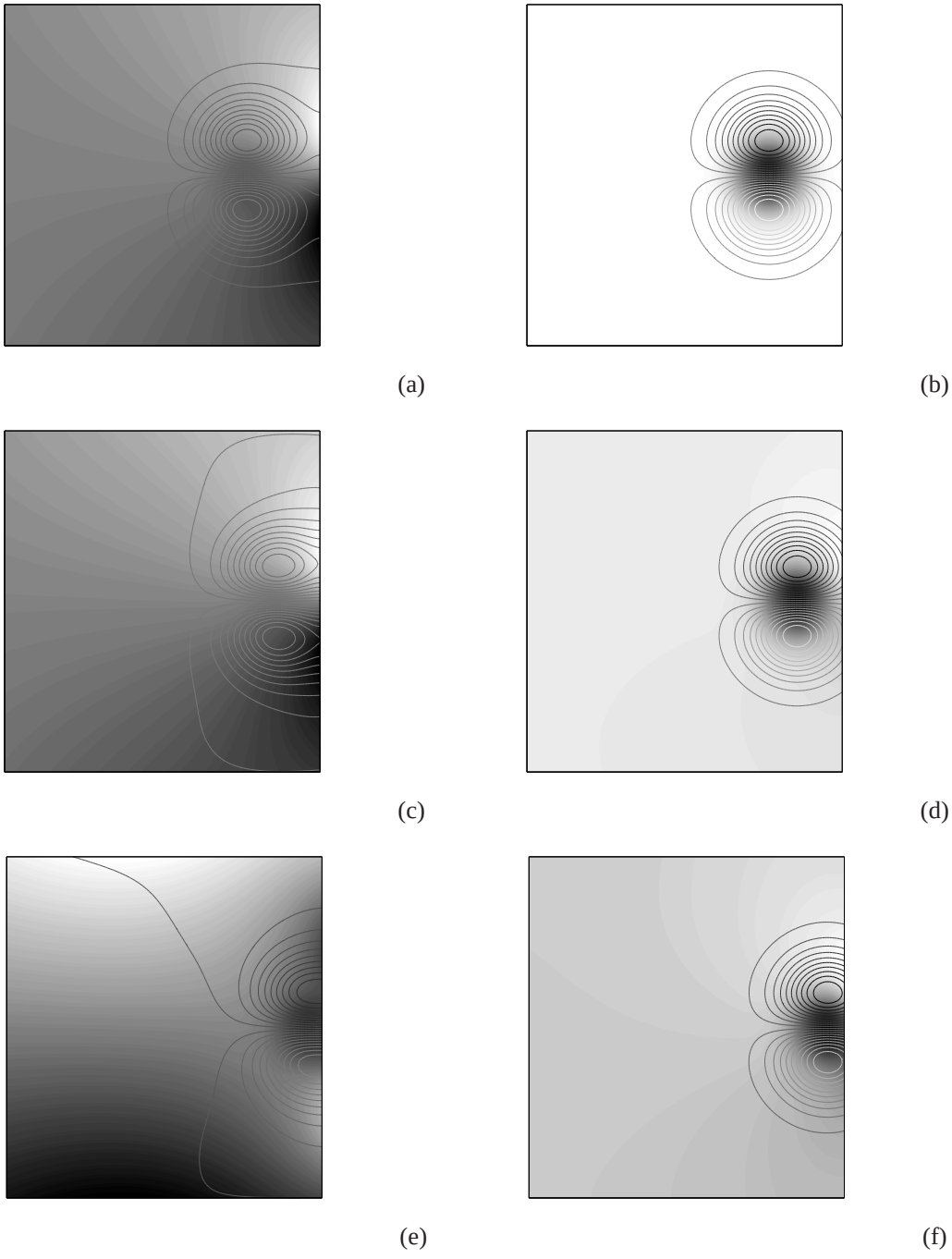

Figure 7: Normalized pressure field and longitudinal velocity contours for 2D vortex test. (a,c,e) Standard NSCBC; (b,d,f) 3D-NSCBC. Frames at increasing time from top to bottom.

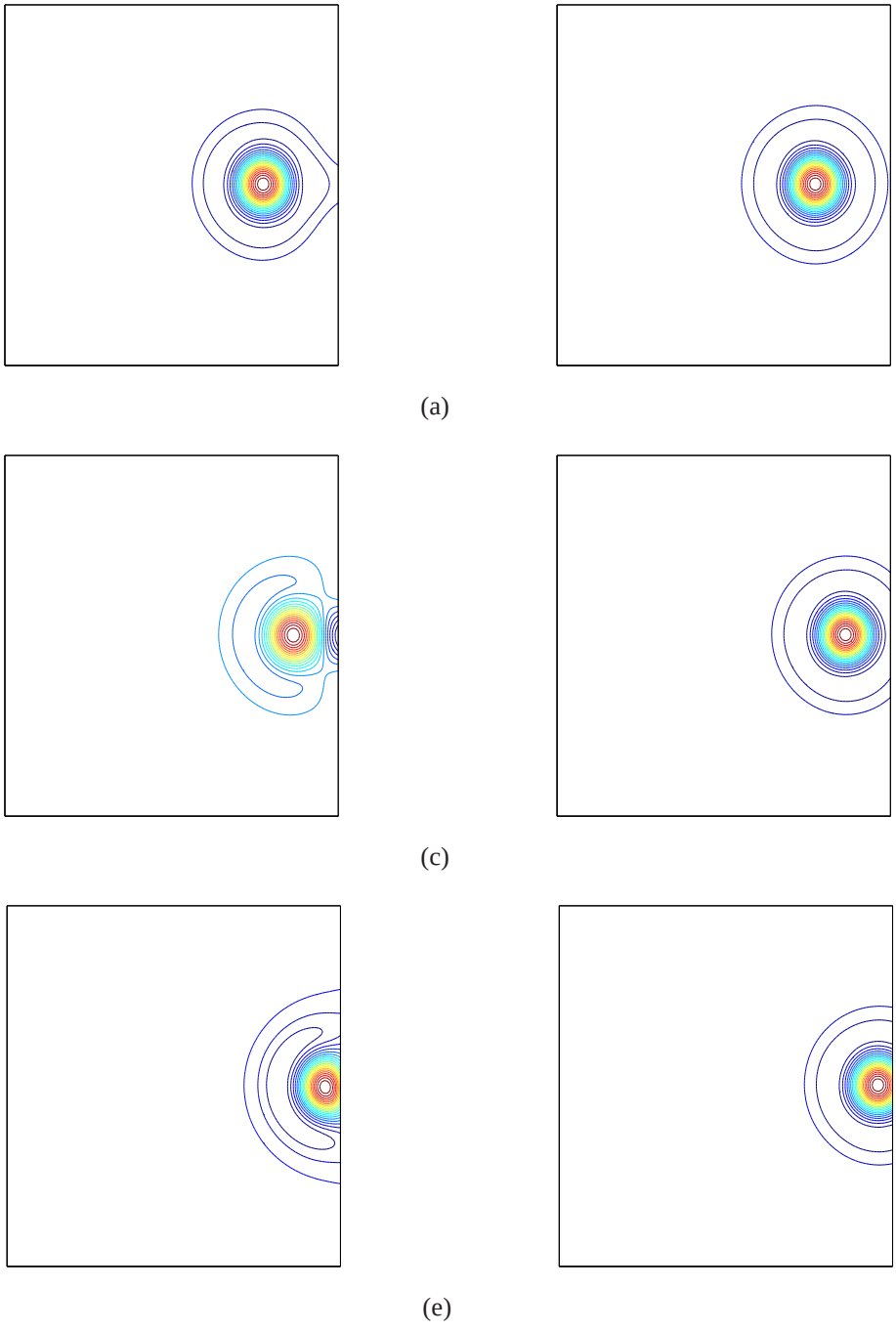

Figure 8: Q contours for 2D vortex test. (a,c,e) Standard NSCBC; (b,d,f) 3D-NSCBC. Frames at increasing time from top to bottom.

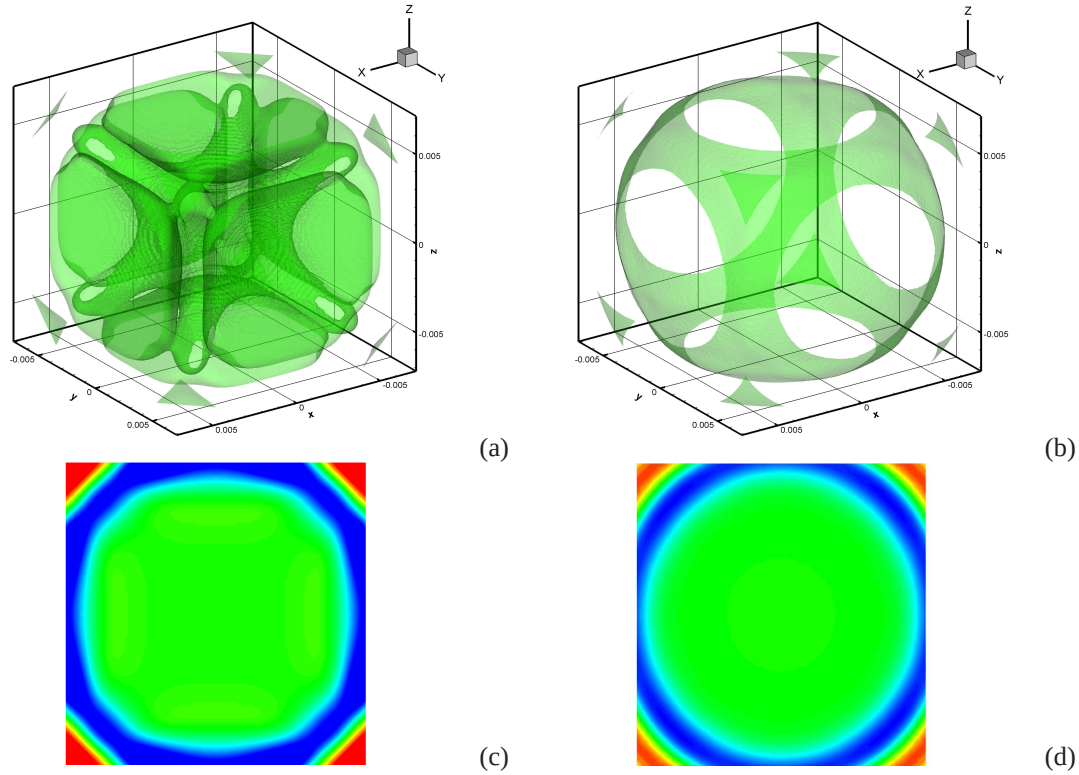

Figure 9: Spherical pressure iso-surface and contours (a,c) standard NSCBC non-reflecting outflows, (b,d) 3D-NSCBC non-reflecting outflows.

through the boundaries. The computational domain is a cube with dimension $L = 0.013m$. The boundaries for the six faces, 12 edges and 8 corners are treated as non-reflecting outflow type. The initial pressure filed with a pulse of amplitude δ is defines as

$$P(r) = P_\infty \left[1 + \delta exp\left(-\frac{r^2}{2R_P^2}\right)\right]. \tag{31}$$

For the present test, $delta$, P_∞, T_0 was set to be 0.001, 1 atm, and 300 K, respectively. R_p was set at 5% of the domain size [75]. The flow field was initialized at rest and then left to evolve. We compare the evolution the spherical wavefront when it approaches the outflow boundary. Figure 9 shows the wavefront by means of pressure iso-surface and slice contours for NSCBC and 3DNSCBC. It's expected to be perfectly spherical. As it can be observed, the 3DNSCBC outflows allow the wavefront curvature to be preserved even when the pressure pulse is outside the computational domain. On the contrary, the pressure field calculated from NSCBC shows significant distortion on the core pressure field and the wave front surface.

To sum up, the treatment of boundary condition in current code was tested and validated. From the

above results, it’s clear that 3DNSCBC can greatly reduce the flow distortion and numerical refection when compared to NSCBC. Hence, 3DNSCBC is used for all the simulations.

Bibliography

[1] Law, C., *Combustion Physics*, Cambridge University press, Cambridge, England, 2006.

[2] Peters, N., *Turbulent Combustion*, Cambridge University press, Cambridge, England, 2000.

[3] Haworth, D., Progress in probability density function methods for turbulent reacting flows, *Prog. Energy Combust. Sci.*, **36**:168–259 (2010).

[4] Pope, S. B., Computations of turbulent combustion: Progressand challenges, *Proc. Combust. Inst.*, **23**:591–612 (1990).

[5] Pope, S. B., Small scales, many species and the manifold challenges of turbulent combustion, *Proc. Combust. Inst.*, **34**:1–31 (2013).

[6] Pitsch, H., Large-Eddy Simulation of Turbulent Combustion, *Annu. Rev. Fluid Mech.*, **38**:453–82 (2006).

[7] Mare, F. D., P., J. W., and R., M. K., Large eddy simulation of a model gas turbine combustor, *Combust. Flame*, **137**:278–294 (2004).

[8] Kim, W. W., S., M., and C., M. H., Large-Eddy Simulation of a Gas Turbine Combustor Flow, *Combust. Sci. Tech.*, **143**:25–62 (1999).

[9] Haworth, D. C. and K., J., Large-eddy simulation on unstructured deforming meshes:towards reciprocating IC engines, *Computers & Fluids*, **29**:493–524 (2000).

[10] Selle, L., Lartigue, G., Poinsot, T., Koch, R., Schildmacher, K. U., Kerbs, W., Prade, B., Kaugmann, P., and Veynante, D., Compressible large eddy simulation of turbulent combustion in complex geometry on unstructured meshes, *Combust. Flame*, **137**:489–505 (2004).

[11] Boileau, M., G., S., B., C., Poinsot, T., and Berat, C., LES of an ignition sequence in a gas turbine engine, *Combust. Flame*, **154**:2–22 (2008).

[12] Ansari, N., Pisciuneri, P. H., Strakey, P. A., and Givi, P., Scalar-Filtered Mass-Density-Function Simulation of Swirling Reacting Flows on Unstructured Grids, *AIAA J.*, **50**:2476–2482 (2012).

[13] Pierce, D. C. and Moin, P., Progress-variable approach for large-eddy simulation of non-premixed turbulence combustion, *J. Fluid Mech.*, **504**:73–97 (2014).

[14] Pitsch, H. and Steiner, H., Large-eddy simulation of a turbulent piloted methane/air diffusion flame(Sandia flame D), *Phys. Fluids*, **12**:2541–2554 (2000).

[15] James, S., Zhu, H., and Anand, M. S., Large eddy simulations of turbulent flames using the filtered density function model, *Phys. Fluids*, **31**:1737–1745 (2007).

[16] Raman, V., Pitsch, H., and Fox, R. O., Hybrid large-eddy simulation/Lagrangian filtered-density-function approach for simulating turbulent combustion, *Combust. Flame*, **143**:56–78 (2005).

[17] Jones, W. P., Martinez, S. N., and Rohl, O., Large eddy simulation of hydrogen auto-ignition with a probability density function method, *Combust. Flame*, **31**:1765–1771 (2007).

[18] Ihme, M. and Pitsch, H., Prediction of extinction and reignition in nonpremixed turbulent flames using a flamelet/progress variable model 2. Application in LES of Sandia flames D and E, *Combust. Flame*, **155**:90–107 (2008).

[19] Pitsch, H. and Lageneste, L., Large eddy simulation of premixed turbulent combustion using a level-set approach, *Proc. Combust. Inst.*, **29**:2001–2008 (2002).

[20] Hawkes, E. R. and Cant, R. S., A flame surface density approach to large-eddy simulation of premixed turbulent combustion, *Proc. Combust. Inst.*, **28**:67–73 (2000).

[21] Hawkes, E. R. and Cant, R. S., Large eddy simulations of an acoustically excited turbulent premixed flame, *Proc. Combust. Inst.*, **28**:51–58 (2000).

[22] Sheikhi, M., Drozda, T., Givi., P., Jaberi, F., and Pope, S., Large eddy simulation of a turbulent non-premixed piloted methane jet flame (Sandia Flame D), *Proc. Combust. Inst.*, **30**:549–556 (2005).

[23] Pope, S. B., *Turbulent Flows*, Cambridge University press, Cambridge, England, 2000.

[24] Bilger, R. W., Turbulent diffusion flames, *Ann. Rev. Fluid Mech.*, **21**:101–135 (1989).

[25] Lockwood, F. C. and Naguib, A. S., The prediction of the fluctuations in the properties of free, round-jet, turbulent, diffusion lames, *Combust. Flame*, **24**:109–124 (1975).

[26] Ihme, M. and Pitsch, H., Prediction of extinction and reignition in nonpremixed turbulent flames using a flamelet/progress variable model 1. A priori study and presumed PDF closure, *Combust. Flame*, **155**:70–89 (2008).

[27] Gao, F. and OBrien, E. E., A Large-eddy simulation scheme for turbulent reacting flows, *Phys. Fluids A*, **5**:1282–1284 (1993).

[28] Colucci, P. J., Jaberi, F. A., Givi, P., and Pope, S. B., Filtered density function for large eddy simulation of turbulent reacting flows, *Phys. Fluids*, **10**:499–515 (1998).

[29] Jaberi, F. A., Colucci, P. J., James, S., Givi, P., and Pope, S. B., Filtered mass density function for large eddy simulation of turbulent reacting flows, *J. Fluid Mech.*, **401**:85–121 (1999).

[30] Gicquel, L. Y. M., Givi, P., Jaberi, F. A., and Pope, S. B., Velocity filtered density function for large eddy simulation of turbulent flows, *Phys. Fluids*, **14**:1196–1213 (2002).

[31] Sheikhi, M. R. H., Drozda, T. G., Givi, P., and Pope, S. B., Velocity-scalar filtered density function for large eddy simulation of turbulent flows, *Phys. Fluids*, **15**:2321–2337 (2003).

[32] Sheikhi, M. R. H., Givi, P., and Pope, S. B., Velocity-scalar filtered mass density function for large eddy simulation of turbulent reacting flows, *Phys. Fluids*, **19**:095106 (2007).

[33] Sheikhi, M. R. H., Givi, P., and Pope, S. B., Frequency-velocity-scalar filtered mass density function for large eddy simulation of turbulent flows, *Phys. Fluids*, **21**:075102 (2009).

[34] Bilger, R. W., The structure of turbulent nonpremixed flames, in *Proceedings of the Twenty-Second Symposium (International) on Combustion*, pp. 475–488, 1988.

[35] Wang, D. and Tong, C., Conditionally filtered scalar dissipation, scalar diffusion, and velocity in a turbulent jet, *Phys. Fluids*, **14**:2170–2185 (2002).

[36] Wang, D. and Tong, C., Experimental study of velocity-scalar filtered joint density function for LES of turbulent combustion, *Proc. Combust. Inst.*, **30**:567–574 (2005).

[37] Rajagopalan, A. G. and Tong, C., Experimental investigation of scalar-scalar-dissipation filtered joint density function and its transport equation, *Phys. Fluids*, **15**:227–244 (2003).

[38] Wang, D., Tong, C., and Pope, S. B., Experimental study of velocity filtered joint density function and its transport equation, *Phys. Fluids*, **16**:3599–3613 (2004).

[39] Tong, C., Measurements of conserved scalar filtered density function in a turbulent jet, *Phys. Fluids*, **13**:2923–2937 (2001).

[40] Wang, D., Tong, C., Barlow, R. S., and Karpetis, A. N., Experimental study of scalar filtered mass density function in turbulent partially premixed flames, *Proc. Combust. Inst.*, **31**:1533–1541 (2007).

[41] Cai, J., Barlow, R. S., Karpetis, A. N., and Tong, C., Noise correction and length scale estimation for scalar dissipation rate measurements in turbulent pratially premixed flames, *Flow,Turb. Combust.*, **85**:309–332 (2010).

[42] Cai, J., Wang, D., Tong, C., Barlow, R. S., and Karpetis, A. N., Investigation of subgrid-scale mixing of mixture fraction and temperature in turbulent partially premixed flames, *Proc. Combust. Inst.*, **32**:1517–1525 (2009).

[43] Cai, J., Barlow, R. S., Karpetis, A. N., and Tong, C., Conditionally filtered diffusion of mixture fraction and temperature in turbulent partially premixed flames, *Proc. Combust. Inst.*, **33**:1505–1513 (2011).

[44] Subramaniam, S. and Pope, S. B., A Mixing Model for Turbulent Reactive Flows based on Euclidean Minimum Spanning Trees, *Combust. Flame*, **115**:487–514 (1998).

[45] Fox, R. D., *Computational Models for Turbulent Reacting Flows*, Cambridge University press, Cambridge, England, 2003.

[46] Meyer, D. W. and Jennt, P., A mixing model for turbulent flows based on parameterized scalar profiles, *Phys. Fluids*, **18**:035105 (2006).

[47] Pope, S., PDF methods for turbulent reactive flows, *Prog. Energy Combust. Sci.*, **11**:119–192 (1985).

[48] Anand, M. S. and Pope, S. B., Calculations of premixed turbulent flames by PDF methods, *Combust. Flame*, **67**:127–42 (1987).

[49] Pope, S. B. and Anand, M. S., Flamelet and distributed combustion in premixed turbulent flames, *Proc. Combust. Inst.*, **20**:403–10 (1984).

[50] Cai, J., Dinger, M. J., Li, W., Carter, C. D., Ryan, M. D., and Tong, C., Experimental study of three-scalar mixing in a turbulent coaxial jet, *J. Fluid Mech.*, **685**:495–531 (2011).

[51] Rowinski, D. H. and Pope, S. B., An investigation of mixing in a three-stream turbulent jet, *Phys. Fluids*, **25**:105105 (2013).

[52] Balarac, G., Si-Ameur, M., Lesieur, M., and Métais, O., Direct numerical simulations of high velocity ratio coaxial jets: mixing properties and influence of upstream conditions, *J. Turbulence*, **8**(22):1–27 (2007).

[53] Silva, C. B., Balarac, G., and Metais, O., Transition in high velocity ratio coaxial jets analysed from direct numerical simulations, *J. Turbulence*, **4**:24 (2003).

[54] Balarac, G., Metais, O., and Lesieur, M., Mixing enhancement in coaxial jets through inflow forcing: A numerical study, *Phys. Fluids*, **19**:075102 (2007).

[55] Balarac, G. and Metais, O., The near field of coaxial jets: A numerical study, *Phys. Fluids*, **17**:065102 (2005).

[56] Villermaux, E. and Rehab, H., Mixing in coaxial jets, *J. Fluid Mech.*, **425**:161–185 (2000).

[57] Rehab, H., Villermaux, E., and Hopfinger, E. J., Flow regimes of large-velocity-ratio coaxial jets, *J. Fluid Mech.*, **345**:357–381 (1997).

[58] Karpetis, A. N. and Barlow, R. S., Measurements of flame orientation and scalar dissipation in turbulent partially premixed methane flames, *Proc. Combust. Inst.*, **30**:665–672 (2005).

[59] Barlow, R. S. and Karpetis, A. N., Measurements of scalar variance, scalar dissipation, and length scales in turbulent piolted methane/air jet flames, *Flow, Turb. Combust.*, **72**:427–448 (2004).

[60] Tong, C., Wyngaard, J. C., Khanna, S., and Brasseur, J. G., Resolvable- and subgrid-scale measurement in the atmospheric surface layer: technique and issues, *J. Atmos. Sci.*, **55**:3114–3126 (1998).

[61] Wang, G., Karpetis, A. N., and Barlow, R. S., Dissipation length scales in turbulent nonpremixed jet flames, *Combust. Flame*, **148**:62–75 (2007).

[62] Cai, J., Dinger, M. J., Li, W., Carter, C. D., Ryan, M. D., and Tong, C., Experimental study of three-scalar mixing in a turbulent coaxial jet, *J. Fluid Mech.*, **685**:495–531 (2011).

[63] Barlow, R. S., H., F. J., A.N., K., and J.-Y., C., Piloted methane/air jet flames: transport effects and aspects of scalar structure, *Combust. Flame*, **143**:433–449 (2005).

[64] Barlow, R. S. and Karpetis, A. N., Scalar length scales and spatial averaging effects in turbulent piloted methane/air jet flames, *Proc. Combust. Inst.*, **30**:673–680 (2005).

[65] Hall, P., Using the bootstrap to estimate mean squared error and select smoothing parameter in non-parametric problems, *J. Multivariate Anal*, **32**:177–203 (1990).

[66] Haworth, D. C., Drake, M. C., and Pope, S. B., A probability density function/flamelet method for partially premxied turbulent combustion, *Proc. Combust. Inst.*, **22**:589–597 (1988).

[67] Pope, S. B., Turbulent premixed flames, *Annu. Rev. Fluid Mech.*, **19**:237–270 (1987).

[68] Bilger, R. W., Perturbation Analysis of Turbulent Nonpremixed Combustion, *Combust. Sci. Tech.*, **22**:251–261 (1980).

[69] Karpetis, A. N. and Barlow, R. S., Measurements of scalar dissipation in turbulent piloted methane/air jet flames, *Proc. Combust. Inst.*, **29**:1929–1936 (2002).

[70] Pitsch, H., *FlameMaster v3.31, A C++ Computer Program for 0D Combustion and 1D Laminar Flame Calculations.*

[71] Smith, G. P., Golden, D. M., Frenklach, M., Moriarty, N. W., Eiteneer, B., Goldenberg, M., Bowman, C. T., Hanson, R. K., Song, S., Gardiner, W. C., Lissianski, J. V. V., and Qin, Z., *http://www.me.berkeley.edu/gri_mech/*.

[72] Barlow, R. S., A.N., K., H., F. J., and J.-Y., C., Scalar Profiles and NO Formation in Laminar Opposed-Flow Partially Premixed Methane/Air Flames, *Combust. Flame*, **127**:2102–2118 (2001).

[73] Lignell, D. O., Chen, J. H., and Schmutz, H. A., Effects of Damkohler number on flame extinction and reignition in turbulent non-premixed flames using DNS, *Combust. Flame*, **158**:949–963 (2011).

[74] Kennedy, C. A. and Carpenter, M. H., Several new numerical methods for compressible shear-layer simulations, *Appl. Numer. Math.*, **14**:397–433 (1994).

[75] Lodato, G., Domingo, P., and Vervisch, L., Three-dimensional boundary conditions for direct and large-eddy simulation of compressible viscous flows, *J. Comp. Phys.*, **227**:5105–5143 (2008).

[76] Poinsot, T. J. and Lele, S. K., Boundary conditions for Direct Simulations of Compressible Viscous Flows, *J. Comp. Phys.*, **101**:104–129 (1992).

[77] Hawkes, E. R., Sankaran, R., Sutherland, J. C., and Chen, J. H., Scalar mixing in direct numerical simulations of temporally evolving plane jet flames with skeletal CO/H2 kinetics, *Proc. Combust. Inst.*, **31**:1633–1640 (2007).

[78] Davidson, L. and Billson, M., Hybrid LES-RANS using synthesized turbulent fluctuations for forcing in the interface region, *International Journal of Heat and Fluid Flow*, **27**:1028–1042 (2006).

[79] Wygnanski, I. and Fiedler, H., Some measurements in the self-preserving jet, *J. Fluid Mech.*, **38**:577–612 (1969).

[80] Wygnanski, I. and Fiedler, H., Velocity measurements in a high-Reynolds-number, momentum-conserving, axisymmetric, turbulent jet, *J. Fluid Mech.*, **258**:31–75 (1994).

[81] Panchapakesan, N. R. and Lumley, J. L., Turbulence measurements in axisymmetric jets of air and helium. Part 1. Air jet., *J. Fluid Mech.*, **246**:197–223 (1992).

[82] Picano, F. and Casciola, C. M., Small-scale isotropy and universality of axisymmetric jets, *Phys. Fluids*, **19**:118106 (2007).

[83] Boersma, B. J., Brethouwer, G., and Nieuwstadt, G., A numerical inverstigation on the effect of the inflow conditions on the self-similar region of a round jet, *Phys. Fluids*, **10**:899–909 (1998).

[84] Wang, Z., He, P., Lv, Y., Zhou, J., Fan, J., and Cen, K., Direct Numerical Simulation of Subsonic Round Turbulent Jet, *Flow,Turb. Combust.*, **84**:669–686 (2010).

[85] Klein, M., Sadiki, A., and Janicka, J., A digital filter based generation of inflow data for spatially developing direct numerical or large eddy simulations, *J. Comp. Phys.*, **186**:652–665 (2003).

[86] Gutmark, E. and Wygnansky, I., The planar turbulent jet, *J. Fluid Mech.*, **73**:465 (1976).

[87] Ramparian, R. and Chandrasekhara, M. S., LDA measurements in plane turbulent jets, *ASME J. Fluids Eng.*, **107**:264 (1985).

[88] Thomas, F. O. and Prakash, K. M. K., An investigation of the natural transition of an untuned planar jet, *Phys. Fluids A*, **3**:90 (1991).

[89] S, S. and Sarkar, S. Mellado, J. P., A study of the flowfield evolution and mixing in a planar turbulent jet using direct numerical simulation, *J. Fluid Mech.*, **450**:377 (2002).

[90] Silva, C. B. and Pereira, J. C. F., Invariants of the velocity-gradient, rate-of-strain, and rate-of-rotation tensors across the turbulent/nonturbulent interface in jets, *Phys. Fluids*, **20**:055101 (2008).

[91] Silva, C. B. and Metais, O., On the influence of coherent structures upon interscale interactions in turbulent plane jets, *J. Fluid Mech.*, **408**:83 (2002).

[92] Silva, C. B. and Pereira, J. C. F., The effect of subgrid-scale models on the vortices obtained from large-eddy simulations, *Phys. Fluids*, **16**:4506 (2004).

[93] Krisman, A., Tang, J. C. K., Hawkes, E. R., Lignell, D. O., and Chen, J. H., A DNS evaluation of mixing models for transported PDF modelling of turbulent nonpremixed flames, *Combust. Flame*, **161**:2085–2106 (2014).

[94] Akhavan, R., Ansari, A., Kang, S., and Mangiavacchi, N., Subgrid-scale interactiosn in a numerically simulated planar turblent jet and implications for modelling, *J. Fluid Mech.*, **408**:83–120 (2000).

[95] Faraway, J. J. and Jhun, M., Bootstrap Choice of Bandwidth for Density Estimation, *J. Am. Stat. Assoc.*, **85**:1119–1122 (1990).

[96] Fan, J. and Gijbels, I., Data-driven Bandwidth Selection in Local Polynomial Fitting: Variable Bandwidth and Spatial Adaptation, *J. R. Statist. Soc. B*, **2**:371–394 (1995).

[97] Ruppert, D., Empirical-bias bandwidths for local polynomial nonparametric regression and density estimation, *J. Am. Stat. Assoc.*, **92**:1049–1062 (1997).